

**UNDERSTANDING GDL PROPERTIES AND PERFORMANCE IN POLYMER
ELECTROLYTE FUEL CELLS**

by

AHMAD EL-KHAROUF

A thesis submitted to the

University of Birmingham

for the degree of

DOCTOR OF PHILOSOPHY

UNIVERSITY OF
BIRMINGHAM

University of Birmingham Research Archive

e-theses repository

This unpublished thesis/dissertation is copyright of the author and/or third parties. The intellectual property rights of the author or third parties in respect of this work are as defined by The Copyright Designs and Patents Act 1988 or as modified by any successor legislation.

Any use made of information contained in this thesis/dissertation must be in accordance with that legislation and must be properly acknowledged. Further distribution or reproduction in any format is prohibited without the permission of the copyright holder.

Centre for Hydrogen and Fuel Cell Research

School of Chemical Engineering

College of Engineering and Physical Sciences

University of Birmingham

10th March 2014

DECLARATION

Hereby I, Ahmad El-kharouf, declare that the work presented in this thesis is my own with no help of more than the cited literature and auxiliary means.

I also confirm that this work has not been submitted to another examination office, neither in content nor in shape.

Date: 10th March 2014
Place: Birmingham, UK

Signature (Ahmad El-kharouf)

ACKNOWLEDGMENTS

This thesis marks the culmination of my PhD journey which I started in June 2010 at the Centre for Hydrogen and Fuel Cell research in the School of Chemical Engineering at the University of Birmingham. What was achieved in this period would not have been possible without the support and encouragement of family, friends, colleagues and supervisors.

Firstly, I would like to thank Professor Robert Steinberger-Wilckens and Dr. Shangfeng Du for their support and guidance during writing this thesis. I would like to thank the Centre for Hydrogen and Fuel Cell research for giving me the opportunity to do my research at the centre. I would like to thank members of the hydrogen and fuel cell research; colleagues, academics and administrators, for their help with the various aspects of the work and other matters during the project period. I also need to acknowledge the support I received from the late Dr. Waldemar Bujalski during critical periods in this project.

Thank you to Dr. Thomas Mason and Dr. Dan Brett for their collaboration. Also, thank you to Dr James Bowen for his support in using the facilities in the Advanced Materials Lab (Part of Birmingham science city initiative funded by Advantage West Midlands).

Finally, I would like to say a massive THANK YOU to my dear family and friends, whom without I would not have managed to get here. ☺

ABSTRACT

Each component in a Polymer Electrolyte Fuel Cell (PEFC) plays a vital part in the cells' performance and durability. The Gas Diffusion Layer (GDL) has the important role of transporting the reactants into, and products out of the cell. This study aims to provide insights for understanding the relationship between GDL properties and the performance of PEFCs.

Ex-situ characterisation techniques were employed to study the mechanical, physical and electrical properties of the GDL. The relationship between the various properties of GDL was investigated and discussed in this work. The study shows that characteristics such as GDL thickness, bulk density, PTFE and MPL content, porosity, hydrophobicity, permeability and electrical conductivity are closely connected. An enhanced understanding of these properties is essential for the development and optimization of GDLs and hence PEFC performance.

The effect of compression on the cathode GDL performance in PEFC membrane electrode assembly (MEA) is discussed using Polarisation (IV) curve and electrochemical Impedance Spectroscopy (EIS). Compression affects the electrical and mass transport properties of the GDL and therefore needs to be optimised. The performance of the MEA with controlled cathode GDL compression was optimised to achieve the maximum power of the MEA. The results show that there is an optimum compression point, at which; a minimum contact resistance and optimum water transport are achieved. The optimum compression level is dependent on the GDL properties. The optimum compression ratio varies for the different GDLs as a result of the difference in properties.

At optimum compression, the performances of the different GDL materials were compared to understand the effect of the GDL properties on the performance. It is clear that GDL properties primarily affect the mass transport ability and the ohmic polarisation of the MEA. GDL characteristics such as structure, thickness, bulk density, PTFE loading, and MPL presence have a direct effect on the MEA performance and need to be optimized for the different PEFC applications.

LIST OF PUBLICATIONS

1. **El-kharouf, A.**, Rees, N.V., Steinberger-Wilckens. Gas Diffusion Layer materials and Their Effect on Polymer Electrolyte Fuel Cell Performance – Ex-situ and In-situ Characterisation. *Fuel Cell - From Fundamentals to Systems*. Manuscript accepted
2. **El-kharouf, A.**, Rees, N.V., Steinberger-Wilckens. The Effect of compression on Membrane Electrode Assembly Performance: Changes in the Gas Diffusion Layer Properties and Performance. 4th European PEFC & H₂ Forum 2013. Proceedings. Submitted
3. **El-kharouf, A.**, Chandan, A., Sharma, S. Rees, N.V., Steinberger-Wilckens, R., Duraman, N., Taechakijviboon, T., Chan S. L.I., 2013. The Use of Carbon Nanotube Thin Films as a Microporous Layer for GDLs in Polymer Electrolyte Fuel Cells. 5th FDFC conference proceedings.
4. Chandan, A. Hattenberger, M., **El-kharouf, A.**, Du, S., Dhir, A., Self, V., Pollet, B.G., Ingram, A., Bujalski, W., 2013. High Temperature (HT) Polymer Electrolyte Membrane Fuel Cells (PEMFC) – A review. *Journal of Power Sources* 231, 264-278.
5. McCarthy, N., **El-kharouf, A.**, Chen, R., Bujalski, W., 2012. The Impact of Cathode Gas Diffusion Layer Structure on Fuel Cell Performance. 13th ABAF conference proceedings.
6. **El-kharouf, A.**, Chandan, A., Hattenberger, M., Pollet, B.G., 2012. Proton Exchange Membrane Fuel Cell degradation and testing: review. *Journal of the Energy Institute* 85, 188-200.
7. **El-kharouf, A.**, Mason, T.J., Brett, D.J.L., Pollet, B.G., 2012. Ex-situ Characterisation of Gas Diffusion Layers for Proton Exchange Membrane Fuel Cells. *Journal of Power Sources* 218, 393-404.
8. **El-kharouf, A.**, Pollet, B.G., 2012. Chapter 4: Gas Diffusion Media and Their Degradation. In: *Polymer Electrolyte Fuel Cell Degradation*. Academic Press, Boston, pp. 215 -247.
9. Mason, T.J., Millichamp, J., Neville, T.P., **El-kharouf, A.**, Pollet, B.G., Brett, D.J.L., 2012. Effect of Clamping Pressure on Ohmic Resistance and Compression of Gas Diffusion Layers for Polymer Electrolyte Fuel Cells. *Journal of Power Sources* 219, 52-59.

TABLE OF CONTENT

ACKNOWLEDGMENTS.....	ii
ABSTRACT	iii
LIST OF PUBLICATIONS.....	v
TABLE OF CONTENT.....	vi
LIST OF ILLUSTRATIONS.....	xii
LIST OF TABLES	i
LIST OF DEFINITIONS AND ABRIVIATIONS.....	ii
CHAPTER 1: INTRODUCTION.....	2
1.1 BACKGROUND.....	2
1.2 FUEL CELLS.....	5
1.3 POLYMER ELECTROLYTE FUEL CELL.....	7
1.4 THESIS OBJECTIVE AND OUTLINE	12
CHAPTER 2: LITERATURE REVIEW.....	15
2.1 GAS DIFFUSION LAYER MATERIALS.....	16
2.2 FABRICATION OF CARBON BASED GAS DIFFUSION LAYERS	17
2.3 GDL CHARACTERISTICS AND PEFC PERFORMANCE	19
2.3.1 GDL STRUCTURE AND SURFACE MORPHOLOGY.....	20
2.3.2 MECHANICAL PROPERTIES	23

2.3.3 TRANSPORT PROPERTIES OF THE GDL	25
2.3.4 HYDROPHOBIC AND HYDROPHILIC PROPERTIES	29
2.3.5 ELECTRICAL PROPERTIES.....	31
2.3.6 THERMAL CONDUCTIVITY	32
2.3.7 CLAMPING PRESSURE	33
2.4 GDL DEGRADATION.....	34
2.4.1 ELECTROCHEMICAL DEGRADATION	35
2.4.2 MECHANICAL DEGRADATION	37
2.4.3 THERMAL DEGRADATION	42
CHAPTER 3: METHODOLOGY AND EXPERIMENT	44
3.1 METHODOLOGY	44
3.2 EXPERIMENTS.....	46
3.2.1 EX-SITU CHARACTERISATION	46
Scanning Electron Microscopy (SEM)	46
Interferometer.....	46
Drop Shape Analyser	48
Helium Pycnometer.....	48
Mercury porosimeter	49
Environmental Mechanical Analyser	51
Universal Mechanical Tester (Zwick/Roell Z030)	52
4-wire Kelvin Milli/Micro-Ohmmeter.....	52

<i>In</i> -plane electrical resistance.....	52
Electrical contact resistance.....	53
3.2.2 <i>IN</i> -SITU CHARACTERISATION	56
MEA fabrication.....	56
PaxiTeck fuel cell fixture and Biologic Fuel Cell test station.....	57
CHAPTER 4: EX-SITU CHARACTERISATION OF GAS DIFFUSION LAYERS...	67
4.1 SAMPLES AND EXPERIMENTS	67
4.1.1 COMMERCIAL GDL SAMPLES	67
4.1.2 PHYSICAL PROPERTIES.....	67
4.1.3 ELECTRICAL PROPERTIES.....	69
4.2 RESULTS AND DISCUSSION.....	69
4.2.1 PHYSICAL PROPERTIES (THICKNESS AND DENSITY)	69
4.2.2 FIBRE STRUCTURE, SURFACE MORPHOLOGY AND ROUGHNESS.....	75
4.2.3 POROSITY, TORTUOSITY AND PORE SIZE DISTRIBUTION	82
4.2.4 PERMEABILITY.....	89
4.2.5 SURFACE WATER CONTACT ANGLE (HYDROPHOBICITY).....	90
4.2.6 ELECTRICAL CONDUCTIVITY AND CONTACT RESISTANCE	92
4.3 CONCLUSIONS.....	98
CHAPTER 5: THE EFFECT OF CLAMPING PRESSURE ON GAS DIFFUSION LAYER PERFORMANCE IN POLYMER ELECTROLYTE FUEL CELLS.....	100
5.1 SAMPLES AND EXPERIMENTS	100

5.1.1	EX-SITU TESTING	101
5.1.2	IN-SITU CHARACTERISATION	102
	MEA fabrication	102
	In-situ testing	103
5.2	RESULTS	104
5.2.1	EX-SITU TESTING: COMPRESSIBILITY MEASUREMENT	104
5.2.2	IN-SITU TESTING	107
5.3	DISCUSSION	117
5.3.1	CHANGE IN THE MEA PERFORMANCE WITH COMPRESSION FOR DIFFERENT GDL THICKNESSES	118
5.3.2	CHANGE IN THE MEA PERFORMANCE WITH COMPRESSION FOR DIFFERENT GDL DENSITIES	120
5.3.3	CHANGE IN THE MEA PERFORMANCE WITH COMPRESSION FOR DIFFERENT GDL STRUCTURES	124
5.4	Conclusions	128
CHAPTER 6: IN-SITU CHARACTERISATION OF GAS DIFFUSION LAYERS ..		130
6.1	SAMPLES AND EXPERIMENTS	130
6.1.1	SAMPLES	130
6.1.2	IN-SITU TESTING	131
6.2	RESULTS AND DISCUSSION	133
6.2.1	THE EFFECT OF GDL THICKNESS ON THE PERFORMANCE	133

6.2.2 THE EFFECT OF GDL DENSITY ON THE PERFORMANCE	137
6.2.3 THE EFFECT OF PTFE LOADING AND MPL APPLICATION ON THE GDL PERFORMANCE	141
6.2.5 THE EFFECT OF THE GDL STRUCTURE ON THE PERFORMANCE	152
6.3 CONCLUSIONS	159
CHAPTER 7: SUMMARY	162
7.1 CONCLUSIONS	162
7.2 FUTURE WORK.....	164
APPENDIX A1: GDL MANUFACTURERS DATASHEETS	- 2 -
A1.1 BALLARD GDLs DATASHEET	- 2 -
A1.2 SIGRACET GDLs DATASHEET	- 3 -
A1.3 TORAY GDLs DATASHEETS	- 4 -
A1.4 FREUDENBERG GDLs DATASHEET	- 5 -
A1.5 ETEK GDLs DATASHEET	- 6 -
APPENDIX A2: CATHODE ELECTRODE FABRICATION	- 7 -
APPENDIX A3: <i>EX-SITU</i> RESULTS- SEM IMAGING	- 14 -
APPENDIX A5: EFFECT OF CLAMPING PRESSURE ON OHMIC RESISTANCE AND COMPRESSION OF GAS DIFFUSION LAYERS FOR POLYMER ELECTROLYTE FUEL CELLS – published paper.....	- 25 -

LIST OF ILLUSTRATIONS

Figure 1.1:	World energy demand increase by resources	3
Figure 1.2:	PEFC components, materials and operation	8
Figure 1.3:	Fuel cell polarisation curve	10
Figure 2.1:	GDL function in PEFC	16
Figure 2.2:	Conventional GDL fabrication process	19
Figure 2.3:	Effect of compression on carbon paper GDL structure	38
Figure 2.4:	Comparison of GDL surfaces in MPL water washing at various times: (a) Carbon paper substrate, (b) GDL with MPL, (c) GDL-1HR (in 1 hour water washing), (d) GDL-5HR (in 5 hour water washing), (e) GDL-10HR (in 10 hour water washing), (f) GDL-50HR (in 50 hour water washing), (g) GDL-100HR (in 100 hour water washing), (e) GDL-200HR (in 200 hour water washing)	40
Figure 3.1:	Research methodology	45
Figure 3.2:	(a) Interferometer showing the sample mounting stage and the objective lenses, (b) SGL 25BC image using the interferometer, (C) 3D structure of SGL 25BC and (d) Hysteresis in measured height over the sample surface.	47
Figure 3.3:	Water contact angle on (a) a hydrophobic surface and (b) a hydrophilic surface	48
Figure 3.4:	(a) Micromertics AutoPore IV Porosimeter, (b) capillary stem and (c) intrusion volume with increasing pressure.	50
Figure 3.5:	Electrical in-plane resistance measurement setup.	53
Figure 3.6:	Electrical contact resistance measurement setup	54

Figure 3.7:	MEA fabrication and testing	56
Figure 3.8:	Bio-logic test station used for MEA in-situ characterisation.	58
Figure 3.9:	MEA testing procedure	59
Figure 3.10:	The effect of the different impedance elements on AC signals	62
Figure 3.11:	EIS plot for JM electrode at different current densities	63
Figure 3.12:	Potential loss contribution of the different polarisations with the change in current density	64
Figure 3.13:	Fuel cell impedance equivalent circuit; a) Randle circuit and b) cell impedance including the mass transport losses	65
Figure 4.1:	SEM images of GDL fibres configuration; surface and edge views of a) & d) Woven fibres in carbon cloth –Ballard 1071HCB, b) and e) straight stretched fibres in carbon paper – Toray H-060, c)& f) Felt fibres in carbon paper- Freudenberg C2.	75
Figure 4.2:	SEM images of several types of woven carbon cloth sample; surface views of: a) Tenax b) Ballard 1071HCB, and c) ETEK 1200W and closer views of d) Tenax, e) Ballard 1071HCB, and f) ETEK 1200W	77
Figure 4.3:	Straight fibres GDL's layer separation after compression	77
Figure 4.4:	SEM images of various types of straight fibres carbon paper samples: a) Toray H-060, b) ETEK 1200N, c) Ballard P75, d) Ballard P75T, e) AvCard 1120, f) Sigracet 25BA	78
Figure 4.5:	A series of SEM images of felt/spaghetti fibres carbon paper samples of: a) Freudenberg C2, b) Freudenberg C6 and c) SGL 10BC	79
Figure 4.6:	Surface roughness for carbon paper GDL substrates	80
Figure 4.7:	MPLs on various commercial GDLs: a) GDS2120, b) Freudenberg C2, c) LT1200W and d) SGL 24BC	80
Figure 4.8:	Surface roughness for MPLs	81
Figure 4.9:	Porosity of commercial GDLs	83

Figure 4.10:	Tortuosity of commercial GDLs	84
Figure 4.11:	Pore size distribution change with GDL thickness in Toray samples – full pore size distribution	85
Figure 4.12:	Pore size distribution change when adding a MPL for samples a) SGL 25BA (without MPL) and SGL 25BC (with MPL) and b) SGL 35 BA (without MPL) and SGL 35BC (with MPL).	86
Figure 4.13:	Pore size distribution gradual change with PTFE loading in the absence and presence of MPL; P75 (Unteflonated substrate), P75T (Teflonated substrate), GDS2120 (Teflonated substrate with an MPL)	87
Figure 4.14:	GDL pore size distribution change with PTFE loading increase; 34BC with 5 wt% PTFE loading, and 34DC with 20 wt% PTFE loading	88
Figure 4.15:	Pore size distribution for commercial woven GDL	88
Figure 4.16:	GDL permeability as measured using mercury porosimeter. The arrows mark GDLs with an MPL.	90
Figure 4.17:	Water contact angle for commercial GDLs and their MPLs	92
Figure 4.18:	Contact resistance change with clamping pressure	93
Figure 4.19:	Commercial GDL contact resistance with POCO graphite plate at 1.5MPa and 2.5MPa	94
Figure 4.20:	Toray H-030 strip resistance change with distance	95
Figure 4.21:	<i>In-plane</i> resistivity of various GDL materials	96
Figure 5.1:	The change in GDL thickness with clamping pressure	105
Figure 5.2:	Change in GDL performance with compression for an MEA using SGL 25BC GDL; compression increases moving from G250 to G100.	108
Figure 5.3:	Change in EIS curve with compression for the MEA using SGL 25BC GDL at (a) low current density (0.1 A.cm ⁻²), and (b) high current density (1.0 A.cm ⁻²)	109

Figure 5.4:	change in GDL performance with compression for an MEA using (a) H-060, (b) H-090 and (c) H-120; compression increases moving from G250 to G100.	111
Figure 5.5:	change in GDL performance with compression for an MEA using (a) LT1200N and (b) LT1200W; compression increases moving from G250 to G100.	113
Figure 5.6:	change in GDL performance with compression for an MEA using (a) SGL 10BC, (b) SGL 24BC, (c) SGL 25BC, (d) SGL 34BC and (e) SGL 35BC; compression increases moving from G250 to G100.	117
Figure 5.7:	The effect of compression on the maximum power and current densities for GDLs with different thicknesses; H-060 (190 μm), H-090 (280 μm), and H120 (370 μm)	119
Figure 5.8:	The effect of compression on the Ohmic resistance for MEAs using GDLs with different thicknesses; H-060 (190 μm), H-090 (280 μm), and H120 (370 μm)	120
Figure 5.9 :	The effect of compression on the maximum power and current densities for MEAs using; (a) SGL 24BC and SGL25BC and (b) SGL34BC and SGL35BC	122
Figure 5.10:	The effect of compression on Ohmic resistance for MEAs using; (a) SGL 24BC and SGL25BC, and (b) SGL34BC and SGL35BC	123
Figure 5.11:	The effect of compression on the maximum power and current densities for MEAs using woven (LT1200W) and non-woven (LT1200N) GDLs	125
Figure 5.12:	The effect of compression on the ohmic resistance for MEAs using woven (LT1200W) and non-woven (LT1200N) GDLs	125
Figure 5.13:	The effect of compression on the maximum power and current densities for MEAs using GDLs of felt and straight fibre GDLs: 10BC (felt fibre) and 34BC (straight fibre).	127
Figure 5.143:	The effect of compression on the ohmic resistance for MEAs using GDLs of felt and straight fibre GDLs; 10BC (felt fibre) and 34BC (straight fibre)	127
Figure 6.4:	IV curves for MEAs with Toray GDLs; H-060, H-090, and H-120 with thicknesses of 190 μm , 280 μm , and 370 μm respectively	135
Figure 6.5:	EIS for MEAs with Toray GDLs; H-060, H-090, and H-120 with thicknesses of 190 μm , 280 μm , and 370 μm respectively. (a) at 0.05	136

A.cm⁻² and (b) at 0.5 A.cm⁻²

- Figure 6.6:** PEFC performance for GDLs; (a) SGL 24BC and SGL 25BC with densities of 0.44 g.cm⁻³ and 0.34 g.cm⁻³ respectively , (b) SGL 34BC and SGL 35BC with densities of 0.41 g.cm⁻³ and 0.31 g.cm⁻³ respectively **139**
- Figure 6.7 :** EIS for MEAs with GDLs; SGL 34BC and SGL 35BC with densities of 0.41 g.cm⁻³ and 0.31 g.cm⁻³ respectively at (a) 0.1 A.cm⁻² current density and (b) 1 A.cm⁻² current density **140**
- Figure 6.8:** PEFC performance for GDLs; H2315 (un-teflonated) and H2315 I2 (teflonated) **143**
- Figure 6.9:** EIS for MEAs with GDLs; H2315 (un-teflonated) and H2315 I2 (teflonated) at (a) 0.1 A.cm⁻² current density and (b) 1 A.cm⁻² current density **144**
- Figure 6.7:** PEFC performance for GDLs; (a) P50, P50T and GDS1120, and (b) P75, P75T and GDS2120 **147**
- Figure 6.8:** EIS for MEAs with GDLs; P50, P50T, and GDS1120 at (a) 0.1 A.cm⁻² current density and (b) 1.0 A.cm⁻² current density **148**
- Figure 6.9:** PEFC performance for GDLs; (a) SGL 24BA and SGL 24BC (b) SGL 25BA and SGL 25BC. (XXBA has no MPL, and XXBC with MPL) **150**
- Figure 6.10:** EIS for MEAs with GDLs; SGL 25BA and SGL 25BC at (a) 0.1A.cm⁻² current density and (b) 1.0 A.cm⁻² current density. (XXBA has no MPL, and XXBC with MPL) **151**
- Figure 6.11:** PEFC performance for GDLs LT1200W (woven) and LT1200N (non woven) **153**
- Figure 6.12:** EIS for MEAs with GDLs; LT1200W (woven) and LT1200N (non woven) at (a) 0.1 A.cm⁻² current density and (b) 1 A.cm⁻² current density. **154**
- Figure 6.13:** PEFC performance for GDLs SGL 10BC (felt fibre structure) and SGL 34BC (straight fibre structure) **156**
- Figure 6.14:** EIS for MEAs with GDLs; SGL 10BC (felt fibre structure) and SGL 34BC (straight fibre structure) at (a) 0.1 A.cm⁻² current density and (b) 1 A.cm⁻² current density **157**

LIST OF TABLES

Table 1.1 Fuel cell types	6
Table 4.1: Commercial GDL materials	68
Table 4.2: GDL ex-situ properties	71-74
Table 4.3: Woven GDLs weave and fibres properties	76
Table 4.4: MPL properties	82
Table 5.2: GDL samples properties	102
Table 5.3: Fuel cell test operating conditions	103
Table 5.3: GDL thickness change with compression	106
Table 6.1: Sets of GDL samples	131
Table 6.2: Fuel cell operating conditions	132
Table 6.3: GDL properties change with thickness	135
Table 6.4: GDL properties change with bulk density	137
Table 6.5: GDL properties change with PTFE loading and MPL application	141
Table 6.6: GDL properties change MPL application	149
Table 6.7: GDL properties change with the substrates structure	153

LIST OF DEFINITIONS AND ABRIVIATIONS

A (m^2)	Cross sectional area.
AC	Alternating current: flow of charge that periodically changes direction.
C (F: Farad)	Capacitance.
C_d (F: Farad)	Diffusion capacitance.
C_{dl} (F: Farad)	Double layer resistance.
CL	Catalyst Layer.
CNTs	Carbon Nano-Tubes.
D ($m^2 \cdot sec^{-1}$)	Diffusivity: a measure of the ability of a substance to allow the diffusion of mass as a result of concentration gradient.
DC	Direct current : a unidirectional flow of charge.
D_{eff} ($m^2 \cdot sec^{-1}$)	Effective diffusion coefficient.
d_{pore} (m)	pore diameter
E_o (V)	Electrode potential.
ECSA ($m^2 \cdot g^{-1}$)	Electrochemical Surface Area: the surface area for electron transfer, per unit mass of the active material within the electrode.
EIA	Energy Information Administration.
EIS	Electrochemical Impedance Spectroscopy.

γ (N.m ⁻¹)	Surface tension
η (Pa.s)	Viscosity: a measure of the fluid resistance to deformation due to shear or tensile stress.
η_{act} (V)	Activation overpotential.
η_{ohmic} (V)	Ohmic overpotential.
η_{tran} (V)	Mass transport overpotential.
k (m ²)	Permeability: a measure of the ability of a porous media to allow fluid to flow through it.
F (C.mol ⁻¹)	The Faraday constant (= 96485 C.mol ⁻¹).
FFP	Flow Field Plate.
FIB	Focused Ion Beam.
GDE	Gas Diffusion Electrode.
GDL	Gas Diffusion Layer.
GHG	Green House Gases
ΔG (J.mol ⁻¹)	Gibbs Free Energy.
ΔH (J.mol ⁻¹)	Enthalpy.
L (H: Henry)	Inductance.
l (m)	Length of the Channel: thickness of the GDL.

L_c (m)	Characteristic length of the pore space
MEA	Membrane Electrode Assembly.
MPL	Microporous Layer.
Nafion ®	Polytetrafluoroethylene: a polymer containing sulfonic acid groups which facilitate the transport of cations through its internal structure. Nafion® membrane is commonly employed as the electrolyte material in the PEFC.
Nafion® is a registered trademark.	
NTC	Negative Temperature Coefficient.
OCV (V)	Open Circuit Voltage.
ϕ (%)	Porosity: the fraction of volume of voids over the total volume.
P (Pa)	Pressure
PEFC	Polymer Electrolyte Fuel Cell.
PSD	Pore Size Distribution.
ρ (Ω .m)	Electrical resistivity.
PTFE	Polytetrafluoroethylene.
Q (m^3 .sec ⁻¹)	Volumetric flow.
R (Ω)	Electrical resistance.
R_d (Ω)	Diffusion resistance.

RH (%)	Relative Humidity.
R_p (Ω)	Charge transfer resistance.
R_s (Ω)	The sum of the electrical resistances of fuel cell components.
S_a (μm)	Mean value of height: an indication of surface roughness.
SEM	Scanning Electron Microscopy.
SHE	Standard Hydrogen Electrode.
S_q (μm)	Root mean square of height: an indication of surface roughness.
ΔS ($\text{J.K}^{-1}.\text{mol}^{-1}$)	Entropy.
σ/σ_o	Pore structure conductance ratio
θ	Liquid-solid contact angle
τ	Tortuosity: an indication of the ration between the length of a path in a porous media to the absolute distance.
ω	Frequency.
Z (Ω)	Electrical impedance.

CHAPTER ONE

INTRODUCTION

CHAPTER 1: INTRODUCTION

1.1 BACKGROUND

The world today is going through a transition phase. It is going through the process of replacing the conventional energy system, that is based and dependent on fossil fuels, with a new, clean and sustainable one. The movement towards this new system, although challenging, is inevitably advancing.

Since the industrial revolution and the ability to utilize fossil fuel in a whole variety of applications, fossil fuels became the main source of energy in use. The state of fossil fuels however is proven to be neither stable nor sustainable. This has become a threatening danger for the world civilization and a major limitation to its economic development. Moreover, the change to a new energy system has become an urgent global concern, since the realisation of the dramatic impact of the continuation of using fossil fuel on the environment. Fossil fuel emissions are considered as the main contributors to climate change and other environmental problems.

The debate about global warming started in the late 19th century, however, not until the 1970s, climate change and global warming have become a global concern [1]. International and national conferences have been held while governments and institutions started to explore strategies and methods to tackle this problem [1]. In 1997, the Kyoto protocol was adopted by many countries, which set the goal of reducing their Green House Gases (GHG) emissions by 5% by 2012 against 1990 levels, and this was extended in 2012 to an 18% reduction by 2020. These ambitious goals, if to be met by the participating countries, require major investment in the

renewable energy sector and a significant shift in energy supply. However, studies and statistics are pessimistic about achieving the goals on time or stopping the damage that has already happened to the environment.

According to the US Energy Information Administration (EIA), the world’s energy demand will increase by 44% by 2030. “Total world energy use rises from 1.38×10^{14} kWh in 2006 to 1.68×10^{14} kWh in 2015 and then to 2.14×10^{14} kWh in 2030” . This increase in demand will be accompanied by an increase in energy production from different resources; EIA [2] suggests that the dependence on fossil fuel will remain, which makes the energy and environment problem more serious.

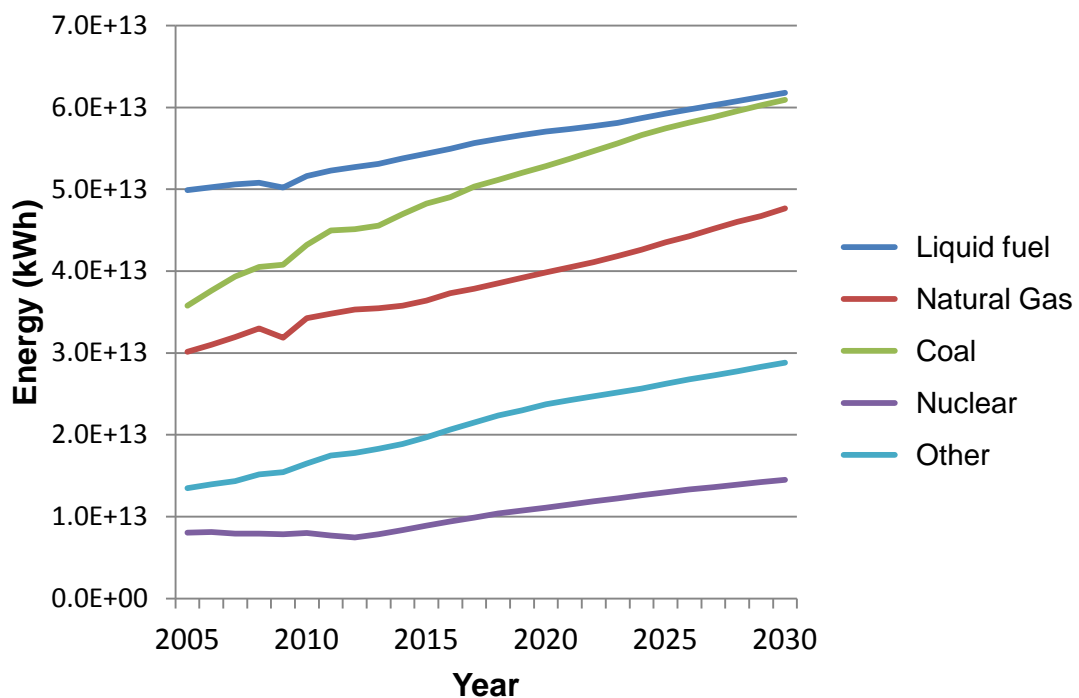


Figure 1.1: EIA scenario of world energy demand increase by resources [2]

Following the scenario presented in Figure 1.1, the production/consumption rate of fossil fuel will increase dramatically to meet the rising energy demand. This increase

in fossil fuel consumption raises the questions; when will we reach the level at which fossil fuel extraction is unfeasible? When will peak production occur? What are the consequences of this high consumption? Many commentators argue that peak oil production has already occurred or will happen in the next few years [2].

The continuous demand for fossil fuel will lead to higher levels of pollution. Burning fossil fuel produces around 21.3 billion tons of carbon dioxide every year, which leads to an increase in the atmosphere of 10.65 billion tons annually after the natural processes that absorb this gas [2]. In addition, burning fossil fuel produces nitric and sulphuric acids which fall to earth as acid rain. These numbers show that the problem is very challenging and real action is required.

In the last few decades, alternative renewable and clean energy sources have been explored, and systems to utilize solar, wind, hydrothermal, and electrochemical energy have started to emerge and develop. Today, renewable energy sources are emerging as a contributor to the world's total energy feedstock with 2% share in 2011 that is expected to rise up to 6% by 2030 [2]. Despite its limited and minor contribution, this signals the start of the process of establishing new energy systems.

Two of the technologies emerging within the new energy system are hydrogen and fuel cell technologies. Hydrogen is used as an energy carrier, through which energy can be stored and transported. A fuel cell is the device that converts the chemical energy stored in hydrogen into electrical energy. In this way, the new energy system aims to replace fossil fuel by hydrogen and the internal combustion engine and gas turbine by fuel cell systems.

1.2 FUEL CELLS

A fuel cell is an electrochemical device that converts chemical energy directly into electrical energy through an oxidation - reduction reaction for a fuel and an oxidant respectively. In general, a fuel cell consists of two electrodes separated by an electrolyte. The fuel and the oxidant are fed to the anode and cathode respectively. At the anode, the fuel is oxidized and at the cathode the oxidant is reduced. The ionic charges produced by the electrode reactions are transported through the electrolyte, while the electrons freed by the reaction flow from the anode to the cathode through an external electrical circuit.

The first fuel cell was demonstrated in 1839 by Sir William Grove. In his experiment, he found that hydrogen and oxygen are consumed at the platinum electrodes producing water and an electrical current [3]. Many types of fuel cells have been developed since Grove's invention. Fuel cells are categorized according to the type of electrolyte used; polymer, alkaline, phosphoric acid, molten carbonate and solid oxide. The electrolyte type determines the cell operating conditions and the materials used in the other components. Table 1.1 summarises the main fuel cell types along with the design details, operating conditions and potential applications.

Fuel cells running on hydrogen have the advantages of potentially having zero emissions, quiet operation, high efficiency throughout the operating range, and modular design. These advantages put fuel cell technology ahead of the combustion engine, however, there are still many challenges preventing it from being commercially used including durability, fuel availability, cost, and public acceptance.

Table 1.1 Fuel Cell Types [4]

	Low Temperature			High Temperature	
Fuel Cell Type	Polymer Electrolyte Fuel Cell (PEFC)	Alkaline Fuel Cell (AFC)	Phosphoric Acid Fuel Cell (PAFC)	Molten Carbonate Fuel Cell (MCFC)	Solid Oxide Fuel Cell (SOFC)
Electrolyte	Polymer	Potassium Hydroxide in asbestos matrix	Immobilized liquid phosphoric acid in SIC	Immobilized liquid molten carbonate in LiAlO ₂	Ceramics
Catalyst	Platinum	Platinum	Platinum	Electrode material	Electrode material
Electrodes	Carbon	Transition metals	Carbon	Stainless steel or Nickel	Perovskite/ metal cermets
Operating Temperature	40-200 °C	65-220 °C	205 °C	650 °C	600-1000 °C
Mobile Ion	H ⁺	OH ⁻	H ⁺	CO ₃ ²⁻	O ²⁻
Fuel	H ₂ / Methanol	H ₂	H ₂	CH ₄ / CO/ H ₂ **	CH ₄ / CO/ H ₂
Efficiency	35-60 %	50-70%	35-50%	40-55%	45-60%
Applications	Vehicles and mobile applications, and low power CHP* systems	Used in space vehicles	CHP systems (200kW)	Medium to large scale CHP systems, up to MW capacity	All sizes of CHP systems, 2kW to multi-MW

* CHP: Combined Heat and Power/ ** With the addition of CO₂

1.3 POLYMER ELECTROLYTE FUEL CELL

PEFC technology was developed in the early 1960s. General Electric announced an initial success in the mid-1960s when the company developed a small fuel cell for a programme with the U.S. Navy's Bureau of Ships and the U.S. Army Signal Corps. The tested unit was portable and compact, but the catalyst was expensive. Later, PEFC were used as part of NASA's Gemini project [5].

In addition to the general advantages of fuel cells, PEFCs have the advantage of low start up and load response time due to their low operating temperature. This is required for some applications; mainly transport. The solid polymer electrolyte also gives PEFC the advantage of being compactable and physically stable with movement. However, the high cost and durability issues mark the main limitations that are currently preventing the technology from reaching commercialisation.

A PEFC has four main components; the polymer electrolyte (membrane), electro-catalyst layers, gas diffusion layers, and flow field plates. Figure 1.2 shows the construction of a PEFC and describes the role of each component in the operation of the cell. The polymer electrolyte is at the centre of the cell and is assembled in between two porous gas diffusion electrodes (GDEs). A GDE consists of a Gas Diffusion Layer (GDL) with a Catalyst Layer (CL) at one side of it. The assembly of the electrolyte and the 2 electrodes is called a membrane electrode assembly (MEA). The MEA is then placed in between two flow field plates (FFPs) making a single cell.

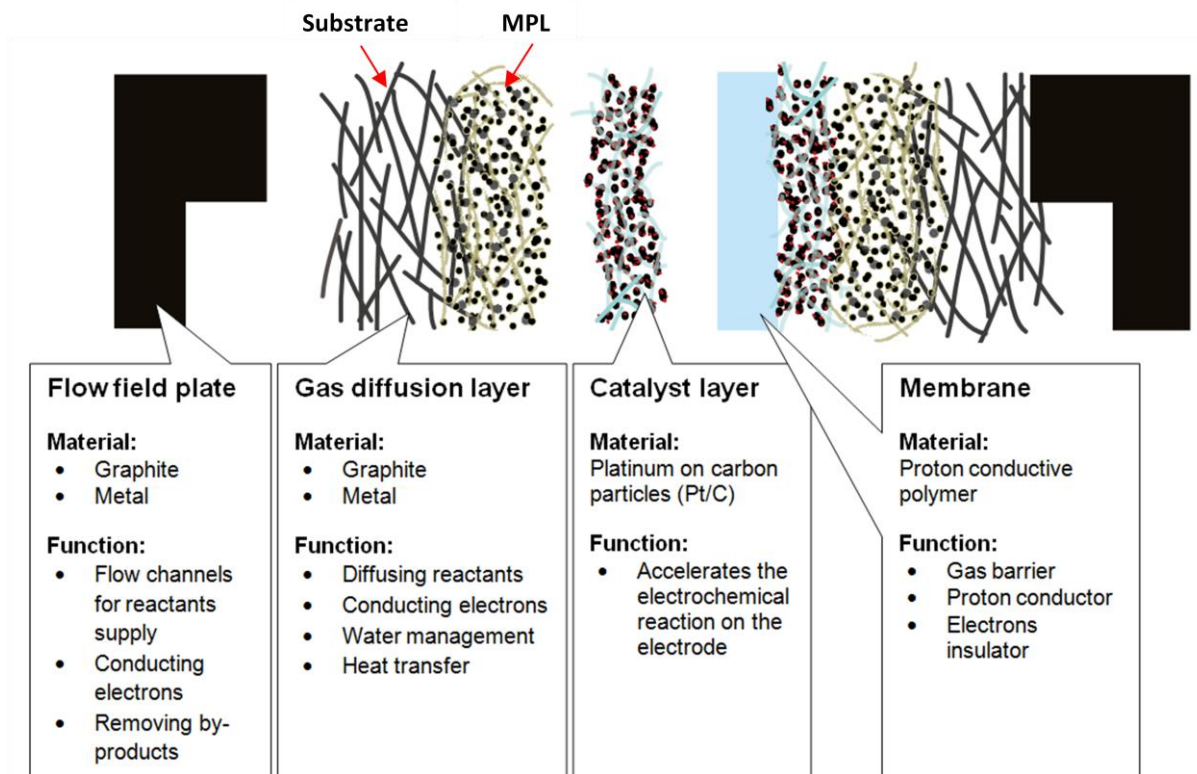
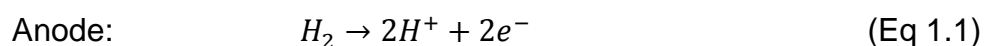
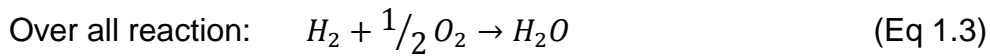
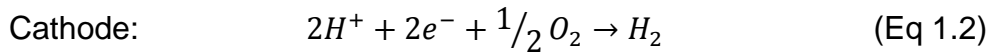


Figure 1.2: PEFC components, materials and operation

Hydrogen and Oxygen (air) are fed to the anode and the cathode respectively through the channels in the FFP. The reactants diffuse through the GDLs to reach the active catalyst sites. On the anode side, the hydrogen is oxidized in the presence of the catalyst producing electrons and protons (Eq. 1.1). Protons flow through the membrane to the cathode side and electrons are conducted by the GDL to the FFP out of the cell to flow through the external electrical circuit (producing an electrical current) to the cathode. On the cathode catalyst active sites, the oxygen reduction reaction takes place (Eq 1.2), where oxygen, protons and electrons combine together producing water and heat. The chemical reaction equations for each side of the fuel cell and the overall (Eq 1.3) reaction are as follows:





The overall reaction of a fuel cell is exothermal. The theoretical reversible energy produced from the reaction is equal to the difference in Gibbs free energy (ΔG) of the overall reaction. Due to the presence of irreversible losses the performance of the cell deviates from the theoretically obtained values ($\Delta G = \Delta H - T\Delta S$). Where, ΔH is the enthalpy of the reaction, T is the temperature, and ΔS is the entropy of the reaction.

The Gibbs free energy for the reaction at 80 °C is $-228.2 \text{ kJ.mol}^{-1}$ (assuming water produced in the liquid state) and the reversible open circuit voltage (OCV), E_o of the cell is 1.18 V. E_o can be calculated for the cell using equation 1.4.

$$E_o = \frac{-\Delta G}{2F} \quad (\text{F is Faraday constant} = 96485 \text{ sec.A.mol}^{-1}) \quad (\text{Eq 1.4})$$

However, the potential achieved by the cells experimentally should be lower than the calculated theoretical value. This is due to the presence of irreversible losses that is related to inefficiencies in the functioning of the different components in the cell. The performance of a fuel cell is usually presented in an I-V or polarisation curve (a plot of voltage against current density) as shown in Figure 1.3.

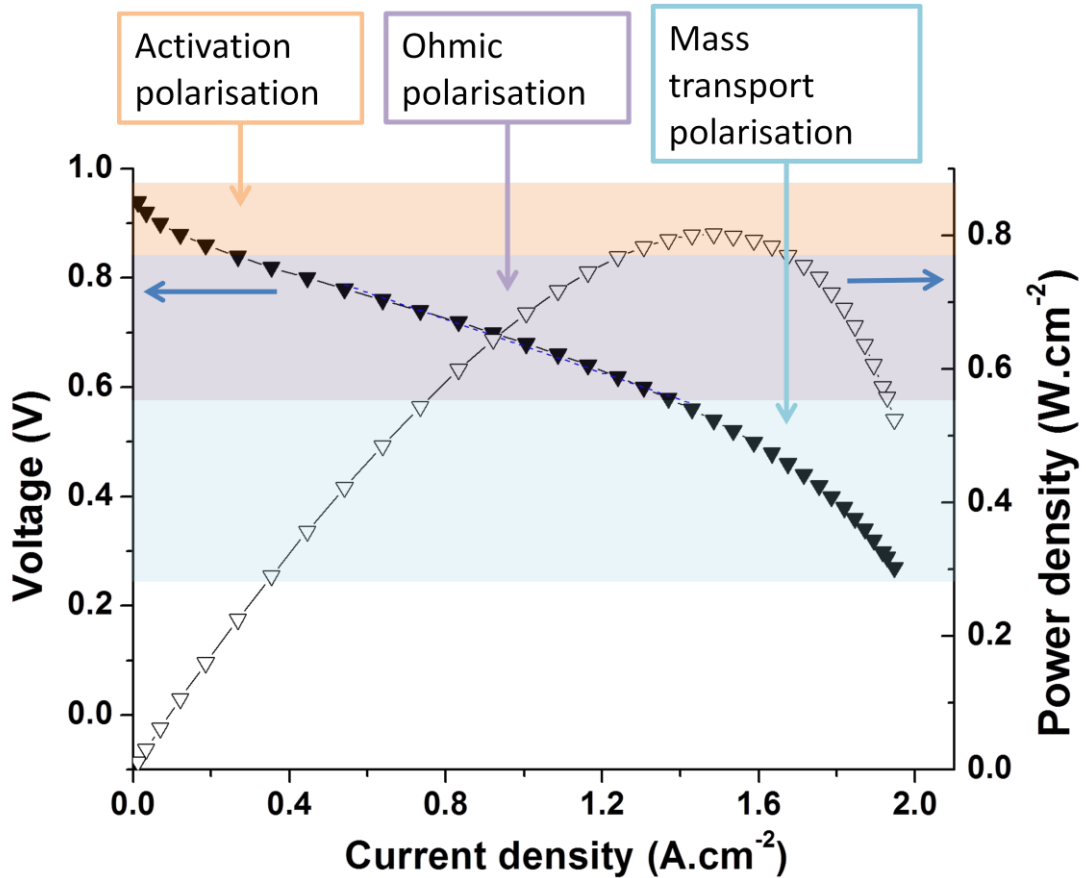


Figure 1.3: Fuel cell polarisation curve

The irreversible losses include activation, ohmic and mass transport overpotentials. The deviation between the measured cell OCV and E_0 is a result of several processes; Fuel crossover from the anode to the cathode, internal electrical current through the electrolyte and fuel contaminants. The activation overpotential (η_{act}) in the cell is related to the activation energy required for the chemical reaction to occur at the surface of the electrode. The ohmic overpotential (η_{ohmic}) results from the flow of electrons through the cell components and the ions through the electrolyte. Finally, the mass transport overpotential (η_{tran}) occurs a result of the inability to transport

sufficient reactants to the electrodes for the reaction. Therefore, a polarisation curve can be modelled mathematically using equation 1.5.

$$V = V_{OC} - \eta_{act} - \eta_{ohmic} - \eta_{tran} \quad (\text{Eq 1.5})$$

The performance of a fuel cell is influenced by the design, the properties of the materials used in the cell, and its operating conditions. The fuel cell operating conditions are determined by the application it is used in. Fuel cells have a low operating voltage with high current densities, but different systems have different voltage and current requirements. In order to meet the voltage required for different applications, single fuel cells are connected in series forming a stack, and the voltage of the stack is the summation of the voltages of the cells. The fuel cell maximum current is controlled by the area of the cells, where increasing the area increases the current. A fuel cell stack is connected to an electrical conditioning circuit. The conditioning circuit regulates the power produced and converts it to the form needed for the device which is to be powered (AC or DC current).

Research on PEFC has been focusing mainly on the development of two components of the cell, namely, the catalyst layer and the membrane. Researches on the catalyst layer are focused on lowering the Pt loading in the cell, finding novel catalyst materials that can replace Platinum, and enhancing the durability and stability of the layer within the cell. Researches on the membrane are focused on increasing the ionic conductivity of the membrane, increasing its mechanical strength, and enhancing its durability. The development of the other components of the cell have received less attention and very little has been done for their development until recent years. Currently, more research is conducted for the

development of the FFP materials and much less on the GDL. The focus of this thesis is the development of a better understanding of the GDL and its role and influence on PEFC performance.

1.4 THESIS OBJECTIVE AND OUTLINE

The performance of the PEFC is dependent on the collective efficiency of its components in performing their functions. The energy loss in each component will appear in the form of activation, ohmic or mass transport overpotential. The GDL has a vital role in the operation of the cell and its development can result in a significant increase in PEFC performance. However, relatively little research has been done on GDL development in comparison with other cell components. Today, a wide range of GDL materials are commercially available in the market, however, very little is known about their properties and the effect of each property on the performance of the cell. This gap in knowledge limits the development of GDL materials and therefore misses the potential in the further enhancement of PEFC performance.

The aim of this thesis research was to perform an experimental study to develop a better understanding of the role of GDL materials on PEFC performance, with the focus on the GDL properties and their behaviour and effect under compression.

The following objectives were identified for the study:

- To develop a database of the *ex-situ* characteristics of a wide range of commercially available GDL materials.
- To develop a better understanding of the relationship between the different properties.

- To perform a comparative study *in-situ* and *ex-situ* between the different types of GDL materials.
- To identify the GDL properties with the most significant effect on PEFC performance.
- To study the effect of compression on GDL properties and its influence on PEFC performance.

Through these objectives, this study offers insights on the role of the GDL in PEFC performance. This assists in the enhancement of PEFC performance which in turn contributes towards the achievement of the overarching goal of fuel cell commercialisation.

Chapter 2 reviews the studies and research conducted on GDLs. Chapter 3 looks at the research methodology adopted in this study. Chapter 4 discusses the results of *ex-situ* characterisation of GDL materials. Chapter 5 presents the experimental results on the effect of compression on GDL properties and fuel cell optimization. Chapter 6 compares and analyses the difference in the performance of GDL materials under optimized compression. Finally, chapter 7 summarises the findings and conclusions from the study and provides recommendations for further work required in the field.

CHAPTER TWO

LITERATURE REVIEW

CHAPTER 2: LITERATURE REVIEW

The Gas Diffusion Layer (GDL) is an important component of the Membrane Electrode Assembly (MEA) in a Polymer Electrolyte Fuel Cell (PEFC). A GDL is an electrically and thermally conductive porous layer that stands between the catalyst layers (CL) and the flow field plate (FFP) in the cell. The porous nature of the GDL is essential for the transport of reactants and products between the FFP and the CL; Hydrogen and oxygen diffuse through the GDL to the CL at the anode and cathode, respectively, for the electrochemical reactions to take place. The GDL also facilitates water management in the catalyst layer and the polymer electrolyte by allowing water vapour to diffuse with the reactants into the MEA and ensure sufficient humidification for the membrane. At the same time, the GDL facilitates the flow of water out of the MEA to prevent water flooding at the catalyst layer [6]. GDLs are electrically connected to the catalyst ink and offer a supporting structure for the catalyst layer. It conducts electrons between the CL and the FFP. Moreover, heat produced in the exothermic reaction in the cell is conducted through the GDL to the FFP to be removed out of the cell (Figure 2.1).

An ideal GDL, therefore, should have: high porosity and permeability to allow the effective transport of reactants to the active sites, optimized porous structure with adequate hydrophobic/hydrophilic properties to hold the required level of humidity in the cell and transport any excess out, high electrical and thermal conductivity, and a stable mechanical structure.

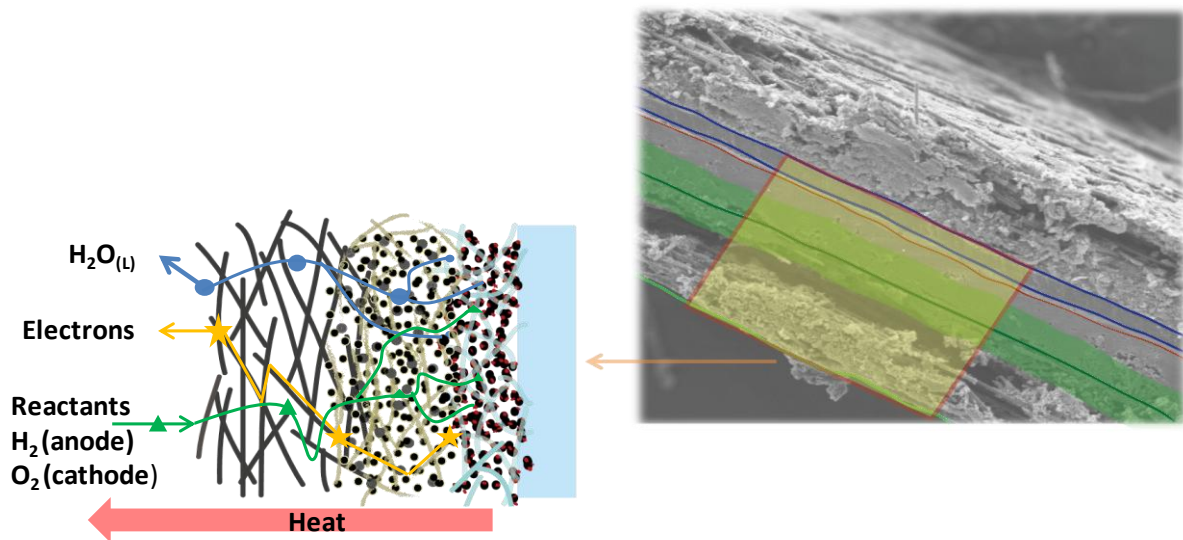


Figure 2.1: GDL function in PEFC

Studies on GDL materials include: (i) methods of *ex-situ* characterisation [7–13], (ii) the effect of the fabrication process on GDL properties [14–17], (iii) comparison of GDL performance in PEFCs under various operating conditions [18–20], and (iv) degradation using both *in-situ* and *ex-situ* testing methods [21–26]. In this chapter, the mentioned previous work on GDL materials is reviewed.

2.1 GAS DIFFUSION LAYER MATERIALS

Carbon based materials are commonly used in GDLs. Carbon is used due to its (i) relative stability in the fuel cell environment, (ii) good electrical conductivity, (iii), high permeability for gases and liquids and (iv) elastic property under compression [27].

Carbon based GDLs are made of a structured carbon fibres layer [28]. Two structures are found; woven (carbon cloth) and non-woven (carbon paper). The fibre structure is then conditioned and modified to enhance its properties as a GDL.

Carbon based GDLs will be the focus of this thesis.

Metal based GDLs were originally investigated for their mechanical strength to allow thinner diffusion layer and to produce a controlled and uniform porous structure [29]. Metal GDLs are made in the form of a metal mesh, metal foam or micro-machined metal substrate [30,31]. Metal GDLs are mainly used in Direct Methanol Fuel cells (DMFCs) due to their relatively large straight pores that enhance the transport properties of the liquid fuel and the water produced.

Titanium [30,32–34], copper [29,35,36], and stainless steel [37,38] are among the materials studied in the literature. The main drawback for metal based GDLs is corrosion [39,40]. Studies on metallic FFPs show that metals corrode in both the anode and the cathode environment. Moreover, corrosion products are found to enhance the polymer membrane degradation [41,42]. So far, a limited amount of work has been done on metal based GDLs in PEFC running on hydrogen. Further research is required to investigate the compatibility of metallic GDL with the current PEFC design and materials, and to investigate new materials and coatings to prevent corrosion.

2.2 FABRICATION OF CARBON BASED GAS DIFFUSION LAYERS

Carbon based GDLs, both woven and non-woven structures, are produced as either a single or dual layer GDL. In the discussion throughout the thesis, the untreated carbon fibre structure is referred to as a carbon substrate. The term GDL includes both single and dual layer GDLs. Carbon substrates are treated and coated to produce a single-layer or a dual-layer GDL.

Single layer GDLs are fabricated *via* a one-stage process whereby the carbon substrate is often coated with a hydrophobic material. Dual layer GDLs are produced

via a two-stage process, here a microporous layer (MPL) is added onto the GDL produced in the one-stage process. The MPL is coated on either one side or both sides of the GDL by depositing a blend of carbon powder with a hydrophobic material [43]. Figure 2.2 shows a diagram of the GDL fabrication steps.

Non-woven carbon substrates are fabricated in four stages: (i) a pre-pregging step (continuous strands are aligned with spools and a surface treatment is followed by a resin bath and the formation of a layered structure), (ii) a moulding step, (iii) a carbonisation step, and (iv) a graphitisation step. Woven carbon substrates are also fabricated in four stages: (i) a carbonaceous fibre production step (made from *meso*-phase pitch spun by melt spinning, centrifugal spinning, blow spinning, etc.), (ii) a fibre oxidation step, (iii) a cloth formation step by weaving or knitting, and (iv) a graphitisation step [6].

The literature on GDL fabrication focuses on the treatment of the carbon substrate and coating of the MPL on available carbon substrates. To the knowledge of the author, almost no work has been reported on the fabrication of the carbon substrate due to the complexity of the process. Some studies are focused on the application of the hydrophobic agent and its loading, and the vast majority look on the materials and application of the MPL.

Studies on the fabrication of the MPL looked at the use of various types of carbon black and different PTFE loading in the blend [16,17,44] and the application process [45,46]. Some studies looked at creating an MPL layer with gradients in porosity and hydrophobic agent [44]. Carbon Nano-tubes (CNTs) and carbon nano-fibres were used in partially or completely replacing carbon black in the MPL blend to modify the surface morphology and the pore properties in the MPL [47–49].

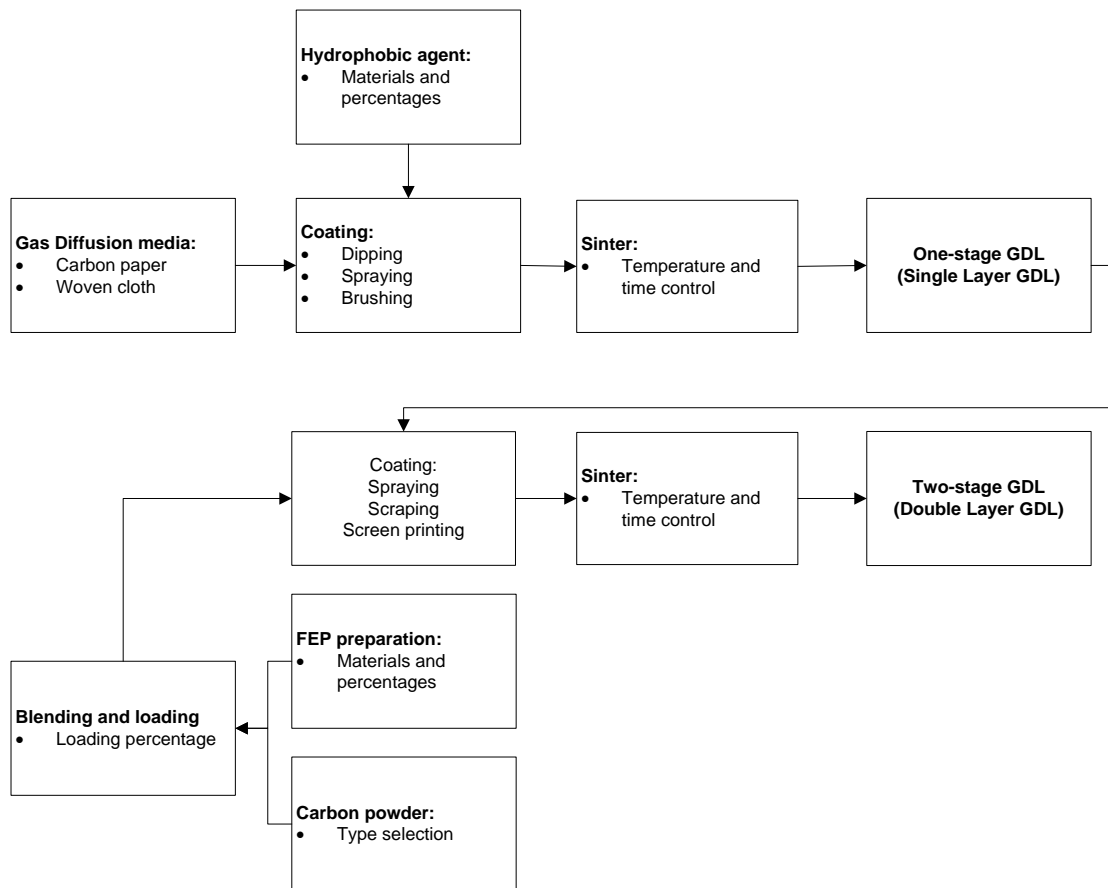


Figure 2.2: Conventional GDL fabrication process [43].

The materials formulation and the fabrication method of the GDL affect the GDL properties, such as thickness, bulk density, porosity, permeability, hydrophobicity, and electrical and thermal conductivity. The variation in GDL properties influences its performance in the MEA.

2.3 GDL CHARACTERISTICS AND PEFC PERFORMANCE

Studies of GDL properties were conducted to understand the effect of the different parameters on the cell performance, so then to modify and optimize the GDL design. Several studies looked at characterisation methods of GDL properties; others examined the effect of these properties on the cell performance. It is generally agreed that understanding the direct effect of each GDL property on the performance

is a complex task. This is due to the interdependence of the different properties. Also due to the complex fabrication of the carbon substrate and the need for specialized equipment and a high level of optimization, academic research has been focused on either the characterisation of commercially available substrates, or the modification of the substrates and the development of the MPL.

Extensive reviews have been published on GDL materials and characterisation by Cindrella et al [50], by Park et al [27] and Arvay et al [51], and water management by Yousfi-Steiner et al [52] and Bazylak et al [53].

2.3.1 GDL STRUCTURE AND SURFACE MORPHOLOGY

The structure of the carbon substrates' effect on the GDL has been the focus of many studies. It is believed that the substrates' structure has a significant effect on the GDL performance [54–57]. The structure of the GDL has been mainly looked at using SEM images. Some studies used Focused Ion Beam (FIB) and X-ray tomography to create 3D images of the structure of the GDL to allow accurate structure modelling [58–60]. Images show that the GDL structure is very heterogeneous. This makes the study of the effect of the structure on the GDL performance; experimentally and mathematically, very challenging.

The structure of the substrate has a direct effect on the mechanical properties of the GDL. Woven GDLs are found to be more compressible and mechanically flexible. However, the 3D structure of the felt structure enhances the mechanical flexibility of the non-woven GDL structure and provides higher compressibility in comparison with the straight fibre structure. Moreover, It is understood that the fibre structure determines the porosity, permeability, and electrical properties of the GDL [25].

The structure also determines the surface roughness of the substrate. Fishman et al [61] studied the effect of the GDL topography on water droplet pinning on the surface of untreated GDL substrates. It was found that surfaces with lower roughness have higher pinning and lower water evaporation. This means that GDLs with lower roughness may require more time to remove the water droplets from the surface to the flow channels. Wang et al. studied the difference between carbon paper and carbon cloth; it was found that carbon cloth performs better in high relative humidity conditions as the fibre structure has smaller tortuosity and a rougher back surface assisting water droplets to detach from the surface. Carbon paper, on the other hand, has higher tortuosity and smoother surface leading to stagnation of water droplets produced at the cathode side, hence operate better in low relative humidity (RH) conditions [62]. Generally, MEA manufacturers prefer the use of non-woven GDLs due to the lower cost and simplicity of applying MPLs and/or catalyst layers directly on it [14]. Hence, a significantly wider range of non-woven GDL materials is produced by suppliers and commercially available in the market. When comparing the performance of carbon paper and carbon cloth, contradictory results are found in the literature, with the majority agreeing that carbon cloth GDL achieve better performance [63,64].

In review of the literature on GDL structures and their effect on other GDL properties and performance, the author thinks that other aspects related to the structure of the substrate need to be considered in such studies, such as the diameter and length of the fibres, and the graphitization level of the substrate. The author believes that these have a significant effect on the other physical, mechanical and electrical properties of the GDL and therefore affect the performance which can explain the conflicting results reported in the literature on the best performing structure.

An MPL is usually applied to one side of the substrate. The application of an MPL creates a smoother surface in contact with the CL. There is no doubt that the presence of an MPL enhances the performance of the GDL [65–67]. The increase in the performance is explained by the enhancement of the transport of reactants and water management in the cell and the decrease in the cell resistance [68]. Moreover, the presence of the MPL increases the durability of the MEA [18].

Studies on MPL layer are mainly focused on the enhancement of water management in the MEA. A GDL in an MEA operates as a water relief “valve”; the “valve” stays shut keeping water within the MEA until a certain pressure is reached. Gostick et al [69] explains that the GDL saturation at water breakthrough (breakthrough pressure) is reduced significantly in the presence of the MPL. The fine pores and high hydrophobicity of the MPL limits the spread of water on the surface of the GDL, prevents water flooding in the catalyst layer, and allows reactants to reach the catalyst sites. The effect of MPL on water management was studied mathematically in [57,70]. Moreover, back diffusion and the humidification of the polymer electrolyte are enhanced in the presence of an MPL resulting in increasing the electrolyte conductivity and the MEA performance [71].

The morphology of the MPL is determined by the size and the loading of the carbon powder particles; for instance, finer carbon powder results in a smoother surface with smaller pores [72]. The loading of the hydrophobic agent affects the properties of the pores. Moreover, the deposition method used in the MPL fabrication affects its structure [45,46,73–76]. The MPL properties need to be optimized based on the operating conditions (especially the humidity conditions) and the application it is used for [68,72,77].

Cracks are usually formed in the surface of the MPL while drying the slurry in the sintering process. It is believed that cracks assist the transport of water through the GDL, however accelerate its degradation [21,78]. Chun et al [75] developed a crack free MPL with higher mechanical durability. The developed MPL shows lower degradation in the MEA performance in comparison to conventional MPLs. It is suggested that a crack-free GDL prevents defects formation on the surface of the MPL. Defects are observed around cracks and believed to accumulate water preventing reactants from reaching the catalyst layer.

In fabricating MPL, Carbon Nano-Tubes (CNTs) has been introduced to the formulation by few research groups to enhance the cell performance. Stampino et al [74] replaced 10% of carbon black in the formulation of the MPL by CNTs. The MPL produced has higher thickness and shows more pronounced cracks, however shows an increase in the performance. Several methods were used for fabricating MPLs from CNTs and carbon nano-fibres. The results show an improvement in the mechanical properties, thinner and more homogeneous crack-free MPL. The CNT MPL surface has a high water contact angle without the use of a hydrophobic agent, and *In-situ* testing shows a decrease in the MEA electrical resistance and an increase in the water transport ability [28,47–49,79].

2.3.2 MECHANICAL PROPERTIES

GDLs in the MEA are subjected to compression force in the cell assembly; thus, GDLs need to be mechanically stable to withstand the mechanical stress. Clamping pressure in the cell is necessary to seal the cell from gas leak and improve conformity to give good electrical connection. Hence, studies on mechanical properties of the GDL are mainly focussed on the effect of PEFC clamping pressure

on the MEA performance [80–83]. The mechanical property of a GDL is usually evaluated against (i) Compressive elastic and plastic deformation, (ii) Compressed electrical properties, and (iii) air permeability under compression.

The optimization of the mechanical properties of the GDL is also dependent on the flow field design used in the cell. Compressible GDL substrates intrude into the flow field with clamping pressure and potentially reduce or block the gas flow area in the flow field. On the other hand, premature fracture occurs with incompressible GDL substrate [84]. Studies show that carbon cloth extrudes into the flow field channels when assembled in a stack. Carbon cloth has 43% - 125% higher intrusion than carbon paper [25]. Kandlikar et al. reported that due to the heterogeneous structure of non-woven GDL substrates, the substrate intrusion into the channels is non-uniform [85]. The intrusion of GDL substrate into the flow field channels (tenting) (i) affects reactants flow distribution, (ii) causes pressure drop across the flow field, and (iii) decreases fuel cell performance and durability [19, 24, 25]. Peng et al [86] found that by controlling the channel width, the level of intrusion can be limited and optimized; substrates with high compressibility require narrow channels to prevent intrusion.

Compression applied on the GDL results in both reversible and irreversible deformations in its structure. The effect of compression on the mechanical structure of the GDL was divided to smoothening of the rough GDL surface at low compression and then crushing GDL pores at higher compression [87]. After compression, the GDL strain changes indicating irreversible deformation in the GDL mechanical structure. It was reported that the structure of the GDL influences the level of strain and its residual [88]. The woven structure is found to have the highest

compressibility and the felt non-woven has low compressibility and very small residual in the strain.

Cyclic compression is found to have irreversible effect on the GDL thickness. The change in the thickness is a result of breakage and displacement in fibres in the GDL structure. The GDL structure reaches stability after 5 compression cycles and the changes become minimal [89]. This is important when considering the cyclic in-cell lateral compressive loads due to thermal expansion, swelling and creep, and also the process of disassembling and reassembling the cell [25,90].

2.3.3 TRANSPORT PROPERTIES OF THE GDL

Several methods are reported in the literature for measuring GDL porosity; Kerosene immersion method [50,91], Mercury intrusion porosimetry [92], water intrusion porosimetry [93], and capillary flow porosimetry [94]. The listed methods are useful in comparing the bulk porosity and some aspects of the structure, however, all are limited in assuming that the GDL porous structure can be described by linked cylindrical open pores. New methods, such as hydraulic admittance may lead to more accurate information about the complex pore structures of the GDL [95]. A GDL has either a single (one-stage GDL) or multi-porous layers (two-stage GDL). As carbon substrates have relatively larger pore sizes compared to MPLs, in most cases a GDL is a multi-porous layer with a wide pore size range [50,92]. A typical GDL shows micro, meso- and macropores [95]. The variation in the pore sizes and their percentage in the GDL are described by a pore size distribution (PSD) curve. It is believed that porosity and PSD only affect the performance at high current density operation due to the high need for reactant and water transport [20,96].

GDL porosity needs to be optimized against its thickness; It is reported that GDLs with low thickness are more sensitive to water accumulation [71]. GDLs with low porosity need to have small thickness and optimal thickness exists for higher porosity [97]. Prasanna et al [20] studied the effect of thickness, permeability and pore size distribution on the performance of the cell. They found that there is an optimum thickness at which minimum mass transport losses, reduced electrical contact resistance and adequate structure integrity is achieved. Moreover, PSD has an important effect on water transport; small pores in the MPL closer to the CL enhance water transport and prevent water flooding [98].

Porosity and PSD have a direct impact on the effective diffusion coefficient (D_{eff}) (see Equation 2.1) [50] and permeability [99] of the GDL. Many studies focused on the measurement of in-plane and through-plane permeability. In house apparatus were designed to measure permeability by having a controlled gas flow through the GDL surface (through-plane) or through its side section (in-plane) and measuring the pressure drop across the inlet and outlet [7,100]. The measured values are then applied into Darcy's law to calculate the permeability (see Equation 2.2). However, many studies show the limitations of Darcy's law in describing the transport of reactants through the GDL. It is emphasised that the effect of gas compressibility needs to be considered specially at high flow in the in-plane direction [100–102] .

$$D_{eff} = D \frac{\phi}{\tau} \quad (\text{Eq. 2.1})$$

Where

D_{eff} is the effective diffusion coefficient ($\text{m}^2 \cdot \text{sec}^{-1}$)

D is diffusivity ($\text{m}^2 \cdot \text{sec}^{-1}$)

\emptyset is the media porosity

τ is the media tortuosity

$$Q = \frac{kA}{\eta} \left(\frac{\partial P}{\partial L} \right) \quad (\text{Eq. 2.2})$$

Where

k is the gas permeability (m^2)

η is the dynamic viscosity ($\text{Pa} \cdot \text{sec}$)

Q is the airflow in $\text{m}^3 \cdot \text{sec}^{-1}$

A is the cross sectional area of the channel media (m^2)

$\left(\frac{\partial P}{\partial L} \right)$ is the change in pressure across the length of the media, where P is pressure

(Pa) and L is the length of the channel; thickness of the GDL (m).

In-plane and *through-plane* permeability depend greatly on several GDL parameters, such as; thickness, density, hydrophobic agent (mainly PTFE) loading, fibre structures, and the presence and type of MPL [7,103–105]. For instance, the MPL permeability is found to be 2-3 orders of magnitude lower than that for the substrate [101], and the application of an MPL to the substrate decreases its permeability by an order of magnitude [7]. Carbon paper GDLs have higher in-plane permeability than through-plane permeability by about 18%. However, carbon cloths have higher through-plane permeability measurements that are 75% higher than in-plane values [100,103]. However, the in-plane permeability is affected by compression.

Compressing the GDL, to half its initial thickness, results in a decrease in permeability in an order of magnitude [100].

In the cell, the GDL is subjected to different levels of compression under the FFP; the GDL is compressed under the lands of the FFP, while there is no compression under the channel. Therefore; permeability under the channel is different than that under the land. Here, In-plane permeability determines the ability to transport the reactants over the FFP land through the GDL. FFP design and the width of the land, and the gas humidity are important factors to the effect of in-plane permeability on the GDL transport properties [102]. Furthermore, *in-plane* permeability of a GDL is an important factor as it influences the gas flow over the FFP land through the GDL to reach the catalyst sites under the land [100].

On the effect of PTFE loading, Ismail et al [106] measured the in-plane resistance for both the substrate and MPL. It was found that the in-plane permeability of the substrate decreases with the increase of PTFE loading, however, the MPL in-plane permeability increases with PTFE loading increase. Moreover, the through plane permeability of MPL coated GDLs increases with PTFE loading due to the increase of the aggregation of carbon particles resulting in bigger pore size [101].

Water transport is another crucial function of the GDL. Recently, Tamayol *et al.* studied water permeability for various commercial GDLs [8]. In their study, the threshold water pressure for permeation through different type of GDLs was measured using a *bespoke* membrane pressurized filtration cell system. It was found that PTFE loading and thickness increase the permeation threshold pressure and is not affected by moderate compression of the GDL. It was also reported that thickness has no effect on water permeability [8].

An added level of complexity in understanding the GDL transport properties is the multiphase flow; gaseous reactants, vapour and liquid water are flowing into and out of the MEA through the GDL. Many studies have been conducted on modelling the transport process within the GDL [107–110]

2.3.4 HYDROPHOBIC AND HYDROPHILIC PROPERTIES

The study of hydrophobicity is directly related to water management in the cell and is important as a property of the surface and pores of the GDL. Hydrophilic pores tend to retain water while hydrophobic pores repel the water out. At the surface, water creates a layer at a hydrophilic surface, however, water forms droplets at the surface of a hydrophobic layer. Moreover, it is easier to detach a water droplet off a hydrophobic surface. The hydrophobicity of the GDL has been varied mainly by controlling PTFE loading; an increase in PTFE loading results in an increase in the hydrophobicity. The modification of the GDL hydrophobicity was also tried using lower PTFE loading by carbonization level [111,112].

The hydrophobicity or hydrophilicity of the GDL is usually discussed through measuring the water contact angle of the cell. This is usually measured on the surface of the GDL or the MPL using Sessile Drop Angle method. However, Gurau et al [113] argue that the methods employed to measure the water contact angle on the surface do not identify the hydrophobic properties of the GDL, but rather affected by surface roughness. Hence, the internal water contact angle of the GDL fibres needs to be measured. An alternative method is presented using Washburn method with a hydrophobic agent and the Owen-Wendt calculation to determine the water contact angle.

Cheung et al [114] studied the effect of pore structure and internal wetting of the GDL on the capillary pressure in Toray TGP-H090. It was found that the magnitude of the capillary pressure shifts the GDL average contact angle. Benziger et al [115] found that the breakthrough capillary pressure for water transport depends on the GDL hydrophobicity. The study suggests that having a pore structure with water contact angle value of 90° lowers the pressure required for the water to flow, while maintaining an adequate level of hydrophobicity to prevent flooding at the catalyst layer.

Studies show that there is an optimum value for PTFE content in the cathode GDL at which the mass transport of the GDL gets enhanced and beyond which the performance drops due to the decrease in porosity and permeability [14,71,116]. Lin et al [71] reported that at the optimum loading both hydrophilic and hydrophobic pores are present to assist the transport of water and gas respectively. However, the optimum contact angle depends on the cell operating temperature [14] and humidity conditions [117]. Tsai et al [117] found that 40% PTFE loading in the media and 30% in the MPL are optimal for MEA operation at low humidity conditions as it enhances the back diffusion through the membrane and increases the membrane conductivity, when the water transport through the GDL is less demanding. Velayutham et al [118] studied optimum loading at 55°C and ambient pressure. It was found that the change in PTFE content in the GDL substrate has a higher impact on the cell performance than the change in the MPL. The optimum performance was found at loadings of 23% PTFE in the GDL substrate and 20% in the MPL. Optimum GDL performance is found for GDLs with lower PTFE loading at the MPL than that at the substrate [44,117,118].

2.3.5 ELECTRICAL PROPERTIES

In assessing the GDL electron transport capability, three parameters are commonly measured, namely, *in-plane*, *through-plane* and contact resistances. Few studies have focused on studying the current distribution across the MEA active area and techniques for measuring it as this parameter is of great importance for PEFC stack developers [119–121].

Electron transport through the GDL is affected by the GDL thickness, gas channel width and electronic conductivity [64,122]. Zhou *et al.* analytically studied the effect of the electrical resistance of the GDL on its performance in PEFC considering the *anisotropic* nature of the GDL structure. They found that GDL *through* and *in-plane* resistances can be neglected as they have little effect on the cell overall performance [123]. However, the interface contact resistance between PEFC components has significant effect. Two types of interface contact resistances are found; contact between the GDL and the CL, and of the GDL with the FFP.

Nitta *et al.* [124] found that the contact resistance between GDL-CL is one order of magnitude higher than the contact resistance between the GDL and the graphite (POCO) FFP. Furthermore, contact resistance depends on the cell compression, material properties, and surface geometry [125]. Non-uniform compression of the GDL may result in an uneven current distribution along the MEA [124]. Moreover, the GDL compressive modulus affects the contact resistance between the GDL and the FFP, therefore the structure of the GDL affects the contact resistance [124,126].

Higier *et al.* studied the difference in electrical contact resistance under the channel and the land of the FFP [127]. They concluded that the variation in contact resistance depends strongly upon the land to channel width ratio. The difference is

significant in wide channels and negligible in narrow channels. The difference in resistance between the channel and land can contribute to local current density variation. The reason for this significant difference is due to an increase in contact resistance between the GDL and the CL caused by 'insufficient' compressions [127].

2.3.6 THERMAL CONDUCTIVITY

Thermal conductivity and thermal contact resistance behaviour is similar to that reported for the electrical properties. Thermal conductivity is an important property for predicting temperature distribution and water management in the cell. The difference in temperature across the GDL-CL has been reported to be between 1.7-4.4 °C [128]. Thermal conductivity is dependent on compression [12,129,130], PTFE content, temperature, and the presence of liquid water in the pores [131].

As with electrical resistance, thermal resistance is also very dependent on clamping pressure. Both through-plane thermal resistance and contact resistance decrease with the increase of compression [128,132]. An increase in thermal conductivity is significantly due to a decrease in contact resistance between the carbon fibres [129]. Again, contact resistance plays a dominant role in the thermal flux under all compressive loads. The contribution of the contact thermal resistance between the GDL and FFP to that of the bulk resistance is 2.7/1 [89].

The fibre distribution plays an important role in thermal conductivity, however both in-plane and through-plane conductivity decreases with the increase in porosity [129][133] but no effect is noticed for the change in the fibres diameter and operating temperature [134]. Teertstra et al [135] studied the effect of measurement orientation on the measured value for in-plane thermal conductivity. The results show that in-plane thermal conductivity decreases with the increase in PTFE loading. Also, due to

the heterogeneous structure of the GDL, the in-plane properties of the GDL vary with the direction of the measurement. Higher PTFE loading increases the thermal conductivity at low compression and decreases it with increasing compression. In contrast, Karimi et al [132] reported that the presence of an MPL reduced thermal conductivity and increased the thermal contact resistance of the GDL.

2.3.7 CLAMPING PRESSURE

As highlighted in the previous sections, clamping pressure has a significant effect on the GDL properties and performance. When assembling a fuel cell, an MEA is pressed between the flow field plates to achieve good electrical contact between the elements and seal the cell to prevent gas leaks. Several studies have been conducted to study the effect of compression on the GDL properties and the fuel cell performance [90,136–139]. It is well understood that compression has a dual effect on the GDL. Higher compression decreases the contact resistance between the GDL and the plates (FFP) [90,126,140–142], however, it also decreases the porosity and transport ability [85,138,143]. This has been studied mathematically and experimentally [80,144,145].

The effect of compression change on fuel cell performance has been reported in the relevant literature. Ge et al [146] showed a decrease in the performance with the increase of the cell compression ratio. It was found that there is an optimum compression for the cell dependent on the type of the GDL, and that excess compression damages the structure of the GDL [85,87]. Dotelli et al [136] used Electrochemical Impedance Spectroscopy (EIS) to study the effect of compression on the performance of the MEA. The results show that the cell resistance decreases with compression, however mass transport resistance increases. Therefore, there is

an optimum compression for the MEA. This is dependent on the GDL type and operating potential and conditions of the cell [81,147,148].

Furthermore, the effect of compression on the inhomogeneous structure of the GDL has been discussed in the literature [80,140,145], and the GDL deformation and intrusion into the flow field channels due to compression has also been reported in [25,85,87]. Bazylak et al [143] showed that the deformation that occurs in the GDL due to compression generates preferential pathways for water transport in the cell. The cracks created on the edge between the channel and land assist water transport. The GDL intrusion in the flow field channels can result in significant disturbance in the flow of reactants in the flow field and in a drop in the performance [149].

2.4 GDL DEGRADATION

The role and characteristics of GDLs are important and affect the overall performance and lifetime of the PEFC [150]. GDL degradation can be detected by the change in its characteristics and properties, and therefore its performance in the PEFC. Due to the difficulty in separating the GDL degradation from MEA sub-components in *in-situ* experiments, GDL degradation studies are often performed by *ex-situ* testing in simulated PEFC operating conditions. Therefore, a good understanding of the GDL properties and testing methods as presented in the previous sections is essential for GDL degradation studies. *In-situ* studies are usually conducted to study the effect of the changes in properties on the PEFC performance.

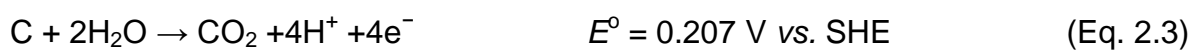
Two main changes have been reported in GDL degradation, namely; (i) wetting behaviour changes due to loss of the hydrophobic agent and carbon surface

changes and, (ii) changes in the structure of the GDL due to carbon corrosion and mechanical stress [26]. In addition, changes in MPL have been observed due to loss of PTFE/C and to carbon oxidation [151]. Causes of GDL degradation can be categorised into (i) electrochemical, (ii) mechanical and (iii) thermal.

Extreme PEFC operating conditions enhance and accelerate GDL and other MEA sub-components degradation. High cell voltages (potentials), low relative humidities, and high temperatures accelerate GDL degradation [150]. Besides, dynamic loading and potential cycling can also accelerate degradation.

2.4.1 ELECTROCHEMICAL DEGRADATION

The carbon particles used in the catalyst layer and the MPL are thermodynamically unstable in the operating conditions of PEFC [6]. At above 0.207 V on a standard hydrogen electrode (SHE), carbon is oxidized to carbon dioxide following Reaction (Equation 2.3) [152]. Hence, at the high cathode electrode potential and in the presence of platinum, the GDL suffers from the loss of carbon particles and structure rigidity due to the electrochemical activity.



Oxidation of carbon (carbon corrosion) leads to performance decrease due to accelerated loss of Electrochemical Surface Area (ECSA), modification of pore morphology and GDL surface characteristics. Hence, carbon loss from the GDL results in significant changes in its properties and the PEFC performance. Potential cycling particularly at high cell potentials results in loss of carbon material [26,150–152]. Aoki *et al.* [153] reported that after electrochemically treating the cathode GDL in an *ex-situ* electrochemical corrosion test, the GDL experienced a loss in

hydrophobicity and the corroded GDL maintained the same oxidant utilization and diffusion losses, whereby cathode flooding was observed at high current densities.

Chen *et al.* [154] studied the electrochemical degradation of the GDL under simulated PEFC conditions at potentials in the range of 1-1.4 V. At high potentials (lower than 1.2 V) significant loss in carbon led to a thinning of the GDL fibres. In addition, the authors observed changes in the GDL morphology, resistance, gas permeability and contact angle. Chen *et al.* also reported that the ohmic resistance, charge transfer and mass transfer resistances increased significantly together with an obvious drop in the overall PEFC performance. Recently, Hiramitsu *et al.* [155] found that carbon oxidation in the GDL resulted in an increase in diffusion overpotential. Moreover, GDL thinning and loss in carbon content is reported. These changes in the GDL properties are not uniform and more severe at the central area of the MEA [156].

Kumar *et al.* reported a decrease in GDL rigidity and an increase in strain under PEFC clamping pressure due to electrochemical degradation. Carbon paper highly suffers from loss of structure rigidity with ageing due to the weak fibres interface in comparison to carbon cloths which possess a more stable structure. This loss in rigidity results in an increase in GDL intrusion into the flow field channels affecting the PEFC performance [23].

Low relative humidities (RHs) [26,150–152] and high temperatures [22] enhance carbon corrosion. Experiments showed an increase in the MPL pore sizes due to the loss of carbon particles in the MPL. The carbon fibres are often treated by PTFE that can protect them, however with time, they lose their hydrophobicity and mass transport losses increase due to water accumulation in the GDL [150]. On the other

hand, it has been reported that carbon loss increases from 8% to 36% when the temperature increases from 120°C to 150°C after 120 hours [150].

It is important to mention that graphitised carbon has a higher oxidation resistance [23], hence it can be used in PEFCs to mitigate oxidation losses. Further studies are required to investigate the effect of graphitised carbon on GDL properties. Hiramitsu *et al.* [155] showed that homogeneous hydrophobic coating of the GDL protects the GDL carbon fibres from oxidation and controls the diffusion overpotential under long term operations of the PEFC.

2.4.2 MECHANICAL DEGRADATION

GDL mechanical degradation occurs due to clamping pressure (compression) applied to PEFC during assembling, erosion by the reactant and water flows, and water freezing at low temperatures. High compression results in GDL deformation and changes in thickness due to the breakage and displacement of fibres under high pressures. The variations in GDL thickness are irreversible and result in a change in electrical and thermal resistance together with a decrease in porosity. Sadeghi *et al.* [89] observed high hysteresis in experiments involving pressure cycling whereby hysteresis became minimal after approximately 5 cycles of compression and the deformation became permanent in the GDL fibre structure. Bazyak *et al.* [157] reported the breakage of fibres and deterioration of the hydrophobic coating after applying high clamping pressures on the GDL. This resulted in a change in the structure and affected the water pathway through the GDL as water takes other preferential pathways created by the breakage of the GDL fibres. Figure 2.3 shows SEM images of the imprint of the FFP channel on the GDL, the fibres under the land

are crushed due to compression while the structure is maintained the same under the channel.

GDLs are subjected to an uneven distribution of pressure due to GDL intrusion into the flow field channels on the FFP and due to the uneven pressure applied by the bolts on the edges of the cell [85]. Maher *et al.* [158] studied the mechanical stress on the MEA prior to and after PEFC operation at various operating conditions . They reported that the variations in temperature and RH resulted in local bending in the MEA and therefore non-uniform distribution of stress across it (formation of cracks was observed) [158]. Another factor which contributes to the mechanical stress on the MEA and GDL is the heterogeneity of both the GDL and CL [159].

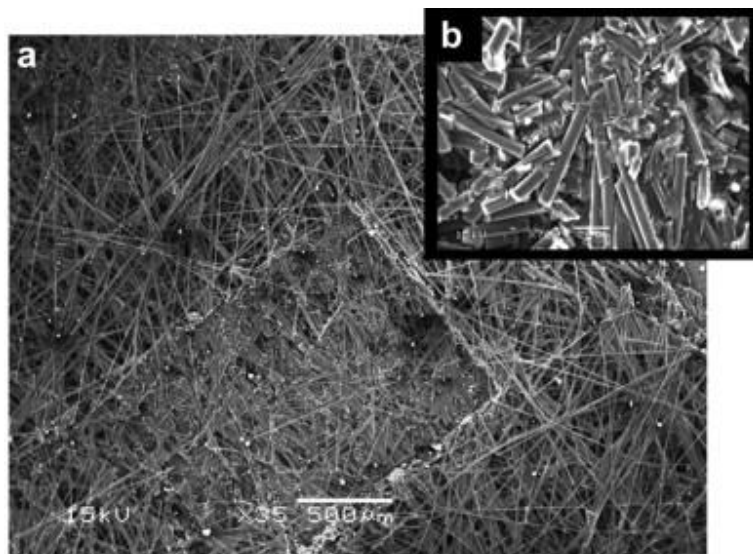


Figure 2.3: Effect of compression on carbon paper GDL structure [83]

As the GDL is in contact with the reactant flows, it has been observed that the flows may erode the GDL surface resulting in a loss in GDL hydrophobicity (due to the loss of the PTFE from both the fibres and the MPL) [160]. This mechanism is enhanced

and accelerated with an increase in flow rates and temperatures, where it has been observed to be higher on the cathode side as the flow of air is higher than that of hydrogen on the anode side. The loss in hydrophobicity was reported to occur in short periods of operation of 100-150 hours [160] which resulted in an increase in GDL electrical resistance and porosity. Wu *et al.* [161] studied the *in-situ* accelerated degradation of GDLs and the effect of elevated temperatures and flow rates on the PEM fuel cell performance. They found that when using the degraded GDL, its performance is comparable to that of a fresh one at high potentials and low current densities; however, at high current densities, concentration losses increase significantly.

Water transport through the GDL also contributes to the GDL degradation. Lin *et al.* [21] studied MPL degradation in a simulated PEFC water flooding conditions. They observed that the MPL was washed out from the GDL surface and moved into the GDL structure, see Figure 2.4. In the conditions they used, however, they found that the performance of the GDL after degradation was better than a GDL without MPL (as the MPL material maintained the ability of the GDL to transport the produced water and prevent flooding and concentration losses in the PEFC).

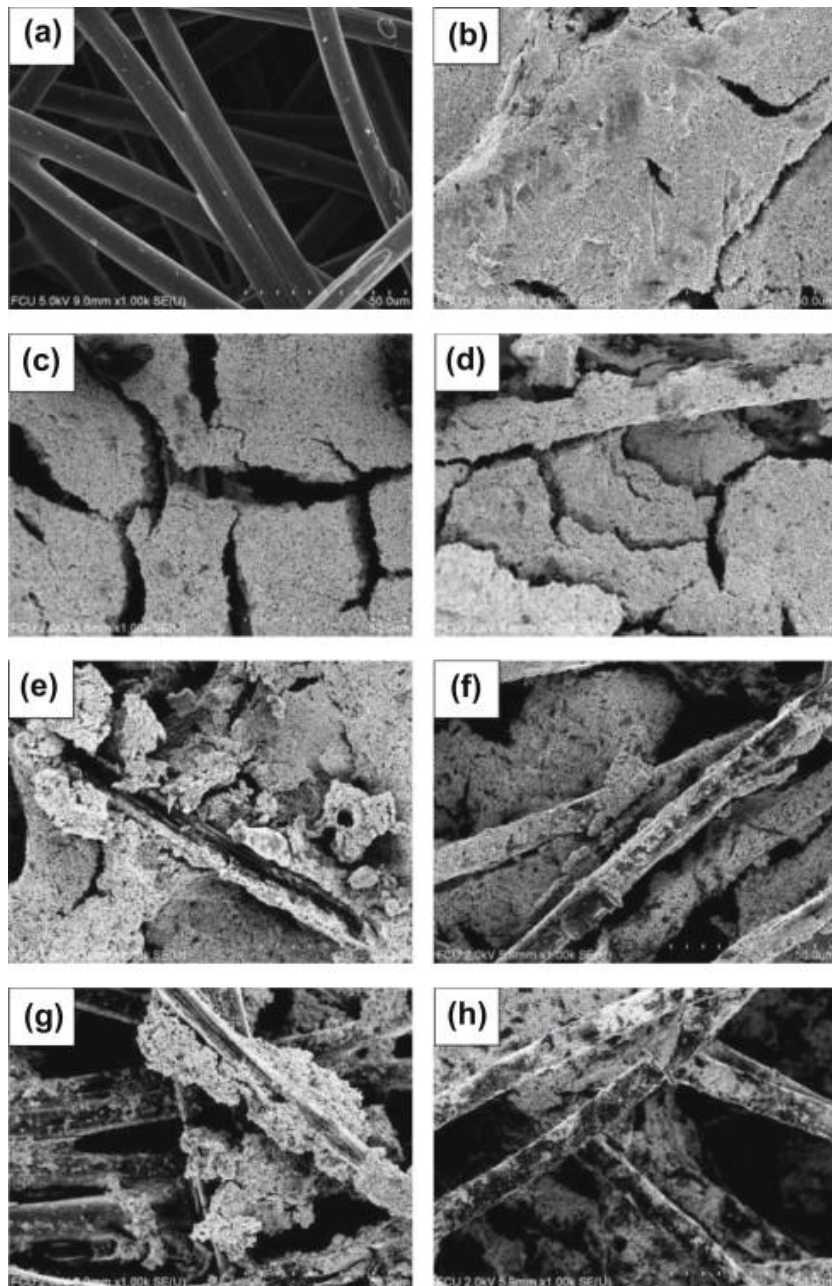


Figure 2.4: Comparison of GDL surfaces in MPL water washing conditions after various times: (a) Carbon paper substrate, (b) GDL with MPL, (c) GDL-1HR (in 1 hour water washing), (d) GDL-5HR (in 5 hour water washing), (e) GDL-10HR (in 10 hour water washing), (f) GDL-50HR (in 50 hour water washing), (g) GDL-100HR (in 100 hour water washing), (e) GDL-200HR (in 200 hour water washing) [21]

In automotive applications, PEFCs can be subjected to sub-zero conditions at start-up conditions. The GDL under such conditions suffers from deformation in its structure and subsequent drop in its performance. This type of degradation can be seen as thermal degradation affecting the GDL mechanical integrity. A few studies have addressed the effect of freezing conditions on the GDL performance and the formation of ice between the GDL/CL/membrane interfaces. The presence of ice applies extra stress on the brittle GDL when clamped within the fuel cell structure causing it to 'crush' [162]. Yan *et al.* [163] reported the effect of freeze-thaw cycles on the MEA properties and performance. They observed a significant damage of the GDL when operated under freezing conditions caused by the backing layer (Teflon) and the binder structure on the GDL carbon paper surface. However, Pelaez and Kandlikar [24] and Lee and Merida [22] reported no effect on the GDL properties due to freezing/thaw cycling in *ex-situ* experiments. In contradiction to the above findings, Lim *et al.* [164] observed, by performing *in-situ* experiments on three types of GDL (carbon paper, carbon felt and carbon cloth), a drop in PEFC performance under freeze/thaw cycling conditions. They found that the carbon felt GDL samples had the least degradation in performance due to its high stiffness that prevents gap forming between the GDL and the membrane and therefore preventing the increase in contact resistance. The *ex-situ* testing also showed that the carbon felt GDL surface was the least damaged compared to the carbon paper GDL, exhibiting the highest damage.

GDL degradation due to freeze/thaw cycling has a more significant effect on GDLs containing MPLs. Lee *et al.* [165] reported damage on the catalyst layer when MPL was present whereby the MPL lost its effect in decreasing the contact resistance and water management after 40 cycles.

It can be concluded that the sub-freezing effect on the GDL is dependent upon the humidification level of the MEA under these conditions and the presence of trapped pools of water within the MEA. Therefore, the effect of freezing can be avoided by either purging the PEFC (removing any accumulated water) or using low RHs before being subjected to freezing conditions as observed by Hou *et al.* [166]. Furthermore, Hou *et al.* also found that the MPL may be weakened by freeze/thaw cycling making it prone to material loss from air flow through the GDL.

Finally, the GDL structure has a significant effect on the GDL mechanical integrity and mechanical degradation tolerance. Poornesh *et al.*[159] found that the heterogeneous carbon fibres in GDL contribute to surface rupture, hydrophobic coating deterioration, and breakage of the fibre under PEFC loading and working conditions. They concluded that using homogeneous fibres may enhance the GDL durability [159].

2.4.3 THERMAL DEGRADATION

No significant studies have been carried out in the literature addressing the effect of temperature on GDLs; however, a few observations were mentioned regarding its effect. High temperature significantly affects the GDL maximum strain, resulting from weakening PTFE within the GDL [122] and enhancing carbon corrosion [150].

Moreover, it is thought that hot press (when fabricating MEAs) and freezing conditions weaken the GDL and MPL structures and lead to material loss during PEFC operation [121,167].

CHAPTER THREE

METHODOLOGY AND EXPERIMENT

CHAPTER 3: METHODOLOGY AND EXPERIMENT

This chapter discusses the methodology adopted in this thesis to develop a better understanding of the various Gas Diffusion Layer (GDL) types available in the market. The study is focused on characterising a wide range of commercially available GDLs. The experiments used in characterising the samples and the method of analysing the results are also discussed.

3.1 METHODOLOGY

Figure 3.1 shows the research methodology used in the research work presented in this thesis. A review of GDL manufacturers and their products was conducted. The available information in manufacturers' datasheets were gathered (datasheets are attached in appendix A1). The information provided from the different manufacturers varies in terms of what is provided and the tests used for obtaining the data. Some manufacturers assign their products to specific relevant applications; however, no clear background is given to the selection method.

Samples were selected to ensure a full range of variety in the samples from the different manufacturers examined. The properties of all samples were obtained by conducting a number of *ex-situ* characterisations under the same conditions.

Properties obtained included the GDL structure and surface morphology, as well as physical and electrical properties.

The GDLs were then used to fabricate the cathode gas diffusion electrodes to be tested in the MEA at the cathode side. Considering that the performance of the GDL is dependent on compression, the clamping pressure for each GDL was optimised for the maximum power density of the MEA. After optimisation, the performance of

the MEAs was analysed and the effect of the cathode GDL on the performance was studied. The study is focused on examining the performance of the GDL at the cathode side, as the demand of water management at the cathode is higher than that at the anode due to the water production from oxygen reduction reaction.

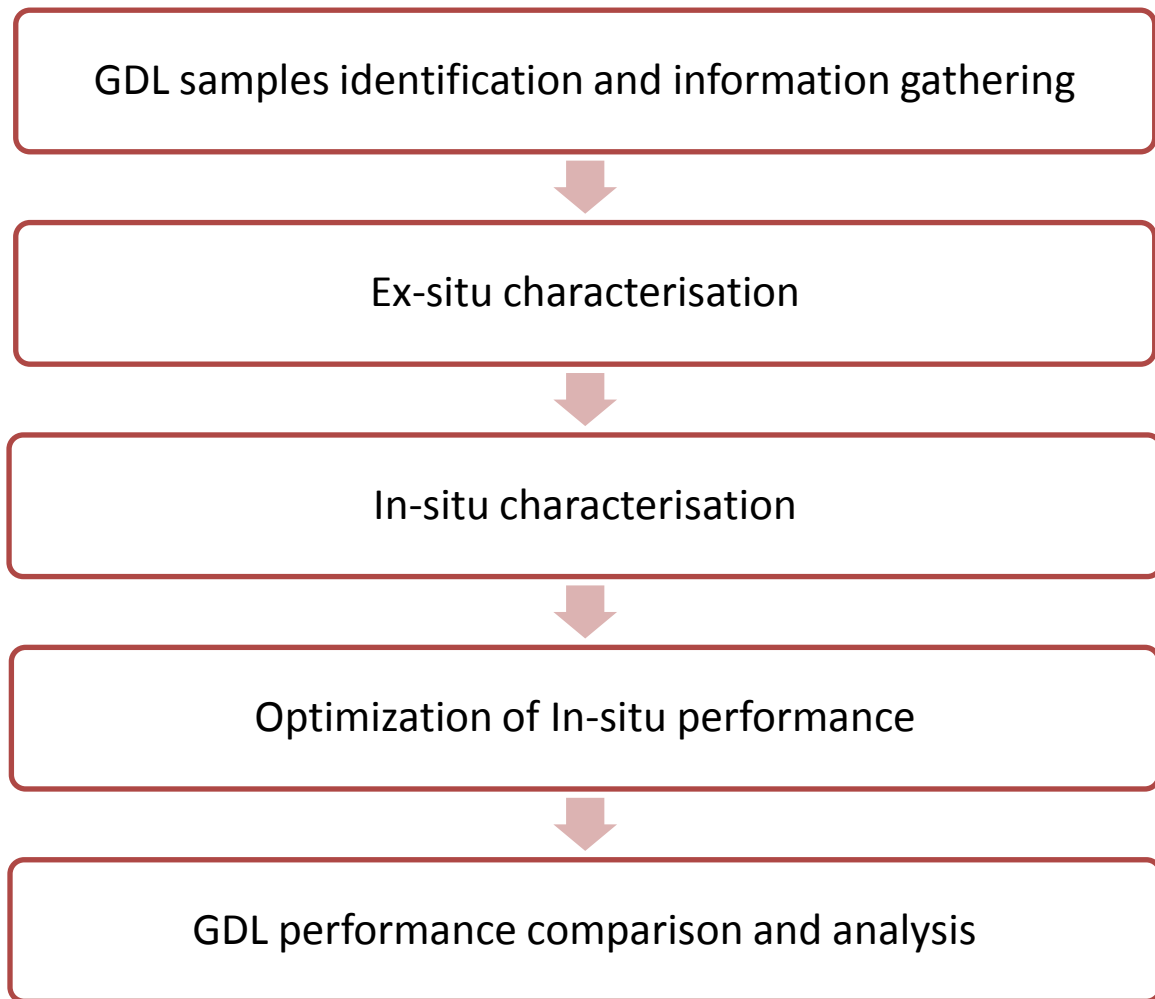


Figure 3.1: Research methodology

3.2 EXPERIMENTS

3.2.1 EX-SITU CHARACTERISATION

Scanning Electron Microscopy (SEM)

SEM images were obtained of the substrate and the MPL of the GDL using a Philips XL 30 SEM. The instrument provides both secondary electron and backscattered electron imaging, with a resolution of 3.2nm at 30kV. SEM images are taken by applying a focused electron beam on the surface of a sample, the interaction between the sample and the electrons produce signals (secondary electrons) with information about the topography and material of the sample. The signals are detected to form an image of the surface of the samples.

The GDL samples were gold coated before imaging to prevent samples charging under the electron beam. All images were taken at 20kV on secondary electron mode. Substrate images were taken at 500 μ m and 50 μ m scales to examine the structure and fibres respectively. The MPL images were taken at 10 μ m – 50 μ m range. Images of the surface and cross section of the different samples were compared and analysed to understand the difference in the GDL structure.

Interferometer

An interferometer (KLA Tencor MicroXAM2) was used to study the topography and roughness of the substrate and MPL surface. In the measurement, the surface is scanned with a focused light beam and the reflected light is used to measure the distance from each segment of the surface. This is then used to give an image of the surface topography and a statistical analysis of the surface roughness. The GDL roughness was tested to examine the effect of roughness on the contact resistance

with the flow field plate (FFP) and have a better understanding of the surface effect on the catalyst layer. An 20x objective lens was used for imaging the GDL substrate and a 50x objective lens for the MPL. In conducting the measurement, the samples were mounted on the interferometer stage, the lens focus is found, and then a scan over the sample surface is conducted. Figure 3.2 shows an image of interferometer used and an example of the data obtained.

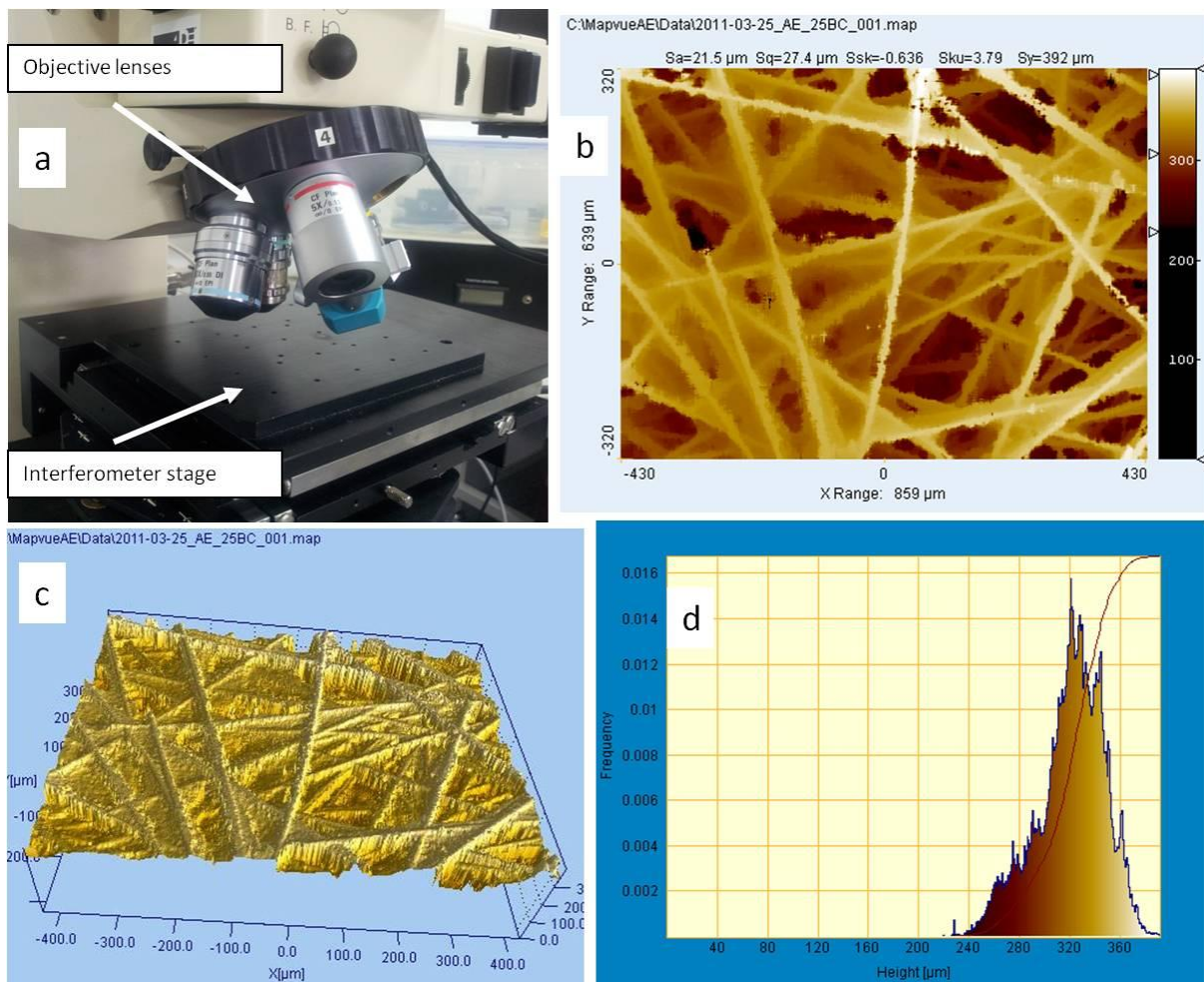


Figure 3.2: (a) Interferometer showing the sample mounting stage and the objective lenses, (b) SGL 25BC image using the interferometer, (C) 3D structure of SGL 25BC and (d) Hysteresis in measured height over the sample surface.

Drop Shape Analyser

A drop shape analyser (Kruss DSA-100) was used to measure the water contact angle on the surface of the substrate and the MPL using the Sessile Drop Method. In this measurement, a 5 μ L water droplet is placed on the surface of the sample, and a photo of the droplet and the interface with the surface is then analysed using DSA3 software to measure the water contact angle as an indication of the hydrophobic or hydrophilic properties of the GDL. The sessile drop contact angle method is limited in its accuracy due to the inhomogeneous surface structure of the GDL and the roughness of the surface, hence, the high standard deviation in the results reported. Moreover, the contact angle for hydrophilic surfaces changes with time as the droplet water diffuses into the pores through the surface.

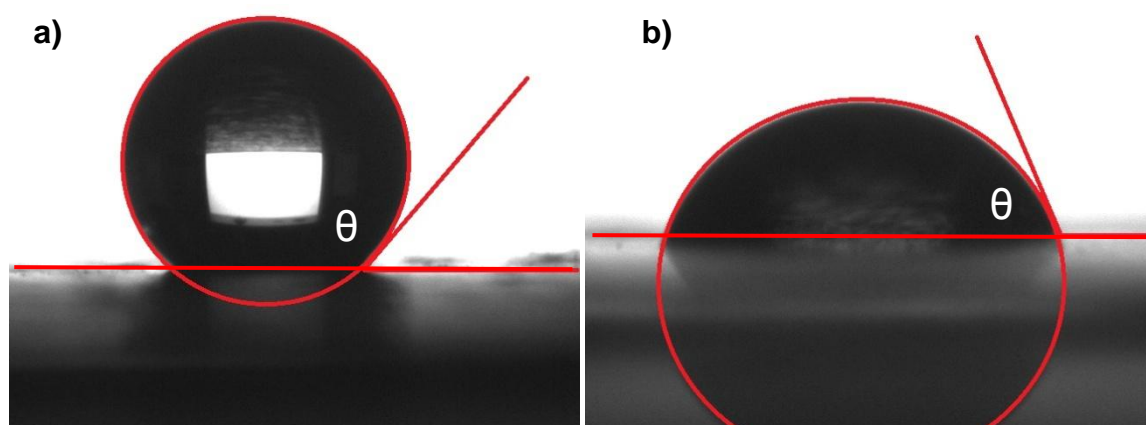


Figure 3.3: Water contact angle on (a) a hydrophobic surface and (b) a hydrophilic surface

Helium Pycnometer

A Helium Pycnometer (Micromeritics AccuPyc II 1340) was used to measure the real (absolute) density of the GDL materials. In a pycnometer, the sample is placed in a chamber of premeasured fixed volume. After evacuating the air from the chamber, helium is pumped in to measure the void volume. The volume of the sample is then calculated by subtracting the volume of the chamber from the void volume after

placing the sample. Density is then calculated by dividing the sample mass over the measured volume.

GDL samples weighing around 50mg were tested in the pycnometer. At each test, 10 measurements were made over 10 cycles of helium pumping and evacuation.

Mercury porosimeter

Bulk density (g cm^{-3}), porosity (%), tortuosity (*dimensionless*), pore size distribution and permeability (m^2) were measured using a mercury porosimeter (Micromeritics AutoPore IV) (see Figure 3.4 (a)). Here, the measured permeability corresponds to mercury permeation through the GDL as a function of increasing pressure (MPa).

The porosimeter is capable of measuring capillary diameter range from $0.003\mu\text{m}$ to $360\mu\text{m}$ through the accurate measurement of intrusion and extrusion volume with a resolution better than $0.1\mu\text{L}$.

Experimentally, GDL samples (ca. 100-200 mg) were placed in the porosimeter stem (Figure 3.4 (b)) to undergo low and high pressure mercury intrusion testing. Mercury was then inserted gradually into the sample by increasing the pressure up to 30,000 Psi (~ 206 MPa) whereby the GDL sample pores were filled starting from the larger pores at low pressures and down to smaller pores at higher pressures. An example of the recorded volume intrusion with change in pressure is shown in Figure 3.4(c). This method allows the measurement and determination of total pore volume, skeletal volume, real and bulk density, total porosity, and pore size distribution.

The Micromeritics AutoPore IV software uses the Washburn's equation (see Equation 3.1) at different pressures in the specified range to determine the pore size distribution and the pore length of the GDL sample based on the assumption that the

pores are of cylindrical geometry. Furthermore, the Katz and Thompson's equation (see Equation 3.2), derived from percolation theory, is used by the software to calculate the absolute permeability (k) of the GDL sample. The permeability values are then used in the expression derived by Jörgen Hager to calculate tortuosity [34]. In our experimental work, all these values were automatically calculated by the Micromeritics Instruments software as detailed and explained in the paper published by Micromeritics Instruments Corp [168].

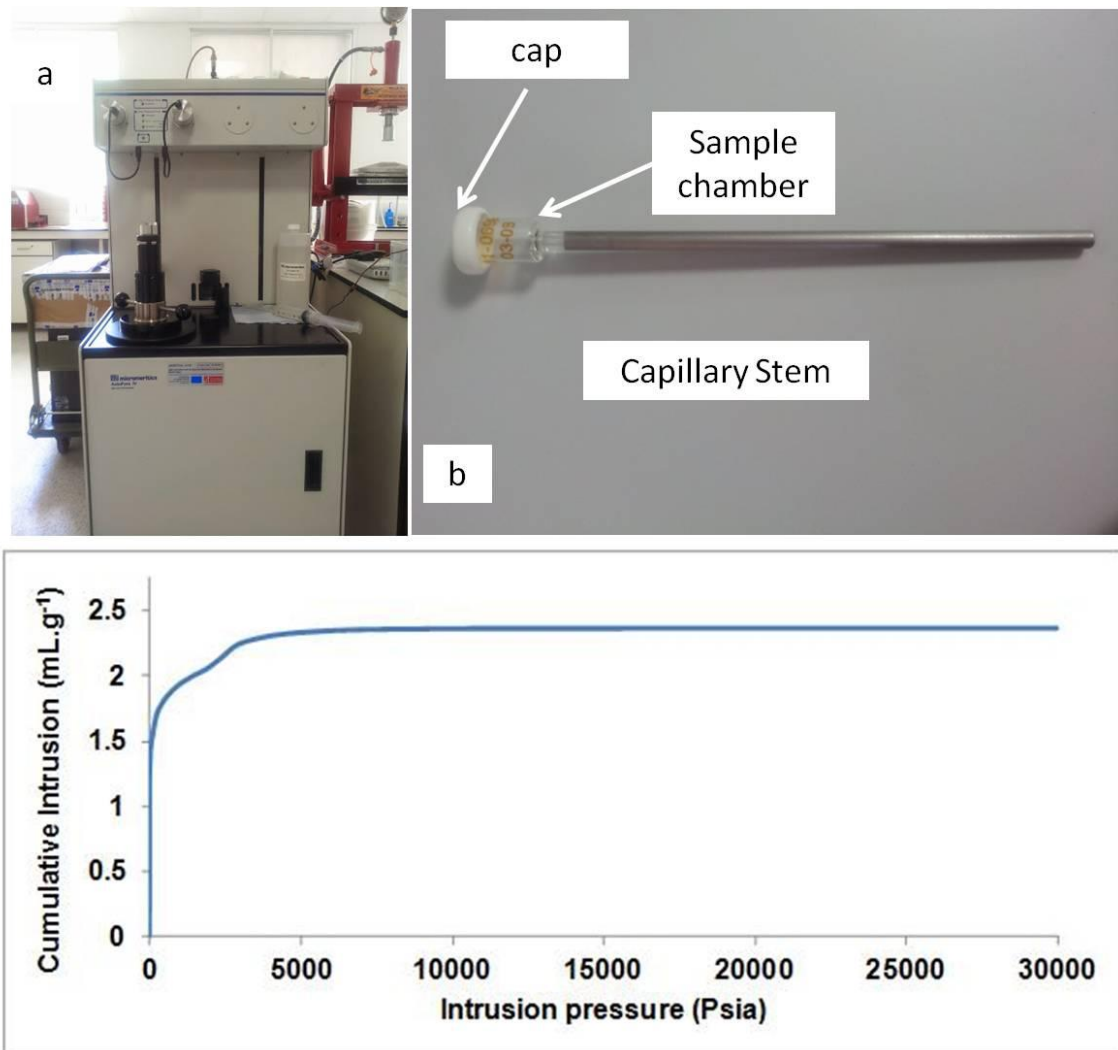


Figure 3.4: (a) Micromeritics AutoPore IV Porosimeter, (b) capillary stem and (c) intrusion volume with increasing pressure.

$$d_{pore} = -\frac{4\gamma\cos\theta}{P} \quad (\text{Eq. 3.1})$$

where,

d_{pore} is the pore diameter in m

γ is the surface tension in $\text{N}\cdot\text{m}^{-1}$

θ is the liquid-solid contact angle

P is pressure in Pa

$$k = \frac{1}{226} (L_c)^2 \sigma / \sigma_o \quad (\text{Eq. 3.2})$$

where,

k is the permeability of the pore structure (m^2)

L_c is the characteristic length of the pore space (m)

σ / σ_o is the pore structure conductance ratio

Environmental Mechanical Analyser

An environmental mechanical analyser (Instron 5848 MicroTester) was used for the study of the mechanical properties of the GDL. The instrument has a force range from 10mN to 2 kN and a displacement resolution of less than 5 μm .

Samples with 4 cm^2 area were subjected to cyclic pressure with an increment of 50 $\text{N}\cdot\text{min}^{-1}$. The deformation in the GDL thickness with pressure was recorded.

Three samples of each GDL material were tested. The axial displacement with the compression was measured. Before conducting the test on the GDL samples, the

test was run with no samples placed to subtract any instrumental displacement from the measured values of the GDL.

Universal Mechanical Tester (Zwick/Roell Z030)

A universal mechanical tester was used for applying pressure for studying the electrical contact resistance under compression. The instrument is a displacement controlled machine with a force range from 10mN to 30kN. The details of the test are described in more details in the “electrical contact resistance”.

4-wire Kelvin Milli/Micro-Ohmmeter

The 4-wire Kelvin method was used to measure the electrical properties (in-plane and through plane) of the GDL. Ohmic resistance measurement of a sample is measured by applying a DC current through the sample and measuring the voltage drop across it. The resistance then can be calculated by dividing the voltage over the current. The 4-wire Kelvin method is a wiring arrangement for the voltage and current sensors to avoid including the resistance of the leads in the measurement. A BS407 precision Milli/Micro-Ohmmeter (resolution of $1\mu\Omega$ and 0.1% resolution accuracy) was used to conduct the measurements.

In-plane electrical resistance

In-plane electrical resistance was measured using the method reported by Williams *et al.* [9]. GDL samples of 2 mm width and 100 mm length were manually cut and the resistance was measured at 10 mm increments (10 points in total) (see Figure 3.5). The measured resistance (R) values were plotted against distances (l) and yielded a linear relationship whereby the slope of the line represented the *in-plane* resistance per unit of distance (R')

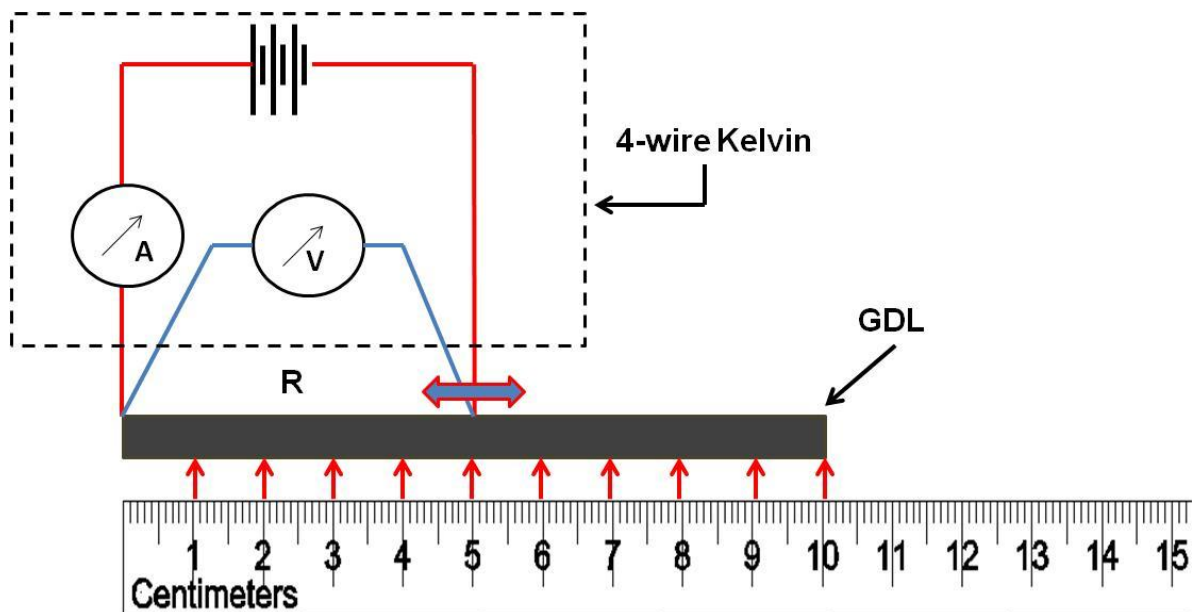


Figure 3.5: Electrical in-plane resistance measurement setup.

The GDL samples *in-plane* resistivity (ρ) values were calculated using Ohm's Law as shown in Equation 3.3:

$$R = (\rho l) / A \rightarrow \rho = (R A) / l \quad (\text{Eq. 3.3})$$

where,

R is the *in-plane* resistance of the GDL in Ω

ρ is the *in-plane* resistivity in $\Omega \text{ m}$

A is the cross-sectional area of the GDL sample in m^2

l is the length of the GDL sample in m

Electrical contact resistance

The contact resistance (R_c) between a 4 cm^2 GDL and 'plain POCO graphite (POCO AXF-5Q) plates (industry standard material often used as a reference material) was measured at various clamping pressures. The clamping pressure was monitored using a controlled compression device (Zwick Roel Z030). The GDLs were pre-

conditioned by applying a pressure of 3 MPa (5 times) before conducting the test. This step was performed to eliminate the effect of ‘irreversible’ deformation of the GDL as (i) the contact resistance values became repeatable and (ii) the irreversible changes were found to be negligible after the 5th compression [90]. Three samples of each GDL type were tested, the resistance values measured show very good repeatability with a standard deviation lower than 5%.

The GDL was placed between the two POCO graphite plates and the two gold plated stainless steel (SS) current collectors as shown in Figure 3.6. The resistance was measured by the 4-wire Kelvin method using a BS407 precision Milli/Micro-Ohmmeter (resolution of 1 $\mu\Omega$ with 0.1% of resolution accuracy). The contact resistance between the POCO plates and the gold plated SS plates was measured using a similar arrangement, where one POCO plate was placed between the two gold plated plates. All measured resistance values were used to calculate the contact resistances using the following equations:

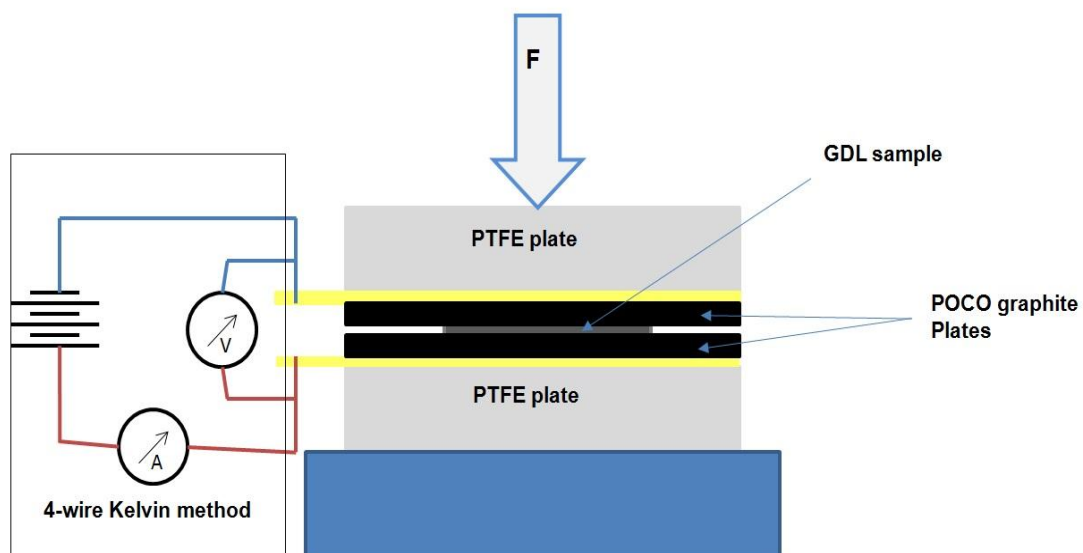


Figure 3.6: Electrical contact resistance measurement setup.

$$R_{\text{measured}} = 2 \times R_{\text{c,SS-Au/FFP}} + 2 \times R_{\text{c,FFP/GDL}} + 2 \times R_{\text{FFP}} + R_{\text{GDL}} \quad (\text{Eq. 3.4})$$

And

$$R_{\text{FFP measured}} = 2 \times R_{\text{c, SS-Au/FFP}} + R_{\text{FFP}} \quad (\text{Eq. 3.5})$$

where,

$R_{\text{c,FFP/GDL}}$ is the contact resistance between the GDL and the POCO graphite flow field plate

$R_{\text{c, SS-Au/FFP}}$ is the contact resistance between the POCO graphite flow field plate and the gold plated stainless steel plate

R_{FFP} is the *through-plane* resistance of the POCO graphite flow field plate

R_{GDL} is the *through-plane* resistance of the GDL

Subtracting Equation (3.4) to Equation (3.5) gives Equation (3.6):

$$R_{\text{measured}} - R_{\text{FFP measured}} = 2 \times R_{\text{c,FFP/GDL}} + R_{\text{FFP}} + R_{\text{GDL}} \quad (\text{Eq. 3.6})$$

Rearranging Equation (3.4), one obtains the contact resistance between the GDL and the POCO graphite flow field plate ($R_{\text{c,FFP/GDL}}$):

$$R_{\text{c,FFP/GDL}} = (R_{\text{measured}} - R_{\text{FFP measured}} - R_{\text{FFP}} - R_{\text{GDL}}) / 2 \quad (\text{Eq. 3.7})$$

If it is assumed that R_{FFP} and R_{GDL} are negligible due to their low resistance value, so that Equation (3.7) may be simplified to:

$$R_{\text{c,FFP/GDL}} = (R_{\text{measured}} - R_{\text{FFP measured}}) / 2 \quad (\text{Eq. 3.8})$$

For example, POCO graphite plates have very low resistivity ($\sim 1.470 \text{ m}\Omega \text{ cm}$) [60] and using Equation (3.3) the resistance of the POCO graphite plate used (area = 4 cm^2 , thickness = 3 mm) was calculated to be $0.110 \text{ m}\Omega$. Thus in our conditions, R_{FFP} and similarly, the GDL *through-plane* resistance ($R_{GDL} < 10^{-3} - 10^{-6} \Omega$) can be neglected under the range of clamping pressures used [142,169]. The simplified equation (3.8) is used for the calculations in this study.

3.2.2 *IN-SITU* CHARACTERISATION

MEA fabrication

The fabrication process of the MEA can be divided into two stages, namely; preparation of electrodes and components assembly (see Figure 3.4). The work for this thesis, the GDL samples under examination were used at the cathode side of the MEA, and commercial Johnson Matthey Gas Diffusion Electrodes (GDEs) (ELE0165; SGL 34BC with loading of 0.4 mgPt/cm^2) were used at the anode side.

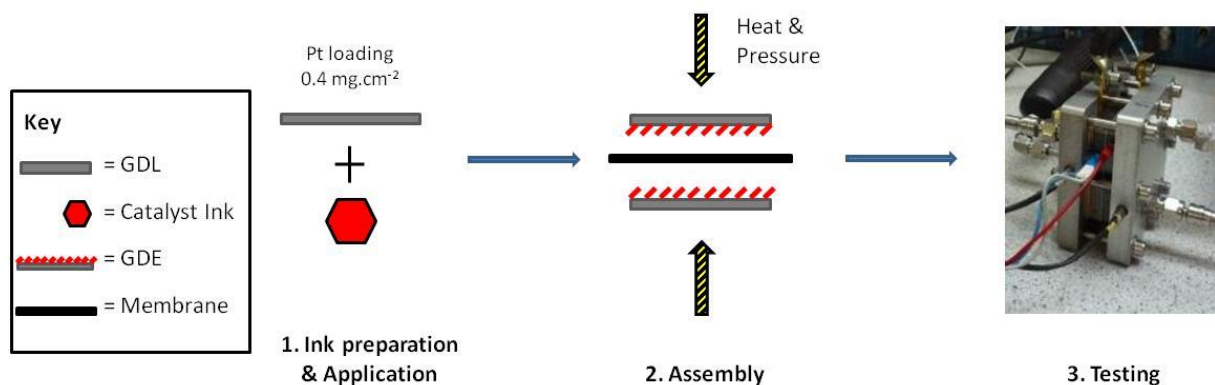


Figure 3.7: MEA fabrication and testing

To prepare the anode GDE, a layer of Nafion solution (10 wt % Nafion solution (Ionpower) and Iso-Propanol (Sigma Aldrich)) was hand painted on the catalyst

coated side of the commercial GDE to enhance contact between the catalyst layer and the membrane at the triple phase boundary.

A catalyst ink is then prepared to fabricate the cathode GDE. Commercially available 45.6 wt % Pt/C carbon powder (Tanaka Kikinzoku Kogyo), 10 wt % Nafion solution, and isopropanol were used to prepare the catalyst ink for the cathode GDE. The composition of the catalyst ink was calculated to achieve Pt loading of 0.4 mg.cm^{-2} and a 1 to 1 Nafion to carbon black weight ratio. The catalyst ink is mixed using Ultrasonic Bath for 30 minutes.

The catalyst ink was then hand painted on the cathode GDL. The actual loading on the GDL was calculated from the difference in the weight between the GDE (GDL after painting) and the GDL. The GDEs were then assembled with a Nafion N212 membrane and hot pressed for 2 minutes at 125°C and 1800N (Fig. 3.7) (Refer to Appendix A2 for the calculations used for GDE fabrication). It is important to note that a major limitation to this GDE fabrication method is the use of hand painting in applying the ink to the GDE. This resulted in a variation in Pt loading and uneven distribution over the surface of the electrode. Other methods can be used for applying the catalyst layer, namely, doctor blade method, screen printing and spraying to achieve a more homogeneous electrode.

PaxiTeck fuel cell fixture and Biologic Fuel Cell test station

The fabricated MEAs were tested in a PaxiTeck single cell fixture (see Figure 3.8) with graphite monopolar plates. The monopolar plates have a single serpentine flow field channel (1mm width x 1mm depth). Gold plated copper current collector plates and the aluminium end plates were used. The aluminium end plates allow the use of electrical heating elements to control the temperature at anode and cathode

separately. The cell temperature was measured using Negative Temperature Coefficient (NTC) sensor inserted into the cathode graphite monopolar plate. The cell potential was measured between the monopolar plates. The cell was connected to an electrical load in the test station through the gold plated current collectors.

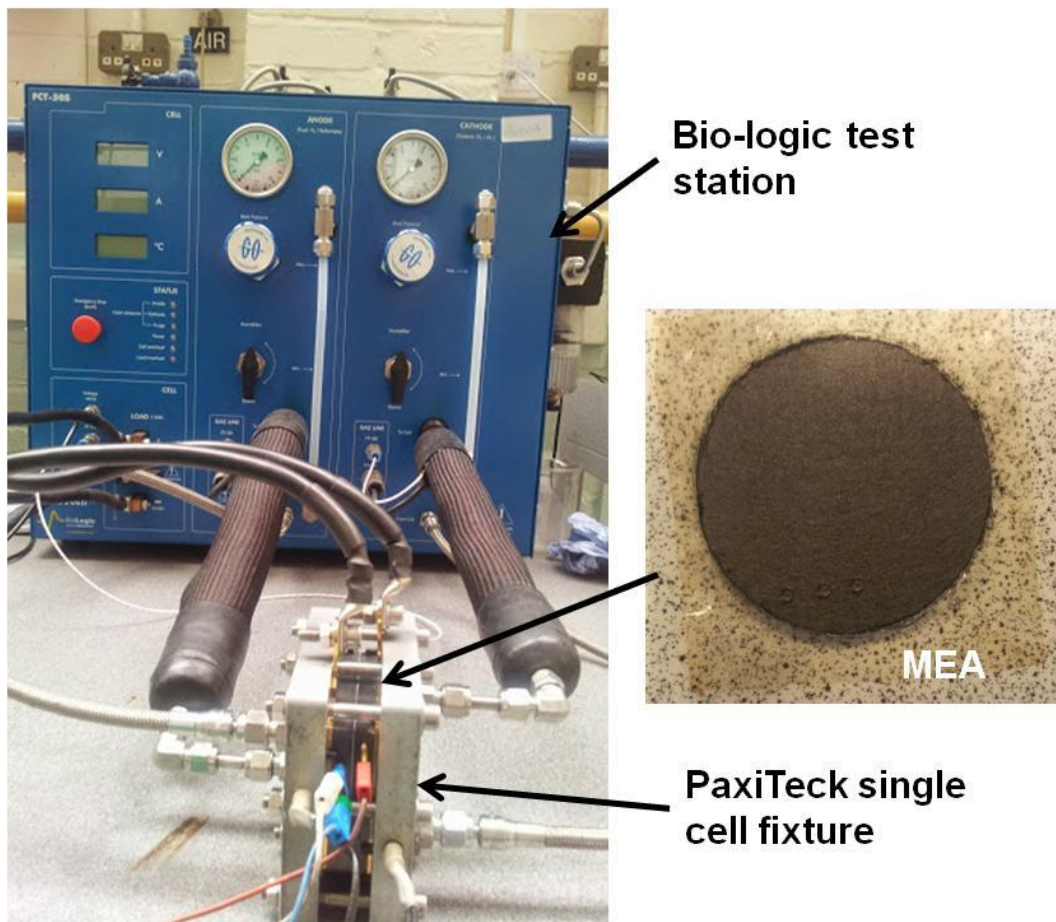


Figure 3.8: Bio-logic test station used for MEA *in-situ* characterisation.

The cell was tested using a Bio-logic FCT-50S test station (Figure 3.8). The test station has a 50A maximum load current and 250W power respectively. The station is computer controlled using FC-lab® software. Reactant temperature and humidity are controlled by the station with sensors and electrical heaters to measure and control the anode and cathode humidifier temperature and reactants line. The reactants back pressure is also controlled.

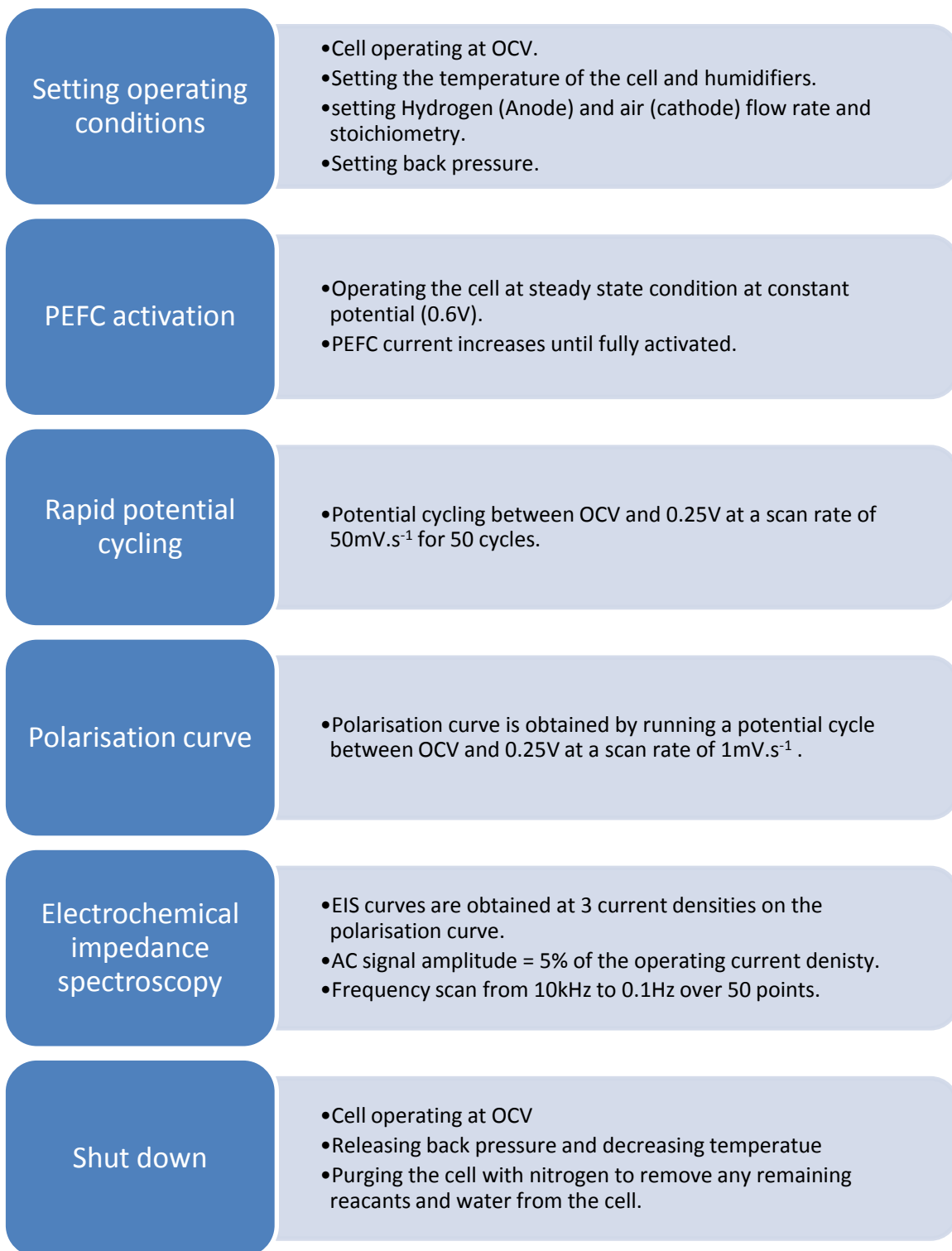


Figure 3.9: MEA testing procedure

All samples were conditioned and tested under controlled operating conditions following a set procedure (Fig. 3.9). The reactants and cell conditions brought to the desired temperature, humidity and pressure. The cell is then conditioned by operating it at constant voltage of 0.6V. At conditioning, the cell's current increases until the cell is fully conditioned (the Nafion membrane is fully humidified). Conditioning time varied for the different MEAs test but usually steady state was reached within 6-7 hours. After conditioning, 50 rapid potential sweep cycles between OCV and 0.25V are conducted followed by a slow potential sweep cycle to obtain the cell polarisation curve. The polarisation curves produced from the rapid sweep show an increase in performance between the first 3 to 5 curves then performance becomes constant.

Electrochemical Impedance Spectroscopy (EIS) is then conducted at 3 current densities; low current density (close to OCV), medium current density, and high current density. Impedance is measured by applying a small AC electrical current or voltage (5% of the DC current or voltage [170]) at different frequencies and measure the output voltage or current respectively. An AC signal (current or voltage) has amplitude, frequency and phase. The value of the system impedance will determine the amplitude and phase shift of the output signal. Using these values the system impedance is calculated.

System impedance is a combination of resistance, capacitance and inductance. A pure resistance affects the amplitude but has no effect on the phase; this presents the real vector of impedance. Capacitors and inductors affect both the amplitude and phase of the signal; capacitance and inductance result in the imaginary vector of the impedance. The capacitor causes a negative phase shift and the inductor causes a

positive shift (see Figure 3.10). Ohmic resistance makes the real element of impedance while capacitance and inductance make the imaginary element. The value of inductance and capacitance impedance is dependent on the frequency of the signal (Equation (3.11) and (3.12)).

$$Z = Z_R + Z_L + Z_C \quad (\text{Eq. 3.9})$$

$$Z_R = R \quad (\text{Eq. 3.10})$$

$$Z_L = j\omega L \quad (\text{Eq. 3.11})$$

$$Z_C = \frac{-j}{\omega C} \quad (\text{Eq. 3.12})$$

Where;

Z is the total system impedance (Ω)

Z_R is the ohmic impedance (Ω)

Z_L is the inductive impedance (Ω)

Z_C is the capacitive impedance (Ω)

R is the Ohmic resistance of a system (Ω)

ω is the frequency

L is the inductance of the system (H)

C is the capacitance of the system (F)

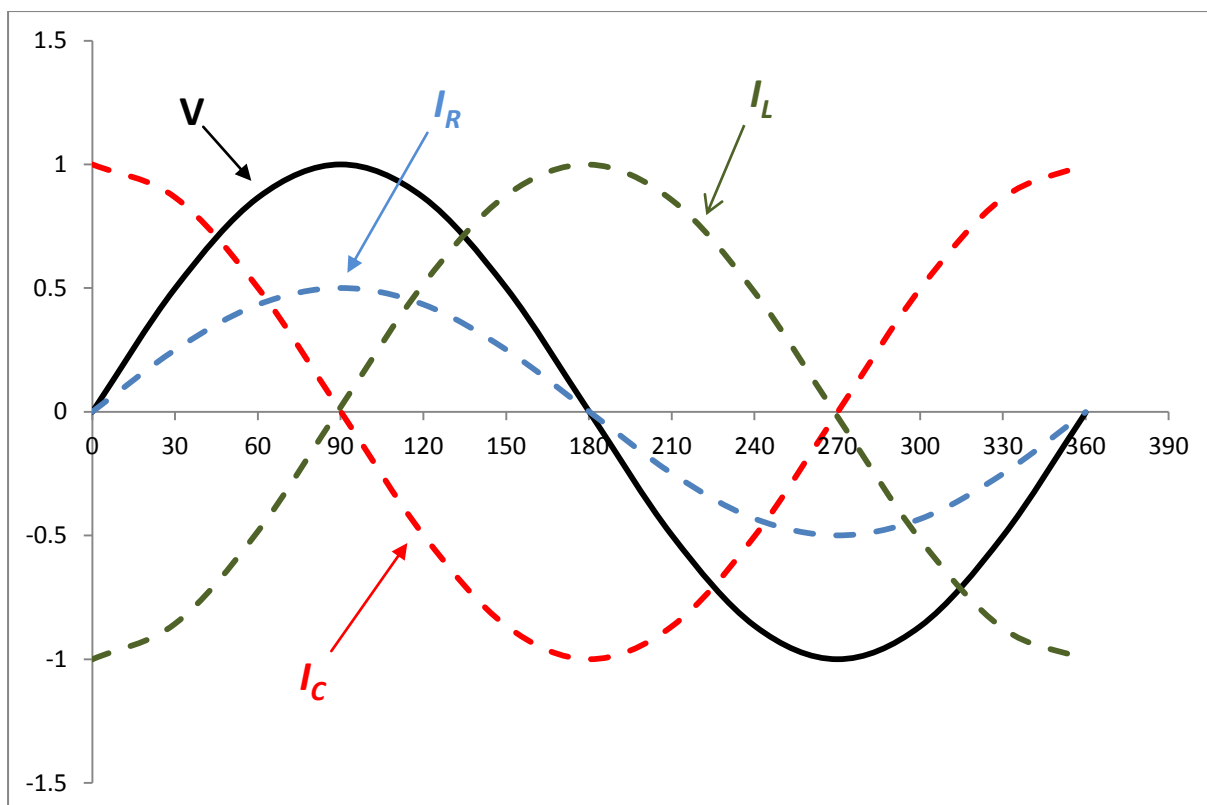


Figure 3.10: The effect of the different impedance elements on AC signals

In an EIS measurement, several AC signals of different frequencies are applied to in the sample (0.1Hz -100kHz [171]). The measured impedance values are then plotted in what is called a Nyquist plot from which information about the system or a single component can be found. Figure 3.11 shows Nyquist plots for a JM electrode MEA at different current densities. The main limitation of the EIS method is the interpretation of the response to relate the result to the different processes in a system. Many studies looked at interpreting EIS curves for fuel cells by modelling the impedance spectrum with an equivalent electrical circuit and measuring the impedance at different operating conditions [171–174]. A fuel cell is usually modelled by a combination of resistors and capacitors.

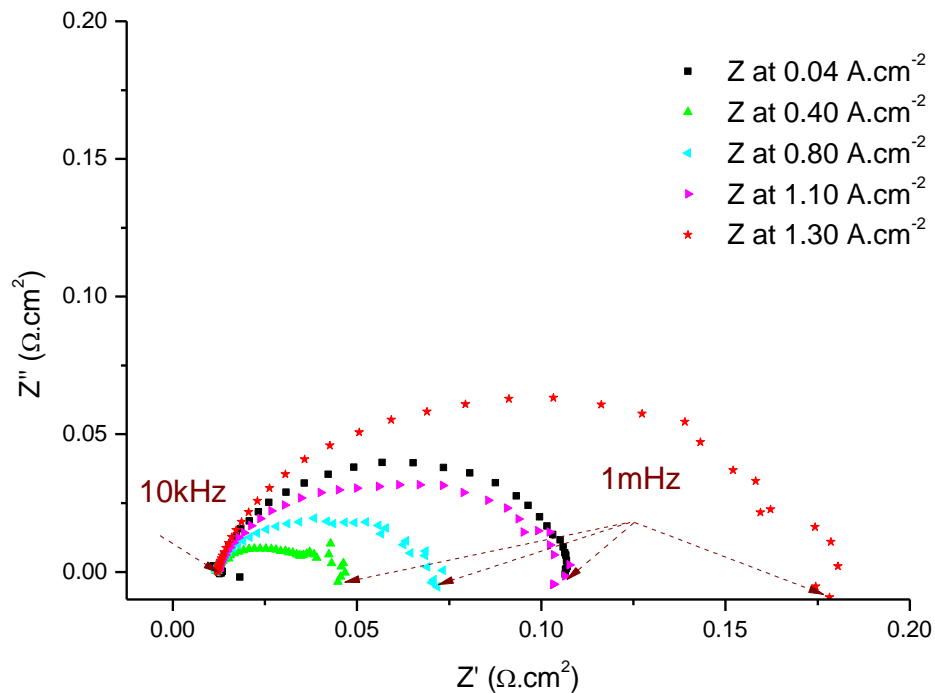


Figure 3.11: EIS plot for JM electrode at different current densities

Figure 3.12 shows the contribution of the three polarisation processes in the MEA to the impedance values at different current densities. At low current density (potential close to OCV), the impedance of the cell is mainly influenced by the electrode kinetics of the ORR reaction. The EIS curve takes a single semicircular arc shape. The diameter (the difference between the low frequency and high frequency resistance) of the semicircle is equal to the charge transfer resistance (a measure of the electrode kinetics). The high-frequency impedance value of the curve presents the cells ohmic resistance. The value of the resistance (R_s) is equal to the sum of the electrical resistances of the different components in the cell.

With the increase in the current density, a new small arc appears at the low frequency impedance region; this arc represents the mass transport resistance in the cell (Figure 3.11). However, the difference between the low-frequency and high-

frequency resistance decreases due to the decrease in the charge transfer resistance (see Figure 3.8). Further increase in the current density results in an increase in the mass transport polarisation, hence the mass transport arc size increases and the overall cell resistance increases.

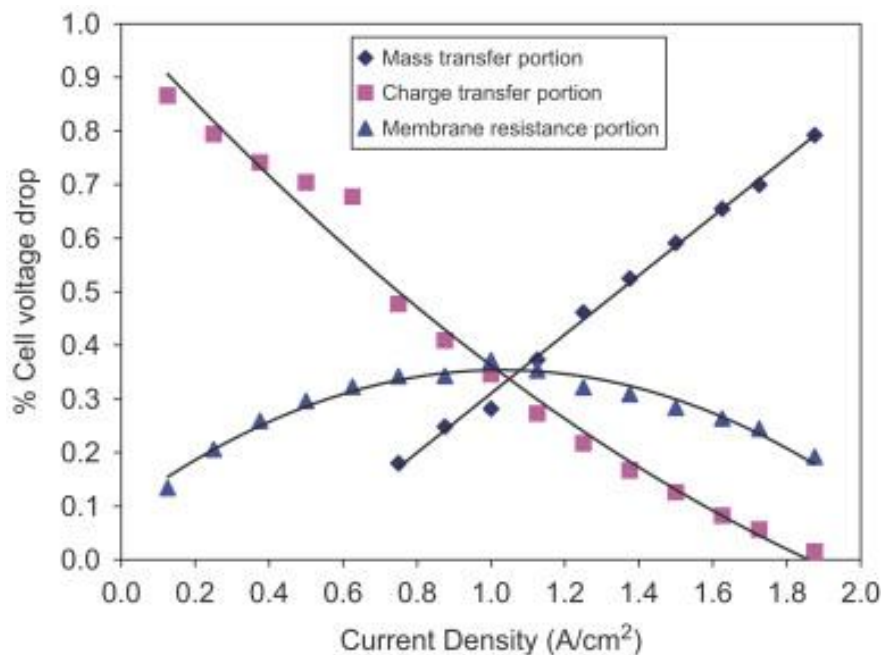


Figure 3.12: Potential loss contribution of the different polarisations with the change in current density [175]

So a Nyquist plot consists of one or several arcs as a result of the different impedance elements (resistance and capacitance). The single arc at low current density can be modelled by Randles equivalent impedance circuit shown in Figure 3.13 (a). R_s represents the ohmic resistance of the different components of a fuel cell; however, the main contributor to the resistance value is the electrolyte resistance. The parallel resistance/ capacitance electrical circuit considers the electrochemical process on the cathode electrode; R_p is the charge transfer resistance and C_{dl} is the double layer capacitance on the surface of the electrode.

Randles equivalent circuit is limited in explaining the cell behaviour to low current densities as it doesn't take into consideration mass transport.

The fuel cell equivalent circuit is modified for high current density to include mass transport effect. Figure 3.11 shows the appearance of a second arc when increasing the current density. The parallel R_d and C_d added to the circuit consider the diffusion losses through the MEA (see Figure 3.13 (b)). The values of the different parameters of the electrical circuit can be calculated using modelling software by fitting the model to the actual experimental data.

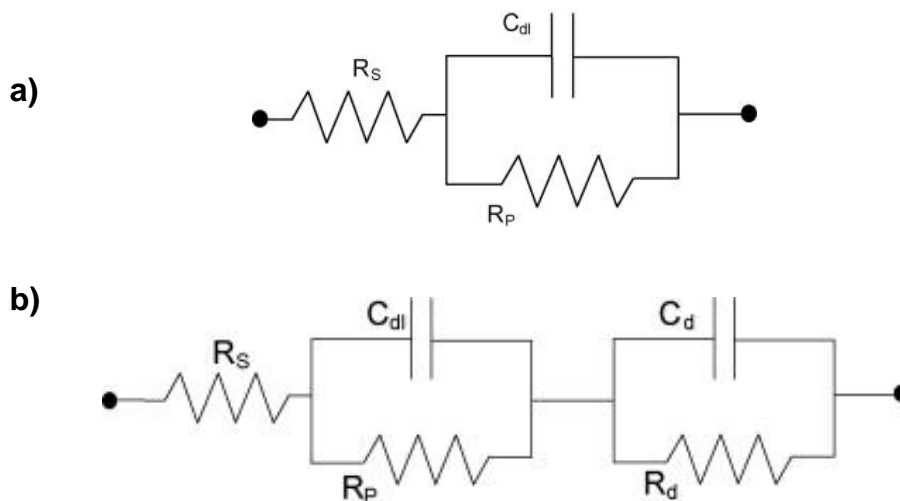


Figure 3.13: Fuel cell impedance equivalent circuit; a) Randle circuit and b) cell impedance including the mass transport losses [176].

In this study, a qualitative comparison between EIS results for the different GDLs is considered by comparing the change in the ohmic resistance of the cell and the size of the mass transport arc.

CHAPTER FOUR

EX-SITU CHARACTERISATION OF GAS DIFFUSION LAYERS

CHAPTER 4: EX-SITU CHARACTERISATION OF GAS DIFFUSION LAYERS

To gain an understanding of the wide range of gas diffusion layer (GDL) materials used in polymer electrolyte fuel cells (PEFCs) and reported in the literature, this chapter will focus on the study of the *ex-situ* characteristics of the GDLs. The chapter discusses the structural, mechanical and electrical properties of the GDL, and looks at the relationship between the different properties of the GDL and the effect of the structure, polytetrafluoroethylene (PTFE) treatment and microporous layer (MPL) application on the GDL properties.

4.1 SAMPLES AND EXPERIMENTS

4.1.1 COMMERCIAL GDL SAMPLES

A range of commercial woven and non-woven GDL samples were tested as shown in Table 4.1. The table describes the GDL materials as reported by the manufacturers' technical data sheets (Appendix A1). The range tested represents samples from all main manufacturers of GDL materials, and the various types and structures.

4.1.2 PHYSICAL PROPERTIES

Real (absolute) density ($\text{g}\cdot\text{cm}^{-3}$) values were measured using a helium pycnometer (Micromeritics AccuPyc II 1340). Bulk density ($\text{g}\cdot\text{cm}^{-3}$), porosity (%), tortuosity (*dimensionless*), pore size distribution and permeability (m^2) were measured using a mercury porosimeter (Micromeritics AutoPore IV).

Table 4.1: Commercial GDL materials

Manufacturer	Type	Description
Ballard	1071HCB	Carbon cloth
	P50	P50 is the carbon paper substrate; P50T is a teflonated carbon paper substrate; GDS 1120 is a teflonated paper with a MPL
	P50T	
	GDS1120	
	P75	P75 is a carbon paper substrate; P75T is a teflonated carbon paper substrate; GDS 2120 is a teflonated paper with a MPL
	P75T	
GDS2120		
Toray	TGP-H-030	Teflonated Carbon papers of various thicknesses
	TGP-H-060	
	TGP-H-090	
	TGP-H-120	
Freudenberg	C2	Felt fibres carbon paper based on H2315 substrate with a MPL applied. The fibres here are not teflonated and partially graphitized .
	C4	
	I2 C6	Felt fibres carbon paper based on H2315 I2 substrate with a MPL applied. The fibres here are teflonated and partially graphitized.
	I2 C8	
E-TEK	LT 1200 N	Non-woven web containing a MPL
	LT 1200 W	Woven web containing a MPL
Sigracet	GDL 10 BC	3D fibres paper including an MPL
	GDL 24 BA	Carbon paper with PTFE and with/without MPL as below: BA stands for 5% PTFE loading and no MPL. BC stands for 5% PTFE loading with an MPL DC stands for 20% PTFE loading with an MPL
	GDL 24 BC	
	GDL 25 BA	
	GDL 25 BC	
	GDL 34 BC	
	GDL 34 DC	
	GDL 35BA	
	GDL 35 BC	
Tenax	TCC2660	
	TCC 3250	

Scanning Electron Microscopy (SEM) (Philips XL30) was used to examine the GDL surface morphology on both sides i.e. the one facing the catalyst layer with or without an MPL, and the other one facing the Flow Field Plate (FFP) (Appendix A3). Similarly, the GDL roughness (μm) of each side was measured (over three areas on the sample surface) using an interferometer (Omniscan Microxam 2).

The water contact angle ($^{\circ}$) of the GDL was measured using the sessile drop method. In this method, the contact angle of the water droplet on the solid surface of the GDL and the MPL was measured using a Drop Shape Analyser (Kruss DSA-100). The water contact angle was measured for fixed volume droplets of $5\ \mu\text{L}$ at three points on the surface of the GDL.

4.1.3 ELECTRICAL PROPERTIES

The in-plane and through plane electrical resistance of the GDL were measured using the 4-wire Kelvin method. Through plane electrical resistance was measured with compression change to explore the effect of compression on the electrical contact resistance between the GDL and the FFP.

4.2 RESULTS AND DISCUSSION

4.2.1 PHYSICAL PROPERTIES (THICKNESS AND DENSITY)

Thickness, area weight, bulk and real (material) density are important physical parameters for GDL materials. Thickness has a direct effect on gas and water permeability, diffusion and electrical conductivity. Area weight and bulk density relate to the fibre structure density, MPL carbon density and PTFE loading in the GDL. Table 4.2 lists the properties for the GDL samples used in this study, from both the manufacturers' reported values and own measured values.

The data in Table 4.2 show that GDL thickness ranges between 110-420 μm with a large variation in the area weight. The real density measured by the pycnometer appears to be within a narrow gap of 1.8-2.15 $\text{g}\cdot\text{cm}^{-3}$ which falls within the region between the density of carbon fibres of 1.8-2.1 $\text{g}\cdot\text{cm}^{-3}$ and PTFE of 2.04-2.17 $\text{g}\cdot\text{cm}^{-3}$ [177]. However, a large variation in the bulk density can be observed which is influenced by the porosity and the density of the fibres/MPL within the GDL; the measured bulk density values of the GDLs are close to the values reported by the manufacturers, and the small deviation can be due to the heterogeneous structure of the GDLs.

Table 4.2: GDL ex-situ properties

Material	Manufacturer materials' properties			Measured properties											
	Thickn ess (μm)	Area weight (g/m^2)	Bulk density (g/cm^3)	Real density (g/cm^3)	Bulk density (g/cm^3)	Surface roughness (μm)		Porosity %	Tortuosity	Mean pore diameter (nm)	Permeability (m^2)	Water contact angle (θ)	Contact resistance ($\text{m}\Omega \text{ cm}^2$)		<i>In-plane</i> resistivity (Ωm)
						Sa	Sq						mercury	Contact angle	
1071HCB	356	123	0.35	1.816± 0.002	0.39	-	-	64.90	1.95	3401.2	2.36E-11	67.96 ± 3.69	52.66	30.87	1.28E-04
P50	170	50	0.32	2.083 ±0.004	0.36	14.7± 0.8	19.83± 0.52	48.66	3.01	993.4	9.21E-12	111.29 ± 7.4	2.13	1.56	2.70E-03
P50T	180	62	0.34	2.151 ±0.004	0.37	15.7± 0.6	19.44± 0.33	44.94	2.55	1528.4	1.41E-11	113.58 ± 0.47	2.60	1.85	2.28E-03
GDS1120	210	79	0.40	2.125± 0.005	0.46	20.0 ± 3.0	24.74± 3.91	44.76	3.24	859.1	4.73E-12	116.09 ± 16.78	-	-	2.62E-03
P75	230	75	0.33	2.083± 0.005	0.35	14.2 ± 0.9	20.04± 1.65	62.39	2.43	2074.7	1.11E-11	107.48 ± 7.48	2.40	1.73	4.27E-03
P75T	255	88	0.33	2.087± 0.003	0.36	14.0 ± 1.0	17.94± 2.27	59.91	2.23	1227.2	1.31E-11	112.57 ± 3.08	2.82	1.99	2.40E-03
GDS2120	260	101	0.40	2.131 ±0.005	0.40	17.0 ± 2.0	23.26± 4.73	60.18	2.62	2998.0	6.06E-12	112.33 ± 1.50	-	-	2.78E-03

	Thickn ess (μm)	Area weight (g/m^2)	Bulk density (g/cm^3)	Real density (g/cm^3)	Bulk density (g/cm^3)	Surface roughness (μm)		Porosity %	Tortuosity	Mean pore diameter (nm)	Permeability (m^2)	Water contact angle (θ)	Contact resistance ($\text{m}\Omega \text{ cm}^2$)		In-plane resistivity ($\Omega \text{ m}$)
TGP-H-030	110	-	0.40	2.071 ± 0.001	0.37	14.0 \pm 1.0	18.18 \pm 0.85	64.58	2.50	2625.1	1.07E-11	132.80 \pm 4.05	2.74	1.99	9.90E-05
TGP-H-060	190	-	0.44	2.002 ± 0.003	0.43	14.1 \pm 0.2	19.16 \pm 0.60	63.06	2.76	2631.1	6.15E-12	128.72 \pm 9.10	3.27	2.40	9.50E-05
TGP-H-090	280	-	0.44	2.019 ± 0.003	0.49	13.0 \pm 0.5	17.89 \pm 0.42	67.16	2.55	3324.0	4.53E-12	138.43 \pm 7.63	3.64	2.77	7.28E-05
TGP-H-120	370	-	0.45	1.985 ± 0.004	0.49	12.2 \pm 0.5	17.31 \pm 0.83	61.77	2.51	1717.8	3.90E-12	120.04 \pm 1.03	4.60	3.23	4.44E-05
C2	250	130	-	1.882 ± 0.002	0.57	14.6 \pm 0.4	19.58 \pm 0.85	49.16	4.51	658.0	9.12E-13	120.80 \pm 3.83			1.45E-04
C4	250	130	-	1.900 ± 0.002	0.49	14.0 \pm 1.0	18.94 \pm 0.60	60.96	4.26	157.6	1.04E-12	117.00 \pm 3.48	3.00	2.23	1.70E-04
I2 C6	250	135	-	1.867 ± 0.002	0.54	9.5 \pm 0.4	12.72 \pm 0.42	46.24	5.02	1148.1	8.57E-13	124.33 \pm 4.29			9.00E-05
I2 C8	230	135	-	1.934 ± 0.002	0.62	8.44 \pm 0.65	11.34 \pm 0.83	46.98	4.91	682.3	6.25E-13	60.73 \pm 6.47	3.37	2.47	1.89E-04
LT 1200 N	185	75	0.41	2.053 ± 0.004	0.39	17.73 \pm 1.94	22.02 \pm 0.79	64.94	2.74	768.5	6.45E-12	90.19 \pm 6.46	-	-	2.93E-04
LT 1200 W	275	200	0.73	1.906 ± 0.002	0.50	-	-	31.83	2.74	1054.7	4.98E-12	96.02 \pm 0.45	-	-	-

	Thickn ess (μm)	Area weight (g/m^2)	Bulk density (g/cm^3)	Real density (g/cm^3)	Bulk density (g/cm^3)	Surface roughness (μm)		Porosity %	Tortuosity	Mean pore diameter (nm)	Permeability (m^2)	Water contact angle (θ)	Contact resistance ($\text{m}\Omega \text{ cm}^2$)		In-plane resistivity ($\Omega \text{ m}$)
GDL 10 BC	420	135	-	1.945 \pm 0.008	0.36	23.70 \pm 1.98	31.29 \pm 2.67	34.64	2.95	2919.1	8.04E-12	122.29 \pm 3.76	-	-	1.18E-04
GDL 24 BA	190	54	-	2.14 \pm 0.01	0.28	13.38 \pm 0.93	17.43 \pm 1.57	73.86	1.40	2207.7	3.67E-11	97.70 \pm 3.74	2.69	1.76	1.94E-03
GDL 24 BC	235	100	-	2.010 \pm 0.003	0.44	13.32 \pm 0.04	18.29 \pm 0.77	40.03	3.00	2450.0	5.09E-12	104.36 \pm 4.11	-	-	2.51E-03
GDL 25 BA	190	40	-	1.941 \pm 0.002	0.21	22.37 \pm 4.27	31.11 \pm 2.80	66.23	1.45	1705.4	4.54E-11		2.52	1.85	4.78E-03
GDL 25 BC	235	86	-	2.009 \pm 0.007	0.34	23.10 \pm 3.91	32.05 \pm 3.00	36.46	2.92	842.1	5.64E-12	112.43 \pm 11.54	-	-	-
GDL 34 BC	315	140	-	1.987 \pm 0.001	0.41	23.86 \pm 0.91	30.77 \pm 0.24	47.48	2.47	2197.3	8.97E-12	125.98 \pm 6.68	-	-	2.22E-03
GDL 34 DC	-	-	-	1.978 \pm 0.004	0.48	24.50 \pm 1.98	31.44 \pm 2.75	40.82	2.62	1592.5	6.91E-12	133.86 \pm 2.22	-	-	2.51E-03
GDL 35 BA	300	54	-	2.022 \pm 0.009	0.19	31.90 \pm 2.65	43.23 \pm 2.76	70.52	1.33	2469.1	5.31E-11	122.74 \pm 7.66	2.55	1.85	5.51E-03
GDL 35 BC	325	110	-	1.980 \pm 0.007	0.31	35.65 \pm 1.93	46.52 \pm 4.64	52.62	1.94	1466.9	1.72E-11	118.20 \pm 10.98	-	-	3.67E-03

	Thickn ess (μm)	Area weight (g/m^2)	Bulk density (g/cm^3)	Real density (g/cm^3)	Bulk density (g/cm^3)	Surface roughness (μm)	Porosity %	Tortuosity	Mean pore diameter (nm)	Permeability (m^2)	Water contact angle (θ)	Contact resistance ($\text{m}\Omega \text{cm}^2$)	In-plane resistivity (Ωm)		
TCC-2660	260	80	0.31	1.793 ± 0.003	0.34	-	-	66.85	1.83	2290.8	2.96E-11	125.83 \pm 2.65	2.01	1.41	3.54E-04
TCC-3250	320	100	0.31	1.803 ± 0.002	0.36	-	-	71.01	2.32	16307.6	1.74E-11	79.13 \pm 6.72	2.38	1.67	7.68E-05

4.2.2 FIBRE STRUCTURE, SURFACE MORPHOLOGY AND ROUGHNESS

The SEM images of the surface and edge view of woven and non-woven GDLs are shown in Figure 4.1. Woven GDL constitutes the carbon cloth group, and the non-woven GDL makes the carbon paper group. The non-woven group can be divided into two types according to the structural configuration of the fibres in the GDL, namely, (i) straight and (ii) felt/‘spaghetti’ fibres.

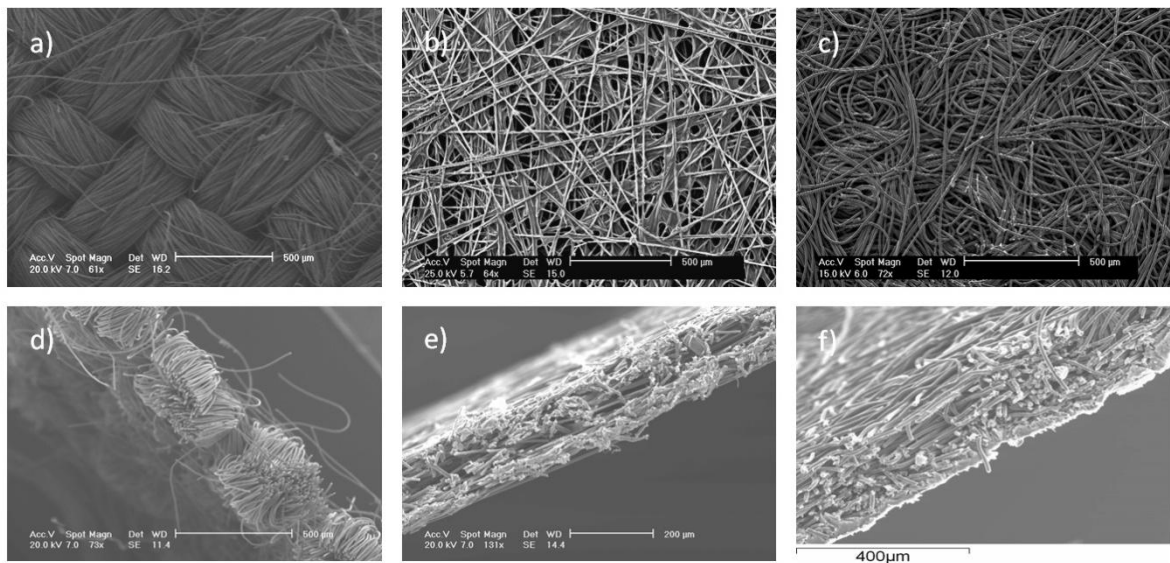


Figure 4.1: SEM images of GDL fibres configuration; surface and edge views of a) & d) Woven fibres in carbon cloth –Ballard 1071HCB, b) and e) straight stretched fibres in carbon paper – Toray H-060, c)& f) Felt fibres in carbon paper- Freudenberg C2.

A small number of commercial woven cloth GDLs are available due to the relatively high cost of manufacturing compared to the non-woven paper GDLs. The main difference noticed from the SEM images in the woven cloth types is in the diameter of the fibres and the weave width as shown in Table 4.3. The SEM image for LT1200W in Figure 4.2(c) also shows the PTFE loading (white PTFE net on the surface) on the

cloth. Here, the woven structure gives the GDLs high mechanical flexibility and compressibility.

Table 4.3: Woven GDLs weave and fibres properties

	Weave width (μm)	Fibre diameter (μm)
1071HCB	350- 500	8-9
TCC2260	200-250	8-9
TCC3250	250-375	11-12
LT 1200W	450-500	8-11

In the straight fibre structure, the fibres create a multi-layered web of interlinked fibres forming the carbon paper. This can be observed in Figure 4.3 that shows the separation of these layers after testing the GDL under compression. Some differences can be seen in the SEM images of this type (Figure 4.4). Graphitised resin and binders can be noticed in some samples (Figure 4.4 (c,d,e,f)); for example, the carbon/PTFE binding agglomerates around the fibres, linking them together and decreasing the pore diameter. SEM images for the Toray papers show clear graphitised wetted fibres (Figure 4.4 (b)). Also, from the SEM images it appears that the fibre structure density differs greatly from one GDL to another. This type of GDL is usually mechanically rigid and brittle and can easily break if bent.

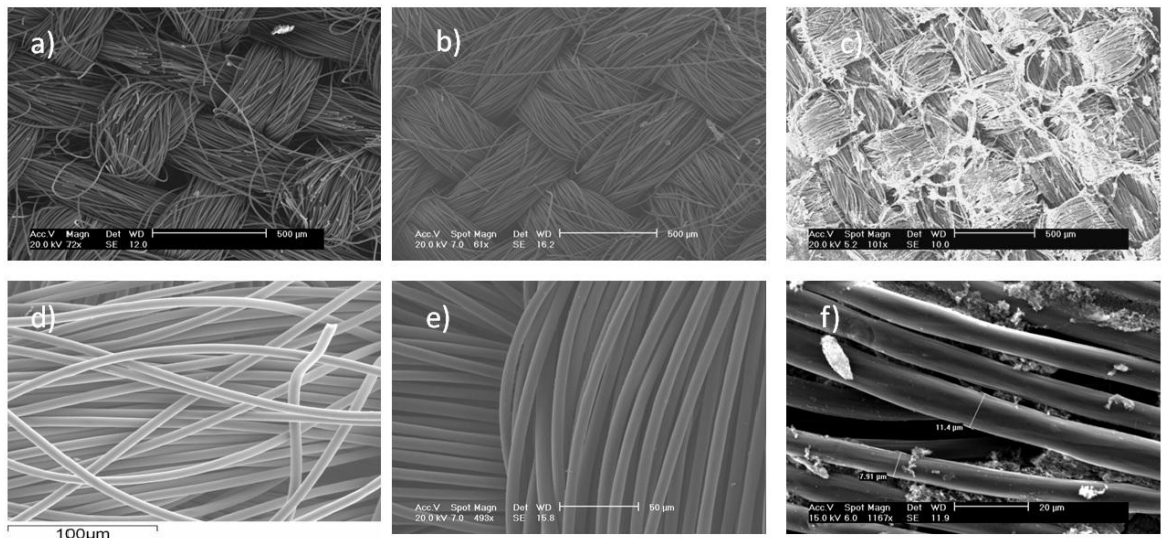


Figure 4.2: SEM images of several types of woven carbon cloth sample; surface views of: a) Tenax b) Ballard 1071HCB, and c) ETEK 1200W and closer views of d) Tenax, e) Ballard 1071HCB, and f) ETEK 1200W

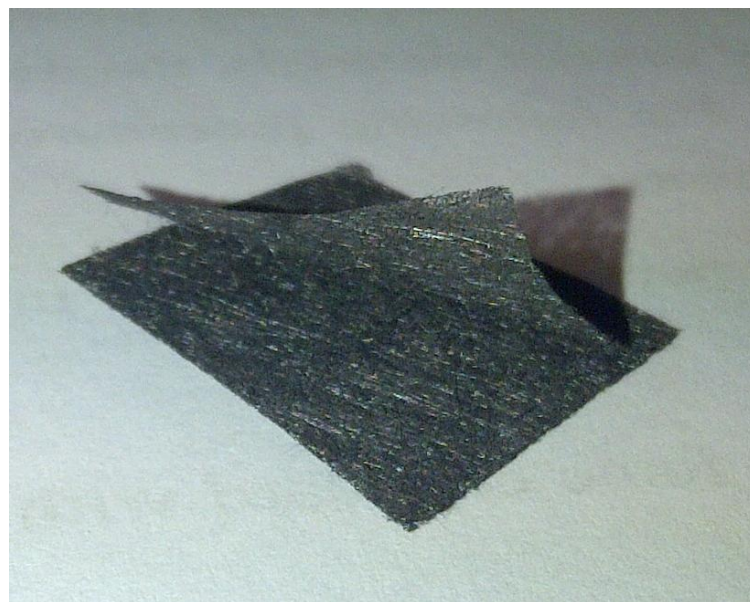


Figure 4.3: Straight fibres GDL's layer separation after compression

Felt fibre structures are clearly observed for all Freudenberg and some SGL GDL samples (Figure 4.5). This structure is often described as a three dimensional (3-D) fibre configuration. This type of structure gives the GDL a higher mechanical

flexibility and a higher compressibility compared to other carbon paper GDLs. It is interesting to note that, as with straight fibre carbon papers, binders can be observed in the SGL 10BC GDL, but not in all Freudenberg GDLs. Furthermore, it can be noticed that the fibre density for Freudenberg GDLs is significantly higher.

The SEM images of the different types of GDLs show a difference not only in the structure, but also a difference in the properties of the fibres used within it. The length and diameter of the fibres are two properties that potentially have an important effect on the behaviour of the GDL structure. Further experimental and theoretical work is required to study the effect of these properties on the GDL.

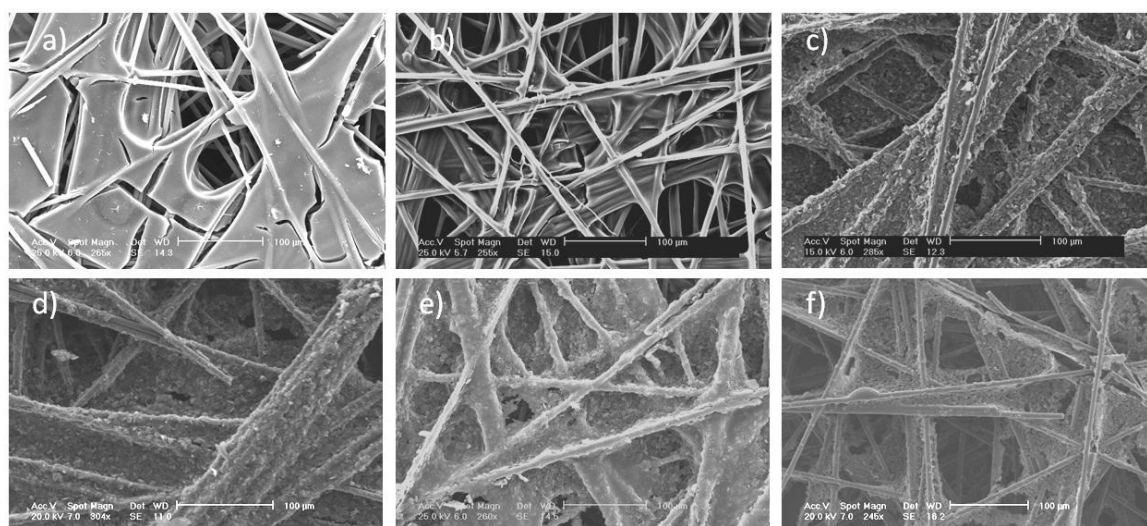


Figure 4.4: SEM images of various types of straight fibres carbon paper samples: a) Toray H-060, b) ETEK 1200N, c) Ballard P75, d) Ballard P75T, e) AvCard 1120, f) Sigracet 25BA

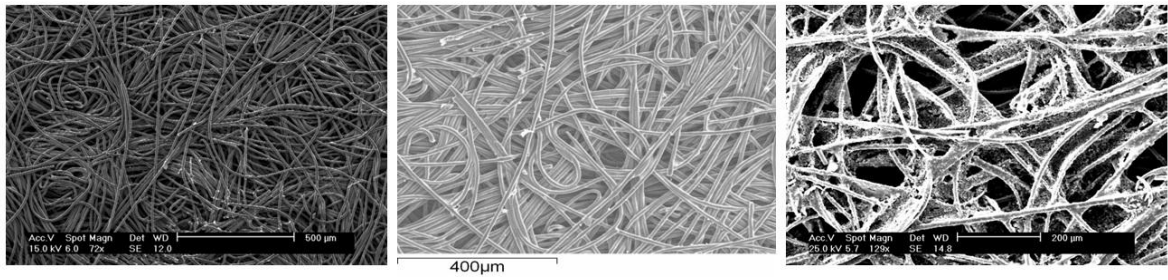


Figure 4.5: A series of SEM images of felt/spaghetti fibres carbon paper samples of: a) Freudenberg C2, b) Freudenberg C6 and c) SGL 10BC

The roughness of the carbon paper substrate surfaces was measured using an interferometer. The mean value of height (S_a) and root mean square of height (S_q) on the surface are listed in Table 4.3. The values of S_q range between 10-45 μm indicating high roughnesses facing the BPP material in the PEM fuel cell (Figure 4.6). Avasarala *et al.* observed a significant effect of the surface roughness of composite BPP on the interfacial contact resistance with the GDL [178]. This can be related to the GDLs roughness as well as to that of the BPP; however, to the author's knowledge, this relationship has not been explored in the literature yet. Figure 4.6 shows a variation in the substrate roughness for the different GDL materials. The results show no change in roughness with teflonation (P50T and P75T compared to P50 and P75) or MPL application (P50T, P75T and SGL XXBA compared to GDS1120, GDS2120 and SGL XXBC respectively). Some types of GDLs are coated on one side with an MPL and the SEM images in Figure 4.7 show the scale of features observed in various types of GDL. The GDS 2120 image shows a very rough surface and coarse pore sizes compared to other types, while the *E-TEK* media exhibit a very smooth and fine pore sizes. It can also be seen that the MPL surfaces have a sporadic distribution of pore sizes.

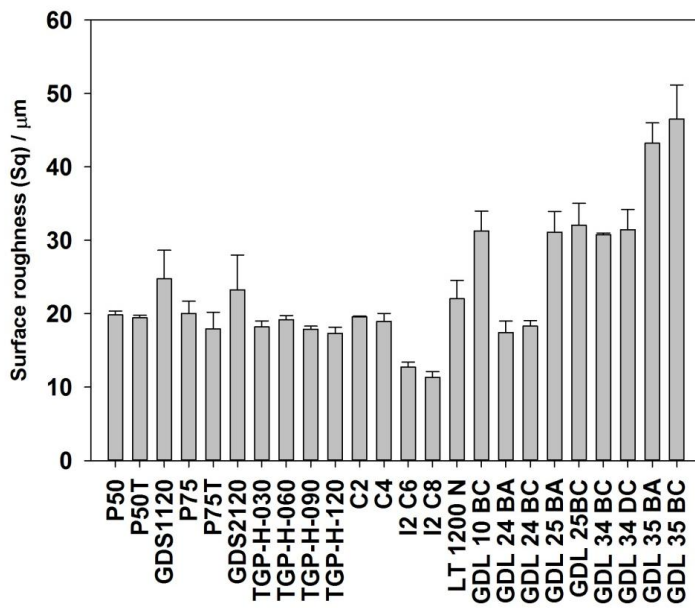


Figure 4.6: Surface roughness for carbon paper GDL substrates

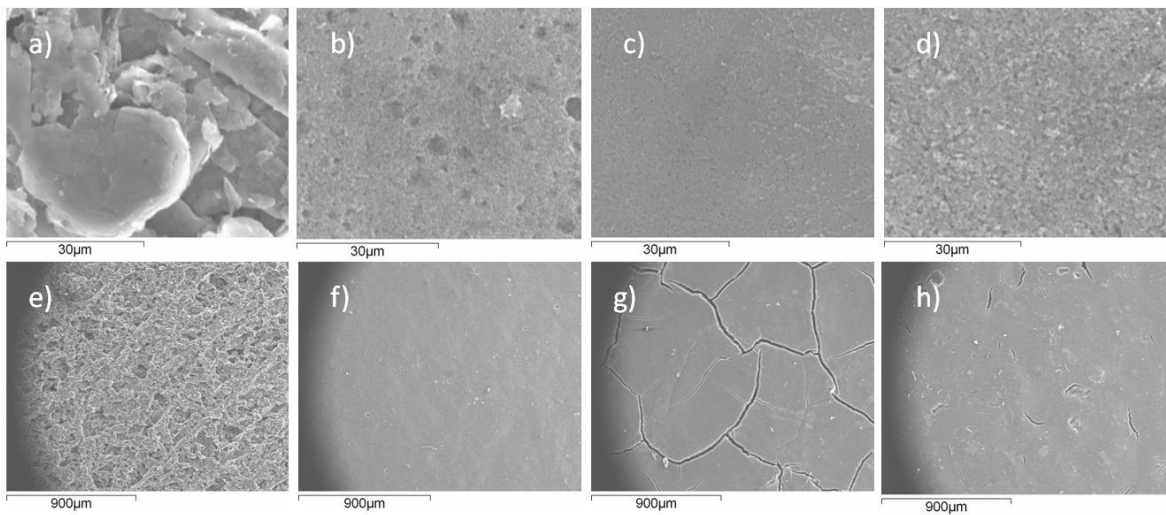


Figure 4.7: MPLs on various commercial GDLs: a & e) GDS2120, b & f) Freudenberg C2, c & g) LT1200W and d & h) SGL 24BC

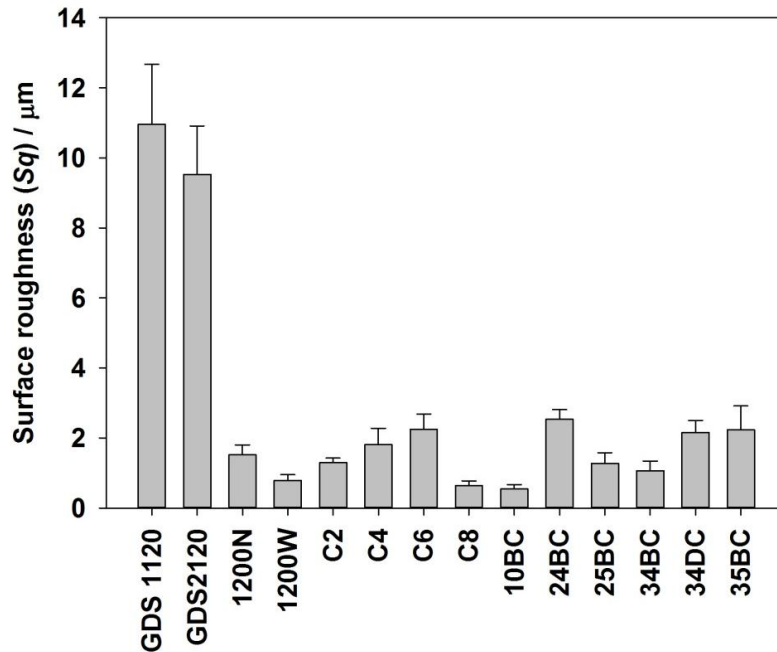


Figure 4.8: Surface roughness for MPLs

The roughness of the surfaces of the MPLs were also measured using an interferometer and the values are shown in Table 4.4. The roughness values of the MPL in GDS1120 and GDS 2120 were found to be 8-10 times higher than the average MPL roughness in other GDL samples (Figure 4.8). Cracks are observed on the MPL surfaces and even larger cracks are obtained on woven GDL containing MPL following the pattern of the weaves (Figure 4.7 (g)). This observation may be due to the rough structure of the woven structure and the GDL bending caused by its high flexibility. The relatively smooth surface of the MPL (in comparison to the substrate roughness) confirms that an MPL creates a smoother surface for GDE fabrication and in turn reduces the cell resistance.

Table 4.4: MPL properties

	Roughness (μm)		Water contact angle (θ)
	Sa	Sq	
GDS1120	8.79 \pm 1.46	10.96 \pm 1.72	122.05 \pm 5.06
GDS2120	7.91 \pm 0.57	9.53 \pm 0.75	104.17 \pm 8.10
Freudenberg C2	1.02 \pm 0.12	1.29 \pm 0.14	120.35 \pm 16.19
Freudenberg C4	1.41 \pm 0.33	1.81 \pm 0.47	121.54 \pm 4.27
Freudenberg C6	1.66 \pm 0.21	2.25 \pm 0.43	83.80 \pm 5.26
Freudenberg C8	0.49 \pm 0.12	0.64 \pm 0.13	131.9 \pm 12.84
LT 1200N	1.18 \pm 0.22	1.51 \pm 0.29	111.73 \pm 18.14
LT 1200W	0.55 \pm 0.13	0.78 \pm 0.17	129.07 \pm 13.76
SGL 10BC	0.41 \pm 0.09	0.54 \pm 0.12	121.16 \pm 5.06
SGL 24BC	1.77 \pm 0.12	2.53 \pm 0.28	94.05 \pm 3.06
SGL 25BC	0.81 \pm 0.15	1.27 \pm 0.31	-
SGL 34BC	0.82 \pm 0.22	1.06 \pm 0.28	89.07 \pm 5.21
SGL 34DC	1.54 \pm 0.23	2.15 \pm 0.34	93.01 \pm 7.00
SGL 35BC	1.48 \pm 0.41	2.23 \pm 0.68	99 \pm 3.39

4.2.3 POROSITY, TORTUOSITY AND PORE SIZE DISTRIBUTION

Porosity, tortuosity and pore size distribution are important factors in determining gas and water transport through/in the GDL. The effective diffusion coefficient (D_{eff}) can be calculated using the measured values, which is an important parameter of the GDL properties. Furthermore, the distribution and variation in pore sizes shown by

the pore size distribution are important for their effect on the capillary pressure driving the water out of the cell [179].

Figure 4.9 and Figure 4.10 show the wide variation in commercial GDL porosity and tortuosity values. Porosity, tortuosity and average pore diameter values are listed in Table 4.2. The table clearly shows that porosity and tortuosity are affected by the presence of PTFE and MPL. Generally speaking, PTFE loading decreases the porosity and tortuosity. The decrease in porosity is mainly due to the blockage and narrowing of the pores and the decrease in tortuosity might be due to the blockage of closed and longer pores leaving shorter open pores for permeability. Adding an MPL introduces an extra layer with lower porosity and smaller pores resulting in a decrease in the overall porosity and an increase in tortuosity.

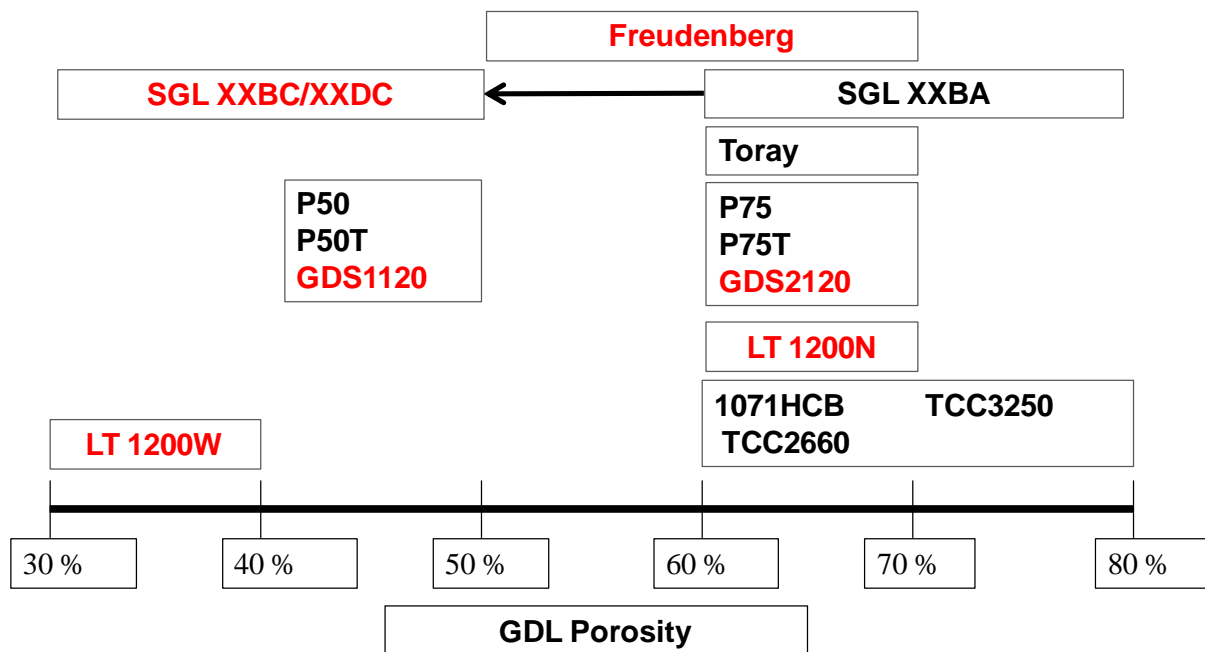


Figure 4.9: Porosity of commercial GDLs (red font indicates GDLs with an MPL).

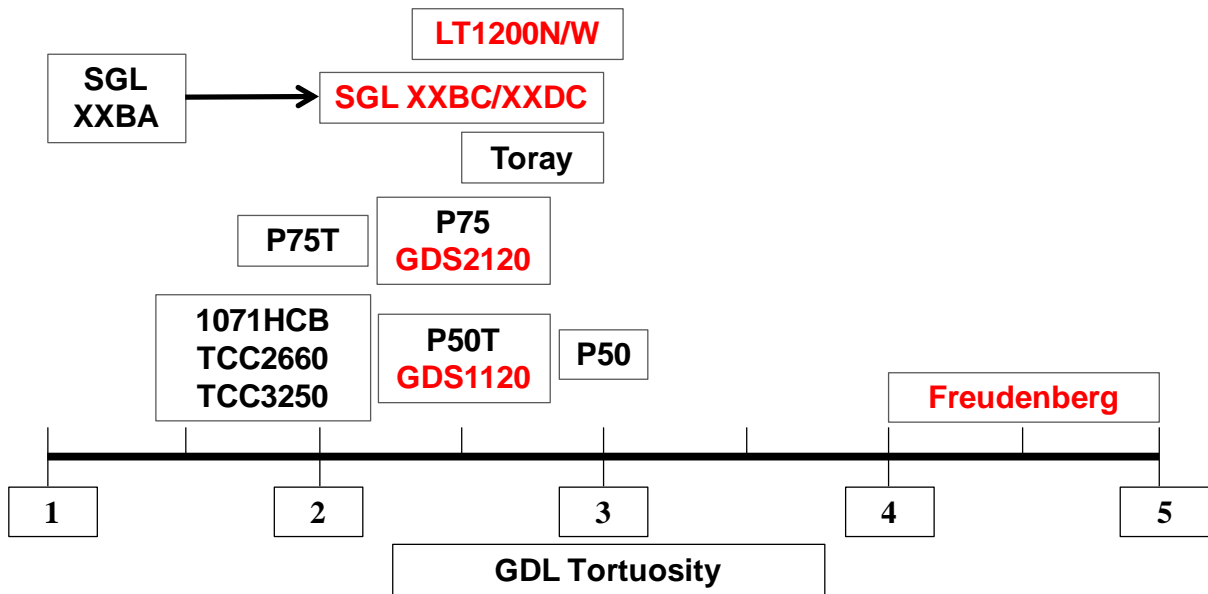


Figure 4.10: Tortuosity of commercial GDLs (red font indicates GDLs with an MPL).

Pore size distribution measurement is commonly determined by the coverage of the volume of mercury intrusion over the range of pore diameters in the GDL material. Table 4.2 also shows that the average pore diameter decreases with increasing thickness (see the values for Toray GDLs); however, the bulk porosity seems to be unaffected (Figure 4.9). The pore size distribution curve for the Toray samples show larger pores in TGP H-030 and TGP H-060 with lower volume intrusion for the latter one. TGP H-090 and TGP H-120 samples show a shift to smaller pore diameters. This observation of high volume intrusion and pore size in TGP H-030 is interesting and could be due to the very small thickness of the GDL (Figure 4.11). Here, the porosity values for the Toray samples are in very good agreement with those obtained by Fishman *et al* [61].

However, applying an MPL on the substrate changes the pore distribution as shown in Figure 4.12. The figure shows that the curve peak shifts to lower pore size values with less volume intrusion causing a significant decrease in the bulk porosity (Table

4.2). Figure 4.13 shows the gradual change in the pore size distribution for the substrate when loaded with PTFE and an MPL. A significant decrease in the intrusion volume can be observed when the GDL is loaded with PTFE; this is also manifested in the decrease in the bulk porosity. However, when the MPL is applied, the GDL maintains constant bulk porosity. P50, P50T and GDS1120 also exhibit a similar behaviour. This finding is very interesting and could be due to the structure of the MPL as shown in Figure 4.8(e) and the surface roughness of the MPL in these GDLs (Table 4.4). Furthermore, it was found that a decrease in the pore diameters was observed with increasing PTFE loading from 5% to 20% (Figure 4.14) with subsequent decrease in porosity values.

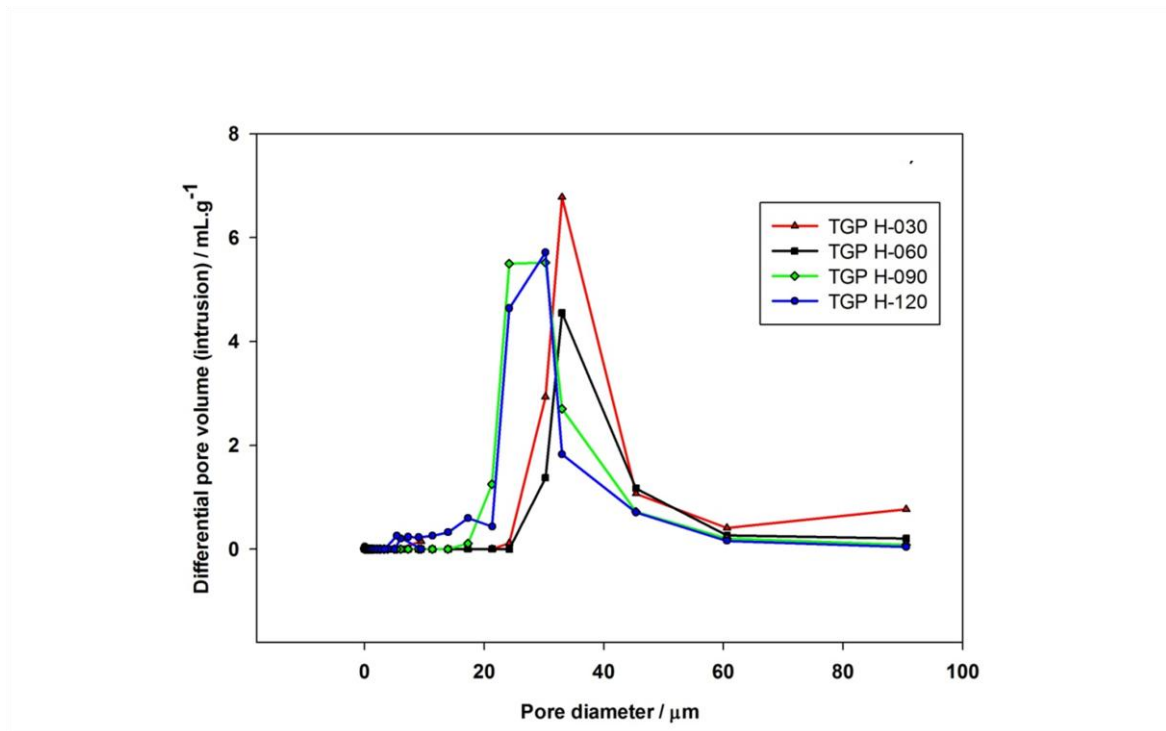


Figure 4.11: Pore size distribution change with GDL thickness in Toray samples – full pore size distribution

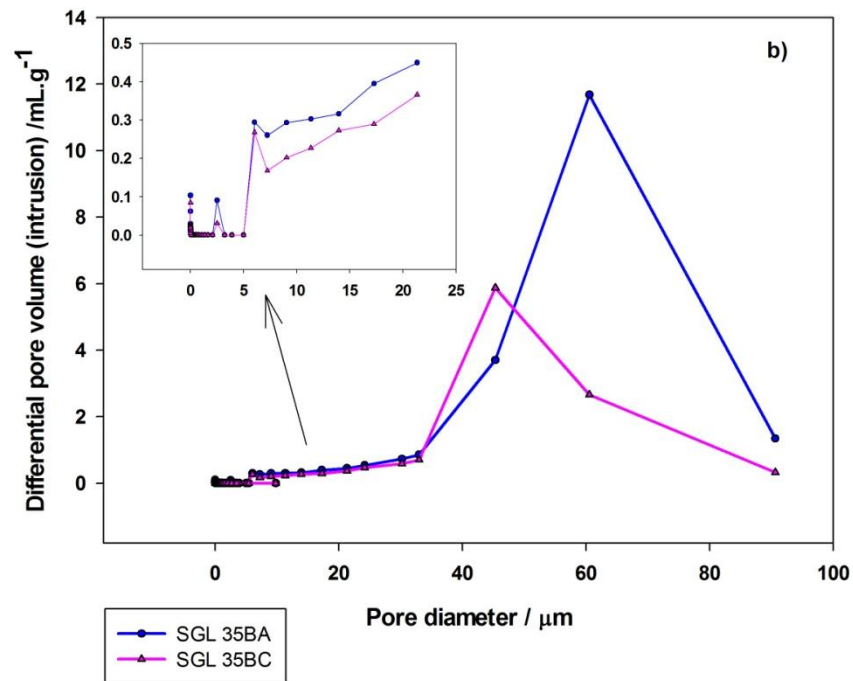
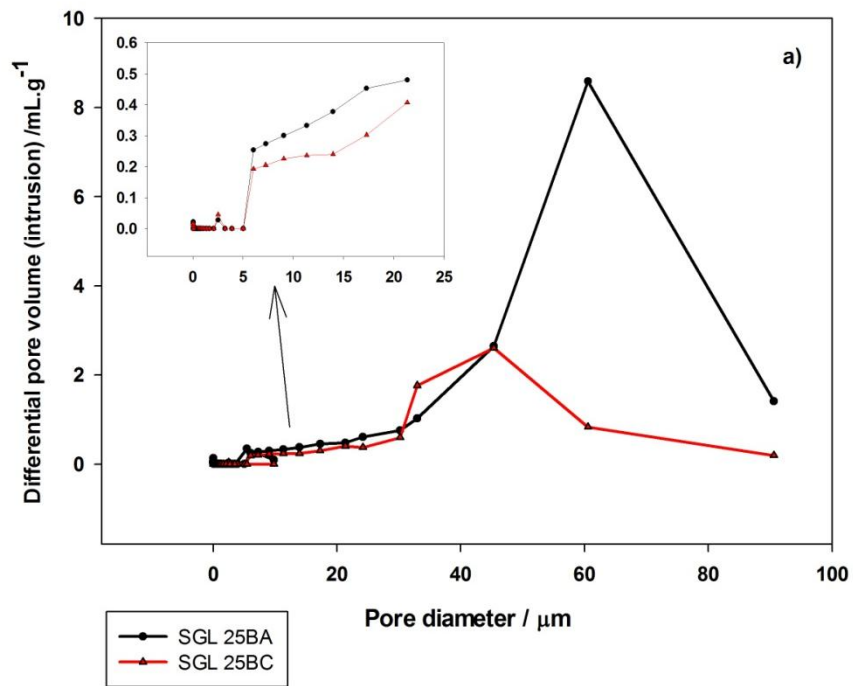


Figure 4.12: Pore size distribution change when adding a MPL for samples a) SGL 25BA (without MPL) and SGL 25BC (with MPL) and b) SGL 35 BA (without MPL) and SGL 35BC (with MPL).

Woven carbon cloths pore size distribution curves show a different trend to that of the GDL papers (Figure 4.15). Volume intrusion can be observed on a wide base of pore diameters that extends to high pore sizes. The results show that the three woven GDLs with no MPL have the same bulk porosity. However, in the case of the presence of an MPL in LT1200W, the curve follows the same trend but with lower intrusion volume. Furthermore, an additional sharp high peak at low pore diameter is observed which is not present in the case of carbon papers. The volume intrusion peak at low pore diameter presents the pores in the MPL of the GDL. Again, the bulk porosity of this GDL is significantly lower than the other woven types.

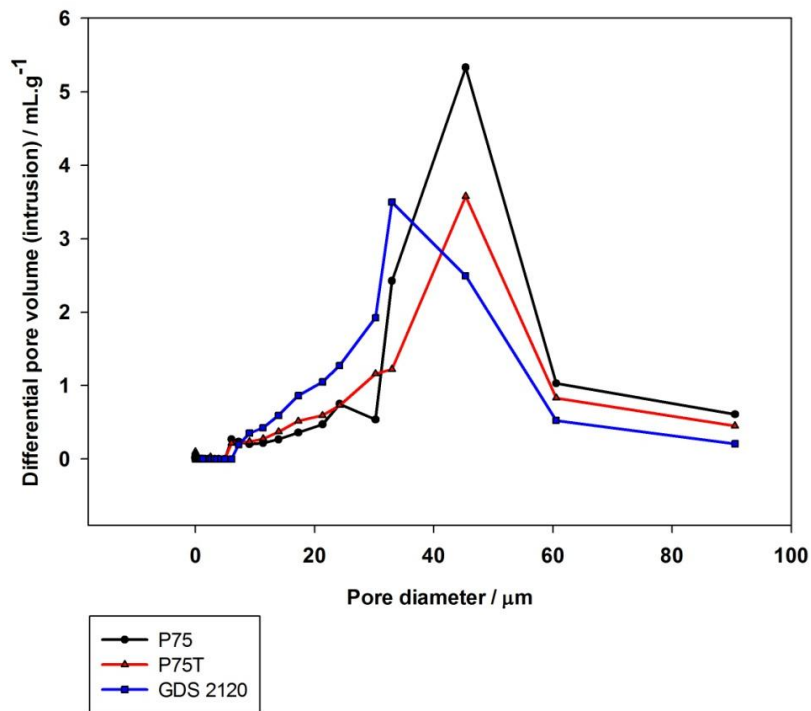


Figure 4.13: Pore size distribution gradual change with PTFE loading in the absence and presence of MPL; P75 (Unteflonated substrate), P75T (Teflonated substrate), GDS2120 (Teflonated substrate with an MPL)

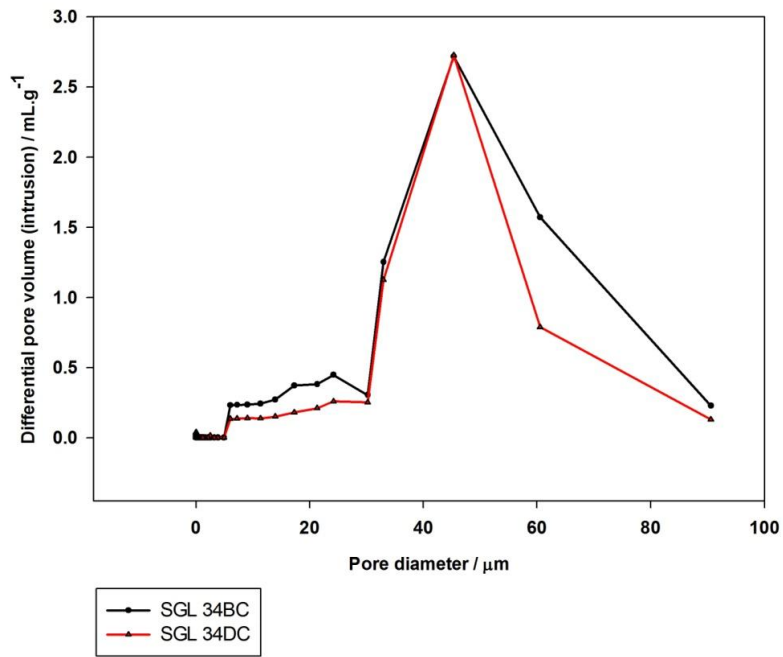


Figure 4.14: GDL pore size distribution change with PTFE loading increase; 34BC with 5 wt% PTFE loading, and 34DC with 20 wt% PTFE loading.

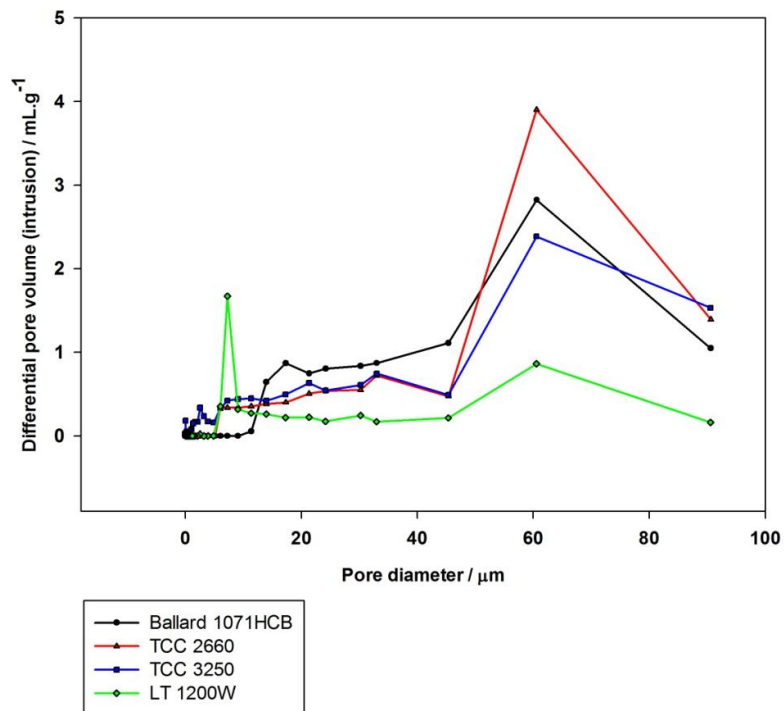


Figure 4.15: Pore size distribution for commercial woven GDL.

4.2.4 PERMEABILITY

In this study, GDL permeability was measured using the mercury intrusion method. Therefore, the values reported here correspond to both *through-plane* and *in-plane* permeability of the GDL. This method is limited to calculating the absolute permeability with the assumption of uniform cylindrical connected pores. The GDL permeability varies in the *through-plane* and *in-plane* directions; therefore, the values reported in this work are used as indicative values for qualitative comparison.

These values show that the presence of MPL, the fibre density, thickness and PTFE loading, affect the permeability of the GDL as shown in Fig. 4.16. The addition of the MPL results in a decrease in the permeability of the GDL. Furthermore, it can be observed that the Freudenberg samples have low permeability compared to all other GDL samples due to the high fibre density in the GDL structure. It is interesting to note that (i) the permeability of the P50 and P75 increase with PTFE loading in P50T and P75T, which may be due to the decrease in tortuosity, and (ii) Toray papers permeability decrease with increasing thickness. Unexpectedly, woven GDLs show relatively lower permeability compared to some paper type GDLs.

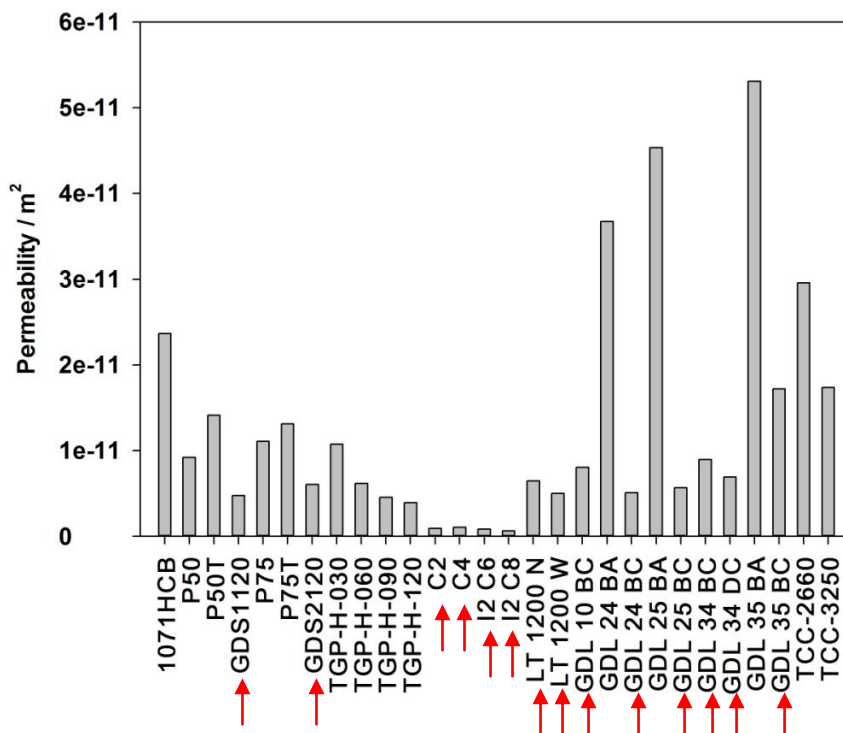


Figure 4.16: GDL permeability as measured using mercury porosimeter. The arrows mark GDLs with an MPL.

4.2.5 SURFACE WATER CONTACT ANGLE (HYDROPHOBICITY)

The hydrophobicity or hydrophilicity of a substrate is a material and surface structure related property; the two parameters describe the strength or weakness of the bonds created between the substrate and the water molecules in contact. They determine the behaviour of water within the GDL and the ease of its transport through it.

Hence, the GDL has an important role in water management and liquid water removal from the MEA. Contact angle measurement is a powerful diagnostic for understanding the interaction of GDL material with water.

In the experiments, both hydrophobic (water contact angle > 90°) and hydrophilic (water contact angle < 90°) GDL surfaces were observed (Figure 4.17), with a

majority of them being hydrophobic. For most commercial GDLs, the MPL shows higher water angle (more hydrophobic) than that of the substrate. However, an interesting feature for the Sigracet GDLs is that the MPL has a lower water contact angle (less hydrophobic) than the substrate itself (Fig. 4.17).

It is important to note that the surface water contact angle depends upon both the hydrophobicity of the material and the roughness of the surface. Therefore, the increase in hydrophobicity on the substrate side could be due to its high roughness. The values of water contact angle for both the substrates and the MPLs are listed in Tables 4.2 and 4.4 respectively. The values reported here are within the value range reported for the various samples in the literature [111,115]. This method of measuring the hydrophobic/ hydrophilic property of the GDL has its limitation because of the effect of the structure on the values obtained. Other methods, such as GDL water adsorption and fibres contact angle, need to be explored to study the hydrophobicity of the fibres and pores.

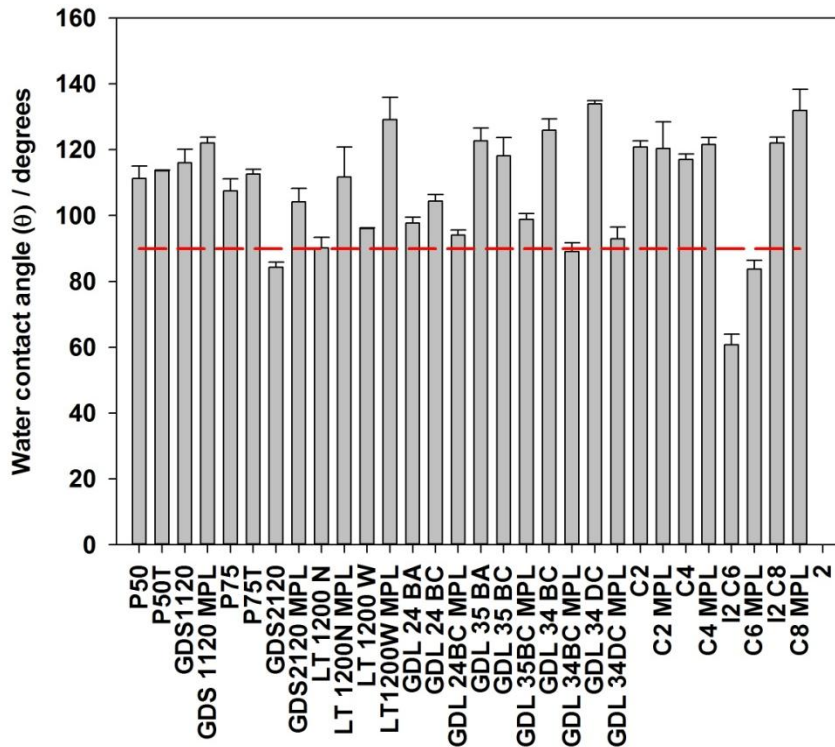


Figure 4.17: Water contact angle for commercial GDLs and their MPLs.

4.2.6 ELECTRICAL CONDUCTIVITY AND CONTACT RESISTANCE

The contact resistance between the GDL and the BPP varies with; (i) the flow field plate material, (ii) the GDL material, (iii) the flow field design (ratio of land to channels) and (iv) the clamping pressure. The change in resistance with clamping pressure is shown in Figure 4.18. The figure shows samples of straight fibre and felt fibre papers and woven fibre cloths. It is important to mention that compression has a partially irreversible effect on the GDL due to deformation. This can be seen when measuring the contact resistance of samples at the pre-conditioning stage. The contact resistance decreases with each compression until it reaches stabilisation, usually after 3 to 5 compression cycles [25].

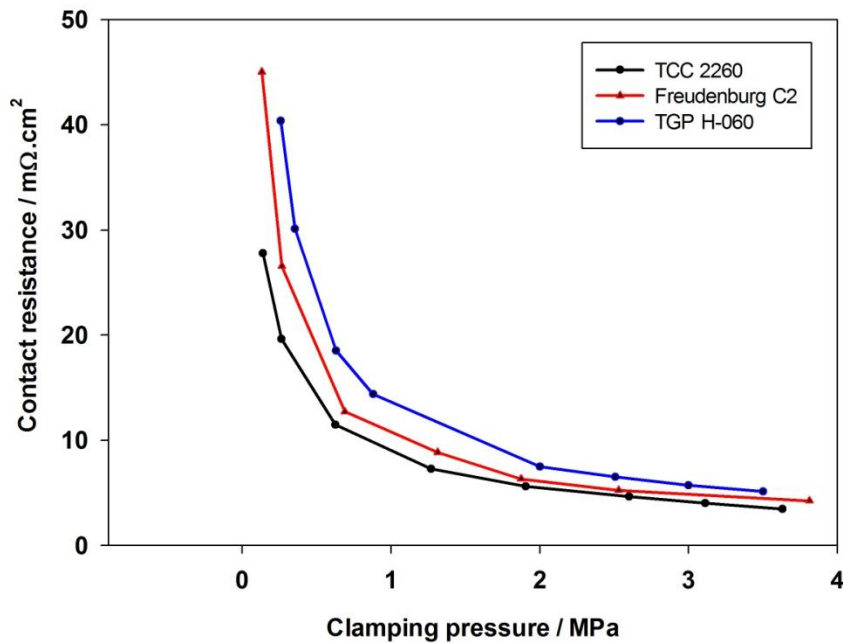


Figure 4.18: Contact resistance change with clamping pressure

Figure 4.19 shows the GDL contact resistance at 1.5 and 2.5 MPa (clamping pressures reported in the literature) [81]. The figure shows that the contact resistances of P50/P75 and P50T/P75T increase when the samples contain PTFE in the substrate. Furthermore, the Toray GDLs show a small increase in contact resistance with the increase in thickness, agreeing with the increase noticed between P50 and P50T in comparison with P75 and P75T. Toray H-030, however, shows a high value for its contact resistance despite the very low thickness of the GDL. This can be explained by the possible contact between the graphite plates in the test through the very thin porous structure of the GDL. The increase in resistance with thickness increase may be due to the increase in the *through-plane* resistance of the GDL with thickness. The woven cloth 1071HCB has significantly high contact resistance (see Table 4.2) compared to all other GDL samples; however, it exhibits a

fairly low *in-plane* resistance. Tenax woven samples have shown comparable values to those obtained for paper GDLs. The values obtained fall within the range reported by Mishra *et al.* [125] and Zhang *et al.*[180].

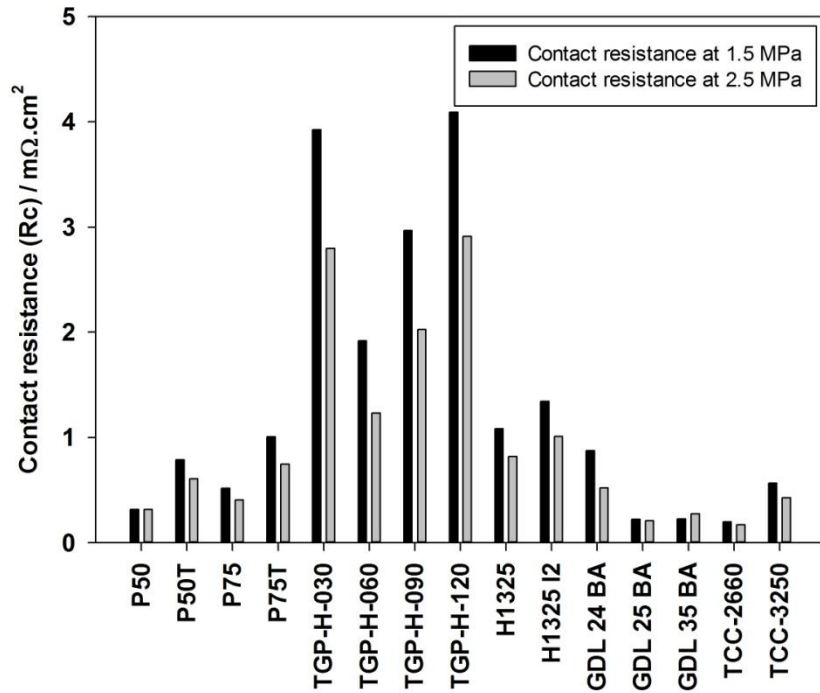


Figure 4.19: Commercial GDL contact resistance with POCO graphite plate at 1.5MPa and 2.5MPa

For the *in-plane* resistance measurements, the resistance (R) was measured at various locations along the GDL strip samples yielding a straight line (Figure 4.20), the slope of which represents the resistance *per unit* distance. The resistivity (in $\Omega.m$) of the GDL was then calculated using Ohm's Law as shown in Equation 3.1. Here, it can be noticed that the plot does not go through the origin (0,0); this is due to the contact resistance between the GDL surface and micro-ohmmeter measurement rods.

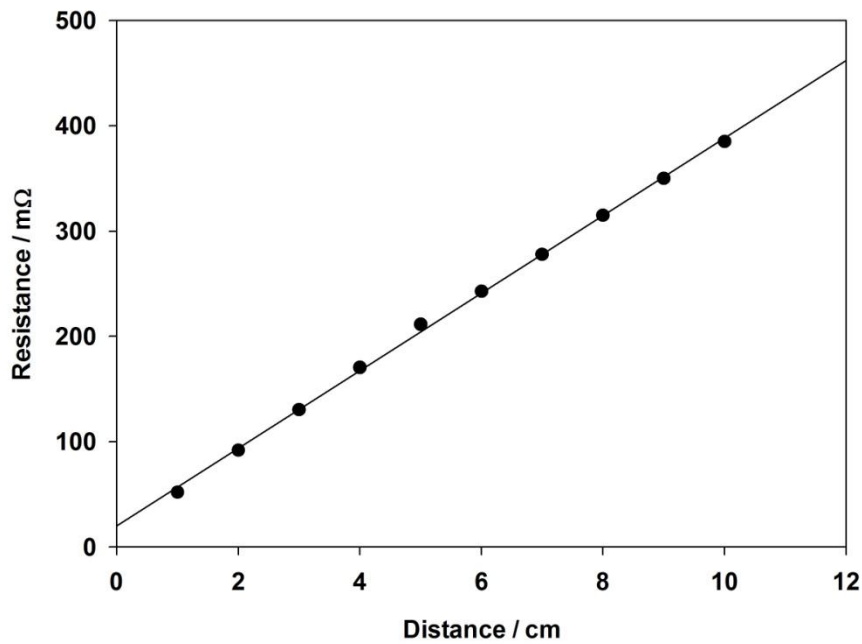


Figure 4.20: Toray H-030 strip resistance change with distance

The results of the *in-plane* resistivity experiments (Figure 4.21) show low values for the woven GDLs, which can be explained by the uniform interconnection between the fibres allowing electrons to flow through the GDL 'easily'. In the same manner, felt fibre GDL papers exhibit lower *in-plane* resistivity values due to electrical connections created by the three dimensional structure across the GDL thickness, rather than the layered webs that are interconnected on contact points at each layer.

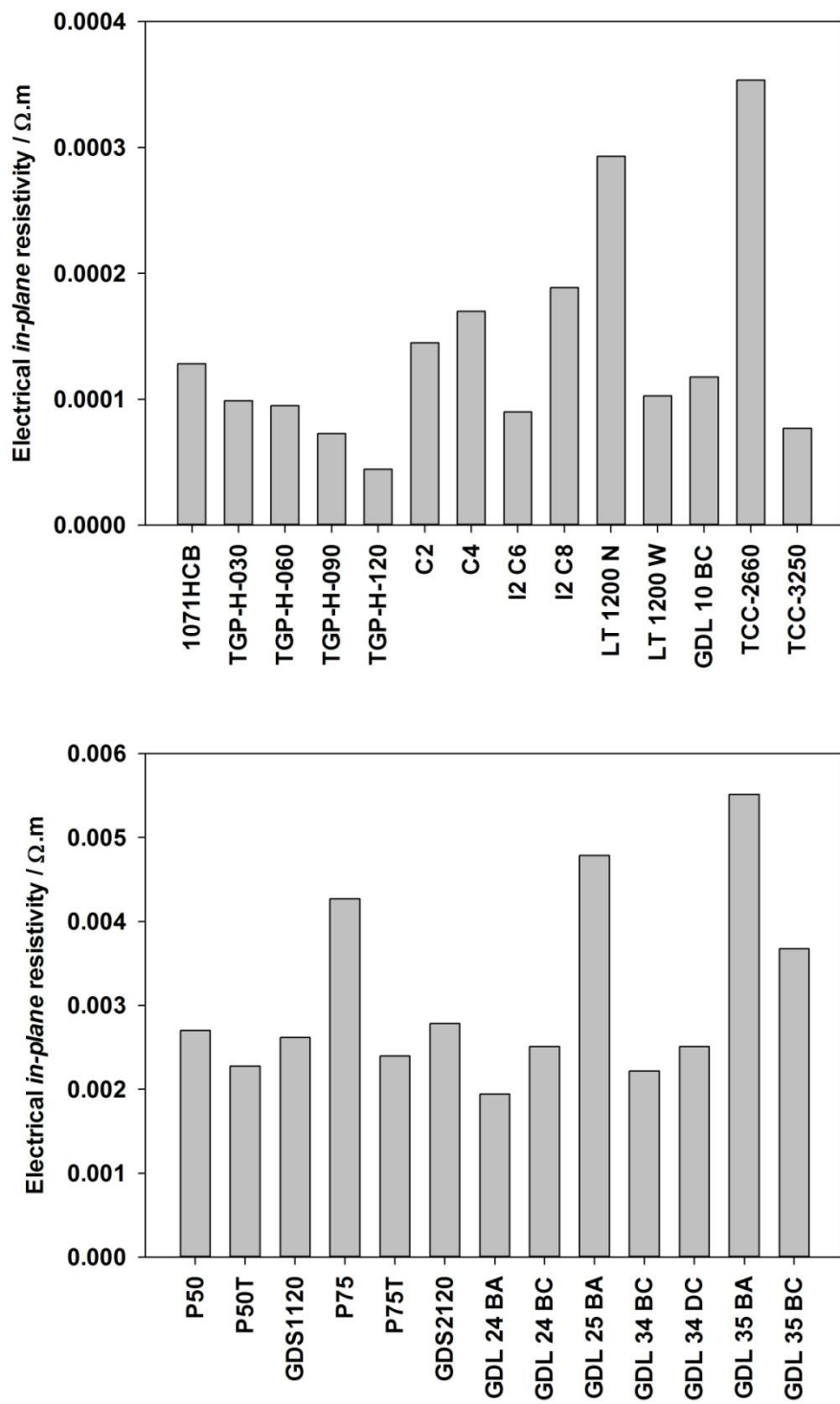


Figure 4.21: In-plane resistivity of various GDL materials

A trend in the *in-plane* resistance can be observed (Figure 4.21) for the Ballard P50 and P70 substrates group. For example, the resistance decreases with PTFE loading but also increases in the presence of an MPL. This interesting finding suggests that possibly some of the MPL penetrates through the substrate, in turn covering some fibres and hence insulating them due to the presence of PTFE and therefore increasing the resistivity. The reason for the decrease in resistivity with PTFE loading is not clear. It can be suggested that the PTFE works as a binder when applied and enhances the contact between the fibres in the GDL. A similar observation was made by Ismail *et al* [181] when increasing PTFE loading in the MPL. Several suggestions were made by the authors to explain this observation; however, the suggestions were not backed up with clear experimental results. Therefore, it is felt that more experimental research is required to explore the reason for this.

In-plane resistivity values for Toray shows the lowest resistivity for GDL papers. This could be due to a high graphitisation level of the GDL fibres which enhances the electrical conductance of the substrate. It is also shown that the GDL resistivity decreases with GDL thickness which can be explained by the increase of the bulk density of the GDL. This observation suggests that higher fibre density provides a larger bulk for electron transfer. On the other hand, the *in-plane* resistivity values of C4 and C8 are higher than those of C2 and C6. Knowing the fact that C2 and C4 are based on the same substrate and similarly for C6 and C8, this finding suggests that the increase in resistivity is directly related to the MPL properties. The resistivity values are in agreement with the values reported by Williams *et al* [9].

4.3 CONCLUSIONS

In this chapter, the data of important *ex-situ* parameters of commercial GDLs used in PEFC are reported. The results indicate that there is a relationship between the GDL properties, substrate structure, PTFE and MPL loading. It was found that PTFE loading in the GDL decreases porosity and resistivity; however, it increases tortuosity, permeability and hydrophobicity. Adding an MPL to the GDL substrate results in a further decrease in porosity and permeability and increase in tortuosity and resistivity. Furthermore, different MPL structures were observed and the variations on their effect on the surface roughness and hydrophobicity were investigated. It was also shown that the contact resistance between the GDL and the POCO flow field plate increases with thickness and PTFE loading. The study shows the need for more research to be done to explore the effect of PTFE on the GDL to assist in explaining the changes in its other properties. Moreover, new methods for measuring GDL characteristics are needed to eliminate errors due to the assumptions made in the design of testing setups.

This chapter offers values and parameters for a wide range of GDL properties that are required for PEFC designers and modellers. A complete study of *ex-situ* characterisation of GDLs coupled with GDL modelling and *in-situ* testing will assist GDL manufacturers in developing GDLs with higher performance for the various fuel cell applications, and will lead to the development of GDL selection criteria for PEFC applications.

CHAPTER FIVE

THE EFFECT OF CLAMPING PRESSURE ON GAS DIFFUSION LAYER PERFORMANCE IN POLYMER ELECTROLYTE FUEL CELLS

CHAPTER 5: THE EFFECT OF CLAMPING PRESSURE ON GAS DIFFUSION LAYER PERFORMANCE IN POLYMER ELECTROLYTE FUEL CELLS

Clamping pressure applied in Polymer Electrolyte Fuel Cell (PEFC) assembly is known to have a significant effect on performance. Compression applied on the Membrane Electrode Assembly (MEA) deforms the Gas Diffusion Layer (GDL) and causes a decrease in the GDL thickness, porosity and electrical resistance. These changes in the GDL properties have a significant influence on the MEA performance. In this study, three sets of GDLs were tested *in-situ* under varying clamping pressure levels to demonstrate the difference in the GDL behaviour with compression, and to optimize the MEA clamping pressure.

The study focuses on the changes in the performance of MEAs with various types of GDLs, and uses the parameters reported in chapter 4 to interpret the behaviour of the MEA under compression. The method used in the study has been applied to the different types of GDLs reported in chapter 4. A selected range is reported here to focus the study on the behaviour change with the change in selected GDL properties.

5.1 SAMPLES AND EXPERIMENTS

A range of commercially available GDL materials were selected to study the effect of the GDL deformation with compression on the MEA performance. The samples are divided into 3 sets with the variation in thickness, density and fibres structure. Table 5.1 shows the three sets of GDLs and their properties. The properties of the GDLs are discussed in detail in chapter 4.

PTFE sheets were used as a gasket. Four different gasket thicknesses were used for the *in-situ* test; 100, 150, 200 and 250 μm . This is to control the level of GDL thickness deformation. The gasket thicknesses are referred to as G100, G150, G200 and G250 respectively.

5.1.1 EX-SITU TESTING

A compressibility test was conducted using a controlled compression device (Instron 5848 MicroTester). The test measures the change in the GDL and gasket thickness under pressure applied. The samples were cut into squares with 4 cm^2 area. Force was applied on the samples with an increment of 50 $\text{N}\cdot\text{min}^{-1}$, and then the axial deformation was measured. The samples were conditioned by cycling the applied force up to maximum pressure 3 times before conducting the test to reduce the effect of irreversible deformation as discussed in chapter 4. The average value of deformation for the 3 samples of each material is reported. The paper attached in Appendix A4 from collaborative work with University College London (UCL) complements the work reported in this chapter.

Table 5.1: GDL samples properties

Variable	GDL type	Fibre structure	Thickness (μm)	Density ($\text{g}\cdot\text{cm}^{-3}$)
Thickness	Toray H-060	Straight fibre paper	190	0.43
	Toray H-090	Straight fibre paper	280	0.49
	Toray H-120	Straight fibre paper	370	0.49
Density	SGL 24BC	Straight fibre paper	235	0.44
	SGL 25BC	Straight fibre paper	235	0.34
	SGL 34BC	Straight fibre paper	315	0.41
	SGL 35BC	Straight fibre paper	325	0.31
Structure	LT 1200W	Woven cloth	275	0.50
	LT 1200N	Straight fibre paper	185	0.39
	SGL 34BC	Straight fibre paper	315	0.41
	SGL 10BC	Felt paper	420	0.36

5.1.2 *IN-SITU* CHARACTERISATION

MEA fabrication

The GDL materials studied were used to fabricate the cathode electrodes. The catalyst ink was prepared using commercially available 45.6 wt % Pt/C powder (Tanaka Kikinzoku Kogyo), Nafion 10 wt% solution (Ionpower) and isopropanol (Sigma Aldrich) as a solvent [182]. The ink was hand painted on the GDL to produce a GDE. The fabricated Gas Diffusion Electrodes (GDEs) had an average Pt loading of $0.45 \pm 0.05 \text{ mg}\cdot\text{cm}^{-2}$. A Johnson Matthey (JM) commercial GDE (GDS 00165) was used for the anode electrode and Nafion N212 for the membrane. The prepared

anode and cathode GDEs were assembled with the membrane using hot pressing at 125°C for 2 minutes under 1800N load.

In-situ testing

The MEAs were assembled as single cells with single serpentine graphite flow field plates (FFPs). This is done using a Paxi-Tech single cell fixture with 8 bolts tightened at 5 N.m torque. The cell is then tested using a Bio-logic test station (FCT-50S) under the operating conditions listed in Table 5.2. All cells were conditioned at steady state at 0.6V at 70°C with 100% RH at both anode and cathode sides. Open Circuit Voltage (OCV) and polarisation (IV) curves for each cell were obtained.

Each MEA was tested under 4 levels of compression, using the four different gasket thicknesses, starting with the thickest gasket (250 µm) (lowest compression) down to the (100 µm) (maximum compression) to avoid any effect of irreversible deformation due to the high compression.

Table 5.2: Fuel cell test operating conditions

Parameter	Value
Temperature	70.0 ± 0.5 °C
Back pressure	2.0 ± 0.1Bar
Hydrogen flow rate	120 mL.min ⁻¹
Stoichiometry	1.4
Air flow rate	300 mL.min ⁻¹
Stoichiometry	2.5

5.2 RESULTS

5.2.1 EX-SITU TESTING: COMPRESSIBILITY MEASUREMENT

The samples were conditioned by force cycling to maximum pressure of 2.4 MPa. The results show a significant irreversible deformation in the GDL thickness in the first compression cycle. This irreversible deformation becomes negligible and the GDL thickness stabilizes after the 5th cycle. This is in agreement with the work done in collaboration with UCL university and jointly published in [90] (Appendix A5). The gasket material, however, shows a reversible behaviour with compression and maintains its original thickness after compression cycling. Moreover, the PTFE gasket material shows no irreversible change in its thickness and a very small deformation with compression. The incompressibility of the gasket material allows the use of the gasket to control the thickness deformation of the GDL when used in-situ in the MEA.

As shown in Figure 5.1, the samples' thickness decreases non-linearly with compression; the thickness drops sharply at first, then gradually the rate decreases as pressure builds up. The sharp drop in the GDL thickness in the first stage of increasing the pressure can be explained by its porous structure. Deformation of the GDL thickness initially can be achieved with low force, as the structure's resistance to deformation is low. As the GDL thickness decreases, its bulk density increases and porosity decreases, this results in an increase in the GDL resistance to deformation and therefore a faster increase in the pressure with lower displacement.

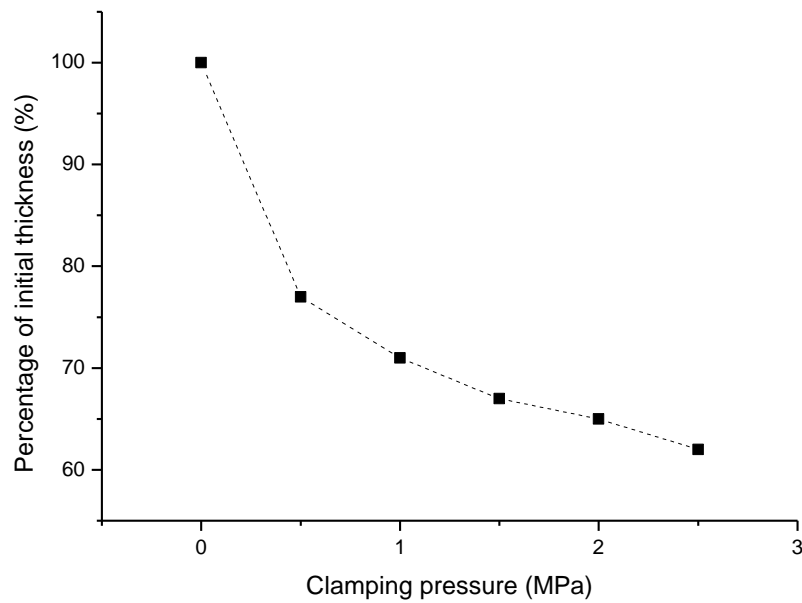


Figure 5.1: The change in GDL thickness with clamping pressure

Table 5.3 shows the irreversible change in the GDL thickness and the thickness of the GDLs at selected pressure values. The results show that the level of the irreversible deformation in the GDL thickness is dependent on the GDL density and structure, however, independent of the thickness.

When comparing the different GDL structures, it is noticed that the woven GDL does not show significant irreversible change in its thickness in comparison with the non-woven GDLs. The irreversible deformation of non-woven structures was measured to be up to 35% of the GDL thickness after conditioning. The felt GDL also shows a high irreversible deformation with compression. The highest irreversible deformation can be seen for SGL 35BC (32%) followed by SGL 10BC (26%), and the least for SGL 34BC (5%).

Table 5.3: GDL thickness change with compression

GDL type	Thickness at 0.0 MPa (μm)	Thickness after conditioning (deformation) at 0.0 MPa (μm)	Thickness at 0.5 MPa (μm)	Thickness at 1.5 MPa (μm)	Thickness at 2.5 MPa (μm)
Toray H-060	190	160	134	116	105
Toray H-090	280	250	226	209	198
Toray H-120	370	340	280	248	220
SGL 24BC	260	210	196	181	173
SGL 25BC	260	190	174	157	148
SGL 34BC	340	300	275	247	235
SGL 35BC	340	230	176	155	144
LT1200W	275	260	204	175	162
LT1200N	185	140	120	100	90
SGL 34BC	315	300	275	247	235
SGL 10BC	420	310	255	227	213

The GDL bulk density has the most significant effect on the GDL irreversible deformation with compression. This explains the very high irreversible deformation of SGL 35BC in comparison to all other GDLs due to its low bulk density.

Toray GDLs show constant deformation in the thickness regardless of the GDL original thickness. The different GDLs show parallel trend lines of decreasing thickness with compression with a deviation equal to the difference in the GDL thickness. The effect of the bulk density can be clearly seen when comparing the pairs of SGL24BC/ SGL25BC and SGL34BC/ SGL35BC (see Table 5.1). GDLs with

higher density show lower deformation level. This can be explained by the smaller pore volume available and stronger structural support of high bulk density GDLs which increases the GDL resistance to deformation.

5.2.2 *IN-SITU* TESTING

Three MEAs of each GDL type were fabricated and tested. The cells were tested under 4 compression levels using the different gasket thicknesses. A polarization curve and EIS curves were obtained for each test to study the effect of compression on the cells performance.

In general, the results show that with the increase of compression (the decrease of the gasket thickness), the performance of the cell shows an increase up to an optimum performance, this is followed by a decrease in the performance with the increase in compression. The polarization curves show a decrease in the ohmic losses (slope of the curve) due to the decrease in the electrical contact resistance and then an increase in mass transport losses with the increase in compression. EIS confirms the decrease in cell ohmic resistance (the curves intersect with the x-axis) with increasing compression until reaching a level when the value of cell resistance stabilizes and the change is negligible. The EIS curves also show the change in mass transport ability with increasing compression. After reaching the optimum level of compression, the mass transport losses increase with increasing compression, which is shown by the expansion of the second semicircle of the curve at high current density. Figures 5.2 and 5.3 show an example of the change of performance and EIS curves with compression for an MEA using SGL 25BC GDL at the cathode. The IV curves for all other MEAs discussed are listed in Appendix A4.

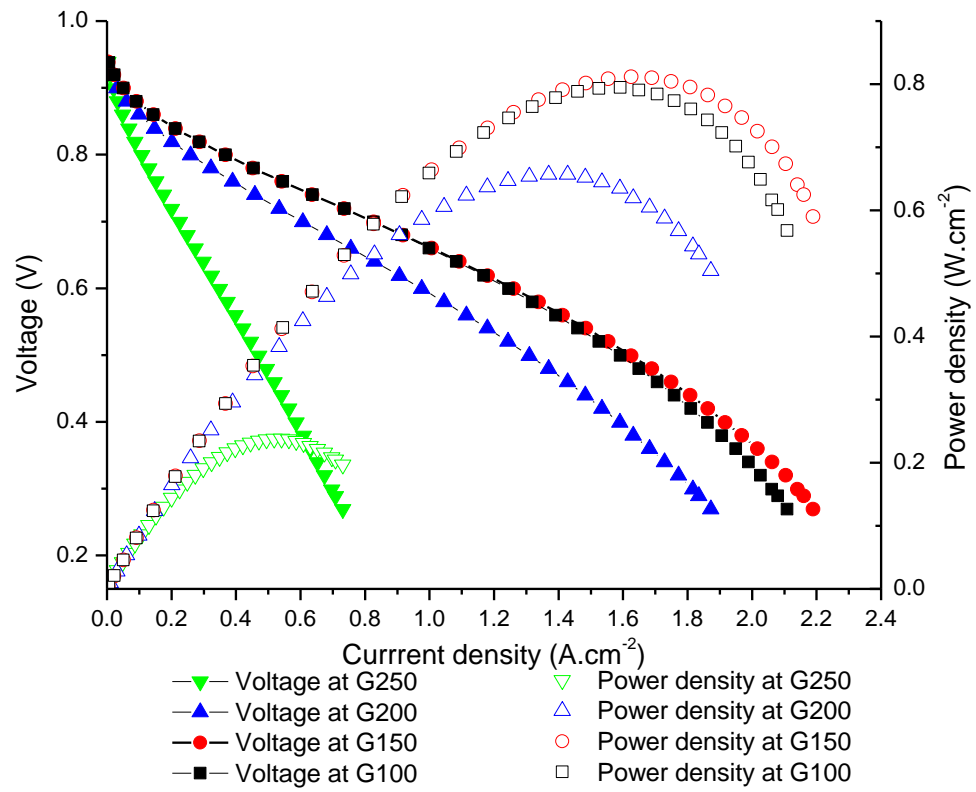


Figure 5.2: Change in GDL performance with compression for an MEA using SGL 25BC GDL; compression increases moving from G250 to G100.

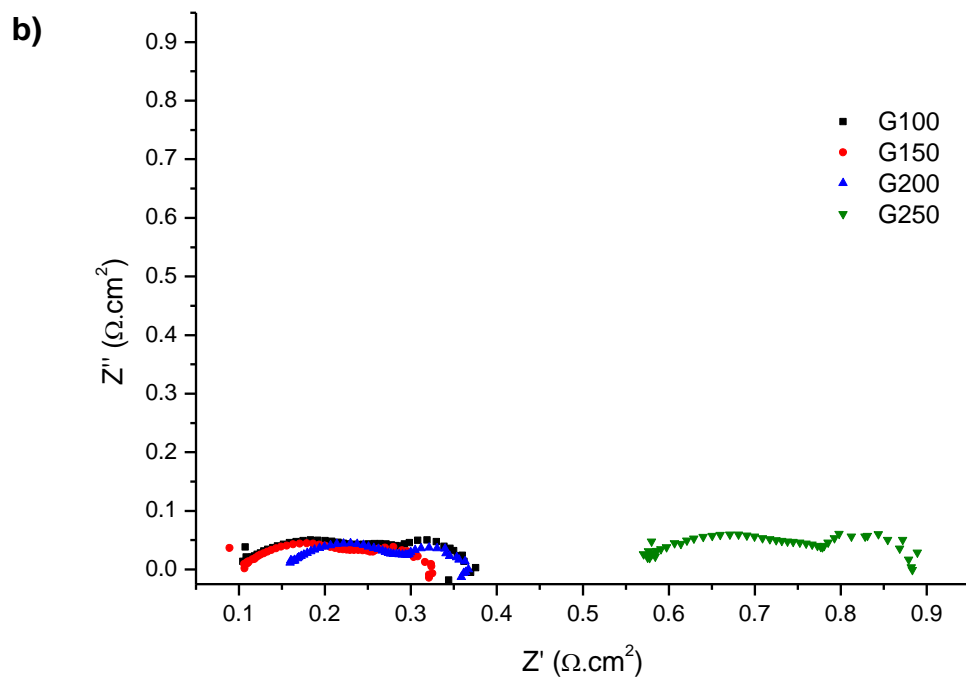
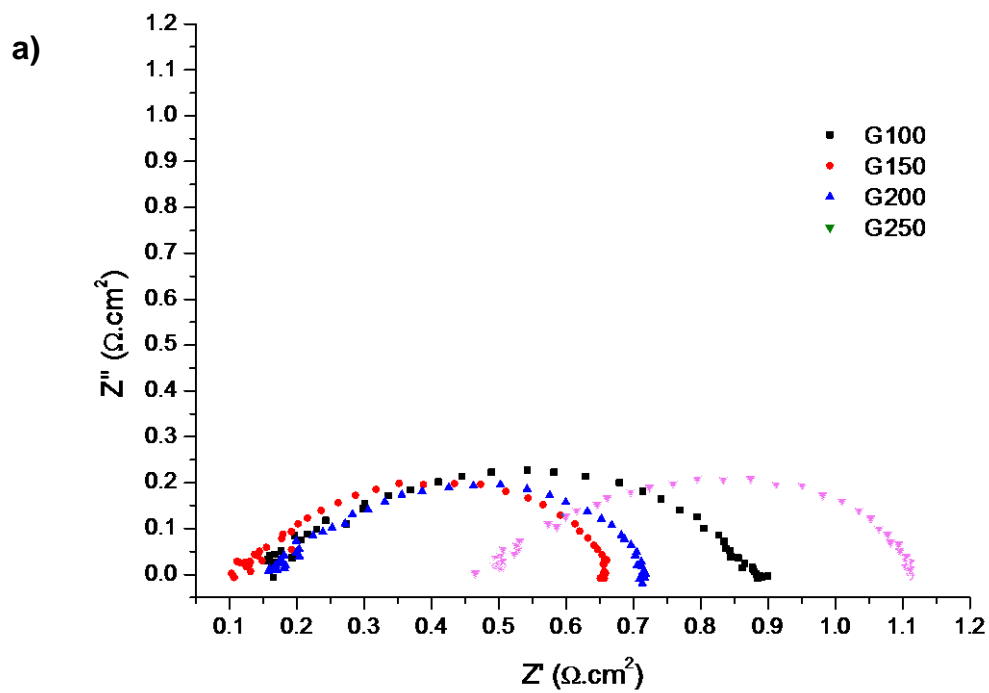
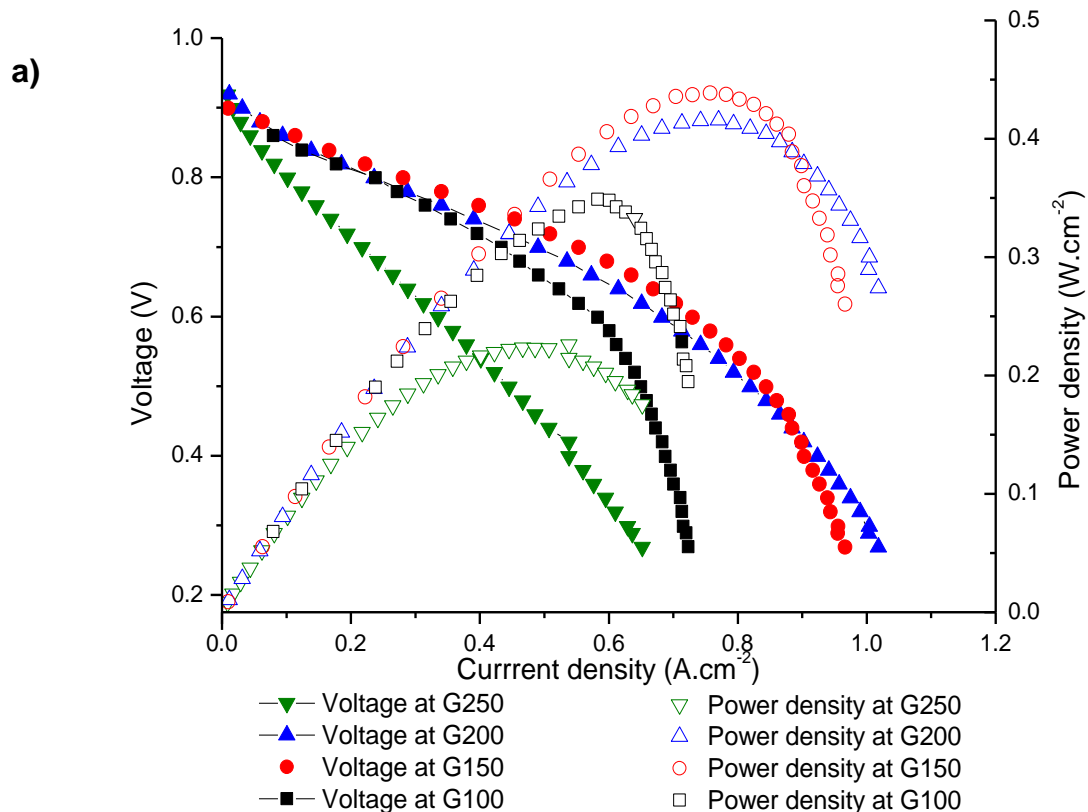


Figure 5.3: Change in EIS curve with compression for the MEA using SGL 25BC GDL at (a) low current density ($0.1 \text{ A} \cdot \text{cm}^{-2}$), and (b) high current density ($1.0 \text{ A} \cdot \text{cm}^{-2}$).

The results for the MEAs using the different Toray GDLs ((a) H-060, (b) H-090 and (c) H-120) (Figures 5.4 (a), 5.4 (b) and 5.4(c)) show an optimum performance at different gasket thickness. It can be noted that the mass transport losses region starts to appear at a certain compression level before which ohmic losses dominate the behaviour of the cell. The MEAs show an optimum performance for H-120, H-090 and H060 with G200, G150 and G150 respectively. The change in the performance with the gasket thickness appears to be relatively greater for H-060 than that for H-090 and H-120. This is due to the low thickness of H-060 which prevents proper contact between the GDL and the FFP at high gasket thickness (Figures 5.4 (a), 5.4 (b) and 5.4(c)).



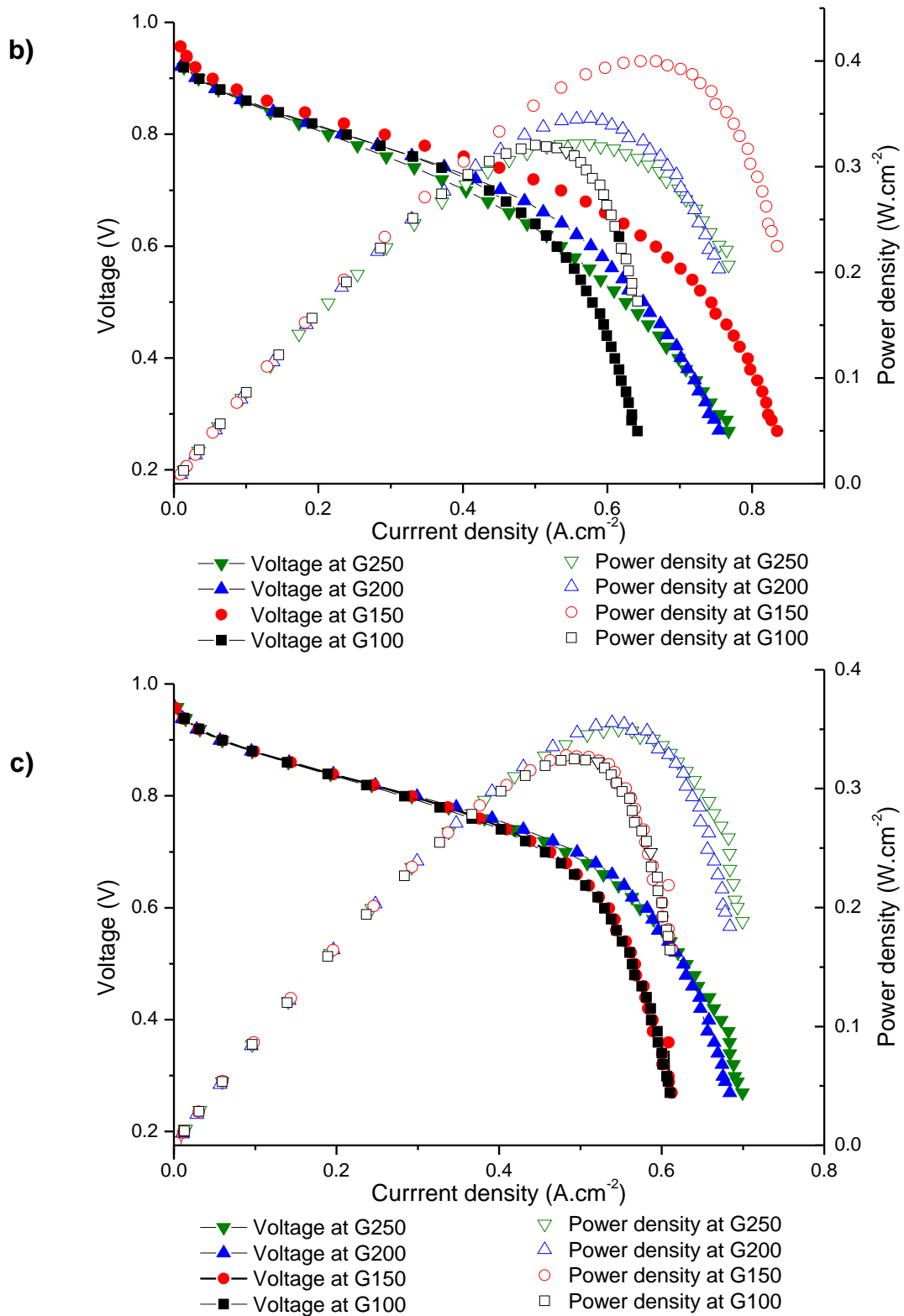


Figure 5.4: Change in the performance of (a) H-060, (b) H-090, and (c) H-120 as a cathode GDL with the change of gasket thickness.

The performance of LT1200W shows a decrease in the performance with the decrease of gasket thickness. The curves show that there is no significant change in the ohmic losses; however, a significant loss can be seen due to mass transport. The cell didn't seal with G100 due to the high thickness and bulk density of the woven GDL. In contrast, LT1200N shows approximately a 9-fold increase in the performance of the MEA when decreasing the thickness (Figure 5.5 (a)). The results show a decrease in cell resistance and the gradual appearance of the mass transport region. A crossing point at high current density is observed between curves for G100 and G150. This is due to the increase of mass transport losses with compression. It is interesting to note that G100 shows higher peak power than G150 but has lower maximum current (Figure 5.5 (a) and 5.5 (b)).

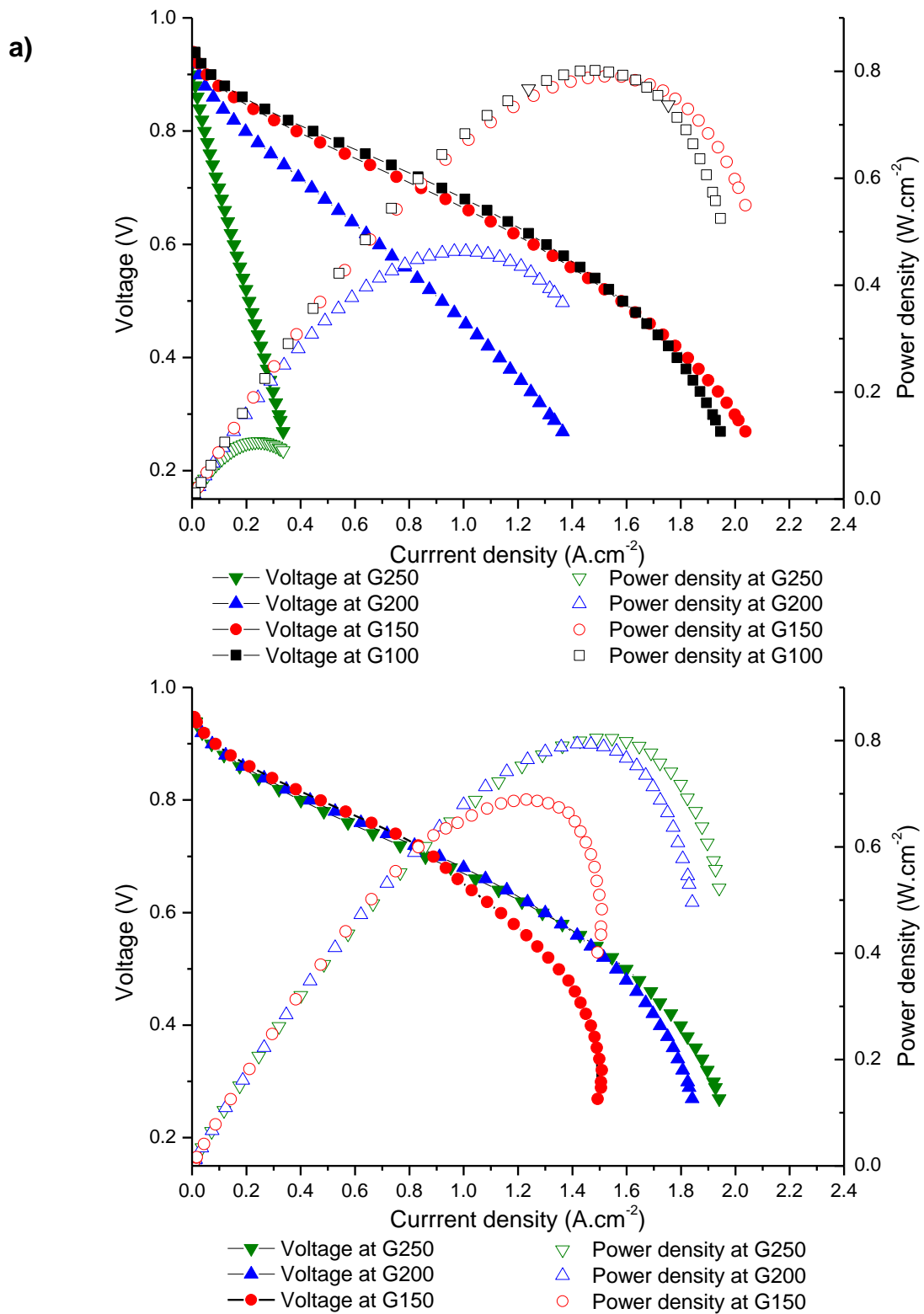
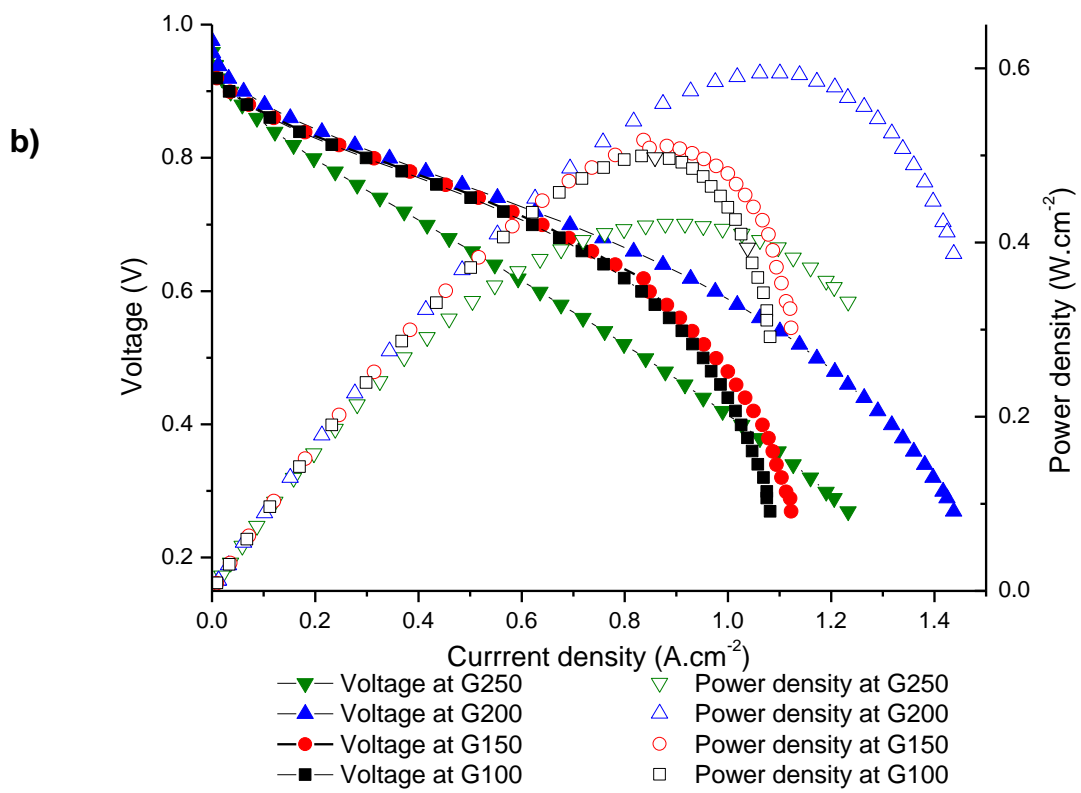
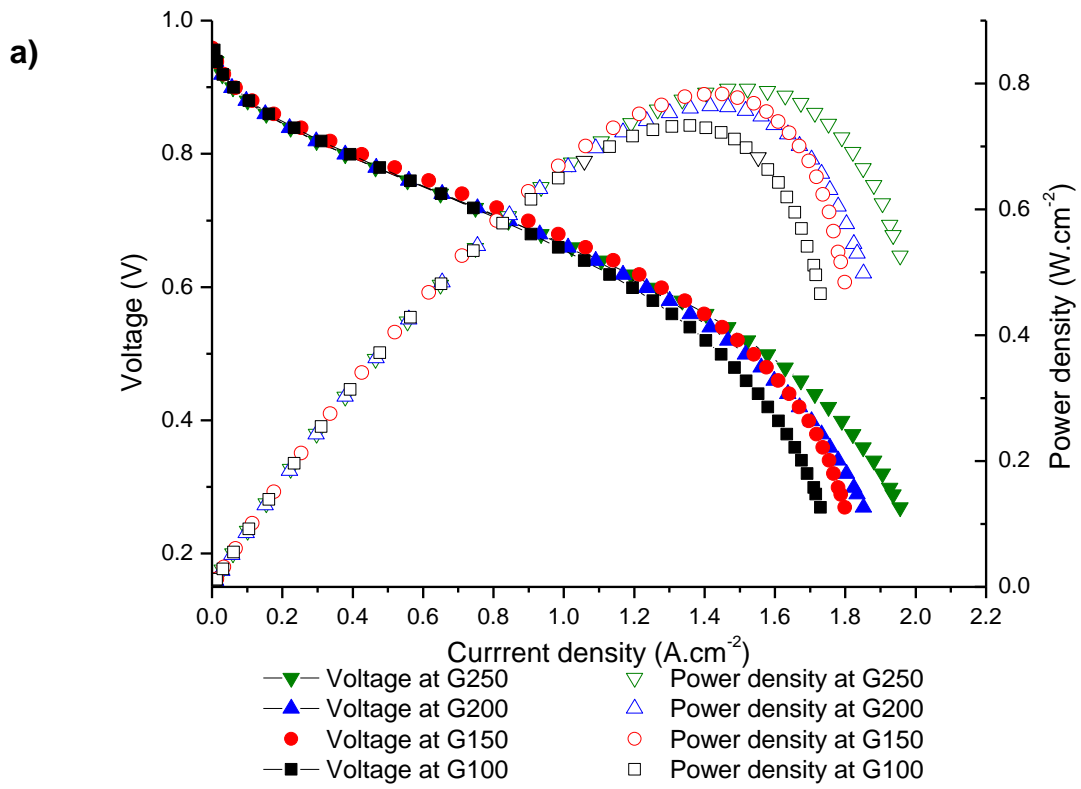
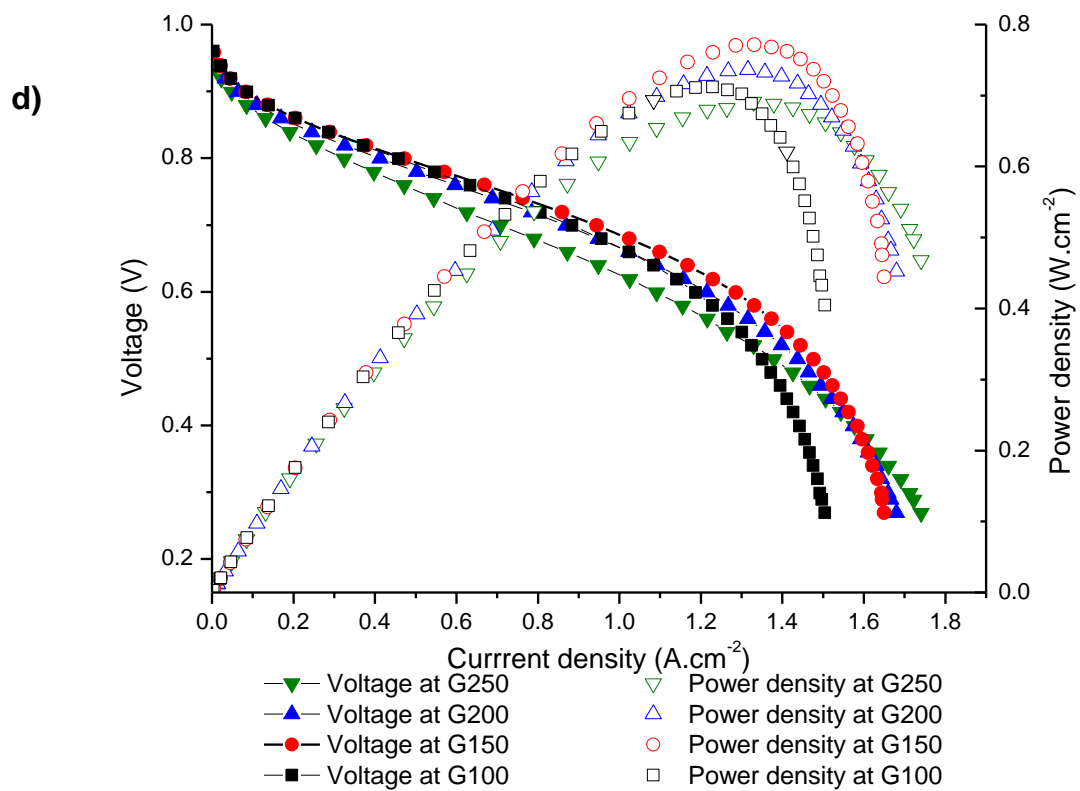
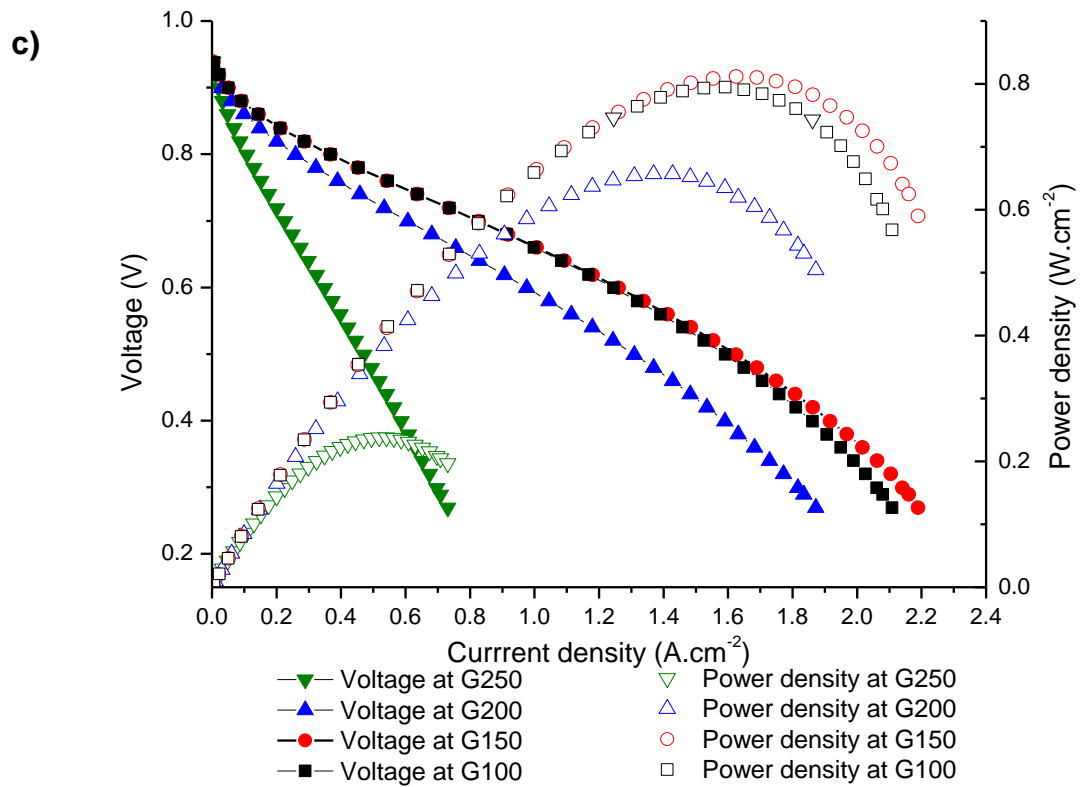


Figure 5.5: Change in the performance of (a) LT1200N and (b) LT1200W as a cathode GDL with the change of gasket thickness.

SGL 10BC shows an interesting performance as the change in the gasket thickness results in relatively low change in the performance. Again, the MEA has its maximum power density at a lower maximum current performance (Figure 5.6 (a)). SGL 24BC shows a maximum performance with G200 gasket. The cell shows a clear increase and then a drop of performance with the decreasing of the gasket thickness. Here the mass transport effect is clear with a significant decrease in the performance when changing from G200 to the G150. SGL 25BC shows a gradual decrease in the MEAs resistance with the decreasing of the gasket thickness (Figure 5.6 (b) and 5.6 (c)). The cell shows very little mass transport loss. SGL 25BC also shows a gradual increase in the performance with the drop of resistance losses. The cell performs the best with G100. SGL 34BC and SGL 35BC show similar behaviour to SGL 24BC and SGL 25BC. The change in the performance of SGL 35BC with compression is more prominent than that of SGL 34BC. The optimum performance of SGL34BC is with G150 and with G100 for SGL 35BC (Figures 5.6 (d) and 5.6 (e)).





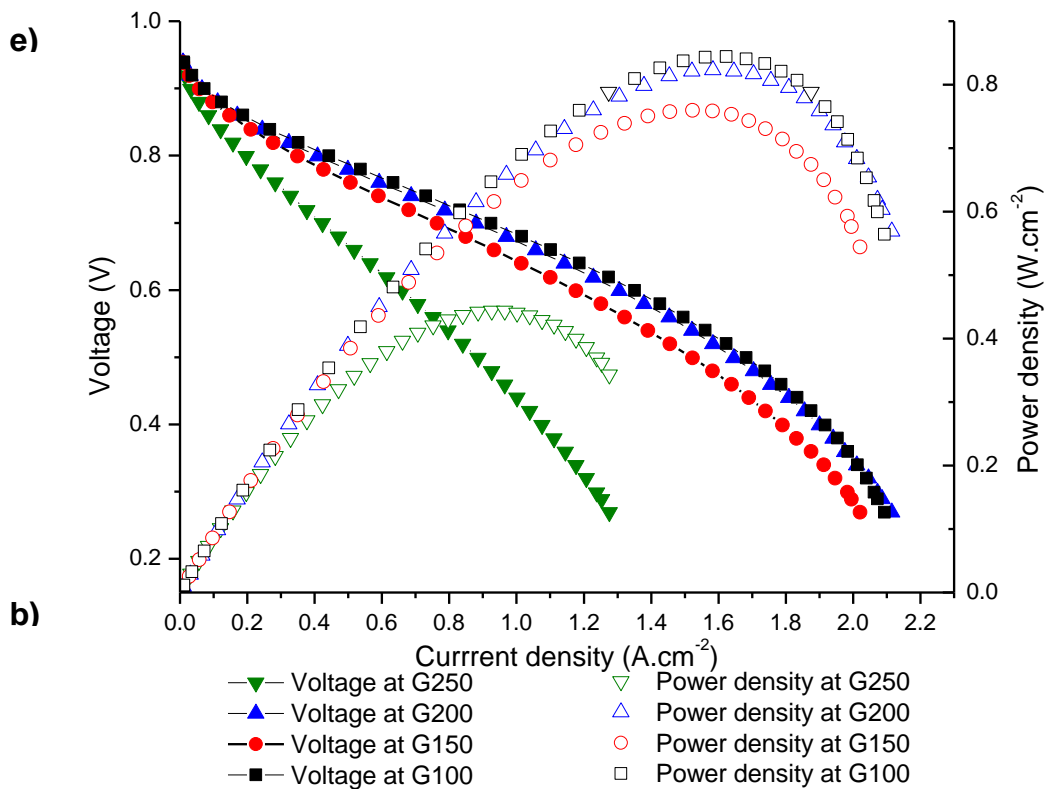


Figure 5.6: Change in the performance of (a) SGL 10BC, (b) SGL 24BC, (c) SGL25BC (d) SGL34BC (e) SGL35BC as a cathode GDL with changing gasket thickness

5.3 DISCUSSION

The pressure applied on the GDL causes an axial reversible and irreversible deformation of its thickness. Therefore, this change in thickness results in an increase in the GDL density and a decrease in its porosity. The change in the GDL porosity has a direct effect on the cell water management.

In the *in-situ* test setup, the clamping force applied by the torque wrench on the bolts results in a total pressure applied on the back of the FFPs. This has been measured to be around 10kN. Due to the very low compressibility of the gasket material (deformation in thickness of up to 5 μm at 2.4 MPa), its thickness is used to control

the pressure applied on the GDL and the deformation in the GDL. It is important to note that the test has its limitations due to the resolution of the change in the gasket thickness (50 μ m). Therefore, the optimum GDL deformation due to compression is within a range around the value measured in the test.

5.3.1 CHANGE IN THE MEA PERFORMANCE WITH COMPRESSION FOR DIFFERENT GDL THICKNESSES

Figure 5.7 shows the change in the maximum power and current density with the change of the gasket thickness for Toray H-120, H-090 and H-060. It shows that the optimum gasket thickness corresponds to the GDL thickness; thicker GDLs require thicker gaskets for optimum performance. The results also show a significant change in the performance of H-060 MEA in comparison to that for H-090 and H-120. This can be explained by the limited contact between the GDL and the FFP at high gasket thickness. This results in high electrical contact resistance that decreases with higher compression (lower gasket thickness) and therefore increases the MEA performance.

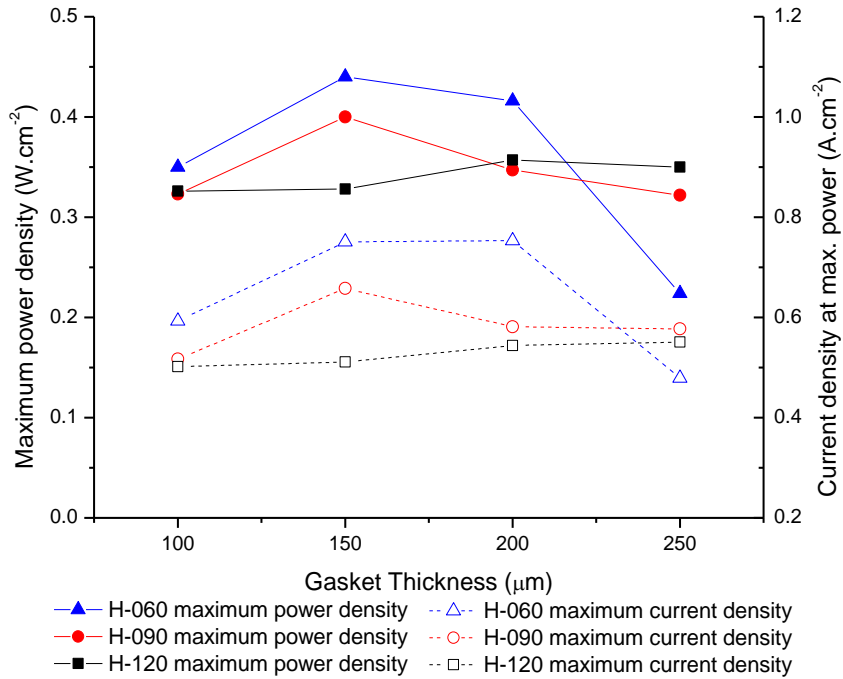


Figure 5.7: The effect of compression on the maximum power and current densities for GDLs with different thicknesses; H-060 (190 μm), H-090 (280 μm), and H120 (370 μm).

Figure 5.8 shows the change in the ohmic resistance for the same MEAs; the ohmic resistance decreases till it reaches a value when changes become insignificant. This is in agreement with the trend reported in the *ex-situ* measurements in chapter 4. Here, we can see that the ohmic losses do not play any role in the change in the MEA performance after a certain level of compression. This confirms that after reaching the optimum compression value, mass transport becomes the limiting factor in the performance of the MEA.

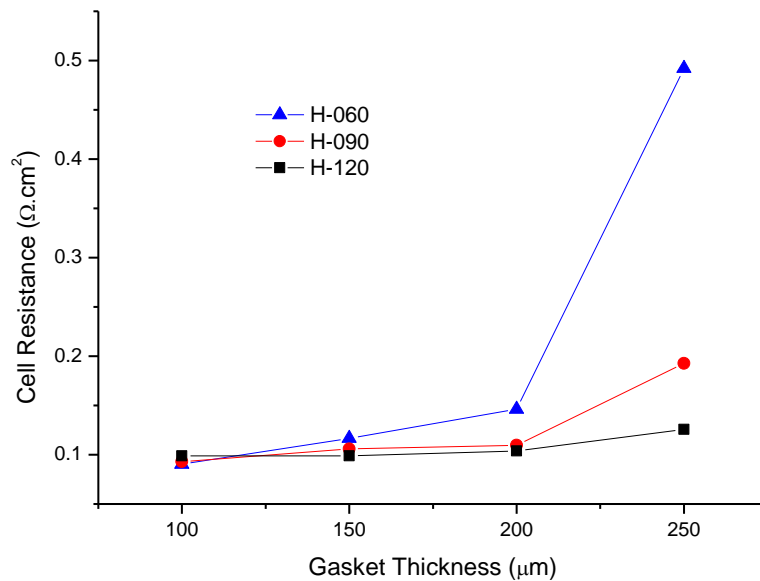


Figure 5.8: The effect of compression on the Ohmic resistance for MEAs using GDLs with different thicknesses; H-060 (190 μm), H-090 (280 μm), and H120 (370 μm).

5.3.2 CHANGE IN THE MEA PERFORMANCE WITH COMPRESSION FOR DIFFERENT GDL DENSITIES

Figure 5.9 shows that GDLs with lower bulk density require higher thickness deformation in order to achieve optimum performance. It is interesting to note that the change in the performance of the high density GDLs is relatively lower than that of lower density GDLs. Moreover, GDLs with lower density appear to achieve significantly higher performance (power density) and can reach to higher maximum current densities.

GDLs with lower bulk density have higher porosity; hence, the GDL can afford higher thickness deformation while maintaining sufficient pore volume for good water and

reactant transport. This can explain the optimum performance for low density GDLs at higher compression with lower mass transport losses.

The effect of porosity can also be noted from the change in the maximum current density with the change of the gasket thickness. GDLs with lower bulk density have a higher ability for water transport at high compression and therefore higher maximum current density.

Curves in Figure 5.10 show the change in the ohmic resistance for the MEAs. GDLs with lower density have a bigger drop in resistance with increasing compression which explains the more significant change in lower bulk density GDLs until it reaches the optimum performance and mass transport becomes the dominating factor.

These results indicate that at a certain current density, a minimum pore volume is required to maintain a constant flow of reactants to the active sites, and adequate water management. Below that limit, water transport losses start to appear on the polarisation curve and porosity becomes a limiting factor for the MEAs performance.

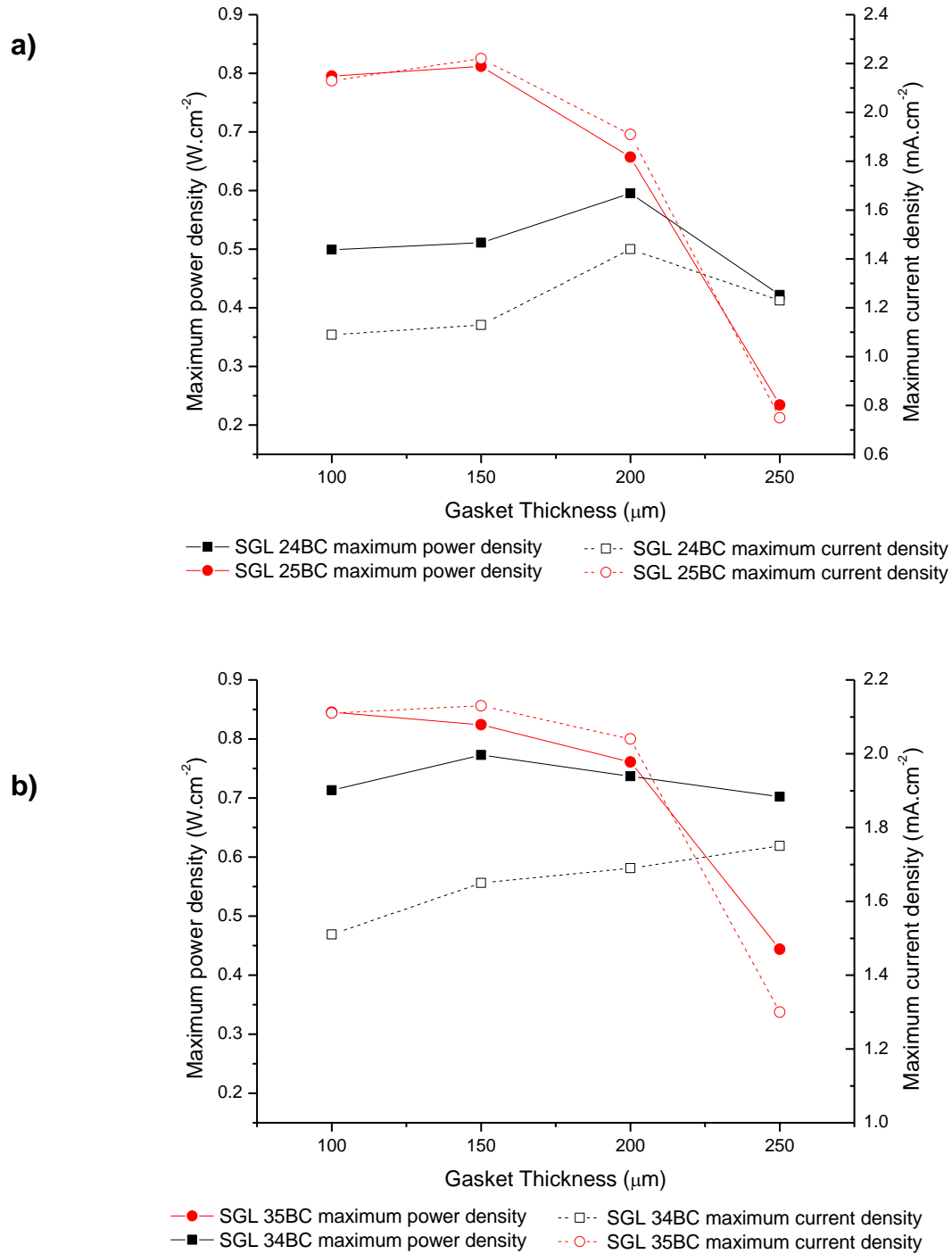


Figure 5.9: The effect of compression on the maximum power and current densities for MEAs using;(a) SGL 24BC ($0.44 \text{ mg}\cdot\text{cm}^{-3}$) and SGL25BC ($0.34 \text{ mg}\cdot\text{cm}^{-3}$) and (b) SGL34BC ($0.41 \text{ mg}\cdot\text{cm}^{-3}$) and SGL35BC ($0.31 \text{ mg}\cdot\text{cm}^{-3}$).

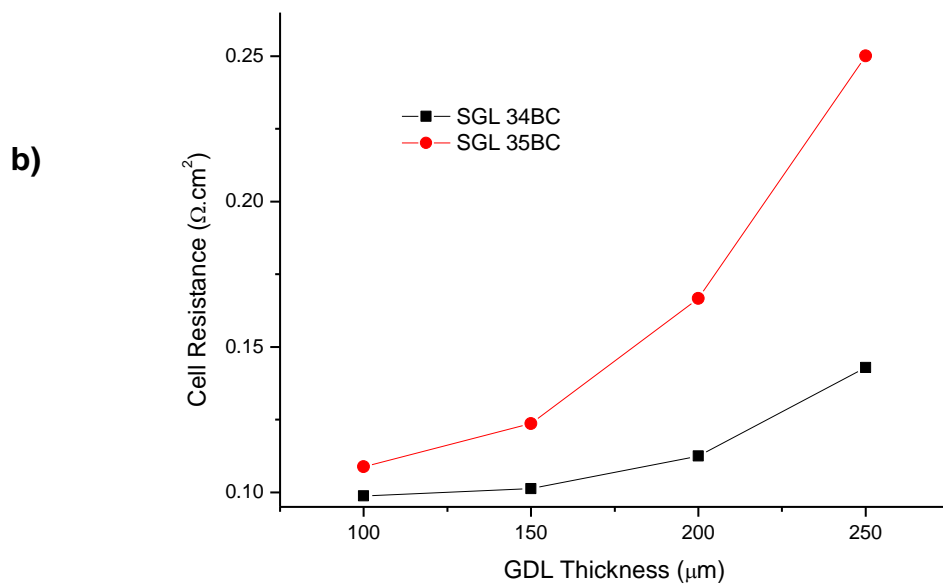
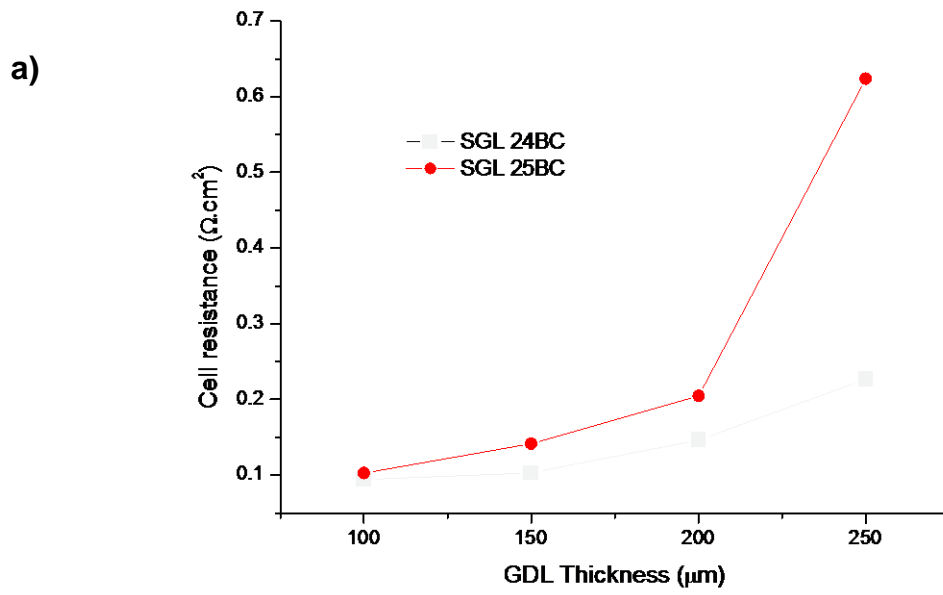


Figure 5.10: The effect of compression on Ohmic resistance for MEAs using; (a) SGL 24BC and SGL25BC, and (b) SGL34BC and SGL35BC.

5.3.3 CHANGE IN THE MEA PERFORMANCE WITH COMPRESSION FOR DIFFERENT GDL STRUCTURES

LT1200W and LT1200N GDLs were used to study the difference in behaviour of woven and non-woven GDLs under compression (see Fig. 5.11). The structure of the fibres in the GDL has a significant effect on the GDL's compressibility. The woven structure allows a higher bulk density to be achieved, which results in a higher ability to resist pressure deformation. Due to the relatively high thickness and low compressibility of the woven GDL, the increase in compression by decreasing the GDL thickness results in a decrease in the performance, however, the change is insignificant. On the other hand, the non-woven GDL with its low thickness and higher compressibility achieves its optimum performance with lower gasket thickness to achieve sufficient compression. Figure 5.12 shows that the significant change in the non-woven GDL performance is due to decrease in the ohmic resistance. The large initial ohmic resistance is due to the bad contact between the GDL and FFP. It is important to note that although valid, the comparison between the woven and non-woven GDL structure in this case has its limitations due to the difference in thickness and density of the GDLs.

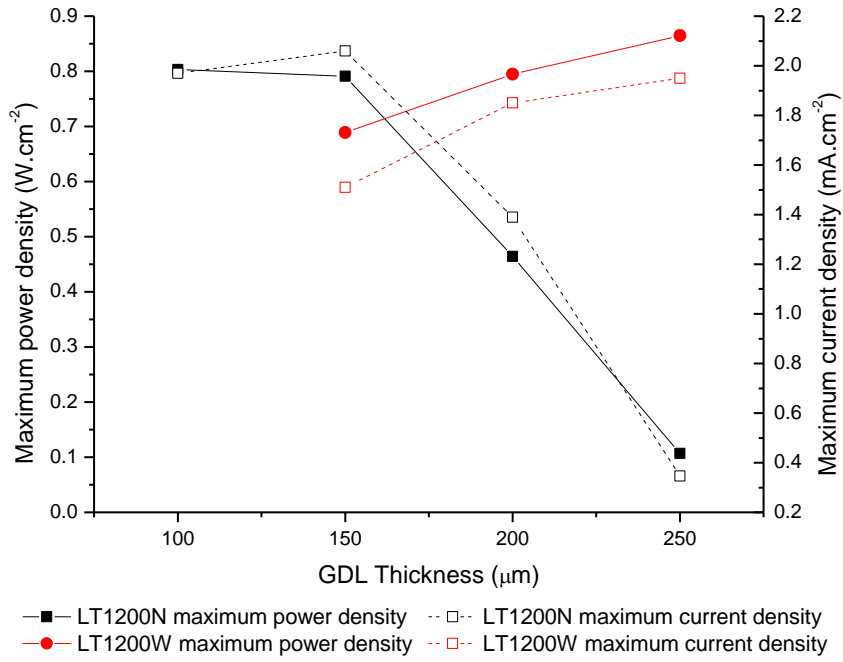


Figure 5.11: The effect of compression on the maximum power and current densities for MEAs using woven (LT1200W) and non-woven (LT1200N) GDLs

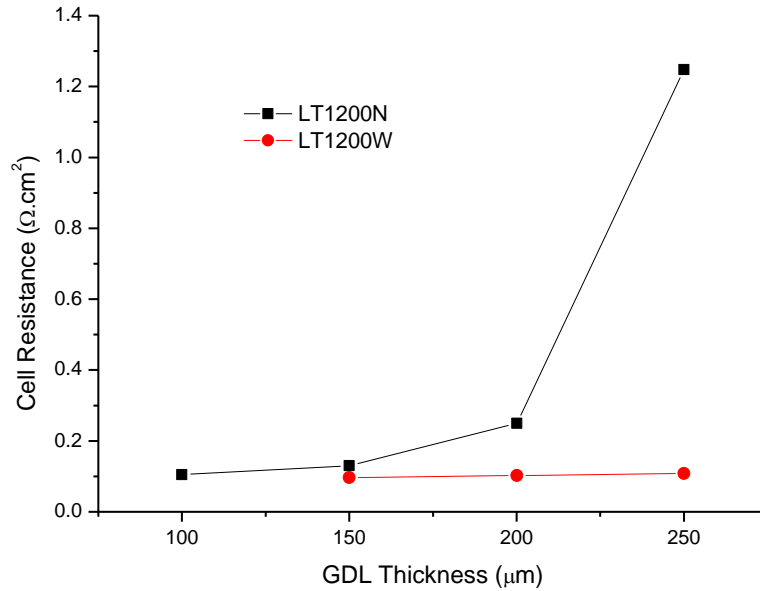


Figure 5.12: The effect of compression on the ohmic resistance for MEAs using woven (LT1200W) and non-woven (LT1200N) GDLs

It is interesting to note that the optimum performance for both structures is very comparable although achieved with different gasket thicknesses. This shows that comparable results can be obtained by the different GDL types, and other properties of the GDL might have a more significant effect on the MEA performance.

Figure 5.13 compares the performance of SGL10BC (felt structure) and SGL 34BC (straight fibre structure) GDLs. When comparing the felt and straight fibres structure, it is noted that SGL 10BC has a relatively stable (constant) performance with compression compared to the clear drop in the performance of SGL 34BC with compression. This can be due to the ability of the felt structure to maintain its open porous structure arrangement with compression despite the big change in thickness.

Figure 5.14 shows the change in the resistance with compression for both GDLs is very small and would not have a significant effect on the MEA performance.

However, SGL10BC shows higher performance and higher values for the maximum current density. This can be explained by its stable porous structure that supports the transport of reactants and water management under compression.

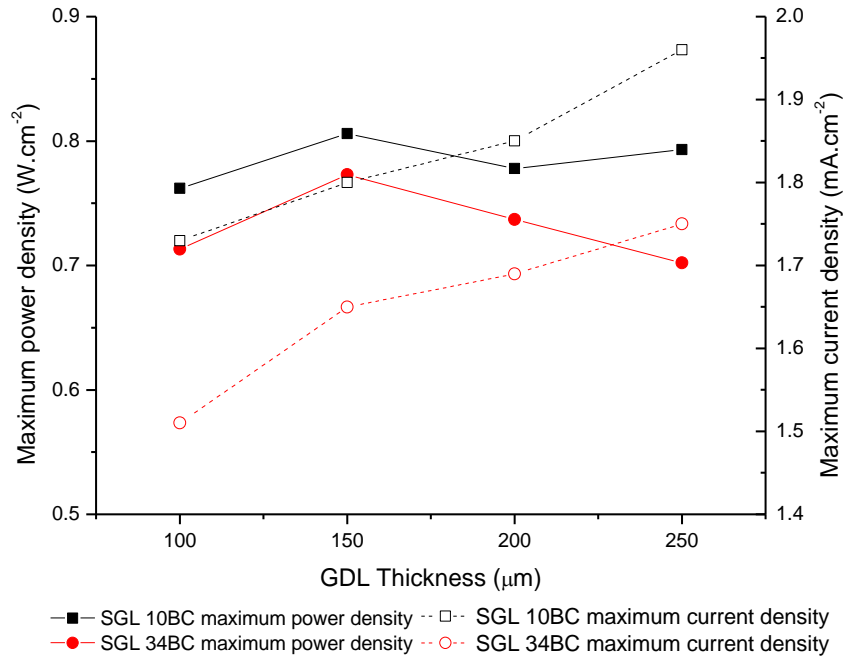


Figure 5.13: The effect of compression on the maximum power and current densities for MEAs using GDLs of felt and straight fibre GDLs: 10BC (felt fibre) and 34BC (straight fibre).

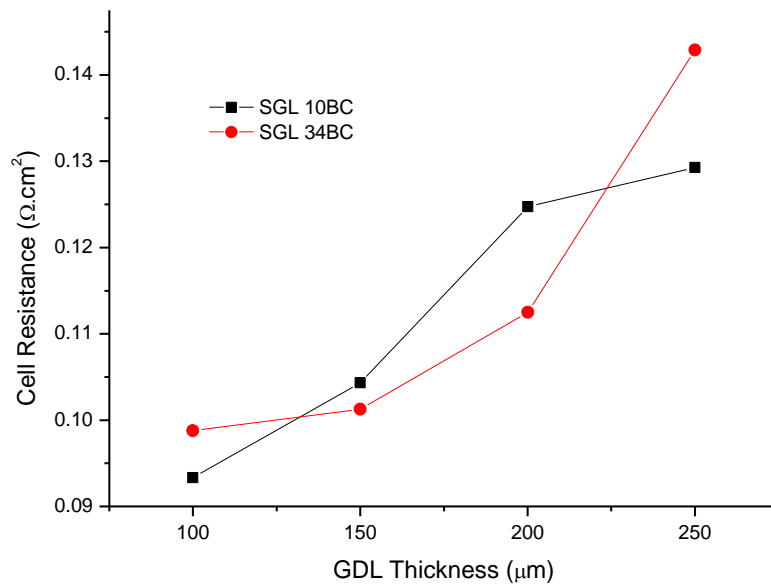


Figure 5.14: The effect of compression on the ohmic resistance for MEAs using GDLs of felt and straight fibre GDLs; 10BC (felt fibre) and 34BC (straight fibre)

5.4 Conclusions

The optimization of clamping pressure for PEFC is proven to be crucial for the optimization of the MEA performance. The GDL is the main component in the MEA affected by clamping pressure. Although this has been discussed in various studies, however, an optimization method has not been developed.

In this chapter, the behaviour of GDLs with various properties was discussed to form the basis for a clamping pressure optimization method. It is found that the optimum clamping pressure of the GDL is independent of the GDL thickness. The density and structure of the GDL, however, influences the MEA's behaviour with compression significantly. It was demonstrated that the effect of clamping pressure is more prominent on GDLs with lower substrate bulk density. High bulk density substrate shows a relatively small change in performance with clamping pressure. However, GDLs with lower bulk density require higher level of compression with higher deformation to achieve optimum performance. Moreover, the structure of the GDL substrate affects the behaviour of the substrate under compression and therefore the change in the MEA performance under compression.

It is also clear from the study that up to the optimum compression, the main parameter affecting the performance of the cell is the ohmic resistance. At compressions higher than the optimum compression, the change in ohmic resistance becomes negligible and mass transport effect increases, causing the drop in the cell performance. Therefore, in GDLs with a structure that can maintain sufficient pore structure at high compression, high GDL deformation was achieved, maintaining high performance and maximum current density.

CHAPTER SIX

IN-SITU CHARACTERISATION OF GAS DIFFUSION LAYERS

CHAPTER 6: /IN-SITU CHARACTERISATION OF GAS DIFFUSION LAYERS

Gas Diffusion Layer (GDL) properties are dependent on the materials, structure and composition used in fabrication. As discussed in chapter 4, changes in one of the GDL parameters will result subsequently in changes in various properties. Therefore, optimising a GDL design is a multi-variable problem that requires a clear understanding of the effect of each property on the performance.

In this chapter, GDL samples are divided into sets in order to minimise the number of variables in the GDL properties affecting the MEA performance. Three MEAs of each type were fabricated to ensure repeatability and reduce the effect of fabrication error on the performance.

The MEAs were tested under optimized cell clamping pressure conditions and under fixed operating conditions. The polarization curves for the MEAs in each set were compared and changes in the performance were discussed in light of the *ex-situ* properties of the GDL. The ohmic and the mass transport regions of the polarization curve are at focus, as the GDL plays a main role in the transport of electrons, reactants and products within in the cell.

6.1 SAMPLES AND EXPERIMENTS

6.1.1 SAMPLES

A selected range of commercial woven cloth and non-woven GDL samples were used in this study. The samples studied are of multi-variant nature; therefore, the samples are studied and discussed in the results section within sets to explore the

effect of one variable at a time. Table 6.1 summarises the samples within each set for study. The properties of these GDLs can be found in chapter 4.

Table 6.1: Sets of GDL samples

Variable	GDL samples
Thickness	Toray H-060, H-090 and H-120
Density	SGL 24BC and SGL 25BC
	SGL 34BC and SGL 35BC
Structure	Woven: ETEK LT1200W and Non-woven: ETEK LT1200N
	Straight fibre non-woven: SGL 34BC and Felt fibre non-woven: SGL 10BC

6.1.2 *IN-SITU* TESTING

The GDL samples were used to fabricate the cathode gas diffusion electrodes (GDEs), while commercial Johnson Matthey (JM) GDE (GDS00165) was used for the anode. The cathode GDE was fabricated by hand painting the catalyst ink on the GDL. The catalyst ink was prepared using commercially available 45.6 wt % Pt/C powder (Tanaka Kikinzoku Kogyo), 10 wt % Nafion (Ionpower) solution and isopropanol (Sigma Aldrich). The average Pt loading on the fabricated GDLs was $0.45 \pm 0.05 \text{ mg.cm}^{-2}$. The GDEs were assembled with a Nafion N212 membrane and hot pressed for 2 minutes at 1800 N at 120°C. The cells had a circular active area with a diameter of 3.8 cm. The MEAs were tested in a single cell housing under optimized clamping pressure using a Bio-logic test station (FCT-50S). The cells were operated with hydrogen and air for the anode and cathode, respectively. The test

was conducted at 70°C cell temperature and 2 bar gauge back pressure (see table 6.2). The cells were operated at fully humidified (100% RH) conditions at both anode and cathode to increase the water transport demand on the GDL.

Table 6.2: Fuel cell operating conditions

Parameter	Value
Temperature	70.0 ± 0.5 °C
Back pressure	2.0 ± 0.1Bar
Hydrogen flow rate	120 mL.min ⁻¹
H ₂ Stoichiometry	1.4
Air flow rate	300 mL.min ⁻¹
Air stoichiometry	2.5

Three MEAs of each GDL type were fabricated and tested in order to ensure repeatability of the results. The results show consistent performance for the MEAs of the same GDL sample with up to ±5% cell potential variation at 1.0 A.cm⁻². A polarization curve (IV curve) and EIS curves at different current densities were obtained for each MEA to study the GDL performance in the MEA.

The discussion focuses on the ohmic and the mass transport regions of the polarization curve as it is thought that the GDL mainly affects these two regions. The current density achieved at 0.25V is referred to as the maximum current density and is used as one of the indications to the mass transport ability of the GDL. The EIS curves are used to identify the change in the MEA's ohmic and mass transport

properties with the change of the GDL and to assist in explaining the difference in the MEA performance.

6.2 RESULTS AND DISCUSSION

The results obtained were analyzed and discussed within sets; however, whenever appropriate, the conclusions from different sets are drawn on to explain the cell behaviour. It is important to note that the results discussed in this chapter are based on tests under certain operating conditions and the behaviour of the cells at different operating conditions might change dramatically.

6.2.1 THE EFFECT OF GDL THICKNESS ON THE PERFORMANCE

Toray GDLs were used to study the effect of the GDL thickness on the MEA performance. The samples have different GDL substrate thickness with no MPL applied. *Ex-situ* results show a minimal effect of the thickness on the other GDL properties (see Table 6.3); the three samples have comparable density, water contact angle, bulk porosity, and contact resistance with the flow field plate (FFP). Therefore, the performance change in the performance of the MEA is a result of the change in thickness.

Table 6.3: GDL properties change with thickness [183]

Sample	Thickness (μm)	Bulk Density ($\text{g}\cdot\text{cm}^{-3}$)	Surface roughness (μm)	Porosity (%)	Permeability (m^2)	Water contact angle ($^\circ$)
H-060	190	0.44	19.16 \pm 0.60	63.06	6.15 E -12	128.72 \pm 9.10
H-090	280	0.44	17.89 \pm 0.42	67.16	4.53 E-12	138.43 \pm 7.63
H-120	370	0.45	17.31 \pm 0.83	61.77	3.90 E-12	120.04 \pm 1.03

Figure 6.1 shows the performance of the MEAs using the Toray GDLs. The figure shows a decrease in the performance of the MEA with increasing GDL thickness. The main effect of the GDL thickness is seen in the mass transport region. The three MEAs show comparable ohmic resistance losses, however, the ohmic resistance region is shortened for thicker GDLs because of the appearance of the mass transport losses at lower current densities (see Figure 6.2).

The polarisation curves show that there is no effect of the GDL thickness on the MEA electrical resistance, which is in agreement with the results obtained from the *ex-situ* testing where it is shown that the change in *through-plane* resistance with thickness is negligible. However, the water transport ability of the MEA is significantly affected with the increase in the GDL thickness due to the decrease in the GDL permeability [183] and the longer distance between the water formation sites and the flow channels.

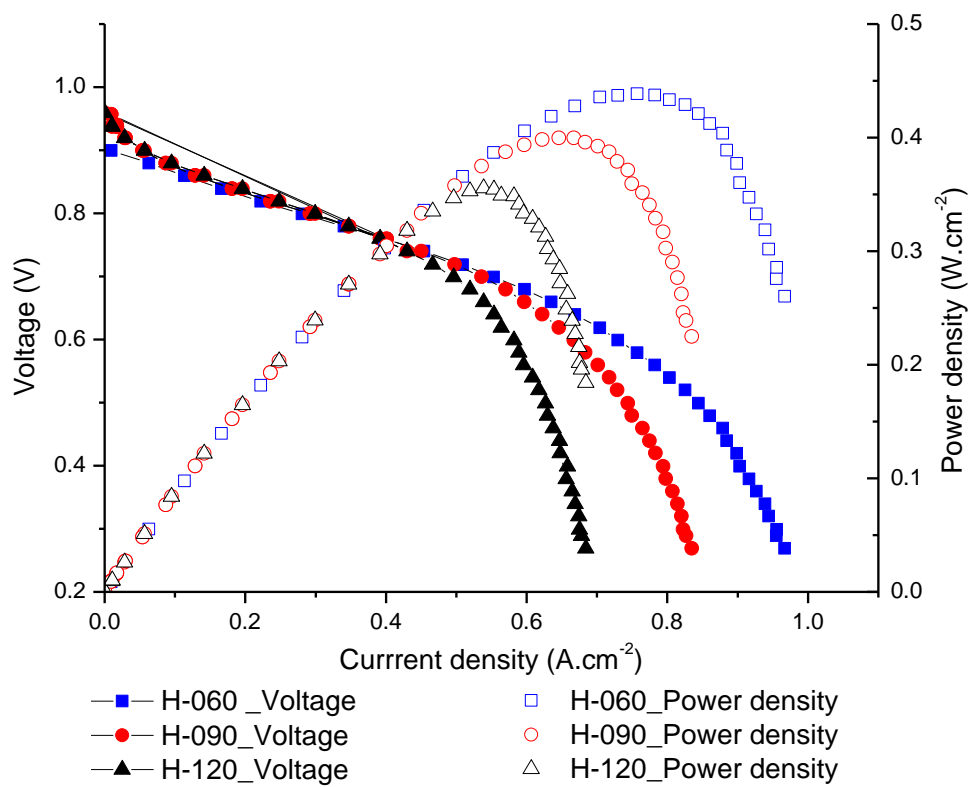


Figure 6.1: IV curves for MEAs with Toray GDLs; H-060, H-090, and H-120 with thicknesses of 190 μm , 280 μm , and 370 μm respectively

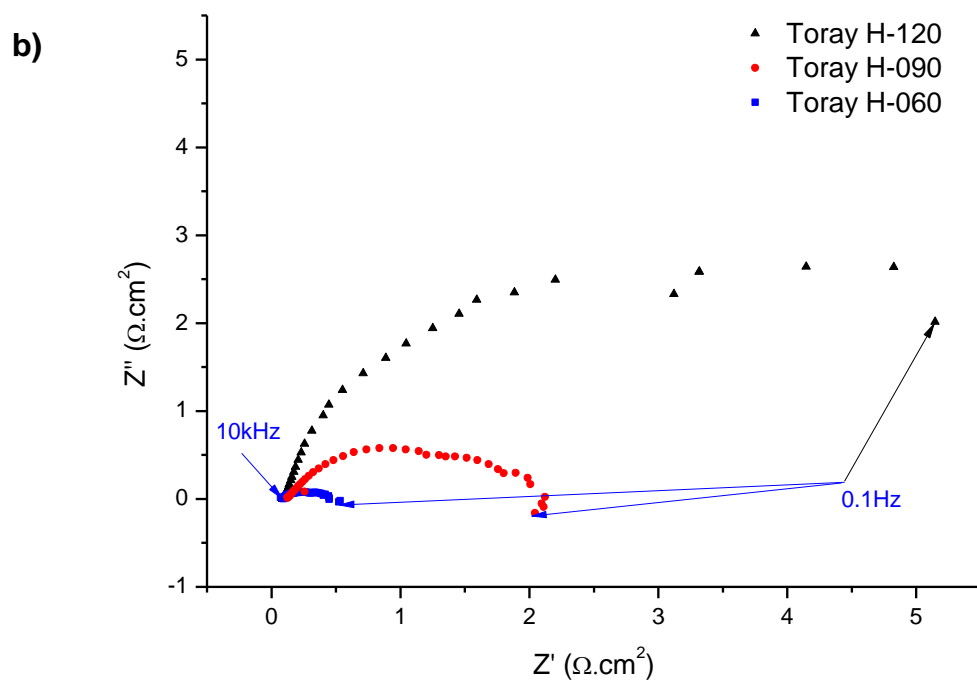
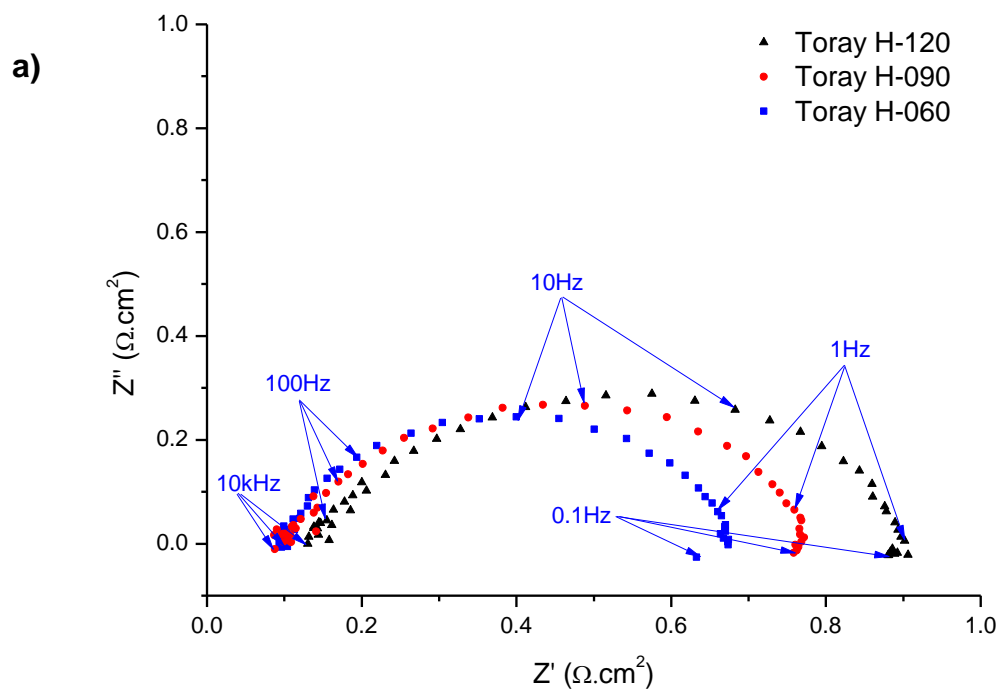


Figure 6.2: EIS for MEAs with Toray GDLs; H-060, H-090, and H-120 with thicknesses of 190 μm , 280 μm , and 370 μm respectively. (a) at 0.05 $\text{A} \cdot \text{cm}^{-2}$ and (b) at 0.5 $\text{A} \cdot \text{cm}^{-2}$.

Moreover, Figure 6.2 shows the EIS curves for the same MEAs at low (0.05 A.cm^{-2}) and intermediate current (0.5 A.cm^{-2}) densities. The results support the finding from the polarisation curves. The three MEAs have a comparable cell resistance of around $0.1 \Omega.\text{cm}^2$ as shown from the low current density curve (Figure 6.2 (a)). However, at intermediate current density the curve (Figure 6.2(b)) shows that the mass transport resistance increases significantly with the increase in the GDL thickness, hence the observed drop in the performance.

6.2.2 THE EFFECT OF GDL DENSITY ON THE PERFORMANCE

The effect of the bulk density of the substrate is studied here in 2 sets of GDLs; SGL 25BC/SGL 25BC and SGL 34BC/ SGL 35BC. In each set the GDLs have the same thickness and water contact angle. However, as a result of the difference in the materials density, GDLs with lower density have higher substrate porosity and higher permeability (Table 6.4).

Table 6.4: GDL properties change with bulk density

Sample	Thickness (μm)	Bulk Density (g.cm^{-3})	Surface roughness (μm)	Porosity (%)	Permeability (m^2)	Water contact angle ($^\circ$)
SGL 24BC	235	0.44	18.29 ± 0.77	36.46	5.09 E^{-12}	104.36 ± 4.11
SGL 25BC	235	0.34	32.05 ± 3.00	40.03	5.64 E^{-12}	112.43 ± 11.54
SGL 34BC	315	0.41	30.77 ± 0.24	47.48	8.97 E^{-12}	125.98 ± 6.68
SGL 35BC	325	0.31	46.52 ± 4.64	52.62	1.72 E^{-11}	118.20 ± 10.98

Figure 6.3 shows that SGL 25BC and SGL 35BC achieve higher performance in comparison with SGL 24BC and SGL 34BC respectively. The lower density GDLs show higher water transport ability that allows operating to higher current densities. This can be explained by the high porosity and the pore size distribution created when applying the MPL on the substrate. The low density and high porosity of SGL 25BC and SGL 35BC with high mean pore size creates greater pore size gradient between the MPL and substrate. This additionally supports the capillary force that carries the water away from the catalyst layer to the flow field channels, hence an improved water transport is observed. In addition, the high porosity of the substrate allows higher clamping pressure to be applied to achieve maximum power density without reducing the water transport ability. Moreover, the effect of the ohmic losses seems to be negligible as the difference in GDL resistance after compression [183] is extremely low in comparison to the overall cell resistance; the change in resistance cannot be seen in the EIS measurement (Figure 6.4 (a)).

The EIS curves shown in Figure 6.4 (b) confirm the effect of the substrate density on the GDL mass transport ability. The MEAs show comparable resistance; however, a significant increase in the mass transport resistance is shown. Therefore, the results here suggest that a GDL with lower bulk density can achieve higher MEA performance and higher maximum current densities.

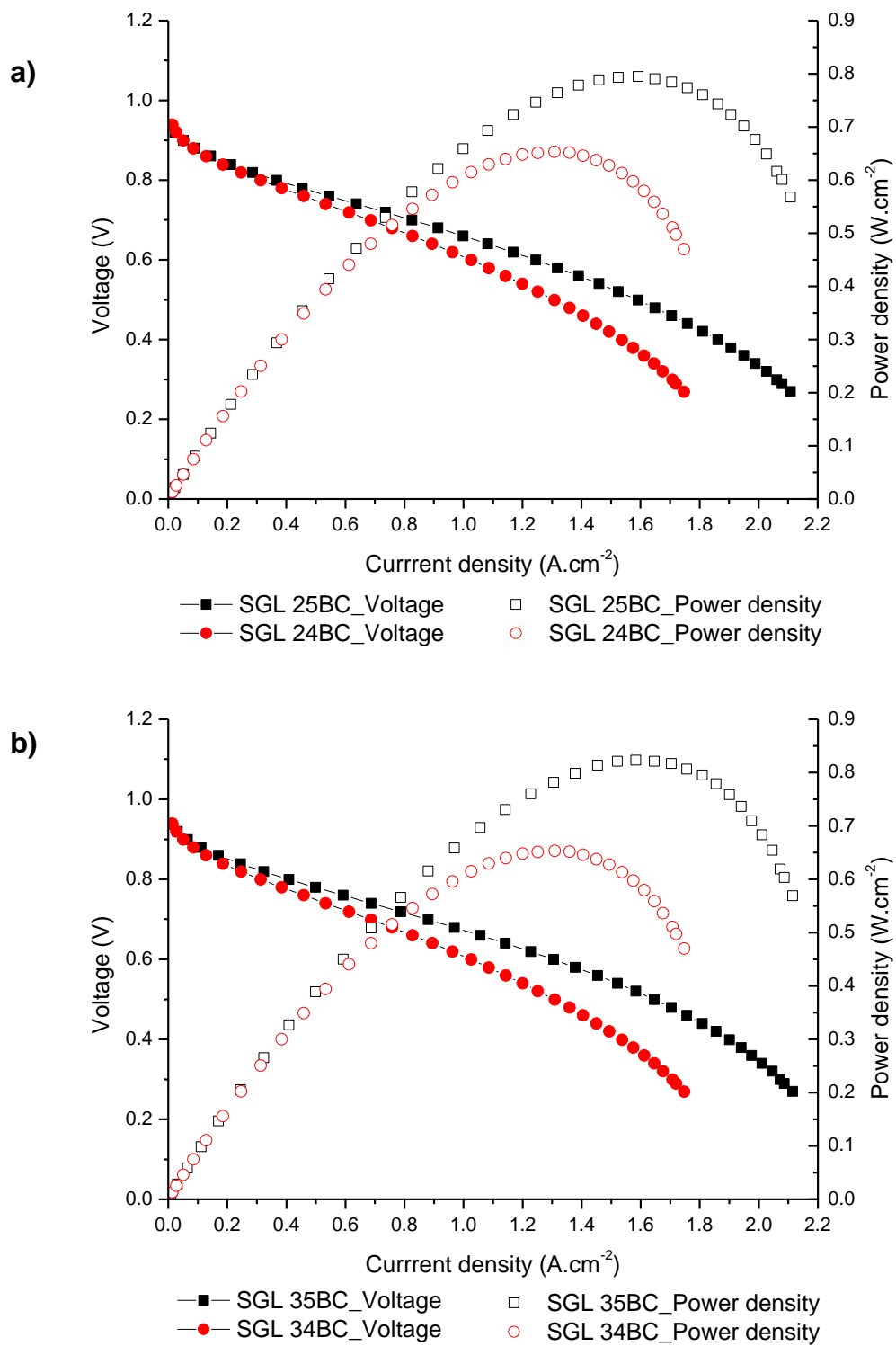


Figure 6.3: PEFC performance for GDLs; (a) SGL 24BC and SGL 25BC with densities of 0.44 g.cm⁻³ and 0.34 g.cm⁻³ respectively , (b) SGL 34BC and SGL 35BC with densities of 0.41 g.cm⁻³ and 0.31 g.cm⁻³ respectively.

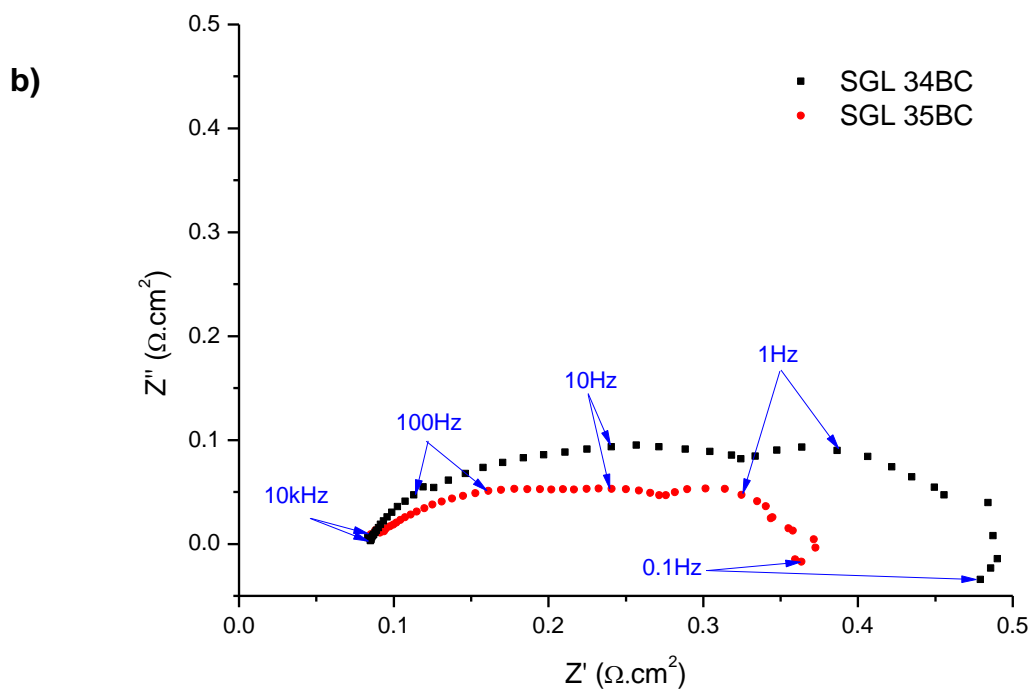
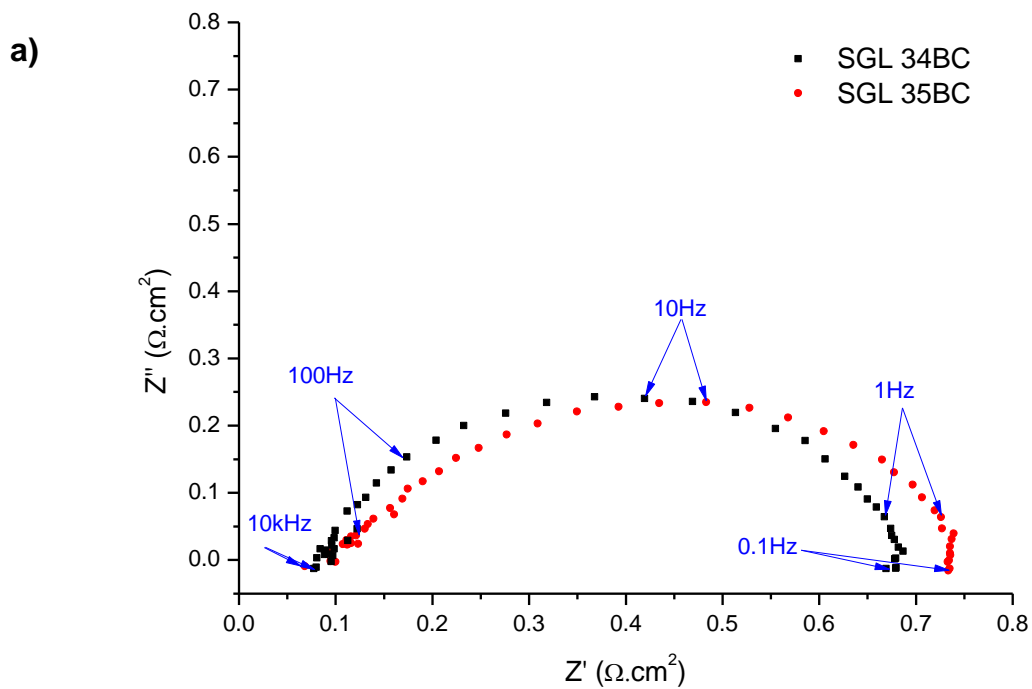


Figure 6.4 : EIS for MEAs with GDLs; SGL 34BC and SGL 35BC with densities of $0.41 \text{ g} \cdot \text{cm}^{-3}$ and $0.31 \text{ g} \cdot \text{cm}^{-3}$ respectively at (a) $0.1 \text{ A} \cdot \text{cm}^{-2}$ current density and (b) $1 \text{ A} \cdot \text{cm}^{-2}$ current density

6.2.3 THE EFFECT OF PTFE LOADING AND MPL APPLICATION ON THE GDL PERFORMANCE

The performance of substrates with and without PTFE loading was compared. Three sets of samples from 2 manufactures, namely; Freudenberg (H2315, H2315 I2) and Ballard (P50, P50T, GDS1120, P75, P75T, and GDS2120) were tested (see Table 6.5). Each set consists of the same substrate before and after PTFE loading.

Freudenberg samples have a felt flexible structure, with low fibres graphitization level; on the other hand, Ballard samples have a straight fibre structure with high fibre graphitization. The properties of the GDLs are summarised in Table 6.5.

Table 6.5: GDL properties change with PTFE loading and MPL application

Sample	PTFE and MPL	Thickness (μm)	Bulk Density ($\text{g}\cdot\text{cm}^{-3}$)	Porosity (%)	Permeability (m^2)	Water contact angle ($^\circ$)
H2315	No PTFE, No MPL	210	0.54	-	-	117.00 \pm 3.48
H2315 I2	PTFE, No MPL	210	0.54	-	-	124.33 \pm 4.29
P50	No PTFE, No MPL	170	0.36	48.7	9.21E-12	111.29 \pm 7.4
P50T	PTFE, No MPL	180	0.37	44.9	1.41E-11	113.58 \pm 0.47
GDS1120	PTFE, MPL	210	0.40	44.8	4.73E-12	116.09 \pm 16.78
P75	No PTFE, No MPL	230	0.35	62.4	1.11E-11	107.48 \pm 7.48
P75T	PTFE, No MPL	255	0.36	59.9	1.31E-11	112.57 \pm 3.08
GDS2120	PTFE, MPL	260	0.40	60.2	6.06E-12	112.33 \pm 1.50

The results show contradictory patterns; the performance of Freudenberg GDL is enhanced with PTFE loading (Figure 6.5). H2315 has relatively a lower performance than H2315 I2. The EIS curve (Figure 6.6) shows that the MEAs have a comparable ohmic resistance value. However, the mass transport semicircle appears for the MEA with H3215 at low current density ($0.1\text{A}\cdot\text{cm}^{-2}$), meaning the inability of the GDL to transport the water produced away from the catalyst layer. At higher current density, the mass transport resistance of H2315 increased significantly that the MEA's overall resistance is 4 times higher than that with H2315 I2. The unteflonated GDL seems to retain liquid water within its pores, preventing sufficient flow of reactants to reach the catalyst layer. The addition of PTFE to the substrate increases the hydrophobicity of the porous structure and prevents blocking the pores with liquid water.

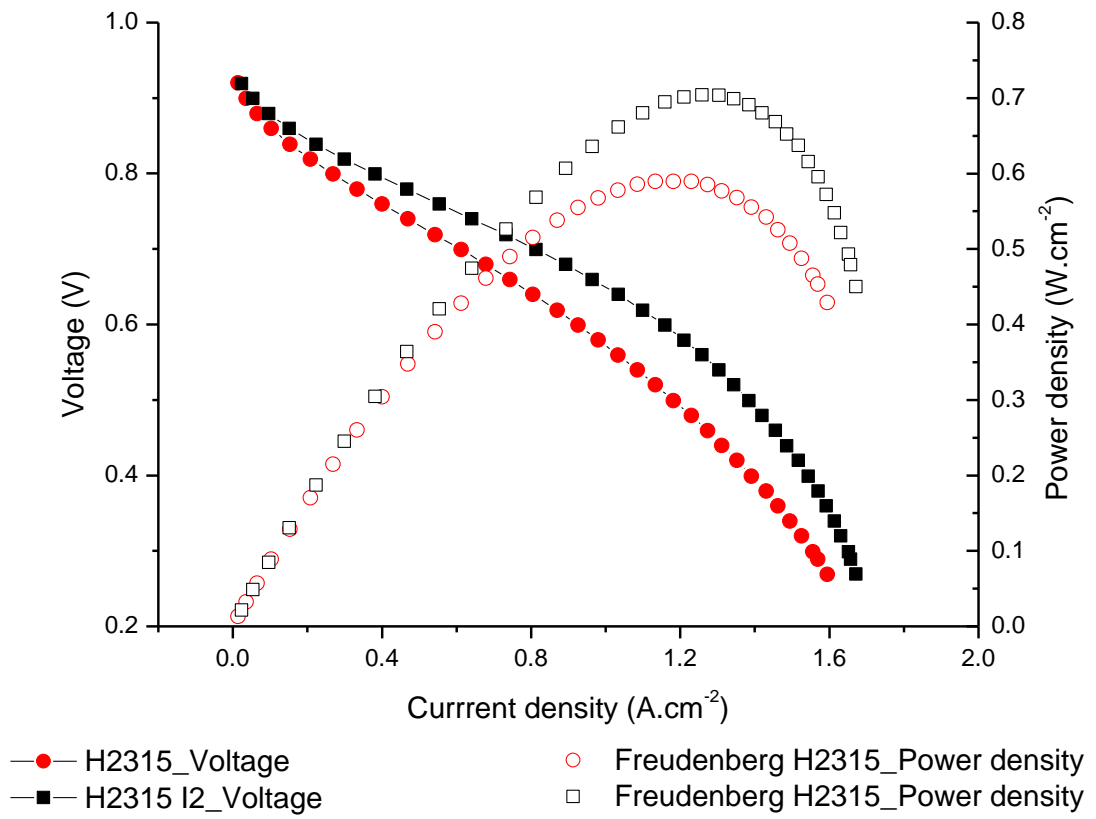


Figure 6.5: PEFC performance for GDLs; H2315 (un-teflonated) and H2315 I2 (teflonated)

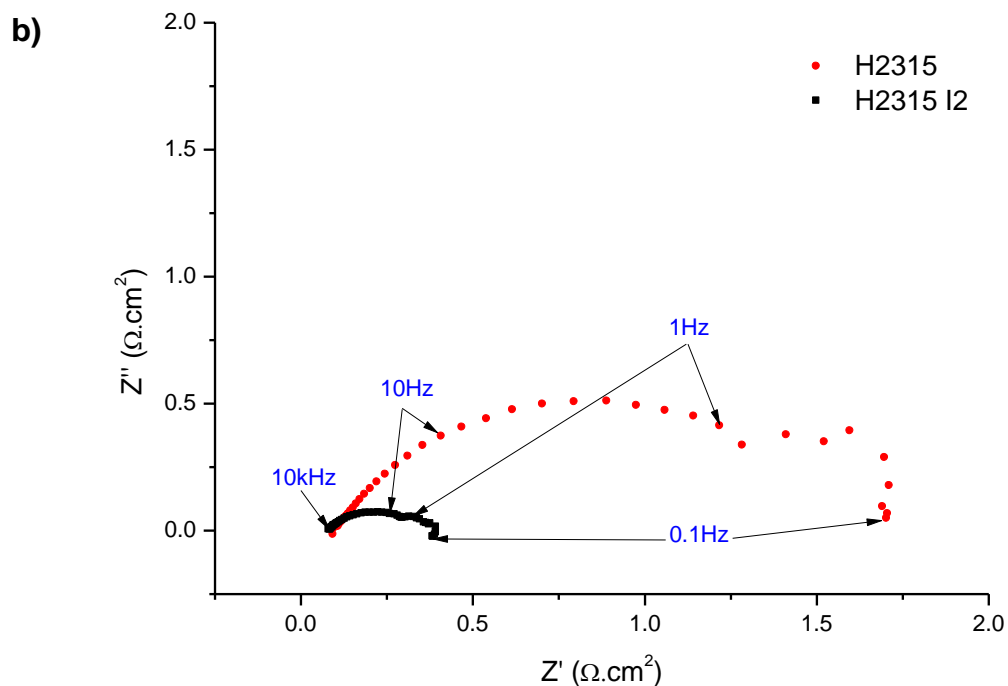
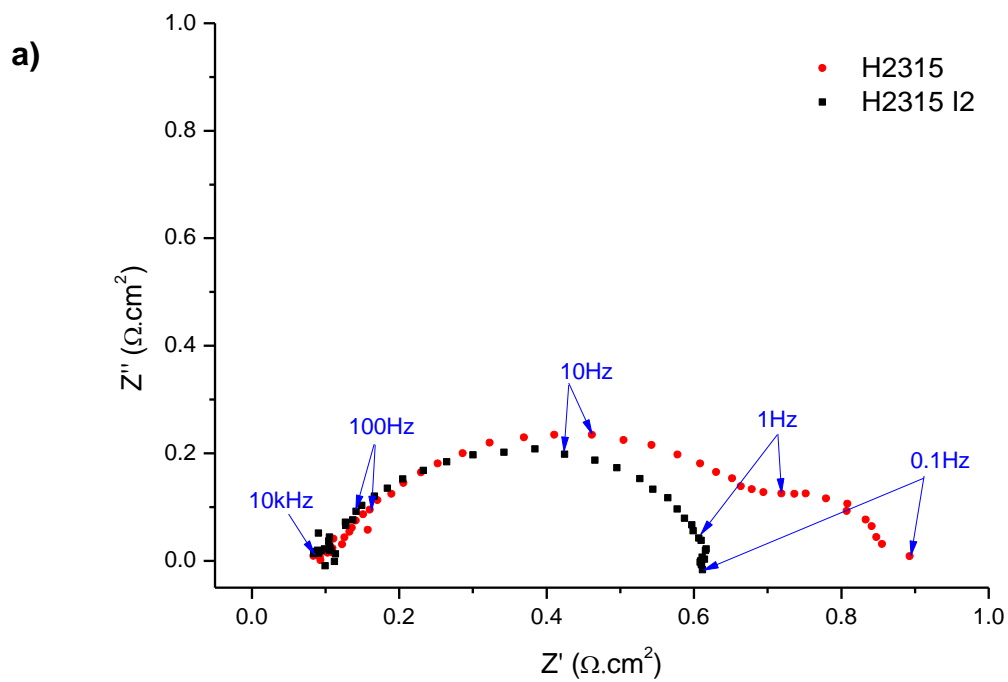


Figure 6.6: EIS for MEAs with GDLs; H2315 (un-teflonated) and H2315 I2 (teflonated) at (a) $0.1 \text{ A} \cdot \text{cm}^{-2}$ current density and (b) $1 \text{ A} \cdot \text{cm}^{-2}$ current density

On the other hand, an opposite behaviour is noticed with P50/P50T and P75/ P75T. A significant drop in the performance is seen when comparing the teflonated samples; P50T and P75T with the non-teflonated ones; P50 and P75 respectively. Here, the loss in performance is related to both an increase in the ohmic and mass transport resistance (see Figure 6.7).

This difference in the GDLs behaviour can be explained by looking at the properties of the GDL fibres used. The fibres used in Freudenberg GDLs are not graphitised, and that is clear from the mechanical flexibility of the fibres. However, un-graphitised carbon is hydrophilic and would retain water within its structure. On the contrary, Ballard GDLs are graphitized fibres, and this is reflected in the fragile mechanical structure of the layer. Graphitization increases the hydrophobicity of carbon, hence the good performance of the P50 and P75. The addition of PTFE to the graphitized fibres resulted in an increase in the electrical contact resistance of the GDL with the FFP as reported in chapter 4 and affected its mass transport properties by blocking pores, hence the decrease in the performance of the Ballard GDLs.

Generally speaking, the addition of a MPL enhances the performance of the cell. However, the effect of the MPL is influenced by the properties of the substrate it's applied on and the properties of the MPL. Figure 6.7 (a) and (b) show the change in Ballard GDLs performance when the unteflonated substrate, teflonated substrate and a teflonated substrate with a MPL. As mentioned earlier, the figures show a significant drop in the performance of the MEA with the teflonated GDL. The performance then increases when applying an MPL, however, the performance stays lower than that of the non-teflonated substrate. This is an interesting performance as

it is expected that the performance is enhanced with teflonation and the application of the MPL. The EIS results reported in Figure 6.8 show the change in the ohmic and mass transport characteristics of the MEA.

The MEA's resistance decreases in the presence of the MPL and the mass transport resistance also decreases significantly. The decrease in the resistance can be explained by the enhancement of the connection between the fibres when adding the MPL, as it provides a layer of conductive carbon that connects the surface of the substrate together. The mass transport enhancement however, is due to the increase in capillary forces in the MPL.

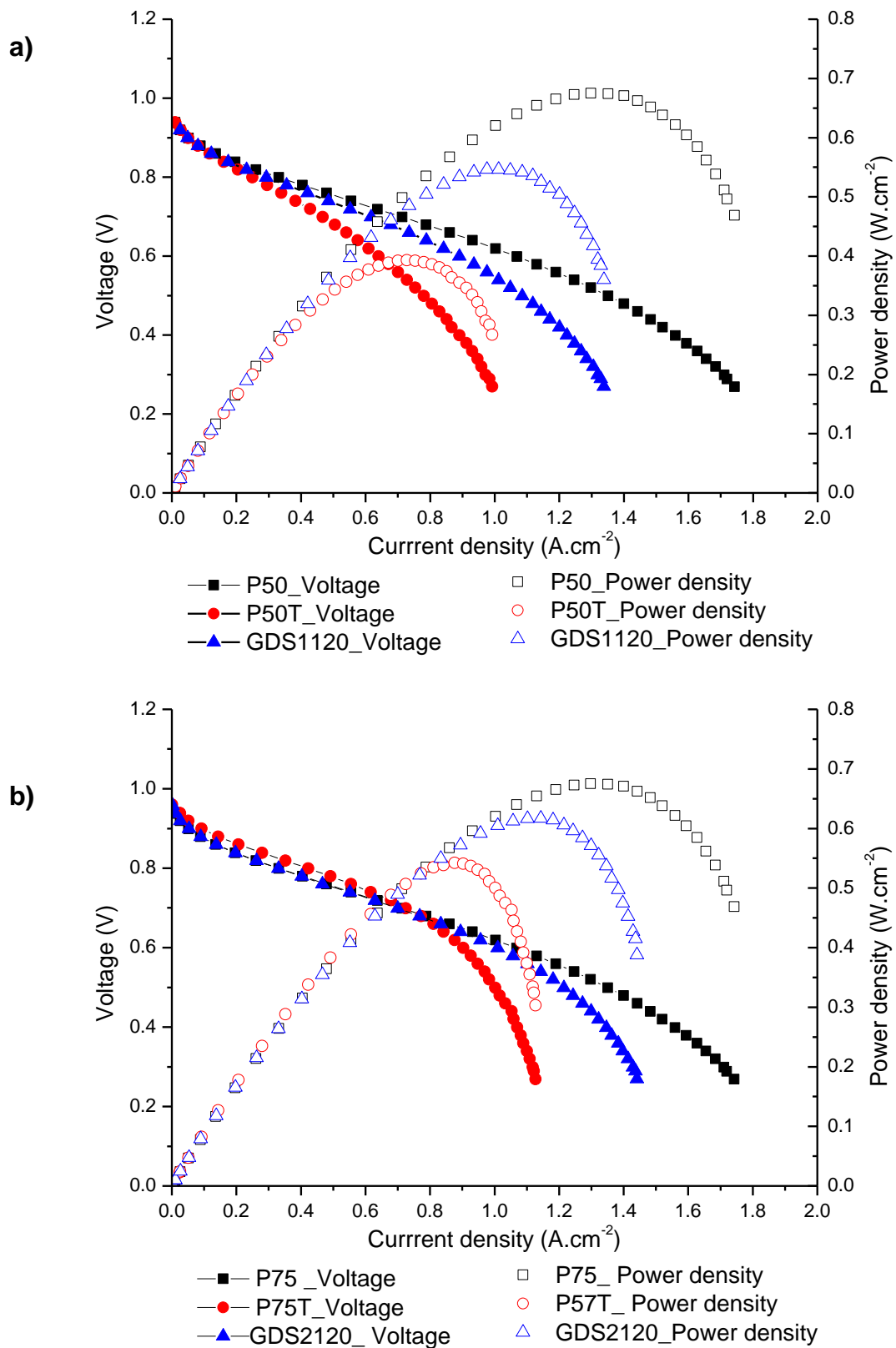


Figure 6.7: PEFC performance for GDLs; (a) P50, P50T and GDS1120, and (b) P75, P75T and GDS2120

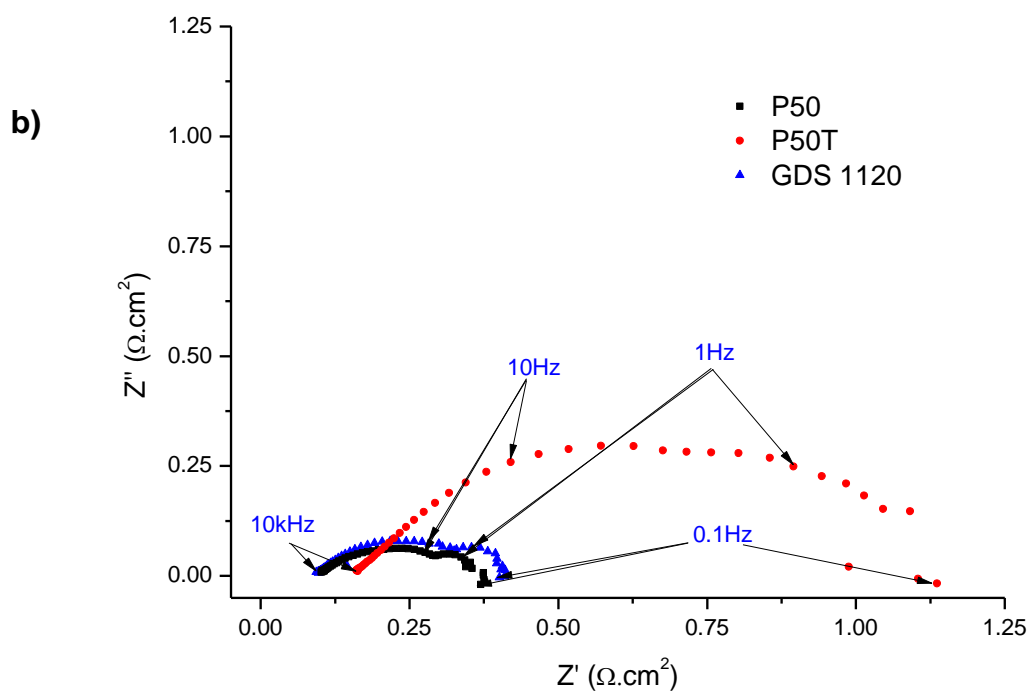
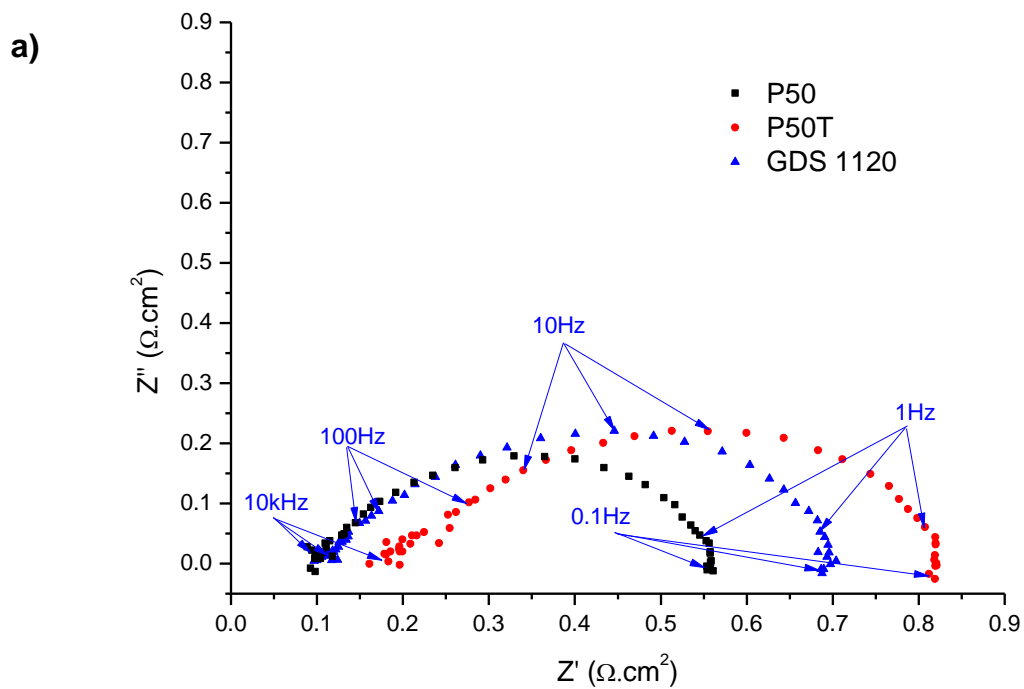


Figure 6.8: EIS for MEAs with GDLs; P50, P50T, and GDS1120 at (a) 0.1 A.cm^{-2} current density and (b) 1.0 A.cm^{-2} current density.

Moreover, when comparing the effect of applying the MPL on the performance of 24BA and 25BA, we can see that the performance of 25BA was enhanced significantly in 25BC (Figure 6.9 (b)), however, the change in the performance between 24BA and 24BC is much less (Figure 6.9 (a)). The enhancement in the performance is again seen in the mass transport region. The application of an MPL creates a layer of fine pores on the surface of the substrate which again has larger pore size. The greater the difference between the MPL and the substrate, the greater the capillary force created to move the water from the smaller pores to the larger ones (Smaller pores in the MPL develop higher capillary pressure in comparison to that in the larger pores; the pressure difference forces liquid water out from the MPL). Hence, the effect of applying an MPL on 25BA, which has larger pore size, is more pronounced than that occurred when applying a MPL on 24BA.

Table 6.6: GDL properties change with MPL application

Sample	MPL	Thickness (μm)	Bulk Density (g.cm ⁻³)	Porosity (%)	Permeability (m ²)	Water contact angle (°)
SGL 24BA	No MPL	190	0.28	66.2	4.54E-11	97.70 ± 3.74
SGL 24BC	MPL	235	0.44	36.5	5.64E-12	104.36 ± 4.11
SGL 25BA	No MPL	190	0.21	47.5	8.97E-12	-
SGL 25BC	MPL	235	0.34	40.8	6.19E-12	112.43 ± 11.54

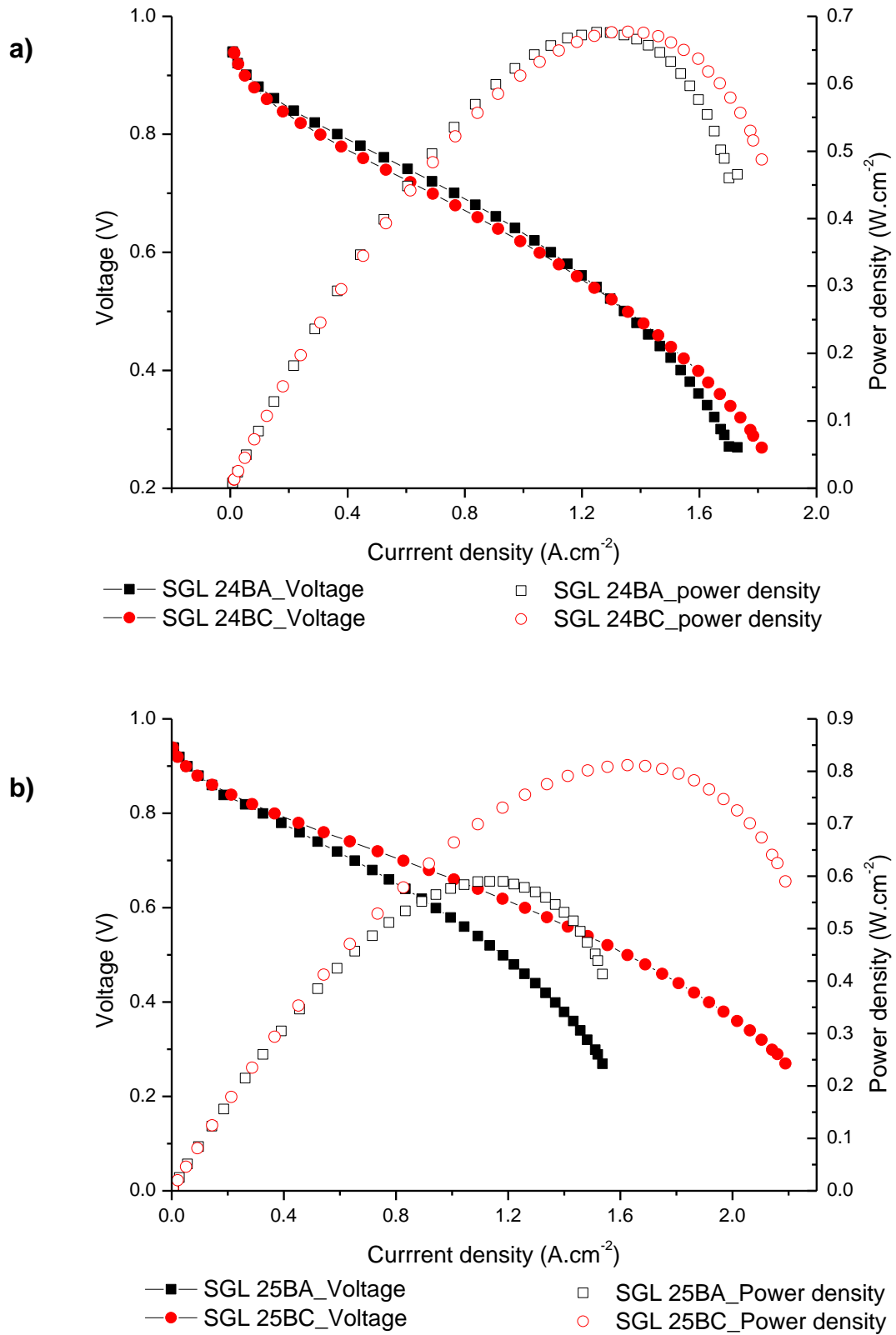


Figure 6.9: PEFC performance for GDLs; (a) SGL 24BA and SGL 24BC (b) SGL 25BA and SGL 25BC. (XXBA has no MPL, and XXBC with MPL)

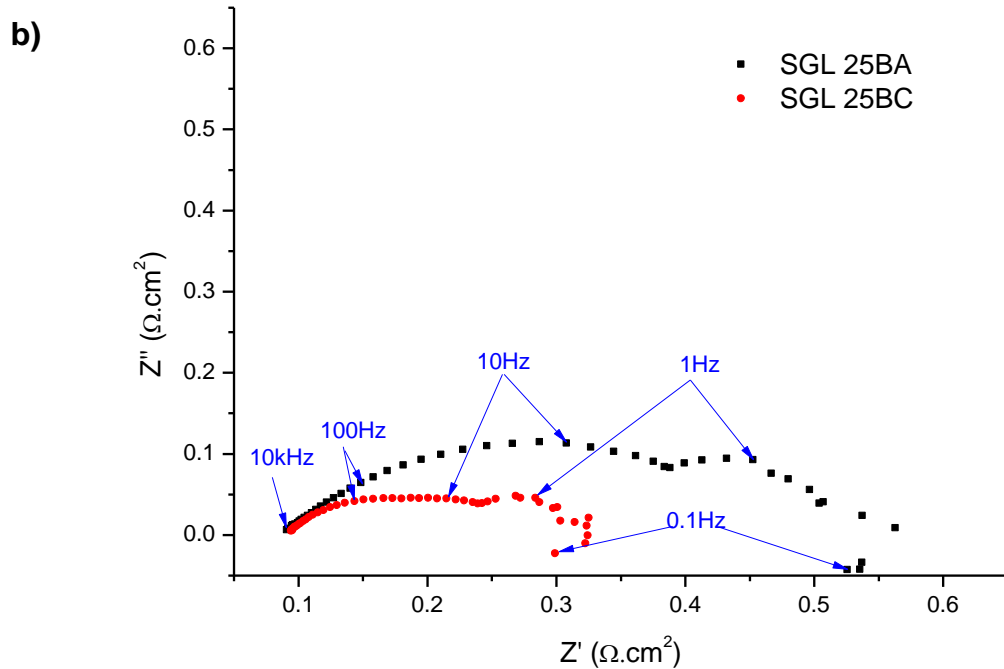
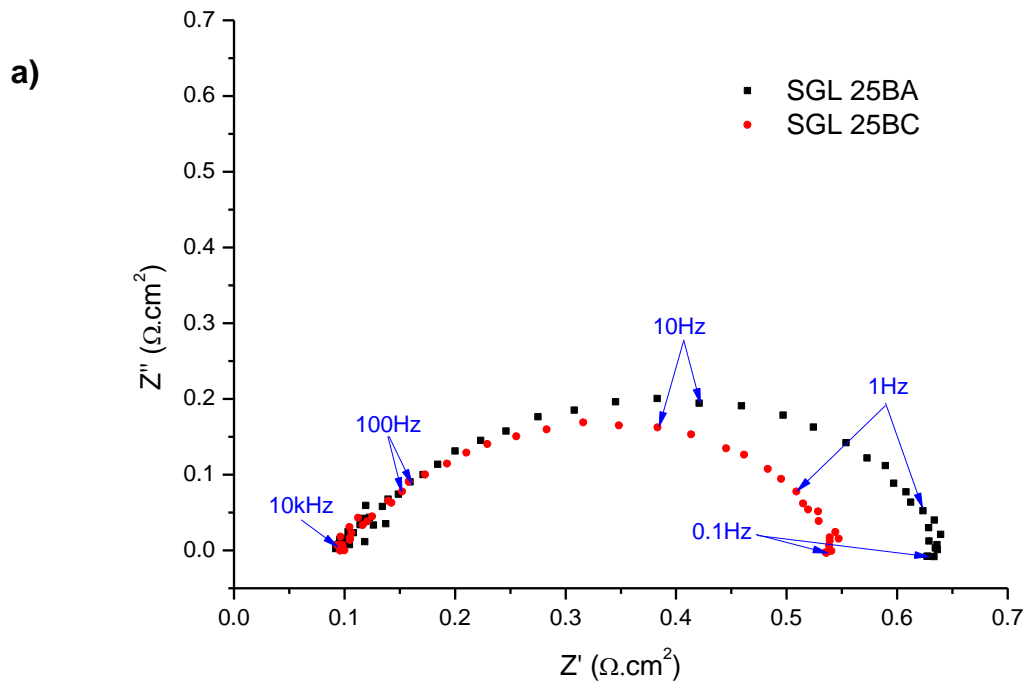


Figure 6.10: EIS for MEAs with GDLs; SGL 25BA and SGL 25BC at (a) $0.1 \text{ A} \cdot \text{cm}^{-2}$ current density and (b) $1.0 \text{ A} \cdot \text{cm}^{-2}$ current density. (XXBA has no MPL, and XXBC with MPL).

6.2.5 THE EFFECT OF THE GDL STRUCTURE ON THE PERFORMANCE

The substrate structure of the GDL determines and controls many of its properties and especially its performance. Therefore, studying the effect of the GDL structure on the MEA performance is rather complex. The change in the MEA performance with different GDL structures cannot be exclusively explained by the change of its structure, but needs to be further explored by understanding the changes in other properties as a result of the structural change.

In comparing GDL structures, woven and felt GDLs are compared to straight fibres structure from the same manufacturer to limit variations due to the material and fabrication process that may influence the performance.

A woven GDL (LT1200W) was compared to the non-woven LT1200N. The woven GDL has a higher thickness with high bulk density; however significantly lower porosity (Table 6.7). The MEAs show an almost identical performance. The results presented in the literature are always in favour of woven GDL as producing a better performance; however, the results here show that the performance of the MEAs is comparable after optimizing the clamping pressure (See Figure 6.11). The MEAs show no difference in the ohmic resistance or mass transport, although the mass transport losses appear at lower current density for LT1200W and therefore achieve lower maximum current density. The EIS curves in Figure 6.12 also confirm the comparable ohmic resistance and mass transport properties of the two MEAs.

Table 6.7: GDL properties change with the substrates structure

Sample	Thickness (μm)	Bulk density ($\text{g}\cdot\text{cm}^{-3}$)	Surface roughness (μm)	Porosity (%)	Permeability (m^2)	Water contact angle ($^\circ$)
LT 1200N	185	0.39	22.02 \pm 0.79	64.94	6.45E-12	90.19 \pm 6.46
LT 1200W	275	0.50	-	31.83	4.98E-12	96.02 \pm 0.45
SGL 10BC	420	0.36	31.29 \pm 2.67	34.64	8.04E-12	122.29 \pm 3.76
SGL 34BC	315	0.47	31.44 \pm 2.75	40.82	6.91E-12	133.86 \pm 2.22

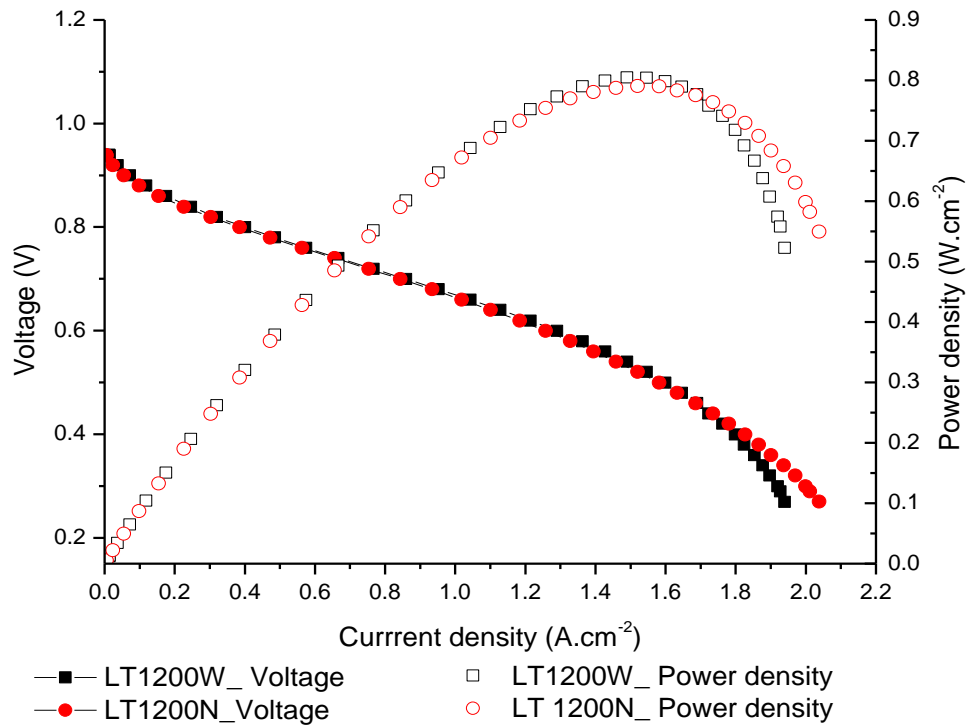


Figure 6.11: PEFC performance for GDLs LT1200W (woven) and LT1200N (non woven)

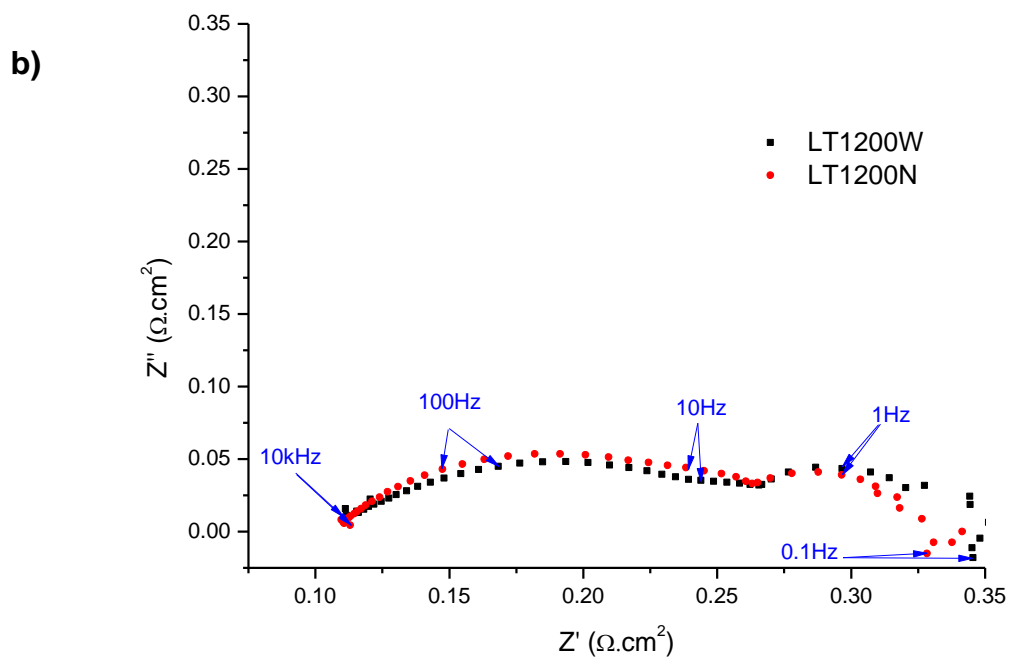
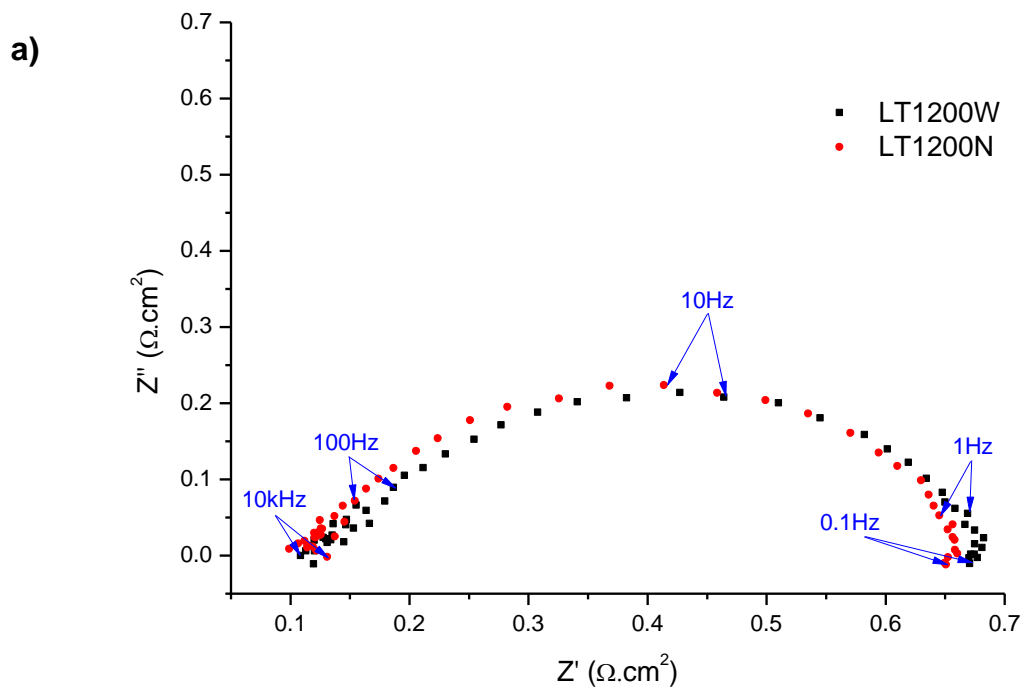


Figure 6.12: EIS for MEAs with GDLs; LT1200W (woven) and LT1200N (non woven) at (a) $0.1 \text{ A} \cdot \text{cm}^{-2}$ current density and (b) $1 \text{ A} \cdot \text{cm}^{-2}$ current density.

Although the results for the woven and non-woven GDLs might appear to contradict what is reported in the literature (woven GDL supposedly having superior performance over non-woven GDLs), when considering the effect of the other variables (thickness and density), the result shows that woven GDLs potentially have a higher performance. Hypothetically, it could be said that if woven and non-woven GDLs that have the same thickness and density are compared, the woven GDL will achieve a better performance and a higher maximum current density. However, one of the main driving factors for producing non-woven GDLs in addition to the reduction of cost and production complexity is to be able to achieve thinner and lower density diffusion layers. Therefore, although such a comparison between the two structures might enhance the understanding on the effect of the structure in the performance, it might be not realistic from a manufacturing point of view.

SGL 10BC and SGL 34BC were used to compare between felt and straight fibres structures. SGL 10BC has a felt structure which is described as a 3D structure due to the way the fibres are distributed within the substrate in comparison to that of the straight fibres. The 2D structure of straight fibres substrate consists of layers of fibre webs assembled to produce the substrate. SGL 10BC has higher thickness and lower porosity than SGL 34BC; however, it has a comparable density and the same MPL (Table 6.7).

Figure 6.13 shows the performance of the MEAs with felt and straight structures. SGL10BC shows a better mass transport ability (higher ability for water transport), and therefore achieving higher maximum current density. The EIS curves in figure 6.14 explain the difference in the performance. The MEA with SGL 34BC has a lower

resistance which explains the slightly higher potential of the MEA at low current density. However; the MEA has a higher mass transport resistance (Figure 6.14 (b)) which explains the appearance of the mass transport losses at lower current density in comparison with SGL 10BC. The good water management ability of SGL 10BC can be attributed to the 3D structure of the substrate that creates and preserves water channels within it for the transport of water out of the cell.

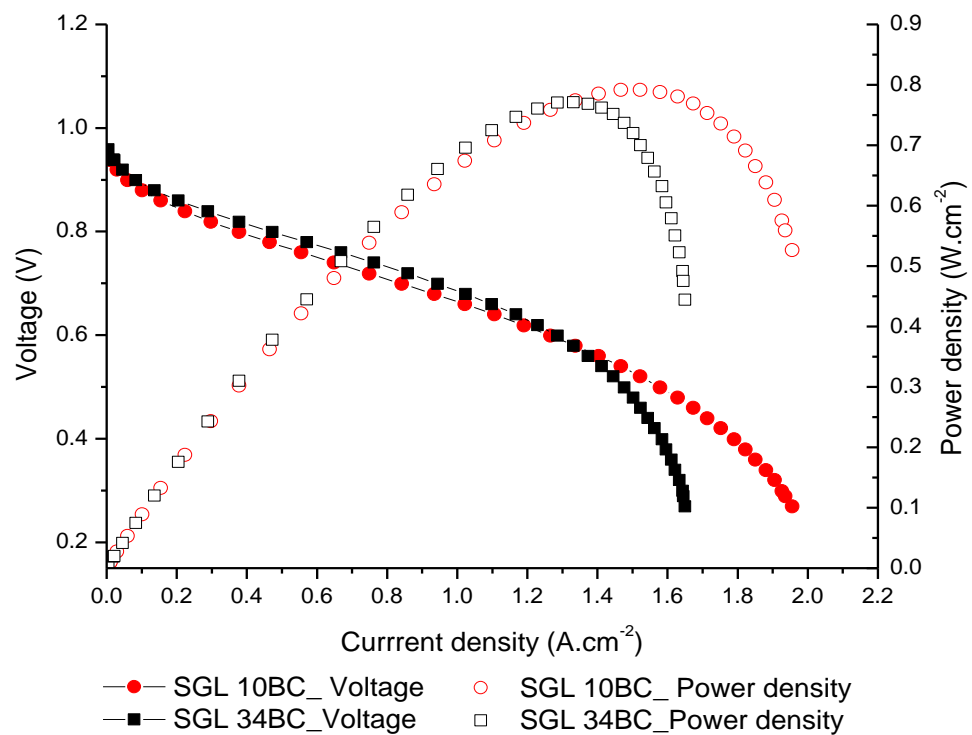


Figure 6.13: PEFC performance for GDLs SGL 10BC (felt fibre structure) and SGL 34BC (straight fibre structure)

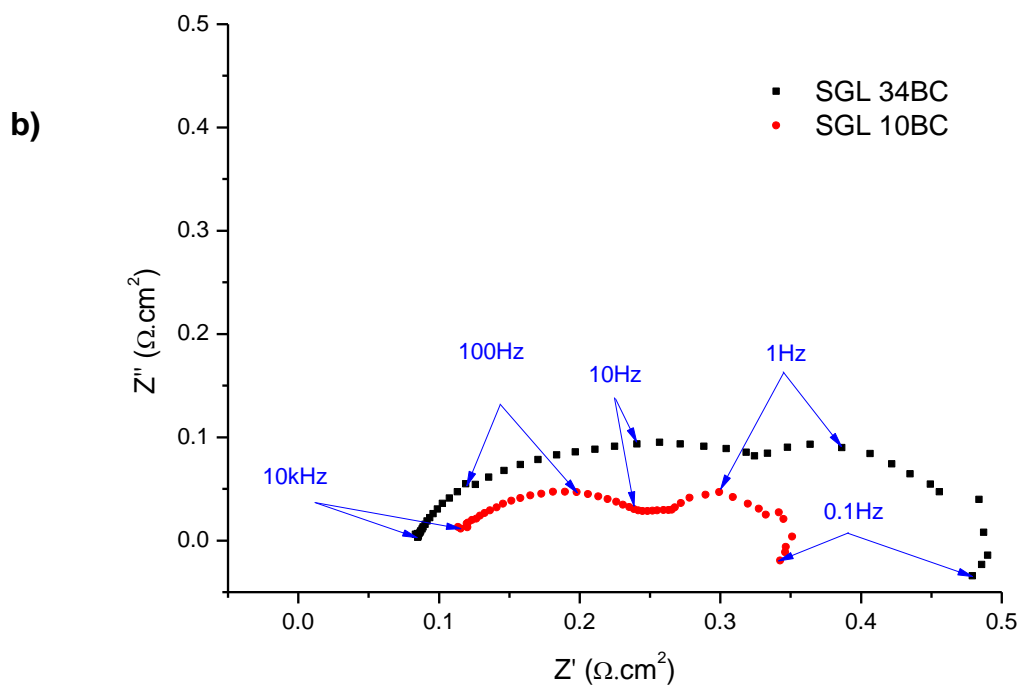
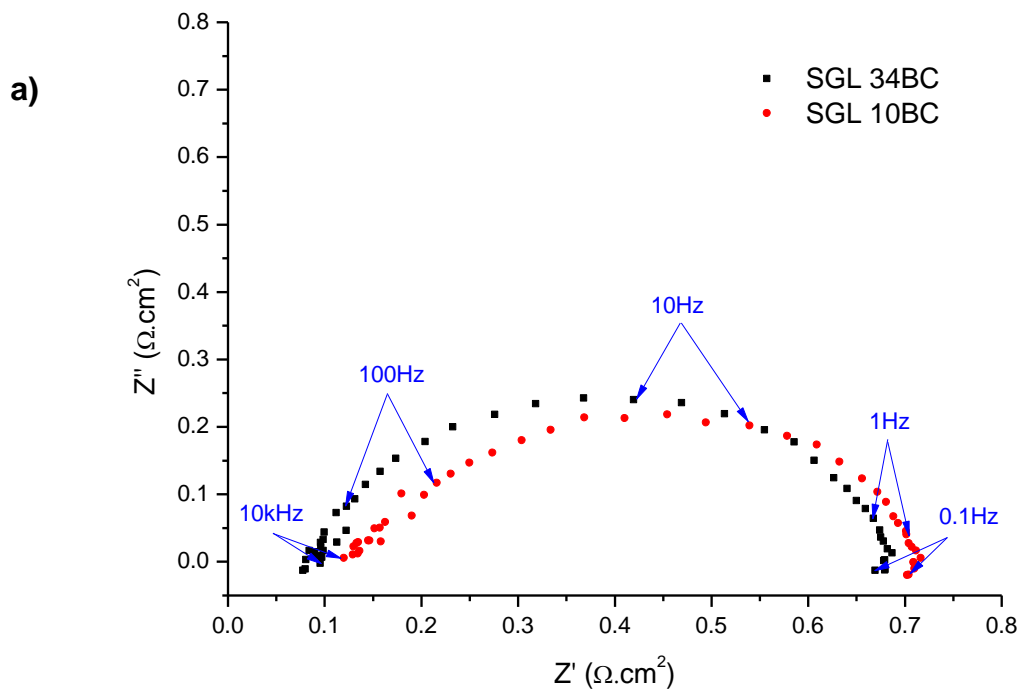


Figure 6.14: EIS for MEAs with GDLs; SGL 10BC (felt fibre structure) and SGL 34BC (straight fibre structure) at (a) 0.1 A.cm^{-2} current density and (b) 1 A.cm^{-2} current density.

Again, when comparing felt and straight fibre non-woven GDLs, the question of the variation in the other properties needs to be addressed. Here, it can be noticed that although the GDL with a felt structure has a higher density and thickness, it still shows a better performance to that of the straight fibres structure. The results suggest that a GDL with a felt structure with lower density and thickness may result in a significant increase in the overall performance of the MEA.

In an overall look at the results of the *in-situ* testing of the GDLs and their effect on the performance of the MEA, it is found that the main change in the MEA performance occurs in the mass transport region of the polarisation curve. The effect of the change in the electrical resistance of the GDL is low and the MEAs of the various GDL types appear to have comparable ohmic resistance. This unapparent effect of the electrical resistance in the MEA can be explained by the low electrical resistance of the GDL (after compression optimization) in comparison to the resistance of membrane that dominates the total MEA resistance. However, the difference in the mass transport region between the MEAs is very clear and pronounced and that is reflected in the performance of the cell. GDLs with better mass transport ability achieve better performance and higher maximum current density. The mass transport ability of the GDL is dependent on the thickness, density and structure of the GDL substrate.

The results suggest that the MEA performance can be enhanced by using a GDL with lower thickness and bulk density. The effect of the structure requires further research to study the effect of thickness and porosity in the felt fibre structure and the woven GDLs. However, from the obtained results, it can be suggested that the felt

structure enhances the performance at high current density and allows achieving higher maximum current density.

6.3 CONCLUSIONS

A selected range of commercial GDL materials were tested as cathode diffusion media in PEFC. The effect of the GDL properties on PEFC performance was studied at optimum clamping pressure for maximum power and current density. The study shows that GDL properties significantly affect the mass transport properties of the MEA. However, the study of the direct effect of GDL properties on the performance is rather complex due to the many interrelated properties.

In the study, it was shown that the MEA performance decreases with an increase in the GDL thickness due to the increase in the mass transport losses, however, the ohmic losses appear to be unaffected. Also, GDL bulk density and porosity have an effect on the performance. GDLs with lower bulk density achieve higher performance and maximum current density. The substrate fibre structure has an effect on the pore structure within the GDL and is strongly interrelated to the other properties of the GDL. The felt 3D structure is found to preserve the pore structure within the substrate, and therefore maintain good water transport ability and achieve relatively high current density.

It is important to remember that the tests presented here are all done under a fully humidified environment and steady state operation. The change in the operating conditions and the load cycle would change the response of the GDL and the overall

performance; hence the performance of these GDLs needs to be studied under these conditions.

CHAPTER SEVEN

SUMMARY

CHAPTER 7: SUMMARY

7.1 CONCLUSIONS

This study has contributed to achieving a better understanding of the effect of various Gas Diffusion Layer (GDL) parameters on the performance of polymer electrolyte fuel cells (PEFCs), as well as optimising the *in-situ* performance in the MEA for a wide range of commercial GDL materials.

Commercially available GDL materials from the main suppliers were characterised *ex-situ* to obtain consistent and comparable data to understand the differences between the various samples. Characterisation was conducted using already developed material property testing facilities. The results show a clear interconnection between the different GDL properties and highlights the similarities and differences between the examined samples.

GDL samples were also characterised *in-situ* as the cathode diffusion layer in an MEA under controlled operating conditions and fully humidified anode and cathode reactants stream. These conditions were selected to examine the transport capacity of the GDL samples under an extreme water transport demand.

Recognising the significant effect of compression on the GDL performance, an optimisation study has been conducted to examine the effect compression on the GDL performance and the effect of thickness, density and structure on the optimum compression ratio for maximum MEA power density. The deformation to the GDL structure with compression has also been examined. The effect of compression ratio on the samples was examined in terms of MEA performance and impedance change.

The optimised *in-situ* performance of GDLs was studied in sets of samples to understand the effect of the various parameters on the performance. The effect of thickness, density, PTFE loading, MPL application and structure were studied. The aim was to identify the significant parameters affecting the MEA performance. The study shows that the mass transport ability of the GDL, which is influenced by its thickness, density, structure, and hydrophobicity, has the highest effect on the optimised MEA performance. The change in the electrical conductivity after optimisation of the different samples has relatively an insignificant effect.

As a result of the conducted research the following conclusions can be made:

- Optimization of GDL properties and clamping pressure within the MEA is essential for achieving high performing PEFC. The GDL mainly affect the mass transport properties of the MEA; after clamping pressure optimization, the GDL contribution to ohmic losses becomes negligible in comparison to that of the membrane, however, the mass transport properties of the GDL becomes the limiting factor for reaching high current densities and performance.
- The mass transport ability of an MEA is related to the water management properties of the GDL including its ability to retain water ensuring sufficient humidification of the membrane, and transporting any excess water away from the catalyst layer while maintaining enough open porous structure for the transport of reactants to the catalyst active sites. This study shows that the most significant properties of the GDL to achieve optimum water management are the presence of an MPL, low bulk porosity of the GDL substrate, and

minimum GDL thickness. The GDL wetting property (hydrophobicity/hydrophilicity) is believed to have a significant effect on water management; however, a more accurate method for measuring this property at the pore structure level is required to quantitatively identify its effect on water management.

- From among the GDLs discussed, SGL 10BC shows the highest performance and maximum current of all. This can be attributed to the felt structure that seems to enhance the water management properties of the GDL.
- The results reported in this study suggest that a double layer GDL with a felt substrate structure of low bulk density and reduced thickness, and with an MPL of fine pores can significantly enhance PEFC performance to achieve higher power and current densities.

7.2 FUTURE WORK

In terms of further work on GDL materials, it is proposed that through a closely collaborative effort between the various institutions working on GDL development, to set a characterisation and testing standard. This will assist the exchange and accumulation of knowledge. Moreover, novel methods of measuring some GDL properties are required, namely, wetting properties, effective porosity under compression and tortuosity.

The performance of the GDL in various PEFC operating conditions, namely, temperatures, humidity and pressure is required. Currently, research is being conducted at the University of Birmingham to explore GDL performance under higher operating temperatures and lower reactants relative humidity. It is believed that the

GDL properties required to achieve optimum performance at these conditions will be different to what was found in this study.

Further work is also required to produce a selection procedure of GDL samples for the various applications. This can be done through testing GDLs *in-situ* under simulated operating conditions for the various applications to examine the effect of GDL parameters on the performance. For instance, it is suggested to study the transient response of GDLs for reactants and water transport under dynamic load conditions.

Moreover, more work needs to be done on the design of the GDL substrate. The results from this study indicate that a felt substrate with low bulk density, an optimised low thickness, and an MPL with small carbon particles would result in a significant enhancement in the performance. This was not possible in this study due to the complexity of substrate fabrication and optimisation.

- [1] Bodansky D. The History of the Global Climate Change Regime. international relations Glob. Clim. Chang., 2001.
- [2] Energy information administration. Annual Energy Outlook 2013. 2013.
- [3] Grove WR. XXIV. On voltaic series and the combination of gases by platinum. Philos Mag Ser 3 1839;14:127–30.
- [4] Larminie J, Dicks A. Fuel Cell Systems Explained. 2nd Editio. John Wiley & sons, Inc.; 2003.
- [5] Smithsonian National Museum of American History. No Title 2013:1–50.
- [6] Mehta V, Cooper JS. Review and analysis of PEM fuel cell design and manufacturing. J Power Sources 2003;114:32–53.
- [7] Feser JP, Prasad AK, Advani SG. Experimental characterization of in-plane permeability of gas diffusion layers. J Power Sources 2006;162:1226–31.
- [8] Tamayol A, Bahrami M. Water permeation through gas diffusion layers of proton exchange membrane fuel cells. J Power Sources 2011;196:6356–61.
- [9] Williams M V, Begg E, Bonville L, Kunz HR, Fenton JM. Characterization of Gas Diffusion Layers for PEMFC. J Electrochem Soc 2004;151:A1173–A1180.
- [10] Litster S, Sinton D, Djilali N. Ex situ visualization of liquid water transport in PEM fuel cell gas diffusion layers. J Power Sources 2006;154:95–105.
- [11] Lu Z, Kandlikar SG, Rath C, Grimm M, Domigan W, White a. D, et al. Water management studies in PEM fuel cells, Part II: Ex situ investigation of flow maldistribution, pressure drop and two-phase flow pattern in gas channels. Int J Hydrogen Energy 2009;34:3445–56.
- [12] Zamel N, Litovsky E, Shakhshir S, Li X, Kleiman J. Measurement of in-plane thermal conductivity of carbon paper diffusion media in the temperature range of -20°C to $+120^{\circ}\text{C}$. Appl Energy 2011;88:3042–50.
- [13] Yang F, Pitchumani R. Measurement and Prediction of Electrical Contact Resistance Between Gas Diffusion Layers and Bipolar Plate for Applications to PEM Fuel Cells 2004;1:2–9.
- [14] Lim C, Wang CY. Effects of hydrophobic polymer content in GDL on power performance of a PEM fuel cell. Electrochim Acta 2004;49:4149–56.
- [15] Park G-G, Sohn Y-J, Yang T-H, Yoon Y-G, Lee W-Y, Kim C-S. Effect of PTFE contents in the gas diffusion media on the performance of PEMFC. J Power Sources 2004;131:182–7.

- [16] Park S, Lee J-W, Popov BN. Effect of carbon loading in microporous layer on PEM fuel cell performance. *J Power Sources* 2006;163:357–63.
- [17] Park S, Lee J-W, Popov BN. Effect of PTFE content in microporous layer on water management in PEM fuel cells. *J Power Sources* 2008;177:457–63.
- [18] Kundu S, Karan K, Fowler M, Simon LC, Peppley B, Halliop E. Influence of micro-porous layer and operating conditions on the fluoride release rate and degradation of PEMFC membrane electrode assemblies. *J Power Sources* 2008;179:693–9.
- [19] Millington B, Du S, Pollet BG. The effect of materials on proton exchange membrane fuel cell electrode performance. *J Power Sources* 2011;196:9013–7.
- [20] Prasanna M, Ha HY, Cho EA, Hong SA, Oh IH. Influence of cathode gas diffusion media on the performance of the PEMFCs. *J Power Sources* 2004;131:147–54.
- [21] Lin J-H, Chen W-H, Su S-H, Su Y-J, Ko T-H. Washing Experiment of the Gas Diffusion Layer in a Proton-Exchange Membrane Fuel Cell. *Energy & Fuels* 2008;22:2533–8.
- [22] Lee C, Mérida W. Gas diffusion layer durability under steady-state and freezing conditions. *J Power Sources* 2007;164:141–53.
- [23] John Felix Kumar R, Radhakrishnan V, Haridoss P. Effect of electrochemical aging on the interaction between gas diffusion layers and the flow field in a proton exchange membrane fuel cell. *Int J Hydrogen Energy* 2011;36:7207–11.
- [24] Paleaz JA, Kandlikar SG. EFFECTS OF FREEZING AND THAWING ON THE STRUCTURES OF POROUS GAS DIFFUSION MEDIA. *Fifth Int. Conf. Nanochannels, Microchannels Minichannels, Puebla, Mexico: 2007.*
- [25] Radhakrishnan V, Haridoss P. Effect of cyclic compression on structure and properties of a Gas Diffusion Layer used in PEM fuel cells. *Int J Hydrogen Energy* 2010;35:11107–18.
- [26] Scholta J, Seidenberger K, Wilhelm F. Gas Diffusion Layer (GDL) degradation in polymer electrolyte fuel cells. *2nd CARISMA Int. Conf. Prog. MEA Mater. from Mediu. high Temp. Polym. electrolytes fuel cells, 2010.*
- [27] Park S, Lee J-W, Popov BN. A review of gas diffusion layer in PEM fuel cells: Materials and designs. *Int J Hydrogen Energy* 2012;37:5850–65.
- [28] Park G-G, Sohn Y-J, Yim S-D, Yang T-H, Yoon Y-G, Lee W-Y, et al. Adoption of nano-materials for the micro-layer in gas diffusion layers of PEMFCs. *J Power Sources* 2006;163:113–8.

- [29] Zhang F-Y, Advani SG, Prasad AK. Performance of a metallic gas diffusion layer for PEM fuel cells. *J Power Sources* 2008;176:293–8.
- [30] Yu EH, Scott K. Direct methanol alkaline fuel cell with catalysed metal mesh anodes. *Electrochem Commun* 2004;6:361–5.
- [31] Chen R, Zhao TS. A novel electrode architecture for passive direct methanol fuel cells. *Electrochem Commun* 2007;9:718–24.
- [32] Yang C-C, Chiu S-J, Lin C-T. Electrochemical performance of an air-breathing direct methanol fuel cell using poly(vinyl alcohol)/hydroxyapatite composite polymer membrane. *J Power Sources* 2008;177:40–9.
- [33] Shao Z-G, Lin W-F, Zhu F, Christensen P a., Zhang H, Yi B. A tubular direct methanol fuel cell with Ti mesh anode. *J Power Sources* 2006;160:1003–8.
- [34] Hottinen T, Mikkola M, Mennola T, Lund P. Titanium sinter as gas diffusion backing in PEMFC. *J Power Sources* 2003;118:183–8.
- [35] Tang Y, Zhou W, Pan M, Chen H, Liu W, Yu H. Porous copper fiber sintered felts: An innovative catalyst support of methanol steam reformer for hydrogen production. *Int J Hydrogen Energy* 2008;33:2950–6.
- [36] Zhou W, Tang Y, Pan M, Wei X, Chen H, Xiang J. A performance study of methanol steam reforming microreactor with porous copper fiber sintered felt as catalyst support for fuel cells. *Int J Hydrogen Energy* 2009;34:9745–53.
- [37] Oedegaard a, Hebling C, Schmitz a, Møller-Holst S, Tunold R. Influence of diffusion layer properties on low temperature DMFC. *J Power Sources* 2004;127:187–96.
- [38] Yi P, Peng L, Lai X, Li M, Ni J. Investigation of sintered stainless steel fiber felt as gas diffusion layer in proton exchange membrane fuel cells. *Int J Hydrogen Energy* 2012;37:11334–44.
- [39] Hamilton PJ, Pollet BG. Polymer Electrolyte Membrane Fuel Cell (PEMFC) Flow Field Plate: Design, Materials and Characterisation. *Fuel Cells* 2010;10:489–509.
- [40] Antunes R a., Oliveira MCL, Ett G, Ett V. Corrosion of metal bipolar plates for PEM fuel cells: A review. *Int J Hydrogen Energy* 2010;35:3632–47.
- [41] Pozio a., Silva RF, De Francesco M, Giorgi L. Nafion degradation in PEFCs from end plate iron contamination. *Electrochim Acta* 2003;48:1543–9.
- [42] El-kharouf a, Chandan a, Hattenberger M, Pollet BG. Proton exchange membrane fuel cell degradation and testing: review. *J Energy Inst* 2012;85:188–200.

- [43] Antolini E, Passos RR, Ticianelli EA. Effects of the carbon powder characteristics in the cathode gas diffusion layer on the performance of polymer electrolyte fuel cells. *J Power Sources* 2002;109:477–82.
- [44] Weng F-B, Hsu C-Y, Su M-C. Experimental study of micro-porous layers for PEMFC with gradient hydrophobicity under various humidity conditions. *Int J Hydrogen Energy* 2011;36:13708–14.
- [45] Sitanggang R, Mohamad AB, Daud WRW, Kadhum AAH, Iyuke SE. Fabrication of gas diffusion layer based on x–y robotic spraying technique for proton exchange membrane fuel cell application. *Energy Convers Manag* 2009;50:1419–25.
- [46] Xie Z, Jin G, Zhang M, Su Z, Zhang M, Chen J, et al. Improved properties of carbon fiber paper as electrode for fuel cell by coating pyrocarbon via CVD method. *Trans Nonferrous Met Soc China* 2010;20:1412–7.
- [47] Tang Z, Poh CK, Tian Z, Lin J, Ng HY, Chua DHC. In situ grown carbon nanotubes on carbon paper as integrated gas diffusion and catalyst layer for proton exchange membrane fuel cells. *Electrochim Acta* 2011;56:4327–34.
- [48] Du C, Wang B, Cheng X. Hierarchy carbon paper for the gas diffusion layer of proton exchange membrane fuel cells. *J Power Sources* 2009;187:505–8.
- [49] Duan Q, Wang B, Wang J, Wang H, Lu Y. Fabrication of a carbon nanofiber sheet as a micro-porous layer for proton exchange membrane fuel cells. *J Power Sources* 2010;195:8189–93.
- [50] Cindrella L, Kannan AM, Lin JF, Saminathan K, Ho Y, Lin CW, et al. Gas diffusion layer for proton exchange membrane fuel cells--A review. *J Power Sources* 2009;194:146–60.
- [51] Arvay a., Yli-Rantala E, Liu C-H, Peng X-H, Koski P, Cindrella L, et al. Characterization techniques for gas diffusion layers for proton exchange membrane fuel cells – A review. *J Power Sources* 2012;213:317–37.
- [52] Yousfi-Steiner N, Moçotéguy P, Candusso D, Hissel D, Hernandez A, Aslanides A. A review on PEM voltage degradation associated with water management: Impacts, influent factors and characterization. *J Power Sources* 2008;183:260–74.
- [53] Bazylak a. Liquid water visualization in PEM fuel cells: A review. *Int J Hydrogen Energy* 2009;34:3845–57.
- [54] Becker J, Wieser C, Fell S, Steiner K. A multi-scale approach to material modeling of fuel cell diffusion media. *Int J Heat Mass Transf* 2011;54:1360–8.

- [55] Kang K, Ju H. Numerical modeling and analysis of micro-porous layer effects in polymer electrolyte fuel cells. *J Power Sources* 2009;194:763–73.
- [56] Sahraoui M, Kharrat C, Halouani K. Two-dimensional modeling of electrochemical and transport phenomena in the porous structures of a PEMFC. *Int J Hydrogen Energy* 2009;34:3091–103.
- [57] Pasaogullari U, Wang C-Y. Two-phase transport and the role of micro-porous layer in polymer electrolyte fuel cells. *Electrochim Acta* 2004;49:4359–69.
- [58] Ostadi H, Rama P, Liu Y, Chen R, Zhang X, Jiang K. MICRO / NANO TOMOGRAPHY FOR ANALYSIS OF GAS DIFFUSION LAYERS OF MICROFUEL CELLS 2009:1–4.
- [59] Wargo E a., Schulz VP, Çeçen a., Kalidindi SR, Kumbur EC. Resolving macro- and micro-porous layer interaction in polymer electrolyte fuel cells using focused ion beam and X-ray computed tomography. *Electrochim Acta* 2013;87:201–12.
- [60] Pfrang A, Didas S, Tsotridis G. X-ray computed tomography of gas diffusion layers of PEM fuel cells: Segmentation of the microporous layer. *J Power Sources* 2013;235:81–6.
- [61] Fishman JZ, Leung H, Bazylak A. Droplet pinning by PEM fuel cell GDL surfaces. *Int J Hydrogen Energy* 2010;35:9144–50.
- [62] Wang Y, Wang C-Y, Chen KS. Elucidating differences between carbon paper and carbon cloth in polymer electrolyte fuel cells. *Electrochim Acta* 2007;52:3965–75.
- [63] Yoshizawa K, Ikezoe K, Tasaki Y, Kramer D, Lehmann EH, Scherer GG. Analysis of Gas Diffusion Layer and Flow-Field Design in a PEMFC Using Neutron Radiography. *J Electrochem Soc* 2008;155:B223.
- [64] Sengul E, Erkan S, Eroğlu I, Nurcan B. EFFECT OF GAS DIFFUSION LAYER CHARACTERISTICS AND ADDITION OF PORE-FORMING AGENTS ON THE PERFORMANCE OF POLYMER ELECTROLYTE MEMBRANE FUEL CELLS. *Chem Eng Commun* 2009;196:10.
- [65] Atiyeh HK, Karan K, Peppley B, Phoenix A, Halliop E, Pharoah J. Experimental investigation of the role of a microporous layer on the water transport and performance of a PEM fuel cell. *J Power Sources* 2007;170:111–21.
- [66] Chen J, Matsuura T, Hori M. Novel gas diffusion layer with water management function for PEMFC. *J Power Sources* 2004;131:155–61.
- [67] Qi Z, Kaufman A. Improvement of water management by a microporous sublayer for PEM fuel cells. *J Power Sources* 2002;109:38–46.

- [68] Yan W-M, Hsueh C-Y, Soong C-Y, Chen F, Cheng C-H, Mei S-C. Effects of fabrication processes and material parameters of GDL on cell performance of PEM fuel cell. *Int J Hydrogen Energy* 2007;32:4452–8.
- [69] Gostick JT, Ioannidis M a., Fowler MW, Pritzker MD. On the role of the microporous layer in PEMFC operation. *Electrochem Commun* 2009;11:576–9.
- [70] Park S, Popov BN. Effect of hydrophobicity and pore geometry in cathode GDL on PEM fuel cell performance. *Electrochim Acta* 2009;54:3473–9.
- [71] Lin G, Nguyen T Van. Effect of Thickness and Hydrophobic Polymer Content of the Gas Diffusion Layer on Electrode Flooding Level in a PEMFC. *J Electrochem Soc* 2005;152:A1942.
- [72] Wang XL, Zhang HM, Zhang JL, Xu HF, Tian ZQ, Chen J, et al. Micro-porous layer with composite carbon black for PEM fuel cells. *Electrochim Acta* 2006;51:4909–15.
- [73] Yu J, Yoshikawa Y, Matsuura T, Islam MN, Hori M. Preparing Gas-Diffusion Layers of PEMFCs with a Dry Deposition Technique. *Electrochem Solid-State Lett* 2005;8:A152.
- [74] Gallo Stampino P, Omati L, Cristiani C, Dotelli G. Characterisation of Nanocarbon-Based Gas Diffusion Media by Electrochemical Impedance Spectroscopy. *Fuel Cells* 2010;10:270–7.
- [75] Chun JH, Jo DH, Kim SG, Park SH, Lee CH, Kim SH. Improvement of the mechanical durability of micro porous layer in a proton exchange membrane fuel cell by elimination of surface cracks. *Renew Energy* 2012;48:35–41.
- [76] Gallo Stampino P, Cristiani C, Dotelli G, Omati L, Zampori L, Pelosato R, et al. Effect of different substrates, inks composition and rheology on coating deposition of microporous layer (MPL) for PEM-FCs. *Catal Today* 2009;147:S30–S35.
- [77] Pozio a., Cemmi a., Carewska M, Paoletti C, Zaza F. Characterization of Gas Diffusion Electrodes for Polymer Electrolyte Fuel Cells. *J Fuel Cell Sci Technol* 2010;7:041003.
- [78] Park SB, Kim S, Park Y, Oh M-H. Fabrication of GDL microporous layer using PVDF for PEMFCs. *J Phys Conf Ser* 2009;165:012046.
- [79] Kannan a. M, Kanagala P, Veedu V. Development of carbon nanotubes based gas diffusion layers by in situ chemical vapor deposition process for proton exchange membrane fuel cells. *J Power Sources* 2009;192:297–303.

- [80] Wen C-Y, Lin Y-S, Lu C-H. Experimental study of clamping effects on the performances of a single proton exchange membrane fuel cell and a 10-cell stack. *J Power Sources* 2009;192:475–85.
- [81] Xing XQ, Lum KW, Poh HJ, Wu YL. Optimization of assembly clamping pressure on performance of proton-exchange membrane fuel cells. *J Power Sources* 2010;195:62–8.
- [82] Lee W, Ho C-H, Van Zee JW, Murthy M. The effects of compression and gas diffusion layers on the performance of a PEM fuel cell. *J Power Sources* 1999;84:45–51.
- [83] Mason TJ, Millichamp J, Neville TP, El-kharouf A, Pollet BG, Brett DJL. Effect of clamping pressure on ohmic resistance and compression of gas diffusion layers for polymer electrolyte fuel cells. *J Power Sources* 2012;219:52–9.
- [84] Han K, Hong BK, Kim SH, Ahn BK, Lim TW. Influence of anisotropic bending stiffness of gas diffusion layers on the electrochemical performances of polymer electrolyte membrane fuel cells. *Int J Hydrogen Energy* 2010;35:12317–28.
- [85] Kandlikar SG, Lu Z, Lin TY, Cooke D, Daino M. Uneven gas diffusion layer intrusion in gas channel arrays of proton exchange membrane fuel cell and its effects on flow distribution. *J Power Sources* 2009;194:328–37.
- [86] Peng L, Mai J, Hu P, Lai X, Lin Z. Optimum design of the slotted-interdigitated channels flow field for proton exchange membrane fuel cells with consideration of the gas diffusion layer intrusion. *Renew Energy* 2011;36:1413–20.
- [87] Hottinen T, Himanen O, Karvonen S, Nitta I. Inhomogeneous compression of PEMFC gas diffusion layer. *J Power Sources* 2007;171:113–21.
- [88] Escribano S, Blachot J-F, Ethève J, Morin A, Mosdale R. Characterization of PEMFCs gas diffusion layers properties. *J Power Sources* 2006;156:8–13.
- [89] Sadeghi E, Djilali N, Bahrami M. Effective thermal conductivity and thermal contact resistance of gas diffusion layers in proton exchange membrane fuel cells. Part 2: Hysteresis effect under cyclic compressive load. *J Power Sources* 2010;195:8104–9.
- [90] Mason TJ, Millichamp J, Neville TP, El-kharouf A, Pollet BG, Brett DJL. Effect of clamping pressure on ohmic resistance and compression of gas diffusion layers for polymer electrolyte fuel cells. *J Power Sources* 2012;219:52–9.
- [91] Mathur RB, Maheshwari PH, Dharmi TL, Tandon RP. Characteristics of the carbon paper heat-treated to different temperatures and its influence on the performance of PEM fuel cell. *Electrochim Acta* 2007;52:4809–17.

- [92] Kong CS, Kim D, Lee H, Shul Y, Lee T. Influence of pore-size distribution of diffusion layer on mass-transport problems of proton exchange membrane fuel cells 2002;108:185–91.
- [93] Harkness IR, Hussain N, Smith L, Sharman JDB. The use of a novel water porosimeter to predict the water handling behaviour of gas diffusion media used in polymer electrolyte fuel cells. *J Power Sources* 2009;193:122–9.
- [94] Gostick JT, Fowler MW, Ioannidis M a., Pritzker MD, Volkovich YM, Sakars A. Capillary pressure and hydrophilic porosity in gas diffusion layers for polymer electrolyte fuel cells. *J Power Sources* 2006;156:375–87.
- [95] Arvay a., Yli-Rantala E, Liu C-H, Peng X-H, Koski P, Cindrella L, et al. Characterization techniques for gas diffusion layers for proton exchange membrane fuel cells – A review. *J Power Sources* 2012;213:317–37.
- [96] Chu H-S, Yeh C, Chen F. Effects of porosity change of gas diffuser on performance of proton exchange membrane fuel cell. *J Power Sources* 2003;123:1–9.
- [97] Jeng KT, Lee SF, Tsai GF, Wang CH. Oxygen mass transfer in PEM fuel cell gas diffusion layers. *J Power Sources* 2004;138:41–50.
- [98] Hiramitsu Y, Kobayashi K, Hori M. Gas diffusion layer design focusing on the structure of the contact face with catalyst layer against water flooding in polymer electrolyte fuel cell. *J Power Sources* 2010;195:7559–67.
- [99] Feser JP, Prasad AK, Advani SG. On the relative influence of convection in serpentine flow fields of PEM fuel cells. *J Power Sources* 2006;161:404–12.
- [100] Gostick JT, Fowler MW, Pritzker MD, Ioannidis MA, Behra LM. In-plane and through-plane gas permeability of carbon fiber electrode backing layers. *J Power Sources* 2006;162:228–38.
- [101] Ismail MS, Borman D, Damjanovic T, Ingham DB, Pourkashanian M. On the through-plane permeability of microporous layer-coated gas diffusion layers used in proton exchange membrane fuel cells. *Int J Hydrogen Energy* 2011;36:10392–402.
- [102] Taira H, Liu H. In-situ measurements of GDL effective permeability and under-land cross-flow in a PEM fuel cell. *Int J Hydrogen Energy* 2012;37:13725–30.
- [103] Hussaini IS, Wang CY. Measurement of relative permeability of fuel cell diffusion media. *J Power Sources* 2010;195:3830–40.
- [104] Ismail MS, Damjanovic T, Ingham DB, Pourkashanian M, Westwood a. Effect of polytetrafluoroethylene-treatment and microporous layer-coating on the

electrical conductivity of gas diffusion layers used in proton exchange membrane fuel cells. *J Power Sources* 2010;195:2700–8.

- [105] Ahmed DH, Sung HJ, Bae J. Effect of GDL permeability on water and thermal management in PEMFCs--II. Clamping force. *Int J Hydrogen Energy* 2008;33:3786–800.
- [106] Ismail MS, Damjanovic T, Ingham DB, Ma L, Pourkashanian M. Effect of polytetrafluoroethylene-treatment and microporous layer-coating on the in-plane permeability of gas diffusion layers used in proton exchange membrane fuel cells. *J Power Sources* 2010;195:6619–28.
- [107] Shah a. a., Luo KH, Ralph TR, Walsh FC. Recent trends and developments in polymer electrolyte membrane fuel cell modelling. *Electrochim Acta* 2011;56:3731–57.
- [108] Akhtar N, Qureshi A, Scholta J, Hartnig C, Messerschmidt M, Lehnert W. Investigation of water droplet kinetics and optimization of channel geometry for PEM fuel cell cathodes. *Int J Hydrogen Energy* 2009;34:3104–11.
- [109] Berning T, Djilali N. A 3D, Multiphase, Multicomponent Model of the Cathode and Anode of a PEM Fuel Cell. *J Electrochem Soc* 2003;150:A1589.
- [110] Niu X-D, Munekata T, Hyodo S-A, Suga K. An investigation of water-gas transport processes in the gas-diffusion-layer of a PEM fuel cell by a multiphase multiple-relaxation-time lattice Boltzmann model. *J Power Sources* 2007;172:542–52.
- [111] Wang E-D, Shi P-F, Du C-Y. Treatment and characterization of gas diffusion layers by sucrose carbonization for PEMFC applications. *Electrochem Commun* 2008;10:555–8.
- [112] Wang Y, Al Shakhshir S, Li X. Development and impact of sandwich wettability structure for gas distribution media on PEM fuel cell performance. *Appl Energy* n.d.;In Press, .
- [113] Gurau V, Bluemle MJ, De Castro ES, Tsou Y-M, Mann JA, Zawodzinski T a. Characterization of transport properties in gas diffusion layers for proton exchange membrane fuel cells. *J Power Sources* 2006;160:1156–62.
- [114] Cheung P, Fairweather JD, Schwartz DT. Characterization of internal wetting in polymer electrolyte membrane gas diffusion layers. *J Power Sources* 2009;187:487–92.
- [115] Benziger J, Nehlsen J, Blackwell D, Brennan T, Itescu J. Water flow in the gas diffusion layer of PEM fuel cells. *J Memb Sci* 2005;261:98–106.

- [116] Park S, Popov BN. Effect of cathode GDL characteristics on mass transport in PEM fuel cells. *Fuel* 2009;88:2068–73.
- [117] Tsai J-C, Lin C-K. Effect of PTFE content in gas diffusion layer based on Nafion®/PTFE membrane for low humidity proton exchange membrane fuel cell. *J Taiwan Inst Chem Eng* 2011;42:945–51.
- [118] Velayutham G, Kaushik J, Rajalakshmi N, Dhathathreyan KS. Effect of PTFE Content in Gas Diffusion Media and Microlayer on the Performance of PEMFC Tested under Ambient Pressure. *Fuel Cells* 2007;7:314–8.
- [119] Sun H, Zhang G, Guo L-J, Liu H. A novel technique for measuring current distributions in PEM fuel cells. *J Power Sources* 2006;158:326–32.
- [120] Noponen M, Mennola T, Mikkola M, Hottinen T, Lund P. Measurement of current distribution in a free-breathing PEMFC. *J Power Sources* 2002;106:304–12.
- [121] Mench MM, Wang CY, Ishikawa M. In Situ Current Distribution Measurements in Polymer Electrolyte Fuel Cells. *J Electrochem Soc* 2003;150:A1052–A1059.
- [122] Meng H, Wang C-Y. Electron Transport in PEFCs. *J Electrochem Soc* 2004;151:A358–A367.
- [123] Zhou T, Liu H. Effects of the electrical resistances of the GDL in a PEM fuel cell. *J Power Sources* 2006;161:444–53.
- [124] Nitta I, Himanen O, Mikkola M. Contact resistance between gas diffusion layer and catalyst layer of PEM fuel cell. *Electrochem Commun* 2008;10:47–51.
- [125] Mishra V, Yang F, Pitchumani R. Measurement and Prediction of Electrical Contact Resistance Between Gas Diffusion Layers and Bipolar Plate for Applications to PEM Fuel Cells. *J Fuel Cell Sci Technol* 2004;1:2.
- [126] Kleemann J, Finsterwalder F, Tillmetz W. Characterisation of mechanical behaviour and coupled electrical properties of polymer electrolyte membrane fuel cell gas diffusion layers. *J Power Sources* 2009;190:92–102.
- [127] Higier A, Liu H. Effects of the difference in electrical resistance under the land and channel in a PEM fuel cell. *Int J Hydrogen Energy* 2011;36:1664–70.
- [128] Nitta I, Himanen O, Mikkola M. Thermal Conductivity and Contact Resistance of Compressed Gas Diffusion Layer of PEM Fuel Cell. *Fuel Cells* 2008;8:111–9.
- [129] Zamel N, Litovsky E, Li X, Kleiman J. Measurement of the through-plane thermal conductivity of carbon paper diffusion media for the temperature range from –50 to +120°C. *Int J Hydrogen Energy* 2011;36:12618–25.

- [130] Hamour M, Garnier JP, Grandidier JC, Ouibrahim a., Martemianov S. Thermal-Conductivity Characterization of Gas Diffusion Layer in Proton Exchange Membrane Fuel Cells and Electrolyzers Under Mechanical Loading. *Int J Thermophys* 2011;32:1025–37.
- [131] Burheim O, Vie PJS, Pharoah JG, Kjelstrup S. Ex situ measurements of through-plane thermal conductivities in a polymer electrolyte fuel cell. *J Power Sources* 2010;195:249–56.
- [132] Karimi G, Li X, Teertstra P. Measurement of through-plane effective thermal conductivity and contact resistance in PEM fuel cell diffusion media. *Electrochim Acta* 2010;55:1619–25.
- [133] Zamel N, Li X, Shen J, Becker J, Wiegmann A. Estimating effective thermal conductivity in carbon paper diffusion media. *Chem Eng Sci* 2010;65:3994–4006.
- [134] Sadeghi E, Bahrami M, Djilali N. Analytic determination of the effective thermal conductivity of PEM fuel cell gas diffusion layers. *J Power Sources* 2008;179:200–8.
- [135] Teertstra P, Karimi G, Li X. Measurement of in-plane effective thermal conductivity in PEM fuel cell diffusion media. *Electrochim Acta* 2011;56:1670–5.
- [136] Dotelli G, Omati L, Gallo Stampino P, Grassini P, Brivio D. Investigation of gas diffusion layer compression by electrochemical impedance spectroscopy on running polymer electrolyte membrane fuel cells. *J Power Sources* 2011;196:8955–66.
- [137] Nitta I, Hottinen T, Himanen O, Mikkola M. Inhomogeneous compression of PEMFC gas diffusion layer. *J Power Sources* 2007;171:26–36.
- [138] Lee W, Ho C-H, Van Zee JW, Murthy M. The effects of compression and gas diffusion layers on the performance of a PEM fuel cell. *J Power Sources* 1999;84:45–51.
- [139] Ous T, Arcoumanis C. Effect of compressive force on the performance of a proton exchange membrane fuel cell 2007;221:1–9.
- [140] Zhou P, Wu CW, Ma GJ. Contact resistance prediction and structure optimization of bipolar plates. *J Power Sources* 2006;159:1115–22.
- [141] Dohle H, Jung R, Kimiaie N, Mergel J, Müller M. Interaction between the diffusion layer and the flow field of polymer electrolyte fuel cells—experiments and simulation studies. *J Power Sources* 2003;124:371–84.

- [142] Chang WR, Hwang JJ, Weng FB, Chan SH. Effect of clamping pressure on the performance of a PEM fuel cell 2007;166:149–54.
- [143] Bazylak a., Sinton D, Liu Z-S, Djilali N. Effect of compression on liquid water transport and microstructure of PEMFC gas diffusion layers. *J Power Sources* 2007;163:784–92.
- [144] Shi Z, Wang X, Guessous L. Effect of Compression on the Water Management of a Proton Exchange Membrane Fuel Cell With Different Gas Diffusion Layers. *J Fuel Cell Sci Technol* 2010;7:021012.
- [145] Yim S-D, Kim B-J, Sohn Y-J, Yoon Y-G, Park G-G, Lee W-Y, et al. The influence of stack clamping pressure on the performance of PEM fuel cell stack. *Curr Appl Phys* 2010;10:S59–S61.
- [146] Ge J, Higier A, Liu H. Effect of gas diffusion layer compression on PEM fuel cell performance. *J Power Sources* 2006;159:922–7.
- [147] Xing XQ, Lum KW, Poh HJ, Wu YL. Geometry optimization for proton-exchange membrane fuel cells with sequential quadratic programming method. *J Power Sources* 2009;186:10–21.
- [148] Ge J, Higier A, Liu H. Effect of gas diffusion layer compression on PEM fuel cell performance. *J Power Sources* 2006;159:922–7.
- [149] Lai Y-H, Rapaport PA, Ji C, Kumar V. Channel intrusion of gas diffusion media and the effect on fuel cell performance. *J Power Sources* 2008;184:120–8.
- [150] Schmittinger W, Vahidi A. A review of the main parameters influencing long-term performance and durability of PEM fuel cells. *J Power Sources* 2008;180:1–14.
- [151] Wu J, Yuan XZ, Martin JJ, Wang H, Zhang J, Shen J, et al. A review of PEM fuel cell durability: Degradation mechanisms and mitigation strategies. *J Power Sources* 2008;184:104–19.
- [152] Maass S, Finsterwalder F, Frank G, Hartmann R, Merten C. Carbon support oxidation in PEM fuel cell cathodes. *J Power Sources* 2008;176:444–51.
- [153] Aoki T, Matsunaga A, Ogami Y, Maekawa A, Mitsushima S, Ota K, et al. The influence of polymer electrolyte fuel cell cathode degradation on the electrode polarization. *J Power Sources* 2010;195:2182–8.
- [154] Chen G, Zhang H, Ma H, Zhong H. Electrochemical durability of gas diffusion layer under simulated proton exchange membrane fuel cell conditions. *Int J Hydrogen Energy* 2009;34:8185–92.

- [155] Hiramitsu Y, Sato H, Kobayashi K, Hori M. Controlling gas diffusion layer oxidation by homogeneous hydrophobic coating for polymer electrolyte fuel cells. *J Power Sources* 2011;196:5453–69.
- [156] Ha T, Cho J, Park J, Min K, Kim H-S, Lee E, et al. Experimental study on carbon corrosion of the gas diffusion layer in polymer electrolyte membrane fuel cells. *Int J Hydrogen Energy* 2011;36:12436–43.
- [157] Bazylak A, Sinton D, Liu Z-S, Djilali N. Effect of compression on liquid water transport and microstructure of PEMFC gas diffusion layers. *J Power Sources* 2007;163:784–92.
- [158] Sadiq Al-Baghdadi M a. R. A CFD study of hygro-thermal stresses distribution in PEM fuel cell during regular cell operation. *Renew Energy* 2009;34:674–82.
- [159] Poornesh KK, Cho CD, Lee GB, Tak YS. Gradation of mechanical properties in gas-diffusion electrode. Part 2: Heterogeneous carbon fiber and damage evolution in cell layers. *J Power Sources* 2010;195:2718–30.
- [160] Wood DL, Xie J, Pacheco SD, Davey JR, Borup RL. Durability issues of the PEMFC GDL and MEA under steady-state and drive-cycle operating conditions. 2004.
- [161] Wu J, Martin JJ, Orfino FP, Wang H, Legzdins C, Yuan X-Z, et al. In situ accelerated degradation of gas diffusion layer in proton exchange membrane fuel cell: Part I: Effect of elevated temperature and flow rate. *J Power Sources* 2010;195:1888–94.
- [162] Guo Q, Qi Z. Effect of freeze-thaw cycles on the properties and performance of membrane-electrode assemblies. *J Power Sources* 2006;160:1269–74.
- [163] Yan Q, Toghiani H, Lee Y-W, Liang K, Causey H. Effect of sub-freezing temperatures on a PEM fuel cell performance, startup and fuel cell components. *J Power Sources* 2006;160:1242–50.
- [164] Lim S-J, Park G-G, Park J-S, Sohn Y-J, Yim S-D, Yang T-H, et al. Investigation of freeze/thaw durability in polymer electrolyte fuel cells. *Int J Hydrogen Energy* 2010;35:13111–7.
- [165] Lee Y, Kim B, Kim Y, Li X. Effects of a microporous layer on the performance degradation of proton exchange membrane fuel cells through repetitive freezing. *J Power Sources* 2011;196:1940–7.
- [166] Hou J, Yu H, Zhang S, Sun S, Wang H, Yi B, et al. Analysis of PEMFC freeze degradation at -20 °C after gas purging. *J Power Sources* 2006;162:513–20.

- [167] Zhang S, Yuan X, Wang H, Merida W, Zhu H, Shen J, et al. A review of accelerated stress tests of MEA durability in PEM fuel cells. *Int J Hydrogen Energy* 2009;34:388–404.
- [168] Corp MI. *An Introduction To The Physical Characterization of Materials by Mercury Intrusion Porosimetry with Emphasis On Reduction And Presentation of Experimental Data* Paul A . Webb Norcross , Georgia 2001.
- [169] Wilde PM, Mändle M, Murata M, Berg N. Structural and Physical Properties of GDL and GDL/BPP Combinations and their Influence on PEMFC Performance. *Fuel Cells* 2004;4:180–4.
- [170] Yuan X, Sun JC, Wang H, Zhang J. AC impedance diagnosis of a 500W PEM fuel cell stack. *J Power Sources* 2006;161:929–37.
- [171] Yuan X, Wang H, Colinsun J, Zhang J. AC impedance technique in PEM fuel cell diagnosis—A review. *Int J Hydrogen Energy* 2007;32:4365–80.
- [172] Dotelli G, Omati L, Stampino PG, Grassini P, Brivio D. Investigation of Gas Diffusion Layers compression by Electrochemical Impedance Spectroscopy (EIS) on a running PEM-FC. *J Power Sources* n.d.;In Press, .
- [173] Kulikovskiy a. a. A Model for Local Impedance of the Cathode Side of PEM Fuel Cell with Segmented Electrodes. *J Electrochem Soc* 2012;159:F294–F300.
- [174] Mérida W, Harrington D a., Le Canut JM, McLean G. Characterisation of proton exchange membrane fuel cell (PEMFC) failures via electrochemical impedance spectroscopy. *J Power Sources* 2006;161:264–74.
- [175] Tang Y, Zhang J, Song C, Liu H, Zhang J, Wang H, et al. Temperature Dependent Performance and In Situ AC Impedance of High-Temperature PEM Fuel Cells Using the Nafion-112 Membrane. *J Electrochem Soc* 2006;153:A2036.
- [176] Brunetto C, Moschetto A, Tina G. PEM fuel cell testing by electrochemical impedance spectroscopy. *Electr Power Syst Res* 2009;79:17–26.
- [177] Rae PJ, Dattelbaum DM. The properties of poly(tetrafluoroethylene) (PTFE) in compression. *Polymer (Guildf)* 2004;45:7615–25.
- [178] Avasarala B, Haldar P. Effect of surface roughness of composite bipolar plates on the contact resistance of a proton exchange membrane fuel cell. *J Power Sources* 2009;188:225–9.
- [179] Mench MM. *Fuel cell engines*. John Wiley & sons, Inc.; 2008.

- [180] Zhang L, Liu Y, Song H, Wang S, Zhou Y, Hu SJ. Estimation of contact resistance in proton exchange membrane fuel cells. *J Power Sources* 2006;162:1165–71.
- [181] Ismail MS, Damjanovic T, Ingham DB, Pourkashanian M, Westwood A. Effect of polytetrafluoroethylene-treatment and microporous layer-coating on the electrical conductivity of gas diffusion layers used in proton exchange membrane fuel cells 2010;195:2700–8.
- [182] Wee J-H, Lee K-Y, Kim SH. Fabrication methods for low-Pt-loading electrocatalysts in proton exchange membrane fuel cell systems. *J Power Sources* 2007;165:667–77.
- [183] El-kharouf A, Mason TJ, Brett DJL, Pollet BG. Ex-situ characterisation of gas diffusion layers for proton exchange membrane fuel cells. *J Power Sources* 2012;218:393–404.

APPENDICES

APPENDIX A1: GDL MANUFACTURERS DATASHEETS

A1.1 BALLARD GDLs DATASHEET

Refer to the hard copy

A1.2 SIGRACET GDLs DATASHEET

Refer to the hard copy

A1.3 TORAY GDLs DATASHEETS

Refer to the hard copy

A1.4 FREUDENBERG GDLs DATASHEET

Refer to the hard copy

A1.5 ETEK GDLs DATASHEET

Refer to the hard copy

APPENDIX A2: CATHODE ELECTRODE FABRICATION

Membrane electrode assemblies (MEAs) were fabricated for *in-situ* testing of GDL performance. The MEAs were fabricated with an circular active area of 11.34 cm². The ink formulation for electrode fabrication was calculated based on a 0.4 mg.cm⁻² Pt loading using the following equations.

$$Pt_{mass} = 0.4 \times A_{active}$$

$$Pt/C_{mass} = Pt_{mass} \times Pt/C_{wt\%}$$

$$Nafion_{mass} : C_{mass} = 1:1 \rightarrow Nafion_{mass} = C_{mass}$$

$$Nafion_{solvol} = Nafion_{solDensity} \times \frac{Nafion_{mass}}{Nafion_{solcon}}$$

$$Solvent (IPA)_{Vol} \approx 3 \times Nafion_{solvol}$$

The actual loading of Pt on the GDE is calculated using the measured mass of the GDE after catalyst application and drying the GDE, and the GDL before catalyst application.

$$Pt_{actual\ loading} = \frac{(m_{GDE} - m_{GDL})}{(2 + (\frac{Pt/C_{wt\%}}{1 - Pt/C_{wt\%}}))} \times \frac{Pt/C_{wt\%}}{1 - Pt/C_{wt\%}} \times \frac{1}{A_{active}}$$

Table A2.1 lists the GDE samples fabricated, ink formulation and loading applying the above equations. TKK commercial is used with Pt/C_{wt%} = 45.9%, Nafion solvent concentration: 10% and IPA used as a solvent.

date	Cathode			catalyst ink						MEA Area (cm ²)	Catalyst loading (mg.cm ⁻²)
	GDL type	Mass (GDL)	Mass (GDE)	Pt/C type	Pt/C%	Pt/C wt (mg)	Nafion Vol (μL)	Solvent type	Solvent Vol (μL)		
18/6/2012	P50	0.057633	0.0724	TKK	45.9	12.6	66	IPA_water	260_40	11.34	0.387864
18/6/2012	P50T	0.065467	0.082333	TKK	45.9	12.7	66	IPA_water	260_40	11.34	0.443023
18/6/2012	GDS1120	0.0898	0.105367	TKK	45.9	12.7	66	IPA_water	260_40	11.34	0.4088769
19/6/2012	GDS1120	0.1258	0.147767	TKK	45.9	18.6	94	IPA_water	360_40	16	0.4089349
19/6/2012	JM_165	0.166333	0.1669	TKK	45.9	0	66	IPA	114	11.34	
19/6/2012	C2	0.154333	0.168367	TKK	45.9	11.8	66	IPA_water	260_40	11.34	0.3686021
20/6/2012	C4	0.145	0.1595	TKK	45.9	12.3	66	IPA_water	260_40	11.34	0.3808597
20/6/2012	H2315	0.106033	0.1248	TKK	45.9	12.5	66	IPA_water	260_40	11.34	0.4929287
20/6/2012	C6	0.150133	0.164533	TKK	45.9	13	66	IPA_water	260_40	11.34	0.3782331
25/6/2012	C2	0.154367	0.170733	TKK	45.9	12.6	66	IPA_water	260_40	11.34	0.4298899

25/6/2012	C4	0.147067	0.1666	TKK	45.9	12	66	IPA_water	260_40	11.34	0.5130661
25/6/2012	C6	0.158433	0.176667	TKK	45.9	12.9	66	IPA_water	260_40	11.34	0.4789201
25/6/2012	C8	0.1608	0.176167	TKK	45.9	12.2	66	IPA_water	260_40	11.34	0.4036237
25/6/2012	34BC	0.154833	0.173533	TKK	45.9	12.1	66	IPA_water	260_40	11.34	0.4911777
25/6/2012	34DC	0.177633	0.1959	TKK	45.9	12.4	66	IPA_water	260_40	11.34	0.4797956
26/6/2012	LT1200W	0.2183	0.238033	TKK	45.9	12.5	66	IPA_water	260_40	11.34	0.5183194
26/6/2012	35BC	0.115933	0.1343	TKK	45.9	12.2	66	IPA_water	260_40	11.34	0.4824223
26/6/2012	LT1200N	0.085133	0.102833	TKK	45.9	12.3	66	IPA_water	260_40	11.34	0.4649115
26/6/2012	34BC	0.1206	0.1398	TKK	45.9	12.1	66	IPA_water	260_40	11.34	0.5043107
26/6/2012	C2	0.1517	0.167733	TKK	45.9	11.9	66	IPA_water	260_40	11.34	0.4211345
26/6/2012	C4	0.147867	0.166433	TKK	45.9	12.1	66	IPA_water	260_40	11.34	0.4876755
27/6/2012	LT1200N	0.085133	0.104067	TKK	45.9	11.7	66	IPA_water	260_40	11.34	0.4973064
27/6/2012	C6	0.158867	0.177	TKK	45.9	11.8	66	IPA_water	260_40	11.34	0.4762935
27/6/2012	C8	0.1484	0.165233	TKK	45.9	11.7	66	IPA_water	260_40	11.34	0.4421474
28/6/2012	lt1200W	0.222433	0.2407	TKK	45.9	12.2	66	IPA_water	260_40	11.34	0.4797956

28/6/2012	GDS1120	0.1151	0.133033	TKK	45.9	11.5	66	IPA_water	260_40	11.34	0.4710402
28/6/2012	GDS2120	0.089767	0.1068	TKK	45.9	11.6	66	IPA_water	260_40	11.34	0.4474007
2/7/2012	LT 1200N	0.084667	0.101267	TKK	45.9	11.8	66	IPA_water	260_40	11.34	0.4360187
2/7/2012	LT1200W	0.219467	0.239067	TKK	45.9	11.8	66	IPA_water	260_40	11.34	0.5148172
2/7/2012	25BC	0.1048	0.124667	TKK	45.9	11.7	66	IPA_water	260_40	11.34	0.5218215
4/7/2012	24BC	0.120233	0.139567	TKK	45.9	11.7	66	IPA_water	260_40	11.34	0.5078129
4/7/2012	25BC	0.1054	0.126533	TKK	45.9	11.8	66	IPA_water	260_40	11.34	0.555092
4/7/2012	34BC	0.153333	0.171233	TKK	45.9	11.4	66	IPA_water	260_40	11.34	0.4701647
5/7/2012	10BC	0.1709	0.1894	TKK	45.9	12	66	IPA_water	260_40	11.34	0.4859244
5/7/2012	24BC	0.120067	0.1382	TKK	45.9	11.6	66	IPA_water	260_40	11.34	0.4762935
5/7/2012	GDS2120	0.115833	0.135667	TKK	45.9	12.1	66	IPA_water	260_40	11.34	0.520946
5/7/2012	34DC	0.173733	0.190567	TKK	45.9	11.5	66	IPA_water	260_40	11.34	0.4421474
5/7/2012	35BC	0.115067	0.134033	TKK	45.9	11.7	66	IPA_water	260_40	11.34	0.498182
5/7/2012	GDS1120	0.0878	0.102667	TKK	45.9	11.6	66	IPA_water	260_40	11.34	0.3904906
26/7/2012	GDS2120	0.1168	0.135233	TKK	45.9	12.1	66	IPA_water	260_40	11.34	0.4841733

26/7/2012	24BC	0.122	0.140367	TKK	45.9	12.3	66	IPA_water	260_40	11.34	0.4824223
26/7/2012	25BC	0.1055	0.1231	TKK	45.9	11.7	66	IPA_water	260_40	11.34	0.4622848
26/7/2012	35BC	0.117833	0.1341	TKK	45.9	11.8	66	IPA_water	260_40	11.34	0.4272633
26/7/2012	34DC	0.176367	0.193033	TKK	45.9	11.7	66	IPA_water	260_40	11.34	0.4377697
26/7/2012	10BC	0.166667	0.183067	TKK	45.9	11.7	66	IPA_water	260_40	11.34	0.4307654
27/7/2012	10BC	0.161933	0.1798	TKK	45.9	12	66	IPA_water	260_40	11.34	0.4692892
27/7/2012	Toray H-60	0.0949	0.1147	TKK	45.9	11.8	66	IPA_water	260_40	11.34	0.5100705
27/7/2012	Toray H-90	0.1446	0.164067	TKK	45.9	11.9	66	IPA_water	260_40	11.34	0.5013151
31/7/2012	Toray H-120	0.194133	0.212	TKK	45.9	11.6	66	IPA_water	260_40	11.34	0.4692892
31/7/2012	H2315	0.1098	0.1296	TKK	45.9	11.6	66	IPA_water	260_40	11.34	0.5000705
31/7/2012	H2315 I2	0.129567	0.149433	TKK	45.9	11.8	66	IPA_water	260_40	11.34	0.5118215
1/8/2012	P50	0.057833	0.075067	TKK	45.9	11.8	66	IPA_water	260_40	11.34	0.4526539
1/8/2012	P50T	0.064633	0.0817	TKK	45.9	11.2	66	IPA_water	260_40	11.34	0.4482762
1/8/2012	P75	0.0757	0.093867	TKK	45.9	11.7	66	IPA_water	260_40	11.34	0.477169
1/8/2012	P75T	0.0779	0.103867	TKK	45.9	12	66	IPA_water	260_40	11.34	0.6820453

1/8/2012	1071HCB	0.132233	0.1519	TKK	45.9	11.8	66	IPA_water	260_40	11.34	0.5065683
1/8/2012	H-090	0.147267	0.166733	TKK	45.9	11.5	66	IPA_water	260_40	11.34	0.5013151
15/8/2012	Toray H-030	0.05	0.0676	TKK	45.9	11.9	66	IPA_water	260_40	11.34	0.4622848
15/8/2012	10BA	0.102833	0.122833	TKK	45.9	11.4	66	IPA_water	260_40	11.34	0.503237
15/8/2012	24BA	0.0641	0.083733	TKK	45.9	11.9	66	IPA_water	260_40	11.34	0.5056928
15/8/2012	25BA	0.047067	0.066433	TKK	45.9	11.7	66	IPA_water	260_40	11.34	0.5086884
15/8/2012	35BA	0.066067	0.085333	TKK	45.9	11.4	66	IPA_water	260_40	11.34	0.5060618
3/9/2012	TCC 2660	0.091	0.108933	TKK	45.9	11.1	66	IPA_water	260_40	11.34	0.4710402
3/9/2012	TCC 3250	0.109633	0.127967	TKK	45.9	12.1	66	IPA_water	260_40	11.34	0.4815467
03/9/2012	C2	0.153667	0.1567	GG	20	-	66	IPA_water	260_40	11.34	0.0297211
03/9/2012	C2	0.1518	0.177733	GG	20	-	66	IPA_water	260_40	11.34	0.2540989
24/9/2012	H-060	0.095833	0.1127	TKK	45.9	11.5	66	IPA_water	260_40	11.34	0.443023
24/9/2012	H-060	0.095233	0.113767	TKK	45.9	11.3	66	IPA_water	260_40	11.34	0.4868
24/9/2012	H-090	0.143467	0.162333	TKK	45.9	11	66	IPA_water	260_40	11.34	0.4955553
24/9/2012	H-090	0.145867	0.164767	TKK	45.9	11.7	66	IPA_water	260_40	11.34	0.4964309

24/9/2012	H-120	0.185733	0.203833	TKK	45.9	11.6	66	IPA_water	260_40	11.34	0.4754179
-----------	-------	----------	----------	-----	------	------	----	-----------	--------	-------	-----------

24/9/2012	H-120	0.185967	0.206633	TKK	45.9	11.7	66	IPA_water	260_40	11.34	0.5028345
-----------	-------	----------	----------	-----	------	------	----	-----------	--------	-------	-----------

APPENDIX A3: EX-SITU RESULTS- SEM IMAGING

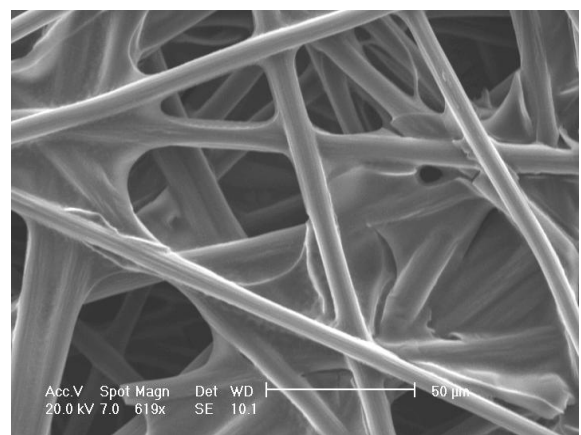
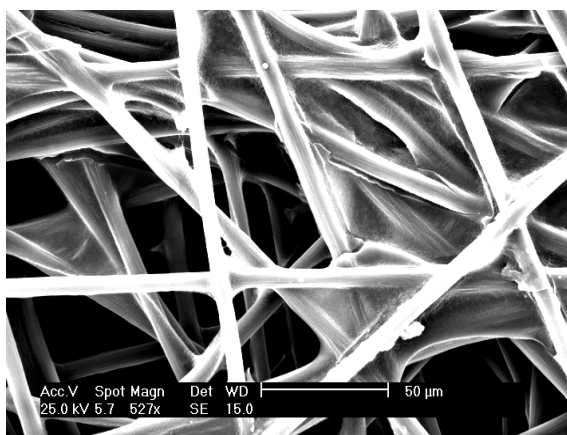
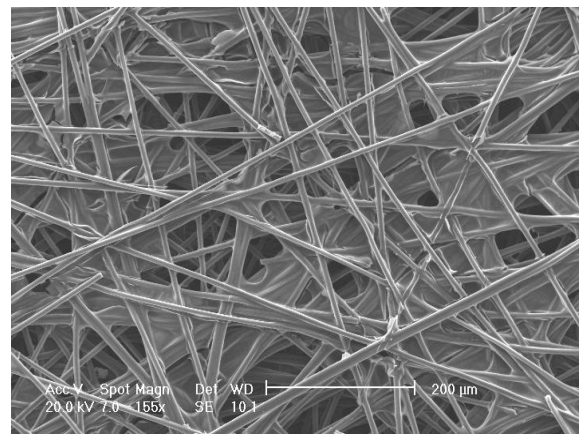
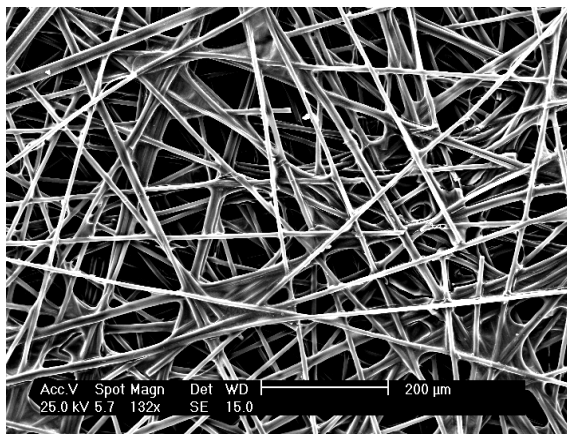
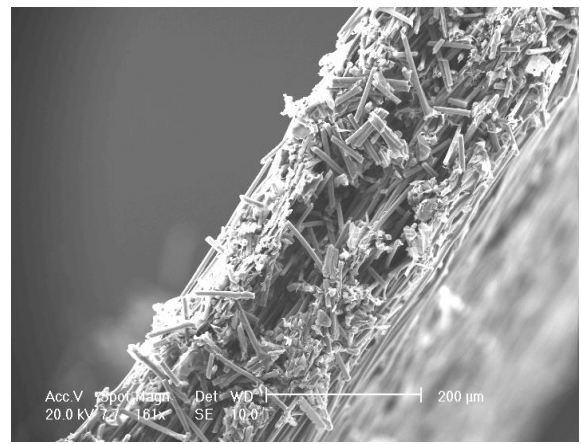
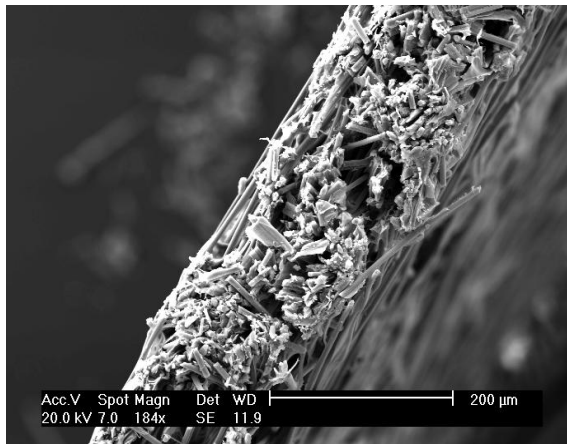


Figure A3.1: Toray H-060

Figure A3.2: Toray H-120

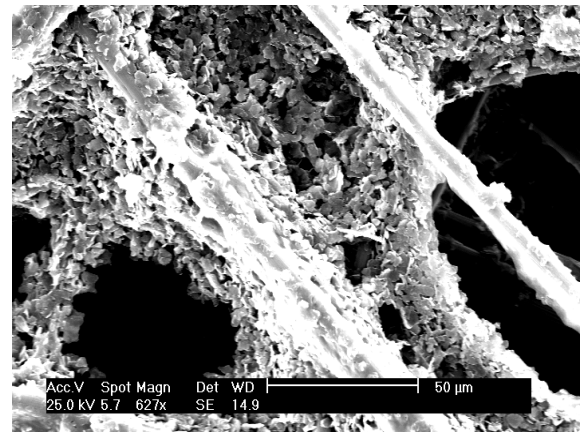
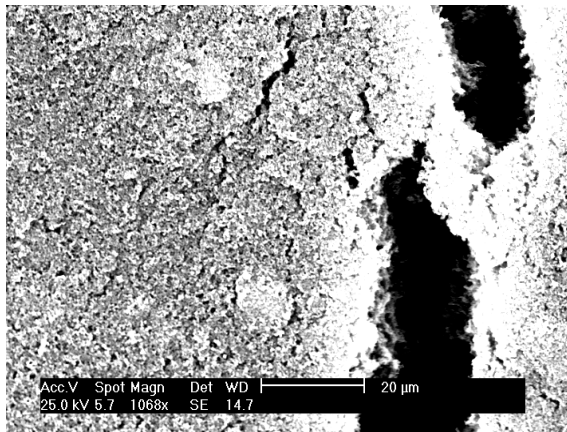
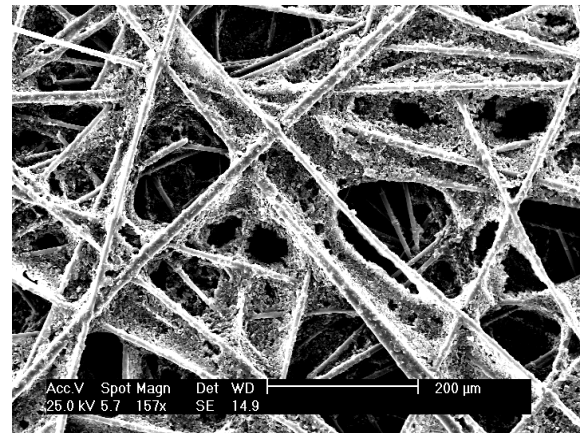
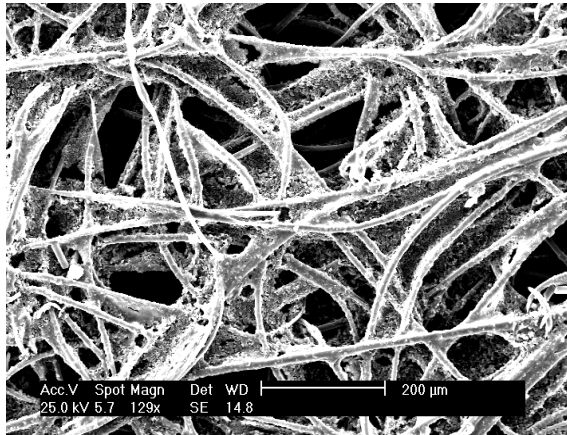
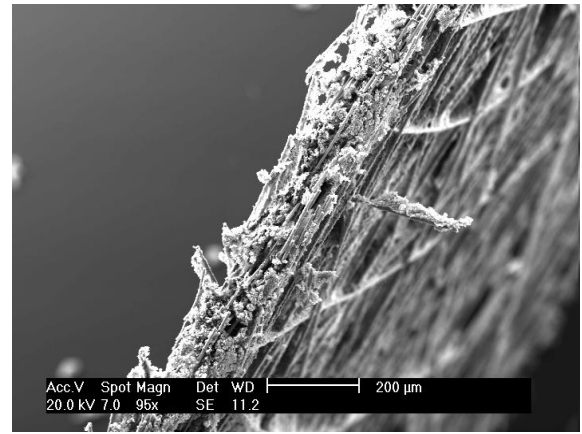
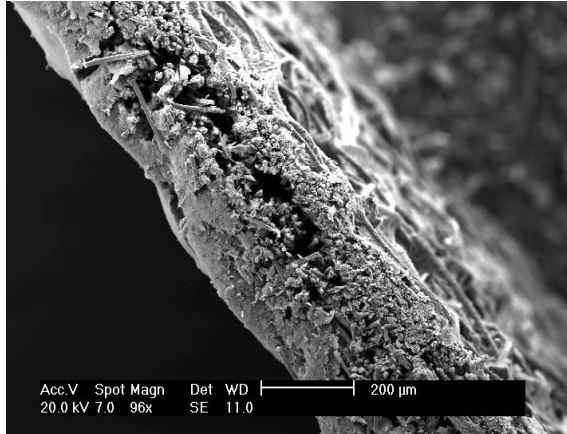


Figure A3.3: SGL 10BC

Figure A3.4: SGL 24BA

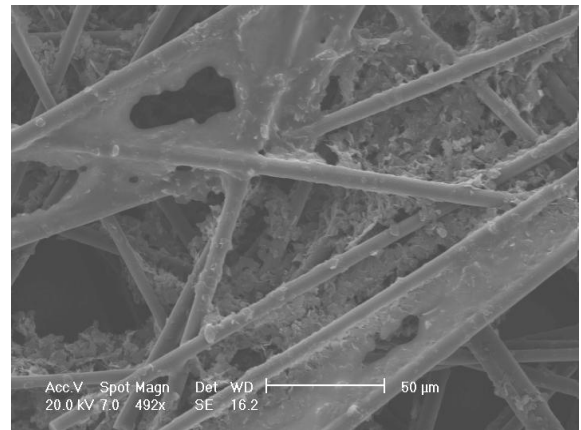
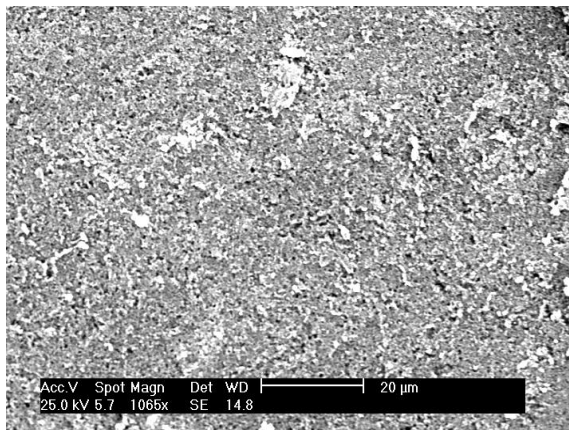
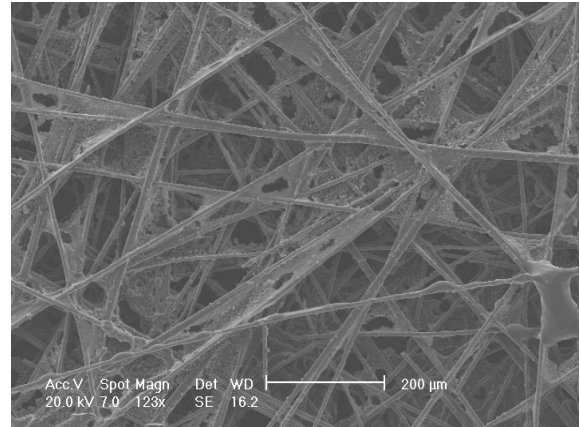
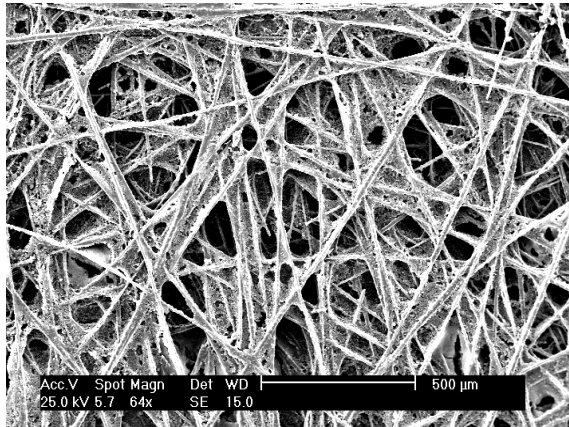
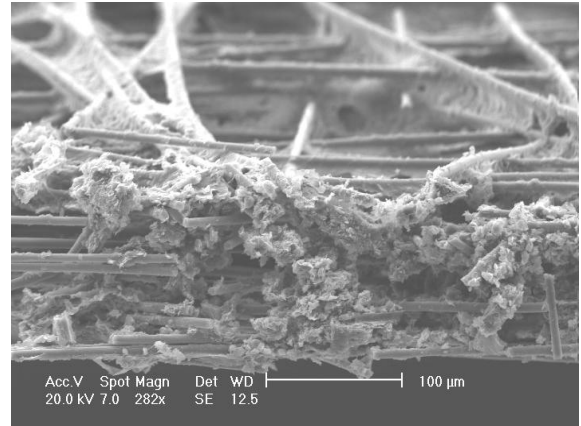
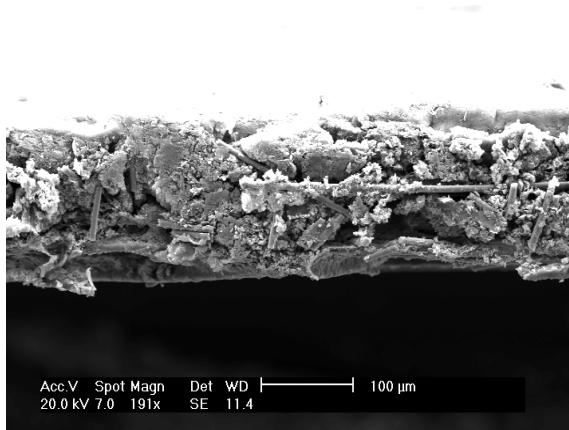


Figure A3.5: SGL 24BC

Figure A3.6: SGL 25BA

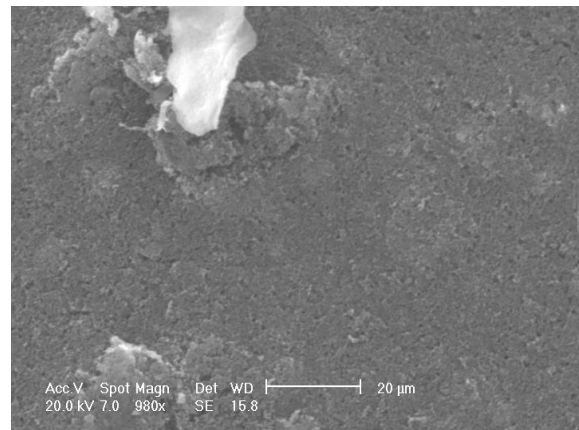
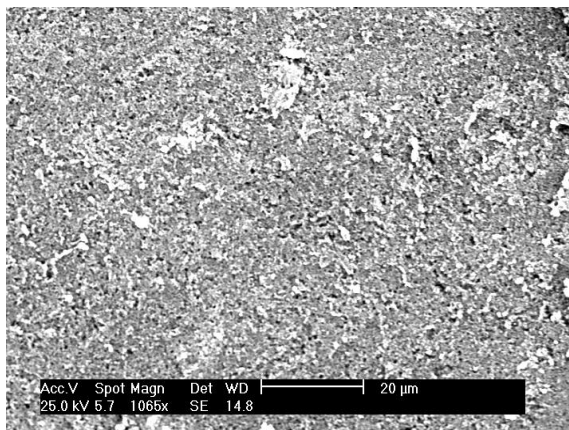
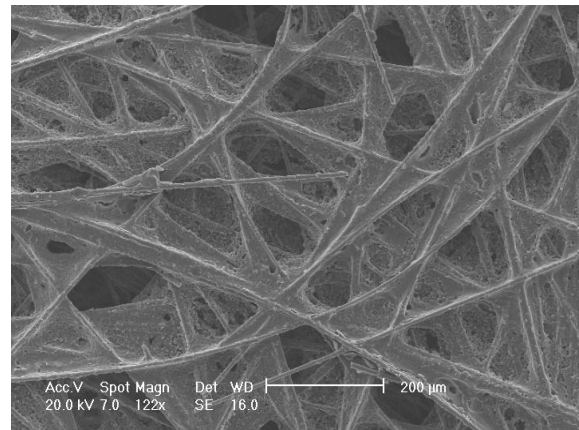
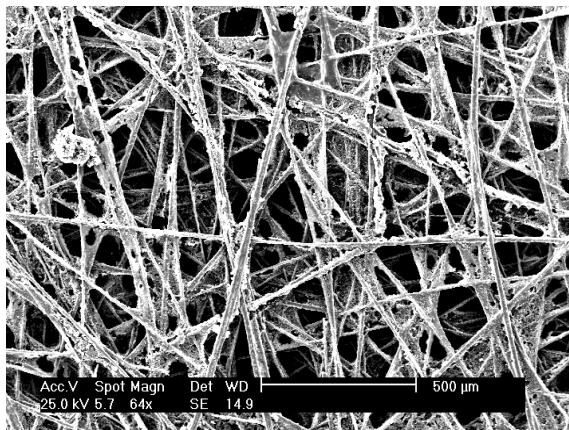
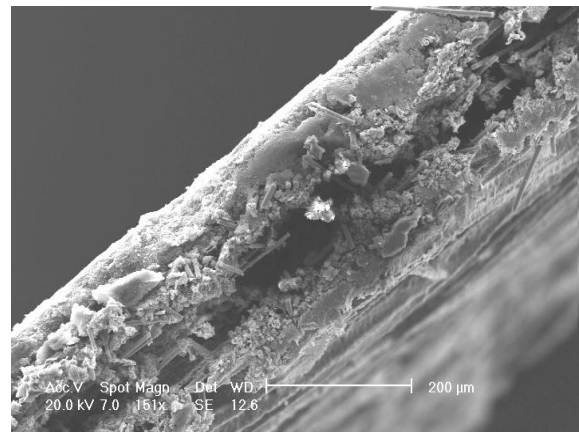
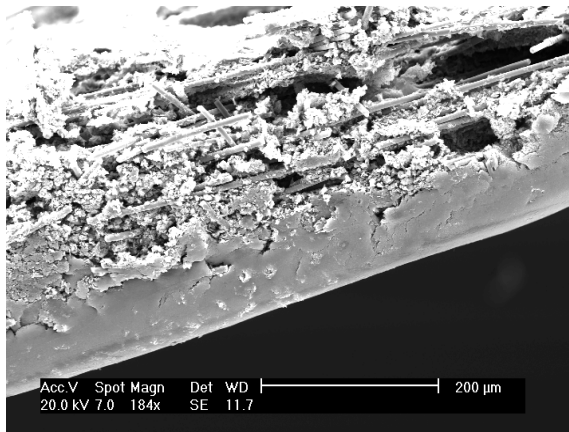


Figure A3.7: SGL 34BC

Figure A3.8: SGL 34DC

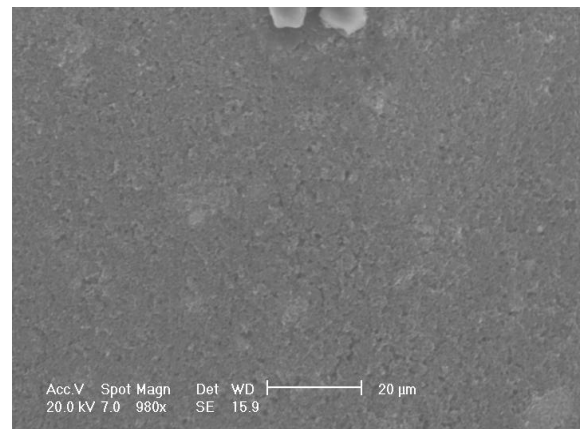
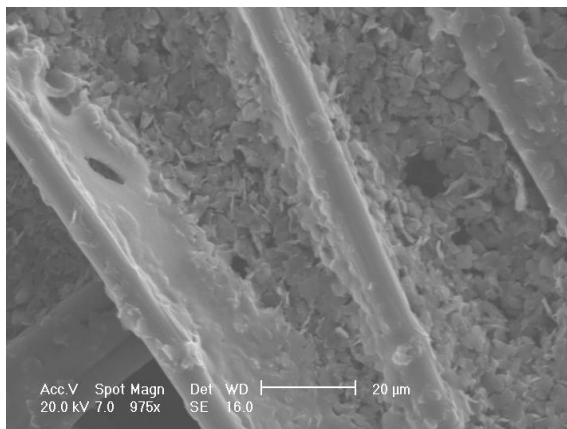
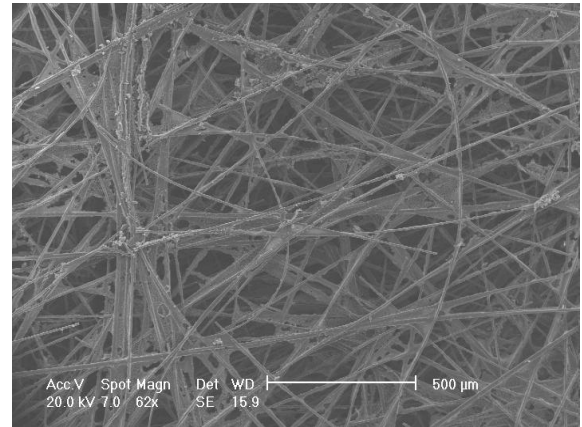
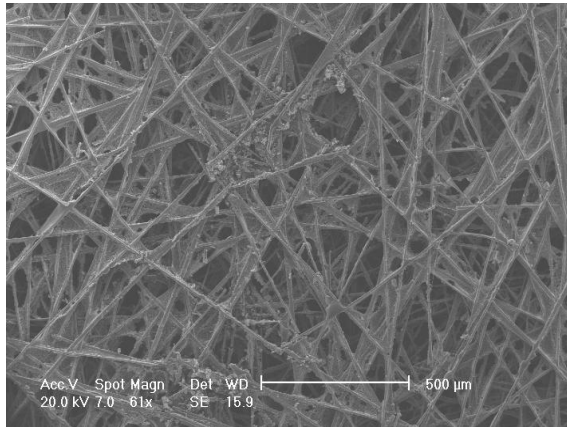
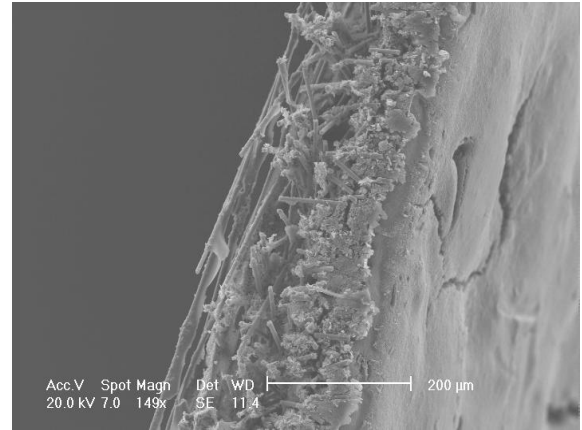
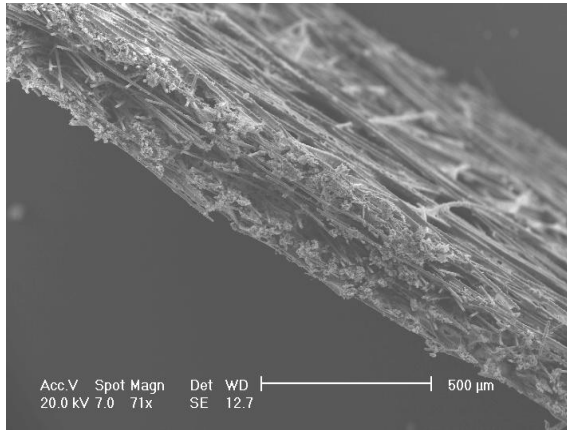


Figure A3.9: SGL 35BA

Figure A3.10: SGL 35BC

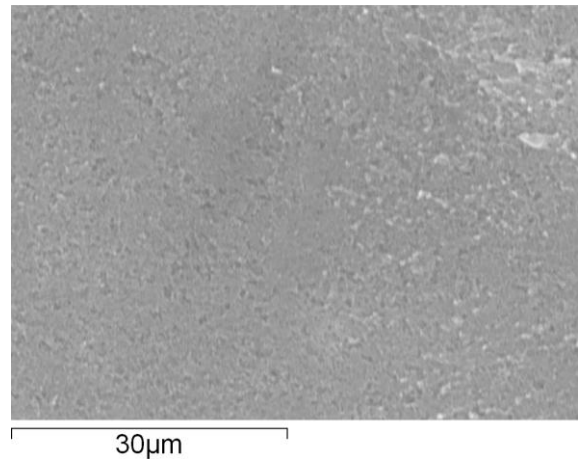
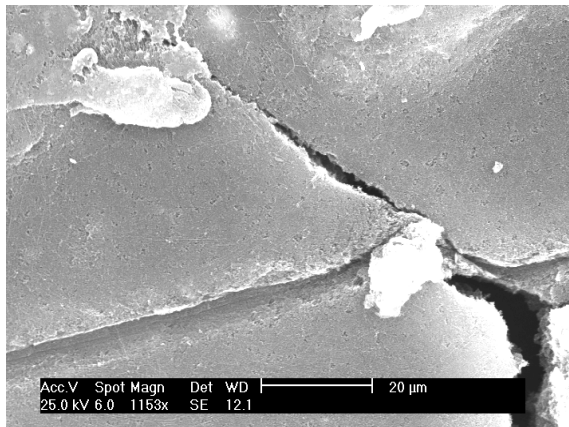
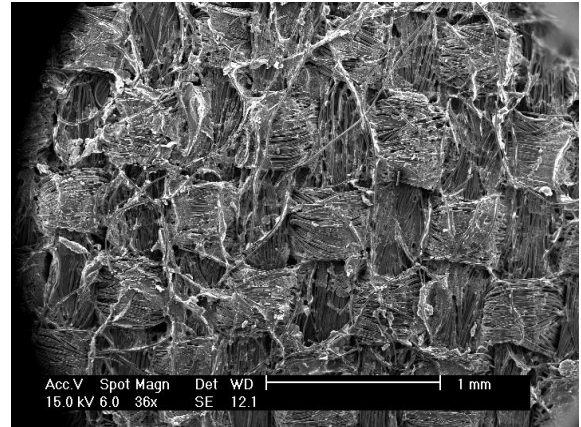
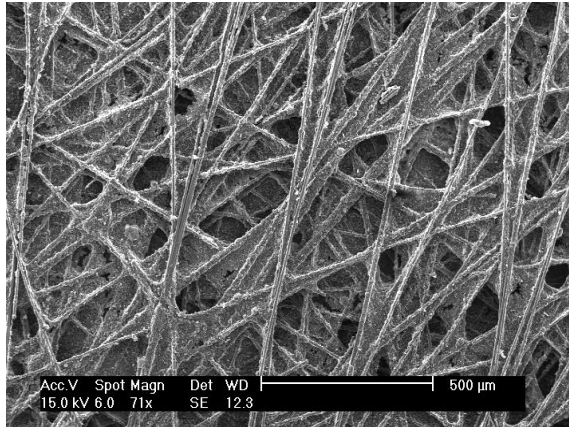
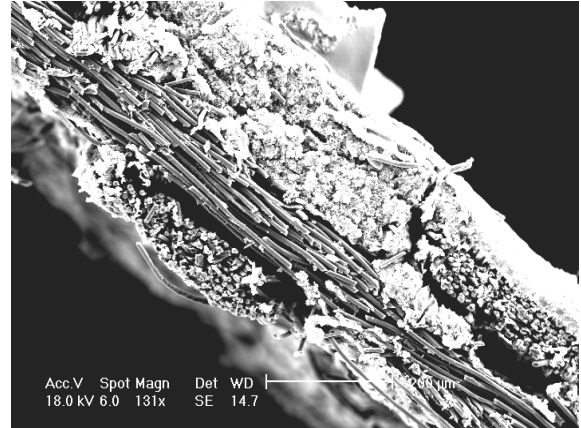
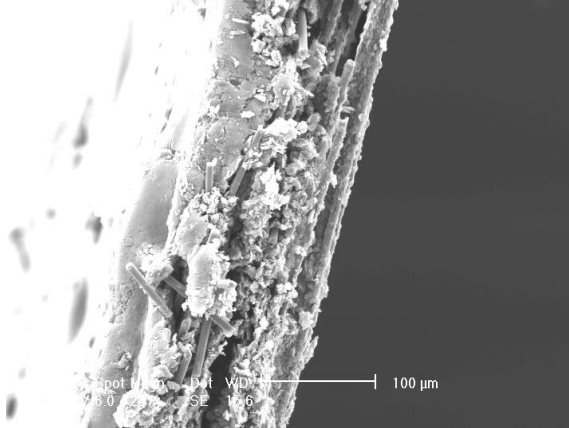


Figure A3.11: LT1200N

Figure A3.12: LT1200W

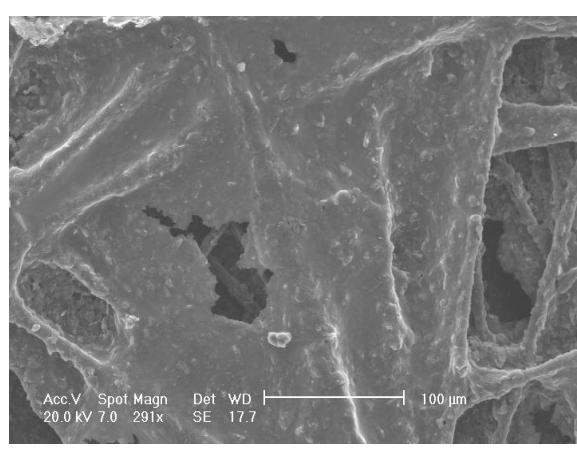
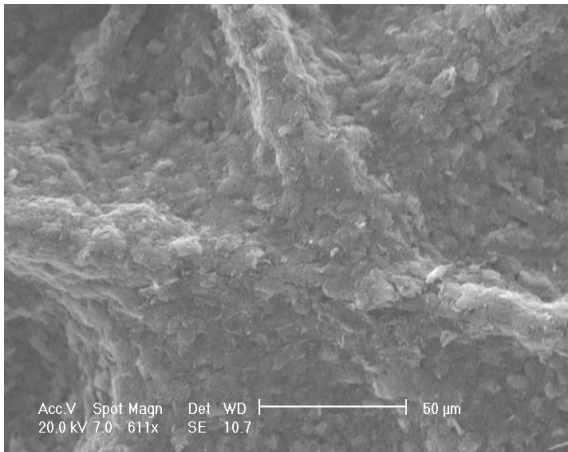
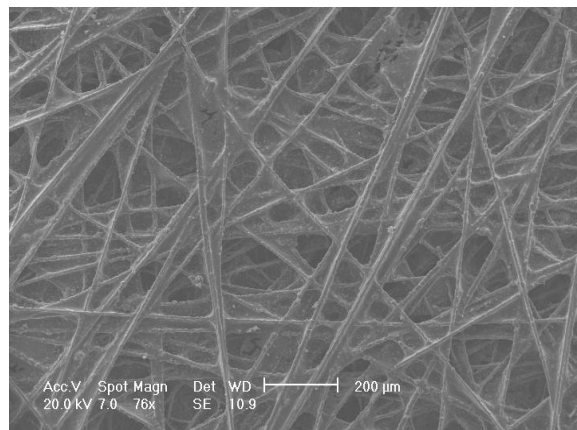
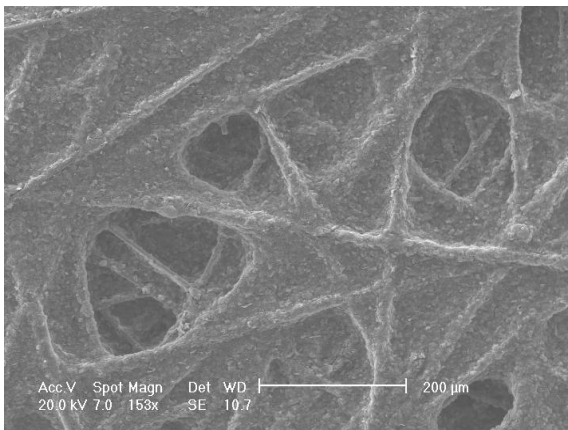
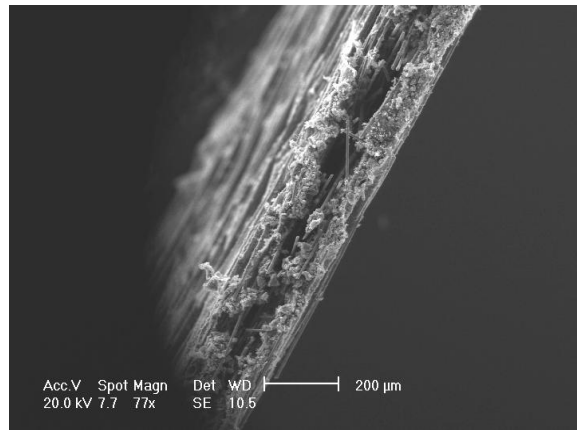
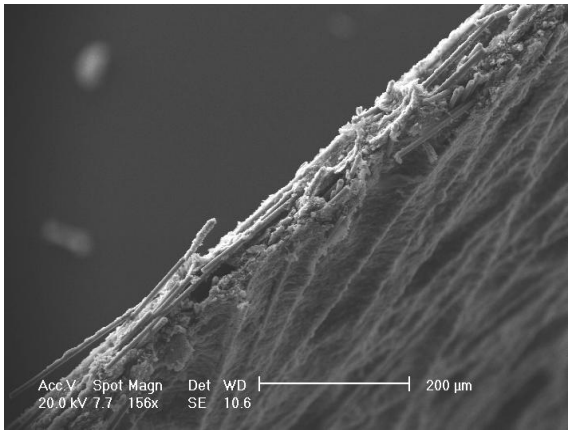


Figure A3.13: P50

Figure A3.14: P50T

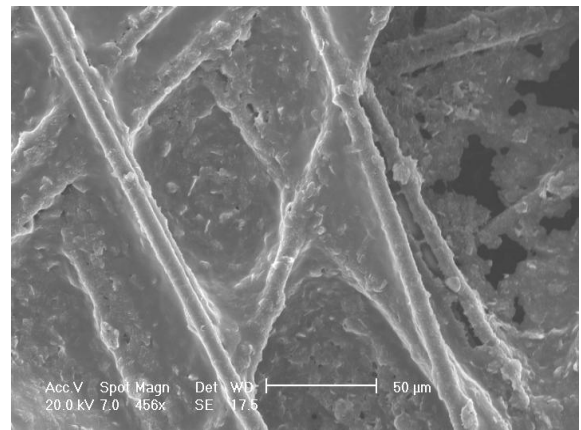
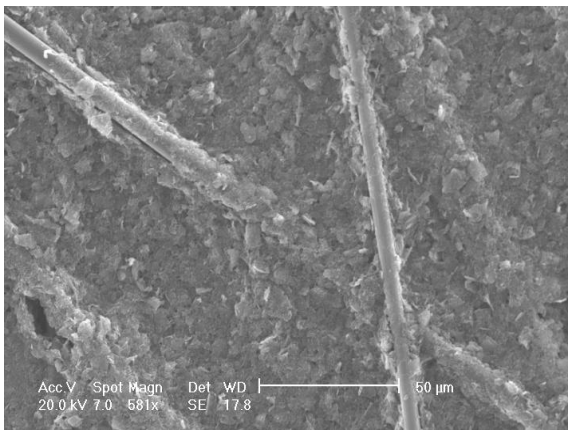
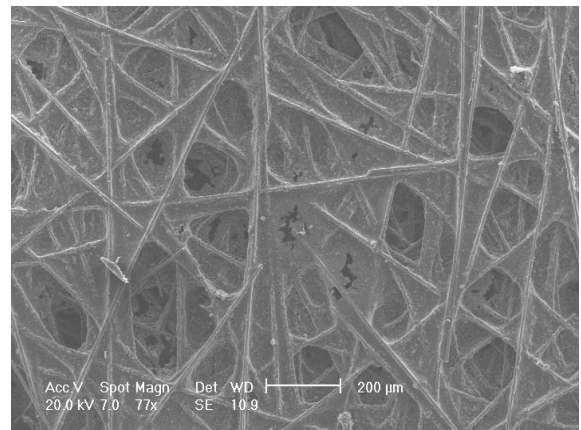
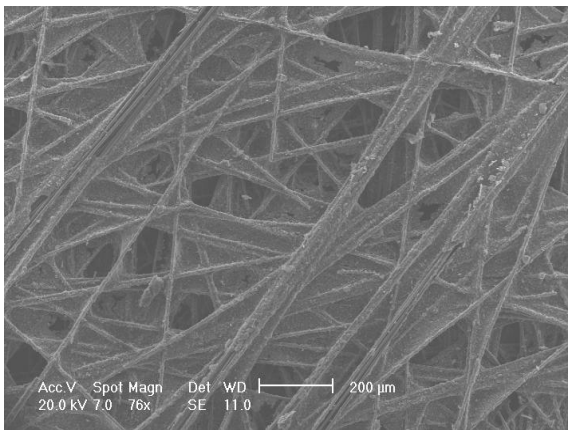
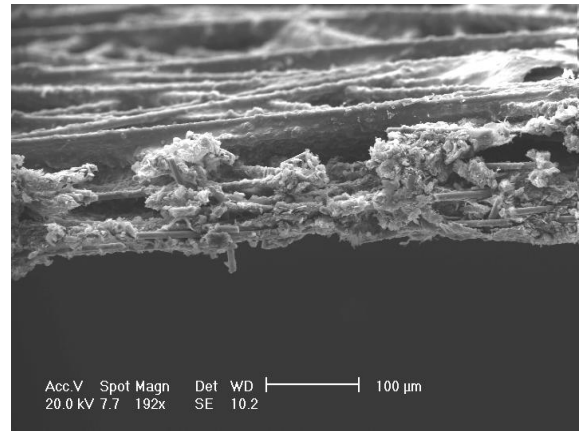
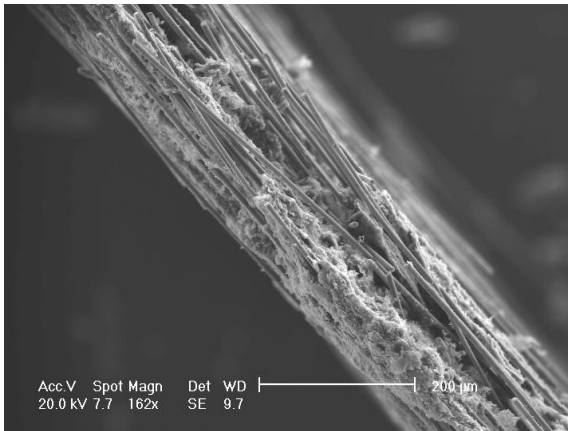


Figure A3.15: P75

Figure A3.16: P75T

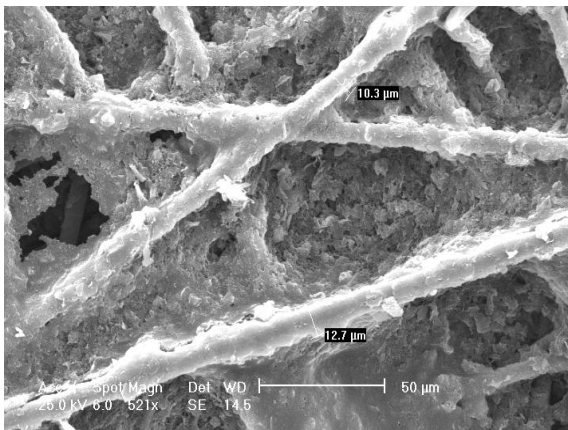
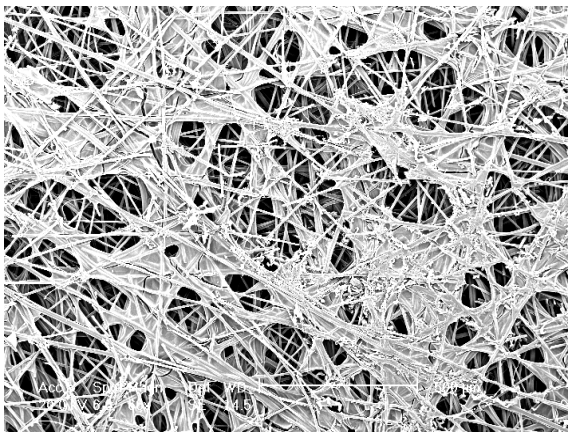
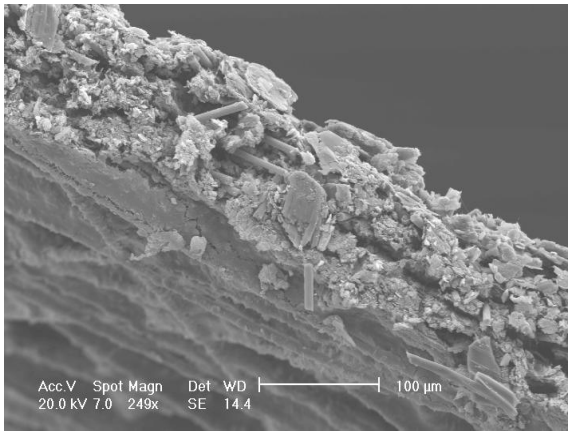
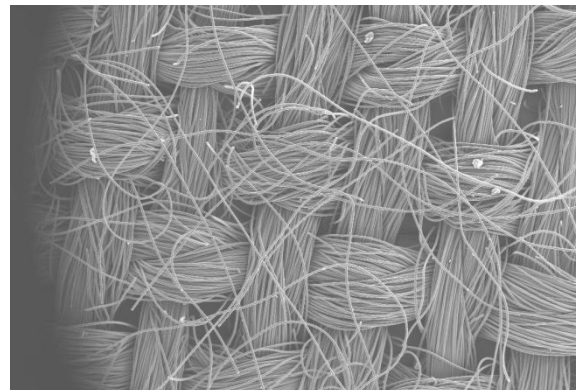
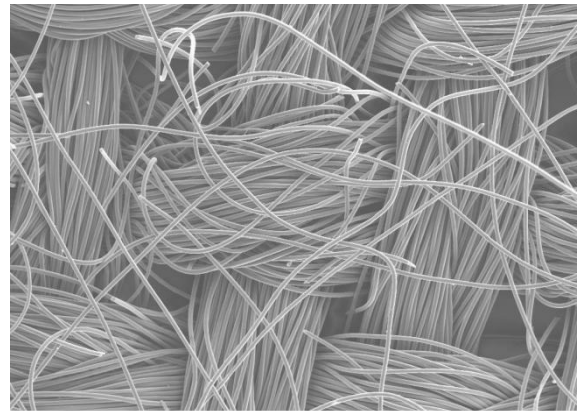


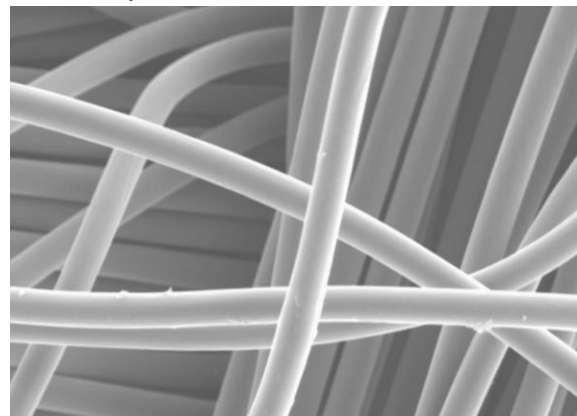
Figure A3.17: GDS 1120



900μm

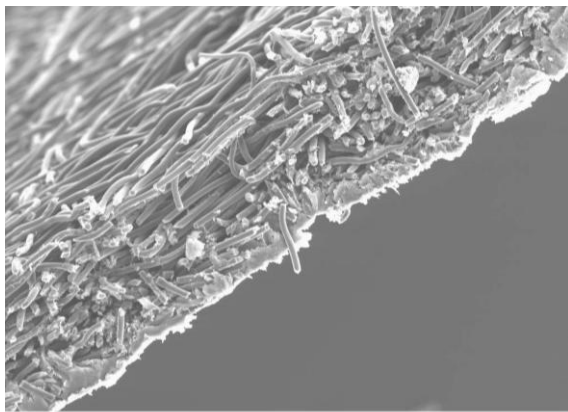


400μm

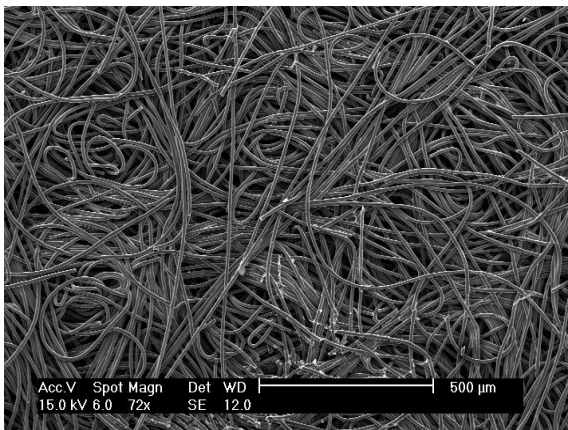


60μm

Figure A3.18: Tenax TCC 2660

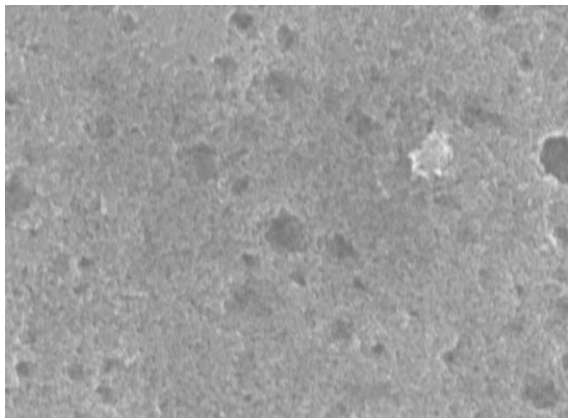


400µm



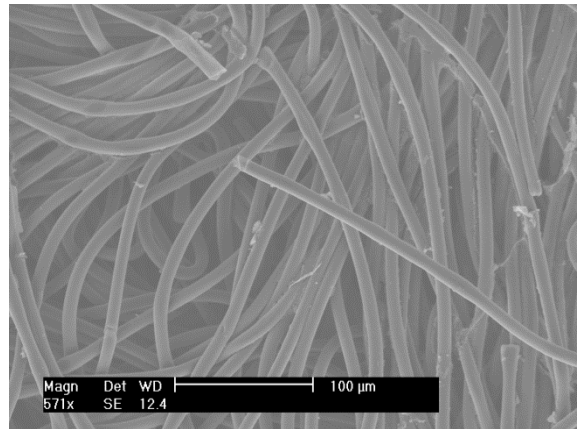
Acc.V Spot Magn Det WD
15.0 kV 6.0 72x SE 12.0

500 µm



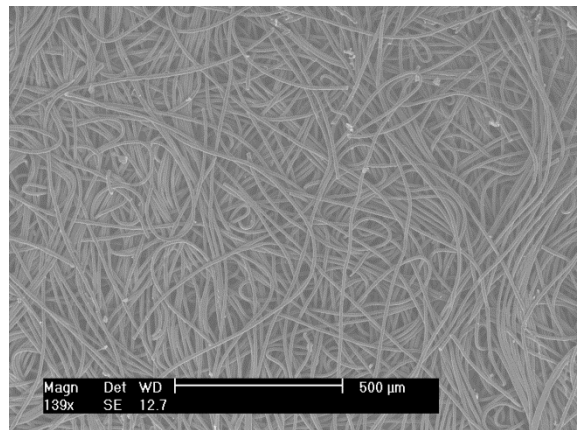
30µm

Figure A3.19: Freudenberg C2



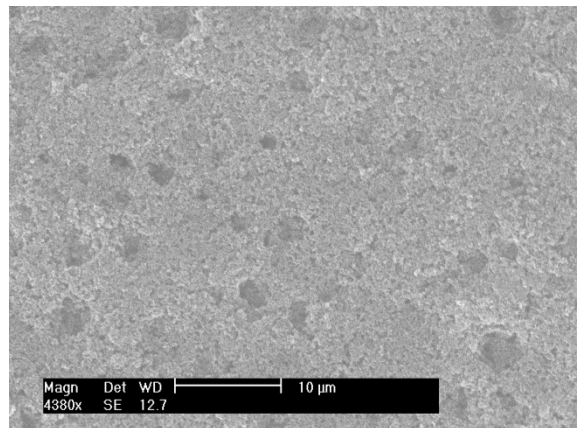
Magn Det WD
571x SE 12.4

100 µm



Magn Det WD
139x SE 12.7

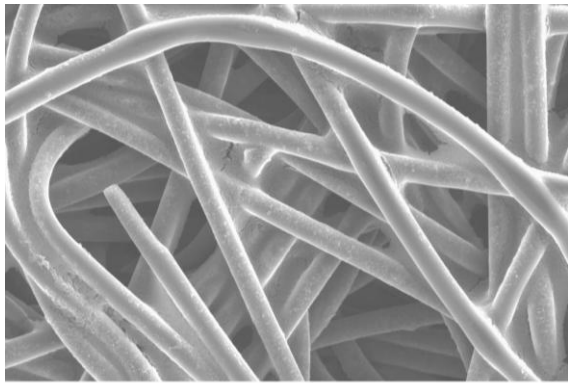
500 µm



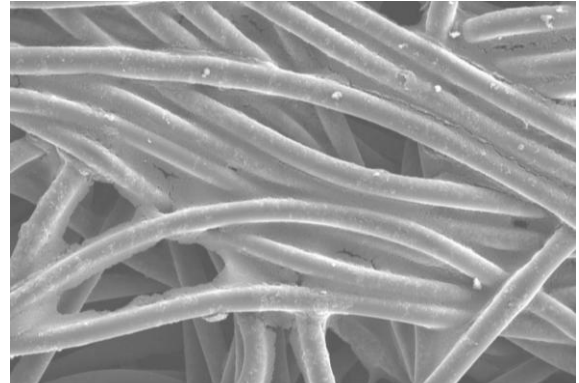
Magn Det WD
4380x SE 12.7

10 µm

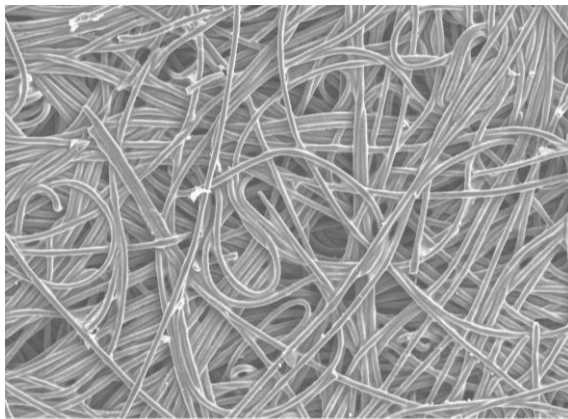
Figure A3.20: Freudenberg C4



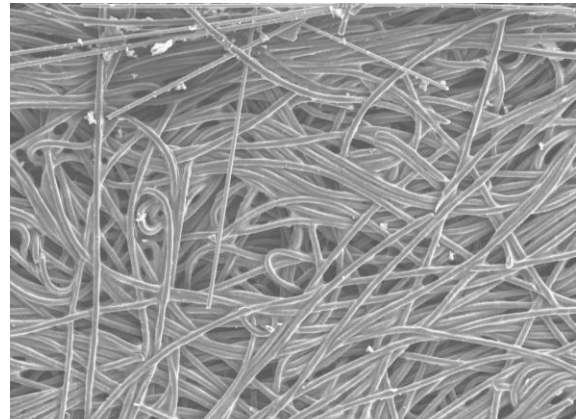
100µm



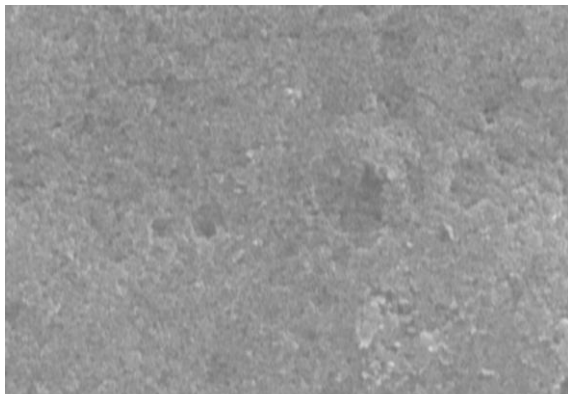
100µm



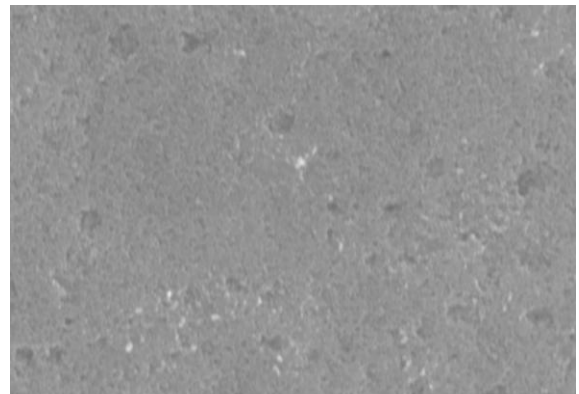
400µm



400µm



30µm



30µm

Figure A3.21: Freudenberg C6

Figure A3.22: Freudenberg C8

**APPENDIX A5: EFFECT OF CLAMPING PRESSURE ON OHMIC
RESISTANCE AND COMPRESSION OF GAS DIFFUSION LAYERS
FOR POLYMER ELECTROLYTE FUEL CELLS – published paper**

Find paper: Mason TJ, Millichamp J, Neville TP, El-kharouf A, Pollet BG, Brett DJL.
Effect of clamping pressure on ohmic resistance and compression of gas diffusion
layers for polymer electrolyte fuel cells. J Power Sources 2012;219:52–9.